



# Politecnico di Bari

Repository Istituzionale dei Prodotti della Ricerca del Politecnico di Bari

Analysis, Modelling and Design of an Indoor Positioning System for biomedical applications

This is a PhD Thesis

*Original Citation:*

Analysis, Modelling and Design of an Indoor Positioning System for biomedical applications / Piccinni, Giovanni. - ELETTRONICO. - (2019). [10.60576/poliba/iris/piccinni-giovanni\_phd2019]

*Availability:*

This version is available at <http://hdl.handle.net/11589/160042> since: 2019-01-18

*Published version*

DOI:10.60576/poliba/iris/piccinni-giovanni\_phd2019

Publisher: Politecnico di Bari

*Terms of use:*

(Article begins on next page)



Politecnico  
di Bari

Department of Electrical and Information Engineering  
ELECTRICAL AND INFORMATION ENGINEERING

Ph.D. Program

SSD: ING-INF/01–Electronics for  
Telecommunications

**Final Dissertation**

---

Analysis, Modelling and Design of an  
Indoor Positioning System for biomedical  
applications

---

by

Piccinni Giovanni:

Supervisor:

Prof. Gianfranco Avitabile

*Coordinator of Ph.D. Program:*

*Prof. Alfredo Luigi Grieco.*

## Summary

The indoor positioning systems (IPS) became very attractive in a recent past, because they can be used in more applications and in different scenarios. In fact, the use of an indoor positioning system allows to provide location-based services (LBS), e.g., safety information, indoor navigation, location-based advertisements and so on. Moreover, the IPS can be exploited in medical surgery applications where it is required a very precise and accurate position estimation. For example, in radiotherapy systems, the treatment zone must be localized with a sub-mm precision to focus the radiation beam in the precise body area and so limit the damages to the healthy.

In this thesis a novel solution is proposed to evaluate the position of an active target placed in harsh indoor environments. The proposed solution exploits a GPS-like scheme composed by a single transmitter and four synchronized receivers. One of them is selected as system origin and the position are evaluated computing the Time Difference of Arrival of the received signals.

The hardware of each nodes is based on the Software-Defined Radio architecture to obtain a scalable and feasible positioning system able to adapt its characteristics as function of the design specifications. Moreover, it requires simple software instructions to change the properties of the transmit signal, whereas the analog blocks can be designed to cover a wide frequencies range. Hence, the target positions are evaluated in digital domain by means of a signal processing algorithm that can be implemented by a FPGA or a DSP.

The transmit signal combines the properties of well-known Zadoff-Chu sequences with the characteristics of the OFDM modulation scheme to obtain a signal very robust against the multipath. The sense signal is composed by only pilot subcarriers that represent a specific coefficient of the Zadoff-Chu sequence.

Chapter 1 resumes the state of art of the indoor positioning system, also describing the main techniques that are implemented to evaluate the position of an active target.

Chapter 2 introduces the Zadoff-Chu sequences and describes in detail the ranging algorithm used by the proposed solution to evaluate the difference distance between two or more receivers.

In chapter 3 there is a detailed description of the system model implemented in the MATLAB environment. Several simulations are performed to evaluate the overall performance before in ideal conditions considering an ideal channel and then considering the severe multipath conditions of

the radio channel. In this chapter is analyzed the influence of the bandwidth, the number of subcarriers and the signal to noise ratio, on the accuracy and the system precision. Moreover, it is implemented a strategy to mitigate the effects of the multipath on the distances estimates. Finally, it is modelled the design of a sub-sampling receiver to reduce the requirements of the Analog to Digital converter that represent the critical block of the Software-Defined Radio architecture.

Chapter 4 describes the design of the different blocks that comprise the analog front-end of the transmitter and receivers. Moreover, the performance of the system is analyzed in severe multipath conditions and using different type of antennas.

The last Chapter illustrates the design of the integrated circuits for the first two blocks of the analog front-end of the receivers. For both, it is introduced a novel design strategy based on the well-known  $g_m$  over  $I_D$  methodology. The design methodology proposed is able to improve the overall performance of the basic circuit topologies. In others word, with the proposed design method, the overall performance of the basic circuit-schemes can be improved to achieve the same results of the complex architectures. In this case is possible to save area on chip and reduce the requirements of the power consumptions of the circuits.

# Contents

Summary.....	1
1 Indoor Positioning Systems: The State of the Art.....	10
1.1 System Technologies.....	10
1.2 Basic Measuring Principles.....	13
1.3 Distance Measurement Techniques.....	14
1.3.1 Frequency-Modulated Continuous Wave systems .....	14
1.3.2 Wideband Spread-Spectrum-based systems.....	17
1.3.3 Impulse-Radio MB and UWB systems .....	19
1.3.4 Multi-Carrier WB and UWB systems .....	21
1.4 Position Estimation Algorithms .....	24
1.4.1 Geometric position estimation algorithms.....	24
1.4.2 Statistical position estimation algorithms.....	27
1.5 Conclusions .....	29
2 Indoor Positioning System: The system design.....	31
2.1 Zadoff-Chu Sequences .....	31
2.2 Orthogonally Frequency Division Multiplexing (OFDM).....	34
2.3 Channel Modeling .....	36
2.3.1 Path gain .....	37
2.3.2 Power Delay Profile.....	39
2.3.3 Small-scale fading .....	40
2.4 Signal Pattern Generation.....	42
2.5 Distance Ranging Algorithm.....	44
2.6 Conclusions .....	53
3 Indoor Positioning System: System Modeling .....	55
3.1 Additive Gaussian White Noise channel.....	55

3.1.1	Bandwidth vs SNR .....	56
3.1.2	Subcarriers vs SNR.....	60
3.2	Multipath Channel.....	64
3.2.1	Multipath Echo Estimation Algorithm .....	70
3.3	Kalman Filtering .....	82
3.4	Analog to Digital Converter: Sub-Nyquist receiver.....	91
3.5	Conclusions .....	96
4	Indoor Positioning System: Hardware Design & Measurements .....	98
4.1	Transmitter and Receiver Architectures.....	98
4.2	AWGN Channel Measurements.....	99
4.3	Radio Channel .....	103
4.3.1	Test-bench #1 .....	103
4.3.2	Transmitter and Receiver Design .....	107
4.3.3	Test-bench #2 .....	112
4.3.4	Test-bench #3 .....	120
4.4	Conclusions .....	124
5	Indoor Positioning System: Integrated Circuit Design.....	126
5.1	Systematic Design Approach .....	126
5.2	Low Noise Amplifier Design.....	129
5.3	Active Mixer Design .....	143
5.4	Conclusions .....	151

# List of Figures

Figure 1.1: (a) FMCW signal (b) FMCW-based system block diagram.....,16

Figure 1.2: Principle of the chopping of the transmit signal..... 17

Figure 1.3: (a) Spread Spectrum Bandwidth effect (b) Spread Spectrum block diagram ..... 18

Figure 1.4: 3D Positioning system based on Spread Spectrum technique proposed by Meier et al.  
..... 18

Figure 1.5: IR-UWB Receiver Block Diagram..... 20

Figure 1.6: IR-UWB block diagram proposed by Mahfouz et al. [REF] ..... 21

Figure 1.7: (a) Iterative search and subtract peak algorithm (b) Multipath received signal vs clean  
received signal. .... 21

Figure 1.8: Direct-conversion trans-receiver chain ..... 23

Figure 1.9: Trilateration-based position estimation in 2D coordinates..... 25

Figure 1.10: 2D Position geometric approach using AOA algorithms..... 25

Figure 1.11: 2D hyperbolic Position Location..... 26

Figure 1.12: 2D position estimation with TOA/AOA combined approach ..... 27

Figure 2.1: (a) Real and imaginary part of a 52-length ZC sequence with  $u=1$ . (b) Real and  
imaginary of a 52-length ZC sequence with  $u=3$ ..... 33

Figure 2.2: Example of correlation function. In blue the cross-correlation function of 52-length ZC  
sequence and its copy cyclically shifted by 10 samples ( $u=1$ ). In red the cross-correlation function  
between two 52-length ZC sequences with different  $u$  values ( $u_1=1, u_2=3$ )..... 33

Figure 2.3: (a) FDM architecture. (b) OFDM architecture..... 35

Figure 2.4: OFDM signal spectrum (linear scale) ..... 35

Figure 2.5: Example of a Channel Impulse Response for an indoor environment..... 41

Figure 2.6: 6 ISI effect of a multipath channel over an OFDM symbol. .... 42

Figure 2.7: Signal pattern for a 52-length ZC sequence and 64-length OFDM symbol..... 43

Figure 2.8: Real and Imaginary part of the transmit signal ..... 43

Figure 2.9: indoor positioning system – system architecture ..... 46

Figure 2.10: Example of angle function for a distance of 2.9 meters..... 47

Figure 2.11: Symbol transmit Frame. .... 48

Figure 2.12: 2-D positioning system model..... 49

Figure 3.1: Fig. 1 System Precision in time domain as function of the SNR ..... 56

Figure 3.2: System precision in frequency domain as function of the SNR.....	57
Figure 3.3: TO and CFO estimation as function of the SNR. The values are extracted for a bandwidth of 100 MHz. ....	58
Figure 3.4: System Mean Error as function of the SNR, evaluated in time-domain .....	59
Figure 3.5: System Mean Error as function of the SNR, evaluated in frequency-domain .....	59
Figure 3.6: Time-domain system precision as function of SNR and the number of subcarriers..	60
Figure 3.7: Frequency-Domain System precision as function of SNR and the number of subcarriers .....	61
Figure 3.8: CRLB as function of the SNR and for different values of subcarriers.....	62
Figure 3.9: TO and CFO estimation as function of the SNR. The number of subcarriers is set to 512.....	62
Figure 3.10: Time-Domain System Accuracy as function of the SNR and the OFDM length. The signal bandwidth is set to 100 MHz.....	63
Figure 3.11: Frequency Domain System Accuracy as function of the SNR and the OFDM length. The signal bandwidth is set to 100 MHz. ....	64
Figure 3.12: TO system precision considering a 64-length OFDM symbol with 100 MHz of bandwidth.....	65
Figure 3.13: TO system accuracy considering a 64-length OFDM symbol with 100 MHz of bandwidth.....	65
Figure 3.14: Cross-Correlation in time domain in presence of multipath echos .....	66
Figure 3.15: Error as function of the multipath echo distance and amplitude.....	67
Figure 3.16: CFO System precision considering a 64-length OFDM symbol with 100 MHz of bandwidth.....	68
Figure 3.17: CFO System accuracy considering a 64-length OFDM symbol with 100 MHz of bandwidth.....	68
Figure 3.18: Angle function considering an undirect path placed to 4.5 m away from the direct path and with $\alpha=0.2$ . ....	69
Figure 3.19: (a) Block diagram of the system in presence of multipath. (b) Block diagram of the system with FIR filter .....	72
Figure 3.20: Breakdown distance as function of the signal bandwidth. ....	77

Figure 3.21: Absolute value of the error in time-domain as function of the multipath echo distance, using a 64-length OFDM symbol with 100 MHz of bandwidth and 20 dB of SNR. .... 78

Figure 3.22: Absolute value of the error in frequency-domain as function of the multipath echo distance, using a 64-length OFDM symbol with 100 MHz of bandwidth and 20 dB of SNR. .... 79

Figure 3.23: TO system precision as function of the SNR and the echo amplitude. The precision is evaluated considering a 64-length OFDM symbol with 100 MHz of bandwidth and 20 dB of SNR. .... 80

Figure 3.24: TO system accuracy as function of the SNR and the echo amplitude. The precision is evaluated considering a 64-length OFDM symbol with 100 MHz of bandwidth and 20 dB of SNR. .... 80

Figure 3.25: CFO system precision as function of the SNR and the echo amplitude. The precision is evaluated considering a 64-length OFDM symbol with 100 MHz of bandwidth and 20 dB of SNR..... 81

Figure 3.26: CFO system accuracy as function of the SNR and the echo amplitude. The precision is evaluated considering a 64-length OFDM symbol with 100 MHz of bandwidth and 20 dB of SNR..... 82

Figure 3.27: Difference distance estimation with the presence of the Kalman Filter..... 85

Figure 3.28: TO System precision without and with the Kalman filter..... 86

Figure 3.29: TO System accuracy without and with the Kalman filter. .... 86

Figure 3.30: CFO System precision without and with the Kalman Filter ..... 87

Figure 3.31: CFO System precision without and with the Kalman filter ..... 87

Figure 3.32: TD System precision in presence of multipath and Kalman Filter ..... 88

Figure 3.33: TD System accuracy in presence of multipath and Kalman Filter..... 89

Figure 3.34: CFO System precision in presence of multipath and Kalman Filter..... 90

Figure 3.35: CFO System accuracy in presence of multipath and Kalman Filter ..... 90

Figure 3.36: (a) Signal Spectrum before the subsampling (b) Signal spectrum after subsampling. .... 93

Figure 3.37: (a) Comparison of system precision in time-domain for different  $k_{ss}$  (b) Comparison of system precision in time-domain for different  $k_{ss}$ ..... 94

Figure 3.38: (a) Comparison of system precision in frequency-domain for different  $k_{ss}$  (b) Comparison of system precision in frequency-domain for different  $k_{ss}$ . .... 96

Figure 4.1: System Architecture of the transmitter and the receiver. ....	98
Figure 4.2: (a) System Architecture of the transmitter and the receiver for the first test-bench. (b) Receiver printed circuit board.....	100
Figure 4.3: Absolute error in AWGN channel measurements.....	101
Figure 4.4: (a) System precision (b) System accuracy .....	102
Figure 4.5: Microstrip Patch antenna with coaxial probe fed connector .....	103
Figure 4.6: Directivity Diagram for the horizontal (a) and azimuthal planes (b). ....	104
Figure 4.7: Microstrip Patch Antenna input matching.....	105
Figure 4.8: Radio Channel: absolute error as function of the distance .....	106
Figure 4.9: Radio Channel: (a) system precision, (b) system accuracy.....	107
Figure 4.10: IF analog Chebyshev: (a) bandpass, (b) input/output matching.....	108
Figure 4.11: PCB Transmitter analog front-end. ....	109
Figure 4.12: RF-Passband filter realized with coupled transmission lines.....	109
Figure 4.13: RF-Passband filter measures of scattering parameters.....	110
Figure 4.14: PCB Receiver analog front-end.....	111
Figure 4.15: Patch antenna with microstrip line feed for 3.35 GHz. ....	112
Figure 4.16: Input matching of the Patch antenna with microstrip line feed.....	112
Figure 4.17: System precision for the subset {A, C, E}. ....	115
Figure 4.18: System precision for the subset {B, D, F}. ....	115
Figure 4.19: TDoA between the receiver 1 and the receiver 2 evaluated for the subset A. ....	116
Figure 4.20: TDoA between the receiver 1 and the receiver 2 evaluated for the subset A. The antenna is moved with steps of 0.5 cm. ....	116
Figure 4.21: TDoA between the receiver 1 and 2 in presence of a metallic doors. ....	117
Figure 4.22: Array 2x2 of microstrip patch antennas with corporate fed network.....	118
Figure 4.23: Array of 2x2 of microstrip patch antennas directivity diagram (a) azimuthal plane (b) horizontal plane.....	119
Figure 4.24: Array of 2x2 of microstrip patch antennas input matching.....	120
Figure 4.25: TDoA estimates using the patch antenna array for bot transmitter and receivers (a) Rx <sub>1</sub> vs Rx <sub>2</sub> (b) Rx <sub>1</sub> vs Rx <sub>3</sub> (c) Rx <sub>1</sub> vs Rx <sub>4</sub> .....	122
Figure 4.26: TDoA estimates using the patch antenna array for bot transmitter and receivers. The receivers are placed close to the metallic doors (a) Rx <sub>1</sub> vs Rx <sub>2</sub> (b) Rx <sub>1</sub> vs Rx <sub>3</sub> (c) Rx <sub>1</sub> vs Rx <sub>4</sub> ..	123

Figure 5.1: (a) $I_D/W$ vs. $g_m/I_D$ (b) transit frequency $f_T$ vs. $g_m/I_D$ (c) intrinsic gain $g_m/g_{DS}$ vs. $g_m/I_D$ for the IHP 0.13 $\mu\text{m}$ process. ....	130
Figure 5.2: Architecture of a conventional four stages Distributed Amplifier. ....	131
Figure 5.3: Design Framework's Flow Chart. ....	133
Figure 5.4: Transistor widths as function of $g_m/I_D$ for a $g_m$ of 60 mS. ....	134
Figure 5.5: Examples of DA Lookup Tables - (a) Gain vs. $g_m/I_D$ (b) Noise Figure vs. $g_m/I_D$ (c) Power DC consumption vs. $g_m/I_D$ (d) FOM vs. $g_m/I_D$ . ....	136
Figure 5.6: Inductors Q factor vs. frequency. ....	137
Figure 5.7: FOM <sub>2</sub> vs $g_m/I_D$ . ....	139
Figure 5.8: DAs performances (a) Transducer gain (b) Input/Output Return Loss (c) Noise Figure of the proposed DAs. ....	141
Figure 5.9: (a) Final three stages DA layout (b) Final four stages DA layout, ....	142
Figure 5.10: (a) Architecture of a conventional double balanced Gilbert cell mixer ....	144
Figure 5.11: (a) Solution space versus $g_m/I_{D(TS)}$ and $g_m/I_{D(SS)}$ ratios. (b) IIP3 of the mixer versus $g_m/I_{D(TS)}$ and $g_m/I_{D(SS)}$ ratios. (c) Average Noise Figure versus $g_m/I_{D(TS)}$ and $g_m/I_{D(SS)}$ ratios. (d) Conversion gain of the mixer versus $g_m/I_{D(TS)}$ and $g_m/I_{D(SS)}$ ratios. (e) DC-power consumption of the system versus $g_m/I_{D(TS)}$ and $g_m/I_{D(SS)}$ ratios. ....	148
Figure 5.12: FOM versus $g_m/I_{D(TS)}$ and $g_m/I_{D(SS)}$ ratios. ....	148
Figure 5.13: Post-Layout mixer conversion gain vs LO power (b) Post-Layout mixer noise figure vs frequency (c) Post-Layout mixer IP3. ....	150
Figure 5.14: Final Layout of the Double-Balanced Gilbert Cell Mixer. ....	151

# 1 Indoor Positioning Systems: The State of the Art

The indoor positioning systems (IPS) became very attractive in a recent past, because they can be used in more applications and in different scenarios. In fact, the use of an indoor positioning system allows to provide location-based services (LBS), e.g., safety information, indoor navigation, location-based advertisements and so on. Moreover, the IPS can be exploited in medical surgery applications where it is required a very precise and accurate position estimation. For example, in radiotherapy systems, the treatment zone must be localized with a sub-mm precision to focus the radiation beam in the precise body area and so limit the damages to the healthy.

The research in this topic focus on both technologies and algorithms used to estimate the target position to improve the accuracy and the precision without a cost or complexity increase of the system. There are many challenges in the IPS design due to the nature of the indoor environment, e.g., high attenuation and signal scattering; fast temporal changes with the presence of people and obstacles, and so on. The most relevant problem that affects every indoor environment is the multipath. In fact, the signal transmitted by an antenna, or a different source, e.g. loudspeaker in case of sound, is reflected by walls and any obstacles present in the environment. When the reflections reach the receiver, they generate interferences that directly affect the distance estimation. It's very hard to resolve this problem especially when the multipath reflections are very close in time with the desired signal. Often, the solution to distinguish the Line of Sight (LOS) signal from Non-Line of Sight (NLOS) paths is to use a diversity scheme. For example, frequency diversity transmits the signal on multiple frequencies, the time diversity repeats the signal multiple times and the space diversity uses multiple antenna to transmit and receive the signal.

## 1.1 System Technologies

The design of an IPS falls in two macro-categories. In the first one, an ad-hoc system is developed according to the target application; in the second one the services of an existing communications network are extended to support the position estimation. Although this last approach is cheaper than the first one, it was not able to achieve great accuracy and precision (currently, of the order of 1m) because the only possible optimization is trough signal processing. On the other hand, the major advantage of the first approach is that the system is totally defined by the designer and so it can be customized to the target application achieving very high accuracy and precision ( $< 1\text{m}$ ). The choice of one of this two approaches, strictly depends on the target application that defines

also other system parameters as cost, coverage area, number of users, scalability and so on. Table I resumes the characteristics of the main technologies employed in the IPS design, indicating for them the accuracy and the typical applications [1]. Note that an IPS can be realized using both RF-based and non-RF-based technologies with the proper advantages and disadvantages. For example, GPS system is used for tracking a mobile device in outdoor environment, so it cannot be used in indoor applications due to the poor signal. For these applications was developed the Assisted-GPS (A-GPS) [2] that uses the cellular network to help the GPS signal in the satellites-tracking. The GPS receiver sensitivity is improved by approximately of 10 dB that allows to achieve a precision of about 10 meters even in indoor position estimation. However, GPS-based methods suffer from poor signal strength and, most importantly, have a low multipath immunity to provide high position accuracy.

Methods based on 802.11b/Wi-Fi [3]-[5], Bluetooth [6] and RFID [7] are very cheap because they exploit the existing communication networks and require low-complexity and low-cost infrastructures to estimate the position of a mobile device. However, the accuracy is not high ( $> 1\text{m}$ ), in fact, in these systems, the accuracy is constrained to the system hardware and to the signal properties, for example, carrier frequency, signal bandwidth, interferences-immunity and so on [8]-[10].

The most accurate RF-based IPSs exploit wideband (WB) and ultra-wideband signals (UWB). Two main approaches are possible: Impulse Radio-UWB (IR-UWB) [11] where it is transmitted a very short pulse ( $< \text{nanoseconds}$ ) with low duty-cycle, and Carrier-Based-UWB (CB-UWB) [12] that exploits the multicarrier techniques as for example the Orthogonally Frequency Division Multiplexing (OFDM). As previously cited, in the RF-based methods, the system accuracy depends on the signal bandwidth. A more accurate system calls for more signal bandwidth. In the WB and UWB systems, the signal occupies a very large spectrum, so, the signal duration is very short (bandwidth is inversely proportional to the signal duration). In LOS scenarios, this property allows to separate the direct signal from the NLOS paths that cause errors in the distance estimation. Hence, these systems are more robust against the multipath because it is possible to implement techniques for reducing the multipath effects. The major drawbacks of these system are related to the hardware complexity and the system costs. In fact, the analog front-end (Amplifier, Filters, Mixers, ...) must be designed to support signals with a very large spectrum bandwidth and,

most of all, they call for high-speed analog to digital converters (ADC) and processors able to manage a massive amount of data to process the signal.

Finally, even a hybrid approach is possible: Priyantha et al. [13] and Fukuju et al. [14] propose two systems that combine both RF and ultrasound signals for extracting the target position. Their systems exploit the difference in propagation speeds between the RF (light velocity) and the ultrasound signal (sound velocity) to calculate the time of arrival at the mobile node. Although these systems exhibit a high precision ( $<10$  cm), they introduce an error source because the sound velocity varies with the temperature and the pressure. Moreover, they require significant preinstalled infrastructure and are sensitive to the placement of the sensors and motion of the mobile node.

From these considerations, there is not a best or a unique solution for implementing an IPS because as it strictly depends on the target application. In our case, an IPS for radiotherapy application is designed using RF-based technologies. The system must locate an active target with an accuracy in cm or mm range to focus the radiation beam in a precise treatment zone. Hence this work focuses on the WB and UWB techniques that allow to achieve the design requirements.

Table I Overview of indoor positioning technologies

<b>Technology</b>	<b>Typical Accuracy</b>	<b>Typical Coverage [m]</b>	<b>Typical Measuring Principle</b>	<b>Typical Application</b>
<b>Cameras</b>	0.1mm – dm	1 – 10	Angle measurements from images	Metrology, robot navigation
<b>Infrared</b>	cm – m	1 – 5	Thermal imaging, active beacons	People detection, tracking
<b>Sound</b>	$\mu$ m - mm	3 – 2000	Distance from time of arrival	Hospitals, tracking
<b>WLAN/WiFi</b>	2-3m	2 – 10	fingerprint	Pedestrian navigation, LBS
<b>RFID</b>	m	20 – 50	Proximity detection, fingerprint	Pedestrian Navigation
<b>Ultra-Wideband</b>	mm - m	1 – 50	Body reflection, time of arrival	Robotics, automation
<b>A-GPS</b>	2-5m	‘global’	Parallel correlation, assistant GPS	LBS
<b>Pseudolites</b>	cm - dm	10 – 1000	Carrier phase ranging	GNSS challenged pit mines

## 1.2 Basic Measuring Principles

Once defined the technology for implementing an IPS, it is necessary to study a technique that can be used to estimate the distance of a mobile device and subsequently the related position. The methods present in literature tend to evaluate the time of flight (ToF), or with direct measurements or indirectly, estimating the phase or the angle of signal arrival. In the first subset, the most used technique, named Time of Arrival (ToA) or Time of Flight (ToF) method, the system estimates the absolute travel time of a signal from a transmitter to a receiver. The distance is obtained multiplying the time estimation times the propagation velocity. This latter term in air it is equal about to the light velocity while in different materials, e.g., cables, its value is reduced by the relative dielectric constant. This technique is simple to implement but requires a very precise synchronization of transmitter and receiver clock, as even a one nanosecond error turns into a distance error greater than 30 cm. To overcome this problem, it is possible to use two or more receivers that share the clock. Selecting one of them as system origin, the IPS evaluates the Time Difference of Arrival (TDoA). In this case any offset in the unsynchronized clocks is a constant term that is eliminate calculating the difference in the time measurements. Hence, in contrast to ToA algorithms, the receivers don't need to know the absolute time at which pulse was transmitted.

Another way to resolve the synchronization problem introduced by ToA algorithms, is to measure the Round-Trip Time (RTT), i.e., the time taken by the signal to travel from a transmitter to a receiver and back. Using the RTT-based algorithms, the receivers are stand-alone devices, i.e., they don't need to share the clock, or a time synchronization is necessary. In this case the system is less complex than the first two methods, but distance measurements need to be carried out sequentially which may cause critical latencies when the mobile target is moved quickly. Moreover, the travel time (ToA, TDoA or RTT) can be indirectly estimated evaluating the Phase of Arrival (PoA) of the signal received. In other words, these systems use the received carrier phase to determine the distance between two devices. To mitigate the phase wrapping on the received signal, the phase is evaluated on multiple frequencies. In these methods the distance is determined by the rate of phase change and the accuracy and the system precision is constrained by the carrier wavelength ( $\lambda = \text{propagation velocity} / \text{carrier frequency}$ ). Often the phase is evaluated in frequency domain and so these algorithms can be combined with ToA, TDoA or RTT techniques, where the distance is estimated in time domain, to improve the distance accuracy.

Another method that can be combined with the previous algorithms is based on the estimation of the Angle of Arrival (AoA) of the signal. The incidence direction measurements are possible only if the system uses a multi-antenna array to transmit or receive the signal and the system accuracy and precision depend on two main factors: the antenna directivity and the minimum step in the beam-steering. A high number of antenna elements is required to achieve a directivity of few grades and so the system complexity accordingly increases.

There is not a best solution even among these algorithms and the choice of one of them defines the system architecture and so the relative costs and complexity. In fact, if TDoA was chosen, the system must comprise at least four receivers to extract the 3D target position. On the other hand, if ToA algorithm was implemented, the system architecture must exhibit a precise time synchronization. However, the choice of the distance algorithm not depends by the system technology. In fact, in literature are present IPSs that use the same technology, e.g. UWB, but implements different estimation algorithms.

### **1.3 Distance Measurement Techniques**

Since this work is focused on the design of an IPS able to estimate the target position with millimeter accuracy and precision, the rest of the section will describe only the subset of the most accurate and precise RF-based methods and systems present in literature. Essentially, they are WB and UWB methods.

#### **1.3.1 Frequency-Modulated Continuous Wave systems**

Wang et al. [15] propose a radar sensor that evaluates the ToA of a static or slow-moving target combining the advantages of the interferometry technology with the properties of the Frequency-Modulated Continuous Wave (FMCW) signals. The radar system operates at 5.8 GHz ISM band and exploits a signal of 160 MHz achieving an average accuracy of 1.65 cm.

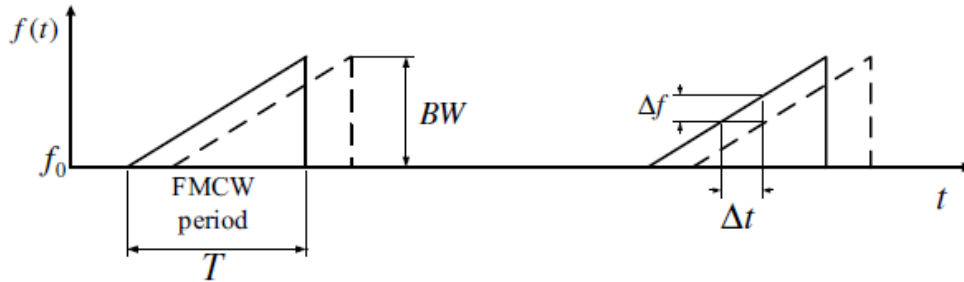
FMCW signals are widely used in radar systems because they allow to evaluate the distance of a moving objects estimating the doppler frequency [16]. Figure 1.1(a) illustrates the operation principle of a FMCW-based system. The transmit signal (solid line) is a linear chirp signal where the frequency sweeps linearly over the time within a set bandwidth. The signal received (dash line) has similar spectrum characteristics but lags the transmitted signal. Down-converting the received signal will produce and output sinewave whose frequency,  $f_{IF}$ , is proportional to the ToA,  $\Delta t$ :

$$f_{IF} = \frac{Bw}{T} \Delta t = \frac{Bw}{T} \cdot \frac{d}{c} \quad (1.1)$$

where  $Bw$  is the signal bandwidth,  $T$  is the period,  $d$  the target distance and  $c$  the speed of light ( $3 \times 10^8$  m/s). The main advantage of the FMCW-based systems is that they don't require high-speed ADCs even to evaluate great distances. In facts, from mixing operation, the resulting signal has a very low frequency, near the DC if the distance value is not high. Considering a distance  $d$  of 10 meters, a bandwidth of 160 MHz and a chirp period of 2 ms, the resulting signal has a frequency of only 2.6 kHz. In this basic form, these systems don't exhibit a high distance range resolution because it is limited only by the sweep bandwidth [16]. Considering a bandwidth of 160 MHz, the minimum distance  $\Delta d$  is:

$$\Delta d = \frac{c}{Bw} = 3.75m \quad (1.2)$$

This value can be divided by 2 if the RTT is evaluated but is too high for evaluating the distance with a mm accuracy. However, combining this technique with other methods as explained by Wang et al. [15] or using fitting algorithm, it is possible to improve range resolution even by a factor of 10 or 100. Figure 1.1(b) shows the block diagram of a FMCW-based system. It is very simple for both transmitter and receiver and, so, it can be integrated in a small chip area and employed in different applications as tank level gauging, unmanned aircraft altimeters and in industrial systems for the verification of product dimension in automated processes.



(a)

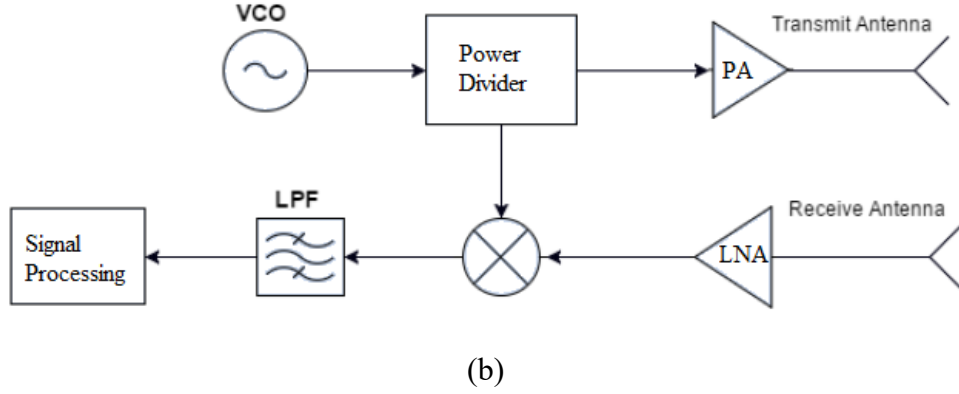


**Figure 1.1:** (a) FMCW signal (b) FMCW-based system block diagram

Another example of the use of the FMCW method combined to another technique to improve the system accuracy is presented by Waldmann et al. [17]. In their work the FMCW signal is combined with short pulses with a bandwidth of 1 GHz centered to 7.5 GHz to achieve an error of 1.7 cm in absence of multipath distortions. Linear modulated signals are used to synchronize two wireless units and afterward the distance between these units is measured using the RTT algorithm.

Hence, there are different methods to combine pulses with the FMCW signal. One way is to use the pulses to modulate the FMCW signal through a mixer; another approach is to insert a dedicated fast RF switch which is driven by a pulse generator in the transmit path. Due to the finite rise and fall times of the RF switch, the chopping of the transmit signal can be approximated by a multiplication of the FMCW signal with a Tukey window given by:

$$w(n) = \begin{cases} 1.0 & , \quad 0 \leq |n| < \alpha \frac{N}{2} \\ \frac{1}{2} \left( 1 + \cos \left( \pi \frac{n - \alpha N/2}{2(1 - \alpha)N/2} \right) \right) & , \quad \alpha \frac{N}{2} \leq |n| < \frac{N}{2} \end{cases} \quad (1.3)$$

where  $N$  represents the number of samples and the switching pulse can be correctly modeled by the appropriate choose of  $\alpha$  which determines the rise and the fall time of the pulse.

At the receiver, the chopped FMCW signal is recovered mixing the received chopped signal with a locally generated no-chopped signal. The result is then filtered with a low-pass filter with a significantly smaller bandwidth than the pulse repetition rate. This filter eliminates all higher frequency mixing products including the rectangular signal parts that have been generated by the RF switch. The filter output is a sinusoidal IF signal without the chopping, which can easily be digitized. The Figure 1.2 sketches the block diagram of the hardware demonstrator proposed by Waldmann et el [17].

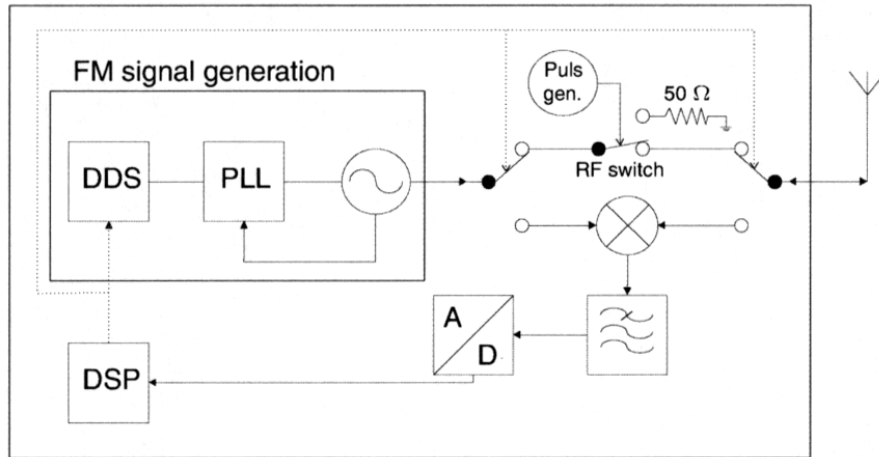


**Figure 1.2:** Principle of the chopping of the transmit signal

A direct digital synthesizer (DDS) generates a signal which serves as the reference signal for a Phase Locked Loop (PLL). In combination with a wideband Voltage-Controlled Oscillator (VCO) the signals with linear frequency modulation are generated. In transmit mode, the output of the VCO is chopped by a fast RF switch and then sent to the antenna. In the receive mode the output of the local oscillator is fed to a mixer, where it is multiplied with the received signal from the antenna. Afterward the signal is low pass filtered and digitized. The digital values are read by a digital signal processor (DSP) where the algorithms are performed to determine the offsets in time  $\Delta t$  and frequency  $\Delta f$  and correct them by reprogramming the DDS.

### 1.3.2 Wideband Spread-Spectrum-based systems

The Spread Spectrum (SS) modulation was born in military applications and now is one of the fundamental building blocks in current and next-generation wireless systems. SS uses a wideband, noise-like signals that are hard to detect, intercept, or demodulate. These are the main advantages of the SS-based systems. Different techniques are available, but all are based on a common principle: *attaching a code (or sequence) to the communication channel*. The manner of inserting this code precisely defines the SS technique. Hence the SS is a RF communications system in which the baseband signal bandwidth is intentionally spread over a larger bandwidth by injecting a higher frequency signal. As a direct consequence, energy used in the signal transmission is spread over a wider bandwidth and appears as noise (Figure 1.3(a)). Figure 1.3 (b) shows a simple block diagram of a SS-based transmitter and receiver. To apply a spread-spectrum technique, simply inject the corresponding spread-spectrum code somewhere in the transmitting chain before the antenna. Conversely, the code can be removed in the receiver chain before data retrieval,

recovering the information into its original bandwidth. Obviously, the transmitter and the receiver must share the same code [18].

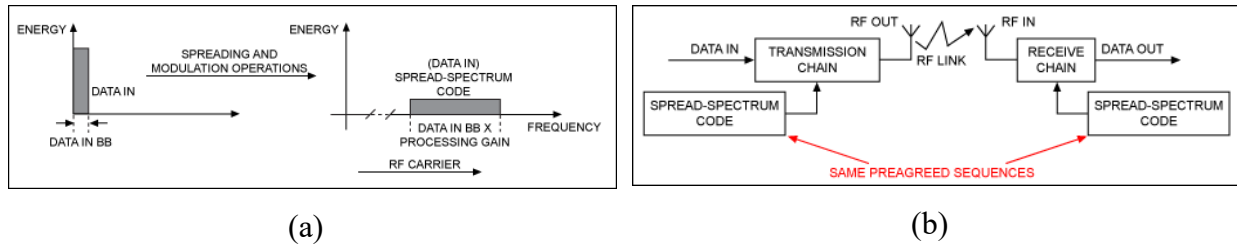


**Figure 1.3:** (a) Spread Spectrum Bandwidth effect (b) Spread Spectrum block diagram

The use of signals with a large bandwidth, allows to exploit the SS-based techniques for measuring the distance between two active nodes and so implementing an indoor positioning system with a high accuracy. In fact, Meier et al. [19]-[20] propose a 3D positioning system based on a wideband pseudo noise (PN) signal with a bandwidth of up to 3.2 GHz centered at 24 GHz. The proposed system is able to operate in an indoor multipath scenario, achieving a system accuracy in the mm range. The system presents the same advantages of the SS-based techniques and, also, the wideband code-based transmission enables channel separation of different transmitters. The system exploits a GPS-like scheme and it comprises three correlator receivers and a single transmitter (Figure 1.4).

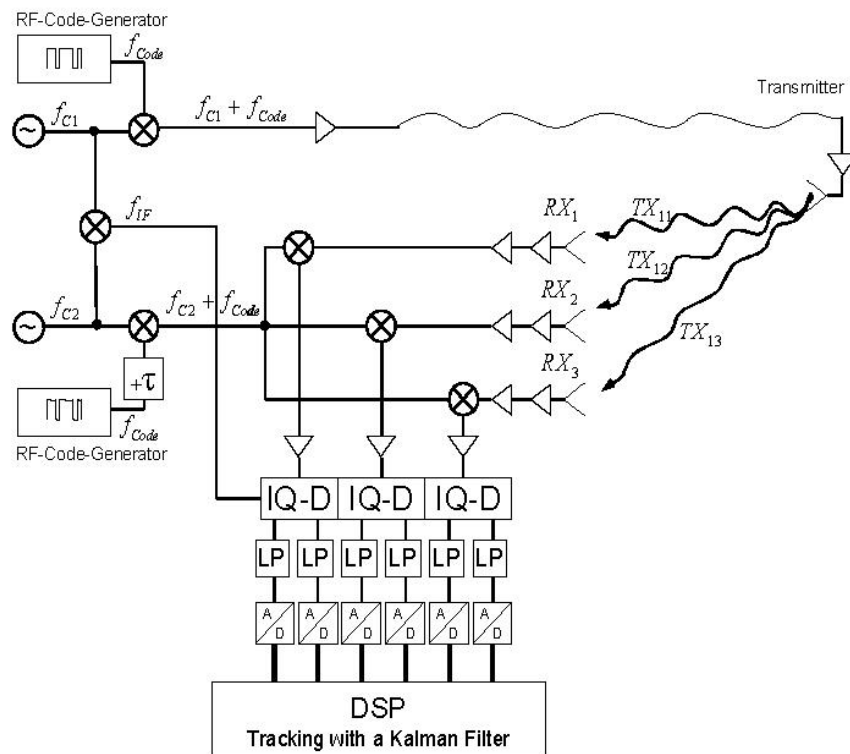


**Figure 1.4:** 3D Positioning system based on Spread Spectrum technique proposed by Meier et al.

The transmitter generates a PN code with a bandwidth of 3.2 GHz that is identical at the receiver side. After, the code is upconverted towards the carrier frequency of 24 GHz and transmitted on the channel. The receivers operate through a correlator scheme: it generates the same fast sequence code  $c(t)$ , with a variable time delay  $\tau$ . After  $c(t - \tau)$  is correlated with the received code  $c(t - \Delta t)$ . When the delay  $\tau$  is equal to the propagation delay  $\Delta t$ , the correlation function (that is an impulsive function from the PN signal properties) exhibits a peak that can be extracted to measure the ToA of the system. The correlator is divided into two parts: the multiplication, which is accomplished on the high frequency front-end, and the summation, which is calculated in the analog part of the baseband.

The critical aspect of this system is the synchronization between the PN code for both the transmitter and the receivers. To overcome this problem, the authors introduce a second transmission path to generate a common time base.

### 1.3.3 Impulse-Radio MB and UWB systems

The systems based on IR-MB or IR-UWB transmit very short pulses in time domain ( $<1$  ns) to estimate the distance between two or more devices. The estimation process involves the detection of the first arrival path of the pulse and it allows to distinguish the paths related to the multipath delays. The impulse-radio is generated in time domain which pulse shaping and filtering is implemented to obtain a signal that has the desired frequency spectrum. Many suitable pulse shaping options are possible. The most practical and feasible pulse shape, used in the IPS design, is the Gaussian pulse and its derivatives expressed by the equation below:

$$g(t) = \frac{t}{\tau} \exp\left(\frac{t}{\tau}\right)^2 \quad (1.4)$$

where  $\tau$  is the pulse width. The Gaussian pulse is widely used because it exhibits the lowest side lobe energy due to the smooth rise and fall of the time domain signal. Generally, these systems generate carrier-free pulses that occupy the bandwidth from 3.1GHz to 10.6 GHz as established by the Federal Communications Commission (FCC) [21]-[22]. One practical way of generating the pulse involves the use of a transmission line to generate tunable Gaussian monocycle pulses. It is also possible to generate the impulse digitally by adding two digital pulses that are delayed from each other. Figure 1.5 sketches the block diagram of a typical IR-UWB receiver. It consists of a wideband analog correlator comprises by a multiplier followed by an integrator. The received

pulse is multiplied with a local copy of the waveform and the result goes in input to the integrator. The output of this last block can be digitally converted and processed to extract the distance range.

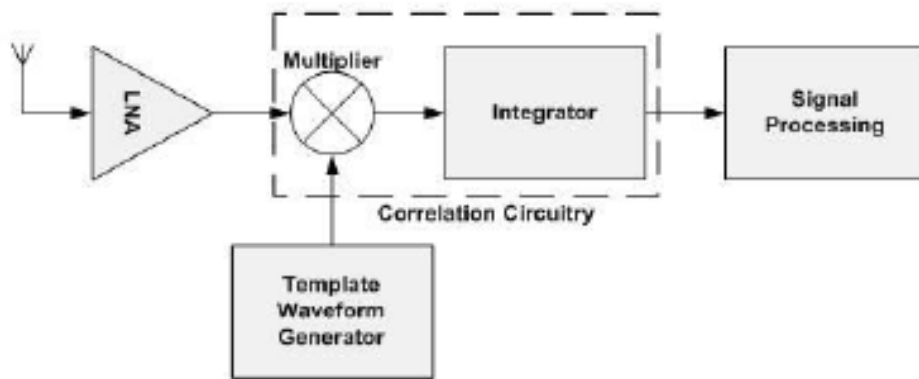


**Figure 1.5:** IR-UWB Receiver Block Diagram

Mahfouz et al. [23] proposes a high-accuracy indoor 3D positioning system that use an 8 GHz carrier signal modulated by a 300-ps Gaussian pulse. The proposed system exploits the same GPS-like scheme presented by Meier et al [20], with four receivers that localize the position of a mobile transmitter. The pulse is generated with a step-recovery diode and the authors propose a novel input matching to prevent pulse echoing, minimize pulse-width broadening, and suppress any significant pulse distortions. Figure 1.6 represents the block diagram of the system proposed by the authors. At the receiver-side, the modulated pulse is firstly amplified by a Low-Noise Amplifier (LNA) and, then, demodulated to obtain the in-phase/quadrature (I/Q) signals. After going through a low-pass filter (LPF) with a passband of DC-5GHz to suppress the 8GHz carrier signal, the I/Q signals are sub-sampled using an UWB sub-sampling mixer, extending them to a larger time scale while maintaining the same pulse shape. The sub-sampling mixer uses extended time techniques to achieve equivalent sampling rate more than 100 GS/S, which yields millimeter-range sample spacing. Finally, the extended I/Q signals are processed by a conventional ADC and standard Field Programmable Gate Array (FPGA) unit.

The authors propose an iterative peak subtraction algorithm with additional pre-processing to extract the peak of the direct path between the transmitter and the receiver. The algorithm is able to detect and subtract multipath peaks from the received signal using a clean template of the received signal to obtain an accurate estimation of the main peak (Figure 1.7). The experimental results have demonstrated that the system proposed achieve a system precision of 1.53 mm in 3D case using four receivers, with an accuracy of only 3.62 mm and a worst case of 5.6 mm.

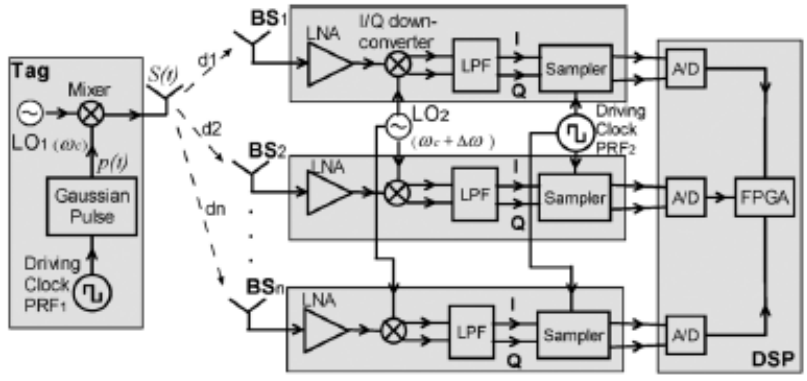


Figure 1.6: IR-UWB block diagram proposed by Mahfouz et al. [REF]

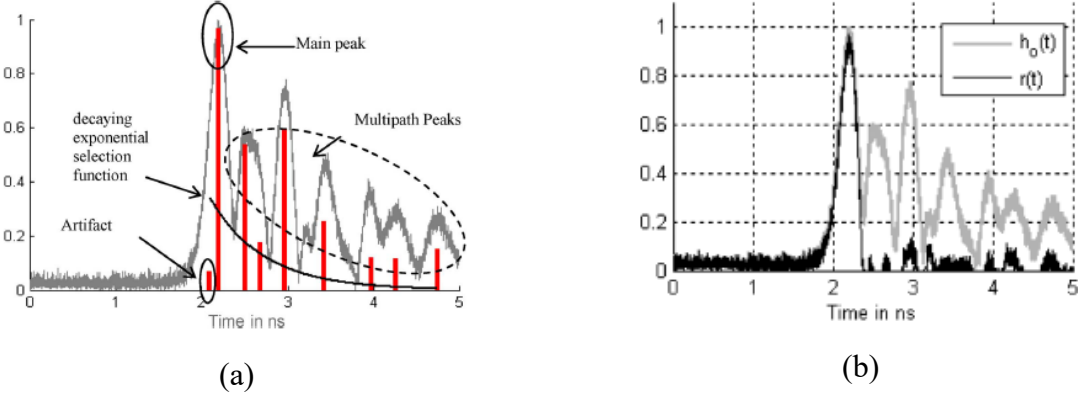


Figure 1.7: (a) Iterative search and subtract peak algorithm (b) Multipath received signal vs clean received signal.

### 1.3.4 Multi-Carrier WB and UWB systems

The MC-UWB systems transmit simultaneously many subcarriers, orthogonally spaced, to estimate the distance between two active devices. These kinds of systems don't exhibit the time-domain resolution offered by the IR-UWB IPSs but, evaluating the phase of arrival of a multicarrier signal, allows to achieve a super resolution in frequency domain. Since each subcarrier is generated based on the same reference clock: changes in the relative phase of the signal with respect to the initial phase pattern determines the change in distance. The MC-UWB systems occupy a very small bandwidth than the IR-UWB systems and, moreover, they offer a high spectral efficiency and flexibility. In fact, it is not necessary to have subcarriers present at each location, and, each of them can be nullified or placed at a frequency which allows it to co-exist with other systems occupying the same band. The MC-UWB time domain signal can be represented as the sum of M subcarriers with a frequency spacing of  $\Delta f$ :

$$s(t) = \sum_{m=0}^{M-1} A e^{2\pi(f_0+m\Delta f)t} \quad (1.5)$$

These two parameters define the bandwidth and the period of the MC-UWB signal: higher  $M$  and wider subcarrier span results in higher multipath resolution and high multipath robustness. The main drawback of a multicarrier-based system is that it needs a robust synchronization and carrier offset procedures because any offset error may introduce high errors in distance ranging.

Another important advantage of the MC-UWB systems is that the baseband signal, in the transmitter path, can be generated in digital domain and then with a Digital to Analog Converter (DAC), converted in analog domain. In this manner, the transmitter architecture is very simple: it does not need  $M$  modulators because the orthogonality between the subcarriers can be obtained applying the Inverse Discrete Fourier Transform operation in digital domain. Moreover, in this domain any offset in the signal amplitude, phase or time delay can be easily avoided or recovered. On the other hand, the transmitter needs highly linear RF components to achieve a good dynamic range that determines the range of operation for the positioning system. Even the receiver architecture is very simple because once down-converted the signal to IF frequencies, it can be acquired and digitalized to apply the signal processing algorithms. As previously described, the critical parts of the receiver are related to the signal synchronization that can be divided in three main categories: carrier and frequency recovery, symbol timing recovery and sampling time recovery.

Ayhan et al. [24] proposes a sub-mm ranging system, which estimates the ToA of a RF signal between two nodes with a frequency domain estimator. In their work, a simulation precision better than 1 mm is obtained for SNRs below 0 dB, by transmitting an Orthogonal Frequency Division Multiplexing (OFDM) like signal whose duration is 9  $\mu$ s, with a 6 GHz bandwidth on a 60 GHz carrier. The propose system exploits a direct-conversion architecture for the transmitter and the receiver, represented in Figure 1.8.

The ranging distance is divided in three main steps: in the first one a coarse distance value is obtained evaluating the correct starting point of the receive signal. In the second one the previous value is fine adjusted through a frequency domain estimator that evaluate the phase of the received signal. In the last one a super fine range estimation is performed calculating the carrier phase offset introduce by the ToA of the system.

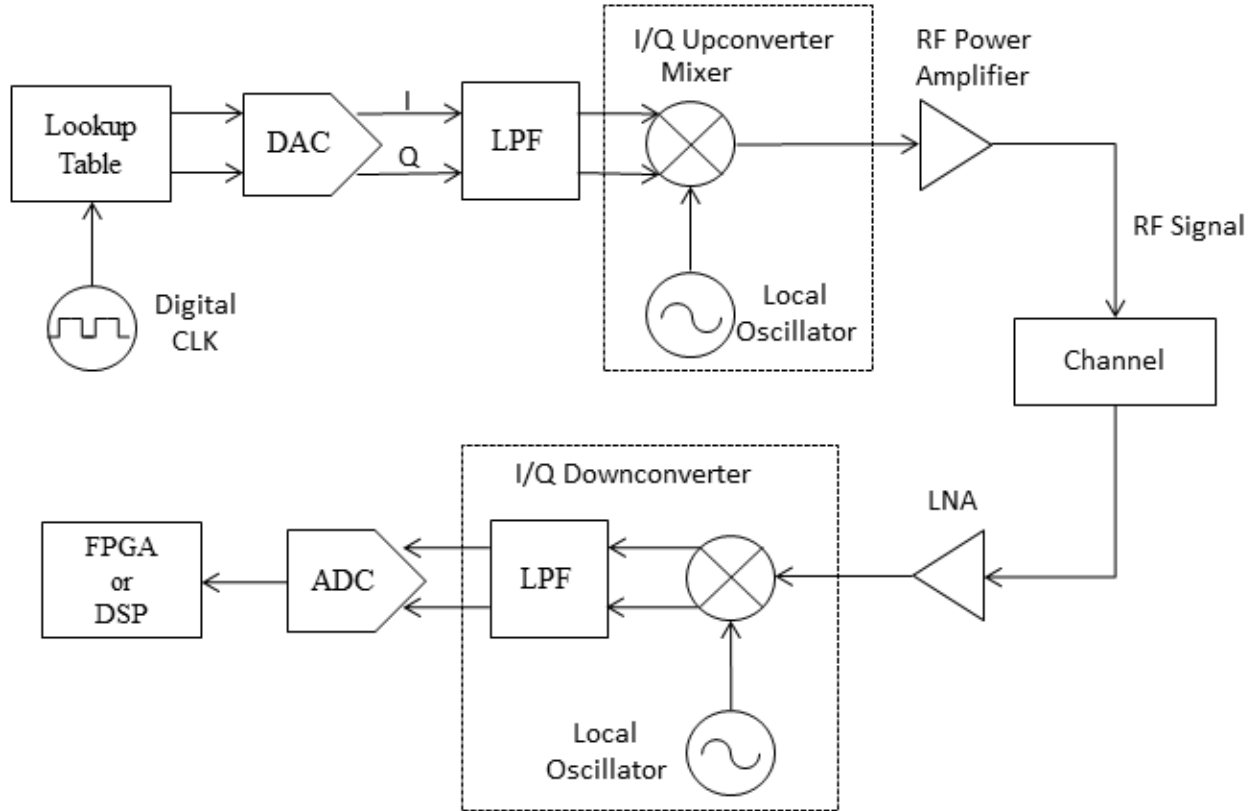


**Figure 1.8:** Direct-conversion trans-receiver chain

Other examples of works that use a multicarrier signal are presented in [25] and [26] where is analyzed and simulated even a totally NLOS scenario achieving a cm-accuracy and precision.

In conclusion, to achieve a mm or sub-mm accuracy and precision in the distance estimation using a RF-based system, the UWB techniques are mandatory. Two main UWB techniques are possible: Impulse Radio based and Multicarrier based. The first one evaluates the propagation delay in time domain transmitting very short pulses that allow to separate the direct path from the multipath reflections. The system can achieve very high accuracy and precision in distance ranging, and the architecture of the transmitter and the receiver require less RF components with relaxed specifications in term of linearity. However, these systems are more sensitive to the pulse shaping that, in turn, is affected by the parasitic capacitances generated within the circuit, and, also, a high-speed ADC is necessary to achieve a super fine resolution. Moreover, the design of the single blocks, e.g. LNA, mixers, input/output matching networks, antennas and so on, are more complex than other methods due to the extremely large bandwidth ( $B \geq 500$  MHz).

The second one uses a multicarrier signal that achieve a high resolution in frequency domain even using more less bandwidth than the IR based systems. This is the main advantage of the MC-based

system because the system requirements, especially in term of ADC are more relaxed. However, these systems require robust algorithms, applied on the received frames, to recover the sampling time, the symbol timing and the carrier phase and frequency offset, and, eliminate any synchronization errors that directly affect the distance measurements.

In Parikh [26] the characteristics of these two methodologies are deeply discussed and a table that resumes the main advantages and disadvantages of these techniques is presented. From this work is evident that if a cm or mm accuracy and precision is necessary the multicarrier-based approach is preferred because the related system architecture is simpler than the IR-based techniques, requiring ADC with lower sampling rates.

## 1.4 Position Estimation Algorithms

Once extracted the distance measurements between the active nodes of the system, these values are exploited to evaluate the target position. The positioning methods can be divided into two macro-categories: mapped and non-mapped methods. The first one uses a calibration table which includes large measurements set corresponding to known positions. The critical aspect of these methods is the updating of the map that can be not a simple procedure in outdoor environments. Moreover, the position accuracy depends on the amount of table entries. Large datasets lead to high position accuracy while a poor look-up-table may degrade the position estimation.

Non-mapped methods are able to evaluate the target position using parameters extracted directly from the signal instead of a pre-computed table. The methods of this category can be divided into two sub-categories: geometric approaches and statistical approaches.

### 1.4.1 Geometric position estimation algorithms

In geometric approaches the position of the target node is determined by the intersection of geometric regions computed on several source nodes. In the case of ToA estimation, at least three source nodes are necessary to estimate the target position that can be evaluate computing the intersection of three regions as depicted in Figure 1.9.

If the region is a circle and the coordinates of the source nodes are well-known, the unique intersection point can be computed resolving jointly the linear equations system based on the circle equations written for three source nodes of the system:

$$d_i = \sqrt{(x_i - x)^2 + (y_i - y)^2}, i = 1,2,3 \quad (1.6)$$

and target coordinates can be obtained from the equations below:

$$x = \frac{(y_2 - y_1)\gamma_1 + (y_2 - y_3)\gamma_2}{2[(x_2 - x_3)(y_2 - y_1) + (x_1 - x_2)(y_2 - y_3)]}$$

$$y = \frac{(x_2 - x_1)\gamma_1 + (x_2 - x_3)\gamma_2}{2[(x_2 - x_1)(y_2 - y_3) + (x_2 - x_3)(y_1 - y_2)]}$$
(1.7)

where

$$\gamma_1 = x_2^2 - x_3^2 + y_2^2 - y_3^2 + d_3^2 - d_2^2$$

$$\gamma_2 = x_1^2 - x_2^2 + y_1^2 - y_2^2 + d_2^2 - d_1^2$$
(1.8)

Han et al. [28] tend to further improve the localization performance by considering the layout of the three reference nodes and their work has demonstrated that the best precision is achieved if the source nodes are placed in the vertices of equilateral triangle. Instead, Yang and Liu [29] consider the effect of noisy environments, and, use different confidence coefficients for three nodes to guarantee the quality of trilateration.

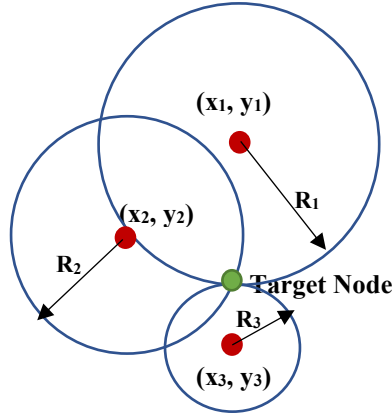


**Figure 1.9:** Trilateration-based position estimation in 2D coordinates

If the AOA approach is used, only two source nodes are necessary because the target position can be computed by the intersection of two lines determined by AOA measurements as sketches in Figure 1.10.

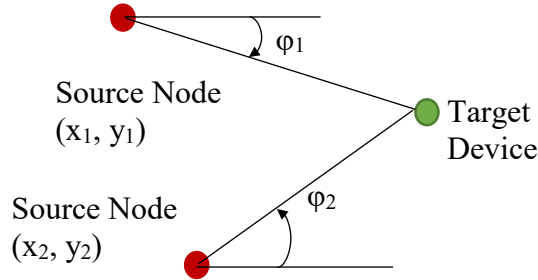


**Figure 1.10:** 2D Position geometric approach using AOA algorithms

Each line gives the equation below:

$$\tan\varphi = \frac{y - y_i}{x - x_i}, i = 1,2 \quad (1.9)$$

The target coordinates can be computed resolving the equations (1.9) jointly:

$$x = \frac{x_2 \tan\varphi_2 - x_1 \tan\varphi_1 + y_1 - y_2}{\tan\varphi_2 - \tan\varphi_1} \quad (1.10)$$

$$y = \frac{(x_2 - x_1) \tan\varphi_2 \tan\varphi_1 - y_1 \tan\varphi_2 - y_2 \tan\varphi_1}{\tan\varphi_2 - \tan\varphi_1}$$

If the distance is estimated evaluating the TDoA between a reference node and the target device, three source nodes are necessary for extracting the 2D position. The region used in this case for the geometric approach is a hyperbola sketched in Figure 1.11 and described by the following equation [30]:

$$d_{i1} = d_i - d_1 = \sqrt{(x - x_i)^2 + (y - y_i)^2} - \sqrt{(x - x_1)^2 + (y - y_1)^2}, \text{ for } i = 2,3 \quad (1.11)$$

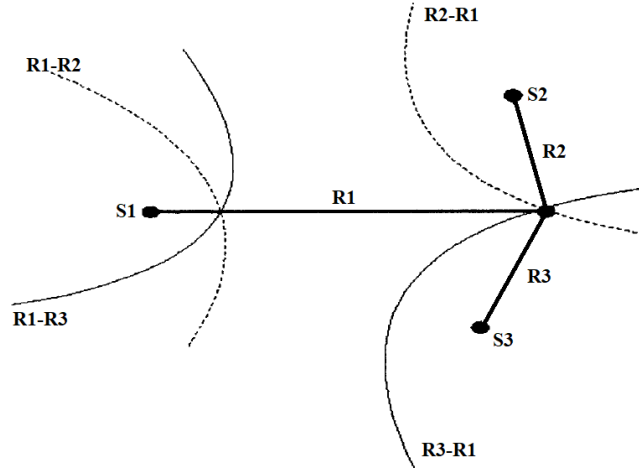


**Figure 1.11:** 2D hyperbolic Position Location

Zhou et al. [31] propose a localization method where the region used is an ellipse rather of circles or hyperbolas. However, the proposed method is quite similar to the techniques previously described. Moreover, combined approaches are possible, for example in Figure 1.12 the combination between TOA and AOA is reported. In this specific case, the system needs only one source that has the ability of measuring both TOA and AOA and the target position can be extracted evaluating the intersection of the line determined by the AOA and the circle defined by the TOA estimation.

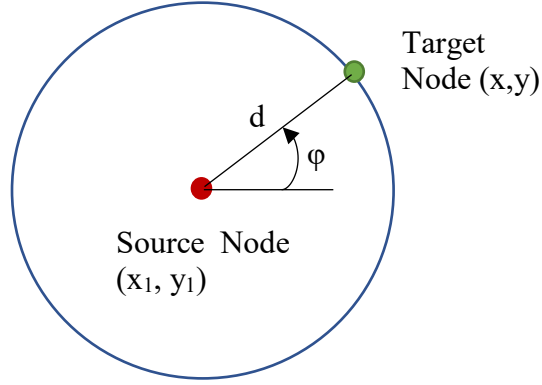


**Figure 1.12:** 2D position estimation with TOA/AOA combined approach

## 1.4.2 Statistical position estimation algorithms

All positioning approaches mentioned in the previous sections are valid if the measurements are not affected by the noise. In this condition the intersection point between the regions exists and it is unique. In practice, the presence of noise on the distance values can result in more than one intersection, so introducing a significant error in the position estimation. To overcome this problem, the position can be extracted using statistical approaches.

These methods consider the noisy measurements as the sum of the true value  $f(x,y)$ , which is a function of target node's position, and the noise  $\eta$ . In vector-space notation the noisy measurements can be written as:

$$\mathbf{z} = \mathbf{f}(x, y) + \boldsymbol{\eta} \quad (1.12)$$

where  $\mathbf{z} = [z_1, \dots, z_{N_m}]^T$ ,  $\mathbf{f}(x,y) = [f_1(x,y), \dots, f_{N_m}(x,y)]^T$  and  $\boldsymbol{\eta} = [\eta_1, \dots, \eta_{N_m}]^T$ .  $N_m$  represents the number of source used in the distance estimation. Assuming that the noise is known except for a set of parameters,  $\lambda$ , it is possible to define a vector of unknown parameters,  $\boldsymbol{\theta}$ , as:

$$\boldsymbol{\theta} = [xy\lambda^T]^T \quad (1.13)$$

where  $(x,y)$  is the position of the target node. Two main statistical methods are possible for evaluating the function  $\boldsymbol{\theta}$ : the first one, named Bayesian method, is used when some prior information about  $\boldsymbol{\theta}$  is available. In the second one, the vector  $\boldsymbol{\theta}$  can be computed evaluating the maximum-likelihood function based on the system observations:

$$\hat{\boldsymbol{\theta}}_{ML} = \arg \max_{\boldsymbol{\theta}} p(\mathbf{z}|\boldsymbol{\theta}) \quad (1.14)$$

Since  $f(x,y)$  is a deterministic function, the likelihood function  $p(\mathbf{z}|\boldsymbol{\theta})$  can be expressed as:

$$p(\mathbf{z}|\boldsymbol{\theta}) = p_{\eta}(\mathbf{z} - \mathbf{f}(x, y)|\boldsymbol{\theta}) \quad (1.15)$$

where  $p(\cdot|\boldsymbol{\theta})$  is the conditional probability density function of the noise for a given parameter vector  $\boldsymbol{\theta}$ .

In the case of independent noise for all measurements  $N_m$  the eq. (1.15) can be expressed as:

$$p(\mathbf{z}|\boldsymbol{\theta}) = \prod_{i=1}^{N_m} p_{\eta_i}(z_i - f_i(x, y)|\boldsymbol{\theta}) \quad (1.16)$$

where  $p_{\eta_i}$  is the conditional probability density function of the  $i^{\text{th}}$  measurement. This assumption is valid in the case which AOA or TOA is estimated. Instead, in TDoA estimation the noise is correlated for several source nodes due to the presence of the common source node. Moreover, in LOS scenarios, the thermal noise is the main noise source and it can be modeled as a Gaussian zero mean random variable:

$$p_{\eta_i}(u) = \frac{1}{\sqrt{2\pi}\sigma_i} \exp\left(-\frac{u^2}{2\sigma_i^2}\right) \quad (1.17)$$

The unknown vector  $\boldsymbol{\theta}$  reduces to  $[x, y]^T$  and the likelihood function in (15) is expressed as:

$$p(\mathbf{z}|\boldsymbol{\theta}) = \frac{1}{2\pi^{N_m/2} \prod_{i=1}^{N_m} \sigma_i} \exp\left(-\sum_{i=1}^{N_m} \frac{(z_i - f_i(x, y))^2}{2\sigma_i^2}\right) \quad (1.18)$$

From the equation above, the Maximum Likelihood function is computed by:

$$\hat{\boldsymbol{\theta}}_{ML} = \arg \min_{[x, y]^T} \left( \sum_{i=1}^{N_m} \frac{(z_i - f_i(x, y))^2}{\sigma_i^2} \right) \quad (1.19)$$

where

$$\arg \min_{(x, y)} f(x, y) := \{(x, y) | \forall (w, z): f(w, z) \geq f(x, y)\} \quad (1.20)$$

Note from eq. (1.19) that stronger noise implies less accurate measurements. Several methods are presented in literature to solve the eq. (1.19) including gradient descent algorithms and linearization techniques using Taylor expansion [32]-[33].

As previously mentioned in TDoA algorithms the noise is correlated due to the presence of a common source node. In this case the noise must be modeled as a multivariate normal random variable. The maximum-likelihood function can be written as:

$$p(\mathbf{z}|\boldsymbol{\theta}) = \frac{1}{(2\pi)^{N_m/2} |\boldsymbol{\Sigma}|^{1/2}} \exp\left\{-\frac{1}{2} (\mathbf{z} - \mathbf{f}(x, y) - \boldsymbol{\mu})^T \boldsymbol{\Sigma}^{-1} (\mathbf{z} - \mathbf{f}(x, y) - \boldsymbol{\mu})\right\} \quad (1.21)$$

where  $\boldsymbol{\mu}$  is a  $k$ -dimensional vector of univariate normal random variables:

$$\boldsymbol{\mu} = [E[X_1], E[X_2], \dots, E[X_k]] \quad (1.22)$$

and  $\boldsymbol{\Sigma}$  is a  $k \times k$  matrix of covariance between each pair of univariate normal random variables:

$$\boldsymbol{\Sigma}[i, j] = \text{Cov}[X_i, X_j], \text{ for } i, j = 1, 2, 3, \dots, k \quad (1.23)$$

Then, the ML estimation of  $\boldsymbol{\theta}$  can be computed by the equation expressed below:

$$\hat{\boldsymbol{\theta}}_{ML} = \arg \min_{\boldsymbol{\theta}} \{(\mathbf{z} - \mathbf{f}(x, y) - \boldsymbol{\mu})^T \boldsymbol{\Sigma}^{-1} (\mathbf{z} - \mathbf{f}(x, y) - \boldsymbol{\mu}) + \log|\boldsymbol{\Sigma}|\} \quad (1.24)$$

Generally, the vector  $\boldsymbol{\theta}$  includes the target position and unknown parameters of  $\boldsymbol{\Sigma}$  and  $\boldsymbol{\mu}$ . However, if the average of the noise is zero and the covariance matrix is known, the vector  $\boldsymbol{\theta}$  just includes the target position and the maximum-likelihood function is expressed by:

$$\hat{\boldsymbol{\theta}}_{ML} = \arg \min_{[x, y]^T} (\mathbf{z} - \mathbf{f}(x, y))^T \boldsymbol{\Sigma}^{-1} (\mathbf{z} - \mathbf{f}(x, y)) \quad (1.25)$$

The maximum-likelihood approach can be applied to solve the trilateration problem. Considering  $n$  reference nodes, the target position can be obtained computing the linear system equations given by (1.6). Then every equation is subtracted to the subsequent one to obtain the system equations expressed below:

$$\begin{cases} x_1^2 - x_n^2 - 2(x_1 - x_n)x + y_1^2 - y_n^2 - 2(y_1 - y_n)y = d_1^2 - d_n^2 \\ \vdots \\ x_{n-1}^2 - x_n^2 - 2(x_{n-1} - x_n)x + y_{n-1}^2 - y_n^2 - 2(y_{n-1} - y_n)y = d_{n-1}^2 - d_n^2 \end{cases} \quad (1.26)$$

Let:

$$\begin{aligned} A &= \begin{bmatrix} 2(x_1 - x_n) & 2(y_1 - y_n) \\ \vdots & \vdots \\ 2(x_{n-1} - x_n) & 2(y_{n-1} - y_n) \end{bmatrix} \\ b &= \begin{bmatrix} x_1^2 - x_n^2 + y_1^2 - y_n^2 + d_n^2 - d_1^2 \\ \vdots \\ x_{n-1}^2 - x_n^2 + y_{n-1}^2 - y_n^2 + d_n^2 - d_{n-1}^2 \end{bmatrix} \\ X &= \begin{bmatrix} x \\ y \end{bmatrix} \end{aligned} \quad (1.27)$$

Adopting the minimum variance estimation method, the coordinates of the target  $(x, y)$  can be calculated resolving the linear equations system  $AX = b$  [34]:

$$X = (A^T A)^{-1} A^T b \quad (1.28)$$

## 1.5 Conclusions

The design of an indoor positioning system involves three main challenges: system technology, distance ranging algorithm and positioning method. For each of them, different solutions can be adopted with the related properties and characteristics. The choice is not trivial and strictly depends

on the requirements of system accuracy and precision. To achieve a mm or sub-mm accuracy the WB or UWB methods are mandatory. The target distances from several source nodes, that define the system architecture, can be estimated evaluating the related propagation delays. In this case, the choice is simpler than the previous because all techniques are quite similar. One exception is the class of the Angle of Arrival algorithms where the distance is computed evaluating the incident direction of the signal. However, these last methods can be combined with the traditional algorithms (ToA or TDoA) to improve the distance accuracy. Finally, once extracted all target distances, the related position can be computed with a geometric-based algorithm (if any noise source on the measurements exist) or a statistical method that consider the noise sources that can be exist in the positioning system.

## 2 Indoor Positioning System: The system design

The objective of this work is the design of an Indoor Positioning System for radiotherapy applications that require to localize a mobile device with a mm or sub-mm accuracy and precision. From the analysis of the technologies, the most accurate techniques use WB or UWB signals that achieve very high resolution, thus, allowing to separate the direct path from the multipath reflections. Due to severe performance requirements for the ADC, and the high costs, the IR-UWB methods are not convenient for a practical hardware realization. Hence the research was focalized on MC-WB techniques that can achieve a high resolution in frequency domain using commercial ADCs with low sampling rate ( $<1$  GSPS). A novel solution was studied to overcome the problems that affect the multicarrier-based solutions, e.g., the high linear requirements for the dynamic range of the system. Moreover, starting from the work of Mahfouz et al. [23], it was implemented a technique to obtain an impulsive autocorrelation function without using complex spread spectrum methods or pseudo-noise like signals. In facts, the main challenge of this work is to design an IPS with a very simple and scalable architecture, able to adapt its characteristics as a function of the system requirements in term of accuracy and precision.

### 2.1 Zadoff-Chu Sequences

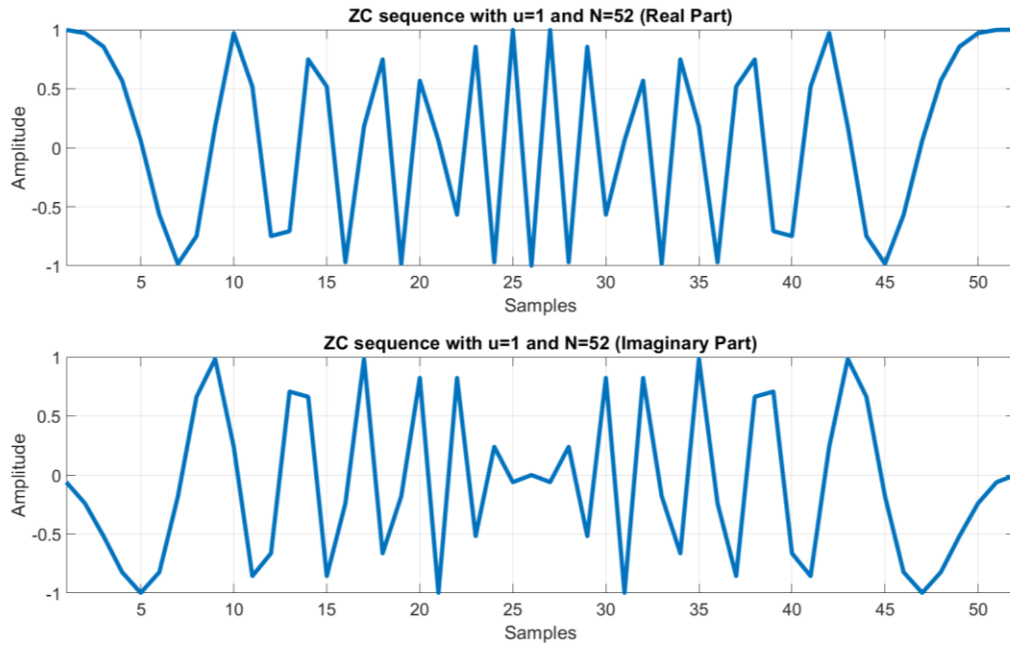
To solve the problem, the combination of the OFDM modulation scheme with the Zadoff-Chu (ZC) sequences is proposed [35]. The result is a signal very robust against the multipath and that exhibits good periodic correlation properties. Moreover, the ZC sequences are part of the Constant Amplitude Zero Auto-Correlation (CAZAC) family of sequences, so the resulting signal have a constant amplitude and a low Peak to Average Power Ratio (PAPR). In this case, the design specifications for the system architecture can be relaxed for two main reasons. The first one is that the sequence have a constant amplitude, so it is not required a high linear dynamic range for the amplifiers and so on. The second one is that the coefficients of the sequence are fixed and depend only by few parameters. If no data are transmitted by the system, the architecture for both transmitter and receiver can be considerably simplified.

Defining  $u$  as the *root index*, the  $n^{\text{th}}$  sample of a Zadoff-Chu sequence with a length of  $N_s$  can be computed as follow:

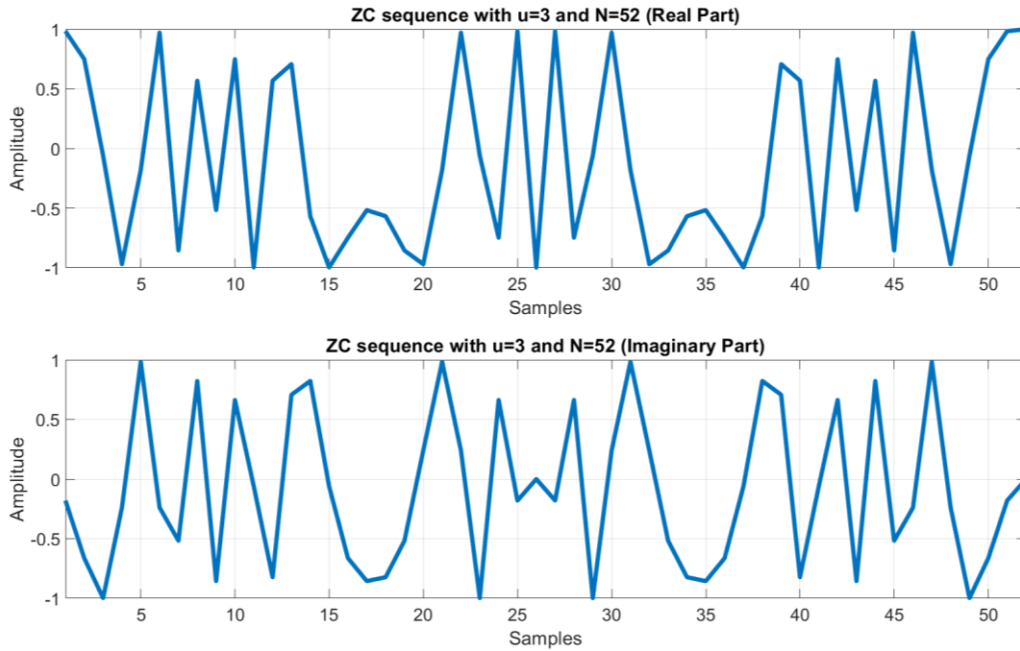
$$x_u(n) = \begin{cases} \exp\left(-j\frac{\pi un^2}{N_s}\right), & N_s \text{ even} \\ \exp\left(-j\frac{\pi un(n+1)}{N_s}\right), & N_s \text{ odd} \end{cases} \quad (2.1)$$

Note that the choice of the Zadoff-Chu expression depends by the value of the sequence  $N_s$ , and more important, the coefficients have complex values.

As previously mentioned, the ZC sequences exhibit another important property that are massively exploited in a lot of modern telecommunications systems to resolve the synchronization problems [36]-[37]. In fact, once obtained a ZC sequence, defining the values of  $N_s$  and  $u$ , if the cross-correlation is computed between the sequence and a cyclical copy of itself, it is non-zero only at the time that correspond to the cyclical shift introduced. Moreover, the ZC sequences are orthogonal as function of  $u$ , so two ZC sequences with different root indexes are uncorrelated. Figure 2.1 are represented two examples of 52-length ZC sequences with root index  $u$  equal to 1 and 3 respectively. Figure 2.2 shows the cross-correlation function between the ZC sequence with  $u=1$  and its copy shifted by 10 samples (solid line), and the cross-correlation function between two ZC sequences with different  $u$  values (dotted line).



(a)



(b)

**Figure 2.1:** (a) Real and imaginary part of a 52-length ZC sequence with  $u=1$ . (b) Real and imaginary of a 52-length ZC sequence with  $u=3$ .

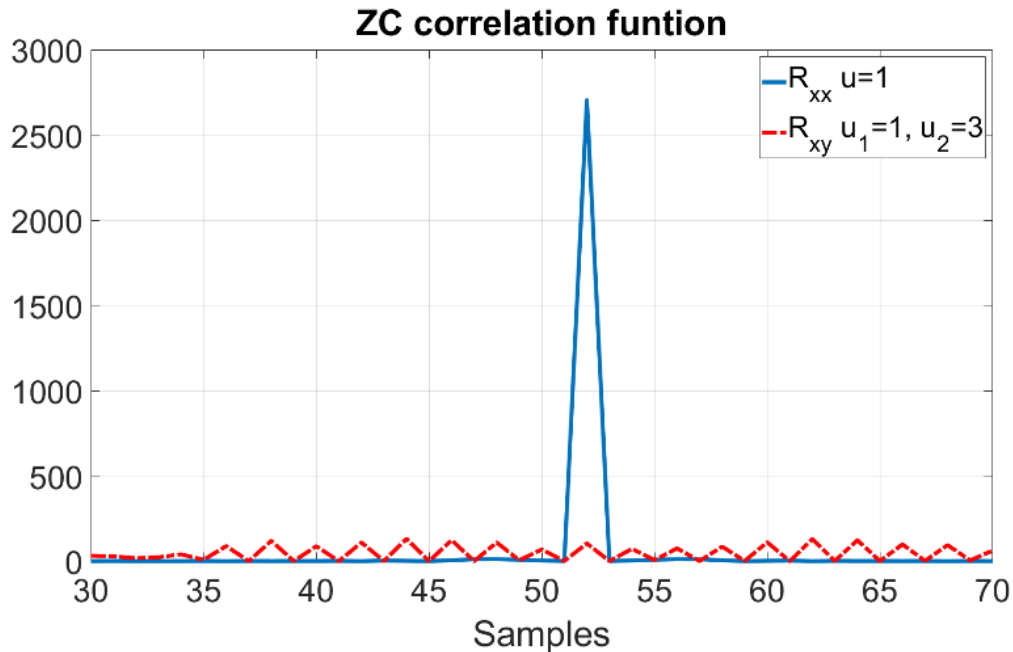


**Figure 2.2:** Example of correlation function. In blue the cross-correlation function of 52-length ZC sequence and its copy cyclically shifted by 10 samples ( $u=1$ ). In red the cross-correlation function between two 52-length ZC sequences with different  $u$  values ( $u_1=1, u_2=3$ ).

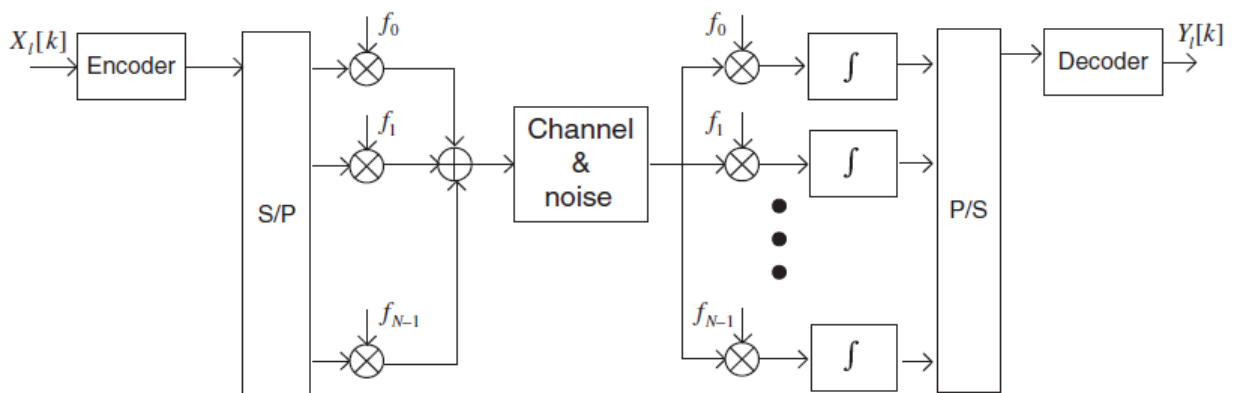
## 2.2 Orthogonally Frequency Division Multiplexing (OFDM)

The coefficients, computed by (2.1), are arranged within the spectrum of an OFDM signal in order to transmit the ZC sequence over the channel and, thus, to measure the propagation delay between the two active devices. The OFDM modulation scheme employs multiple orthogonal subcarriers with overlapped bandwidths to improve the spectral efficiency. The transmitter and receiver architecture are simple because to generate an OFDM signal with  $N$  subcarriers it is not necessary to implement  $N$  modulators or demodulators, as request by the Frequency Division Multiplexing (FDM) modulation schemes (Figure 2.3 (a)). In fact, the orthogonal subcarriers can be obtained through the Discrete Fourier Transform (DFT) and its inverse function (IDFT).

In Figure 2.4 there is an example of the OFDM transmission structure implemented by IDFT/DFT. As all subcarriers have a finite duration  $T$ , the spectrum of the OFDM signal can be considered as the sum of the frequency-shifted *sinc* functions in the frequency domain and spaced by  $1/T$ .

Dividing the frequency band into sub-bands, the OFDM modulation scheme does not need filtering to separate the sub-bands since the orthogonality is preserved among the subcarriers. However, it requires a guard band to combat the adjacent channel interference.

Moreover, the use of the DFT function leads to an efficient hardware implementation using the algorithms of the Fast Fourier Transform (FFT) (Figure 2.3 (b)). Another advantage of the OFDM over single-carrier schemes is its ability to cope with severe channel conditions, e.g., attenuation, narrowband interference and frequency fading due to multipath. Also, channel equalization is simplified because OFDM may be viewed as the composition of many slowly modulated narrowband signals rather than one rapidly modulated wideband signal.



(a)

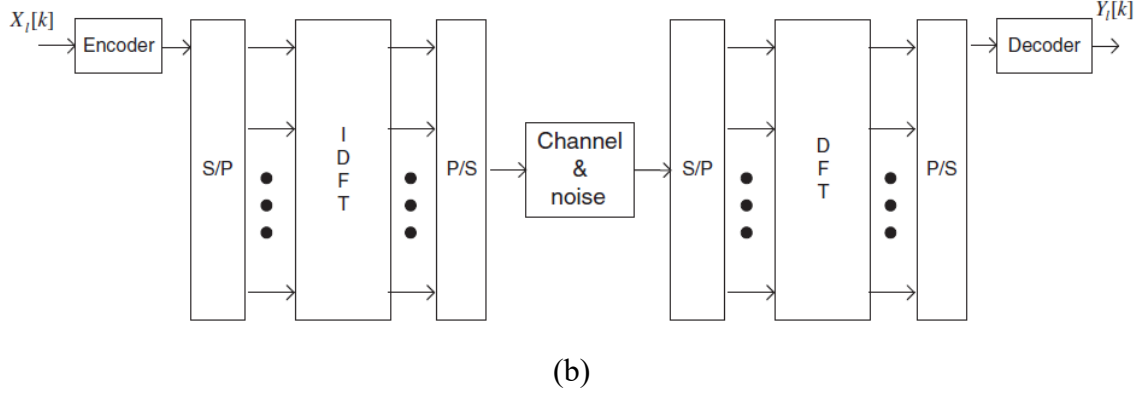


**Figure 2.3:** (a) FDM architecture. (b) OFDM architecture

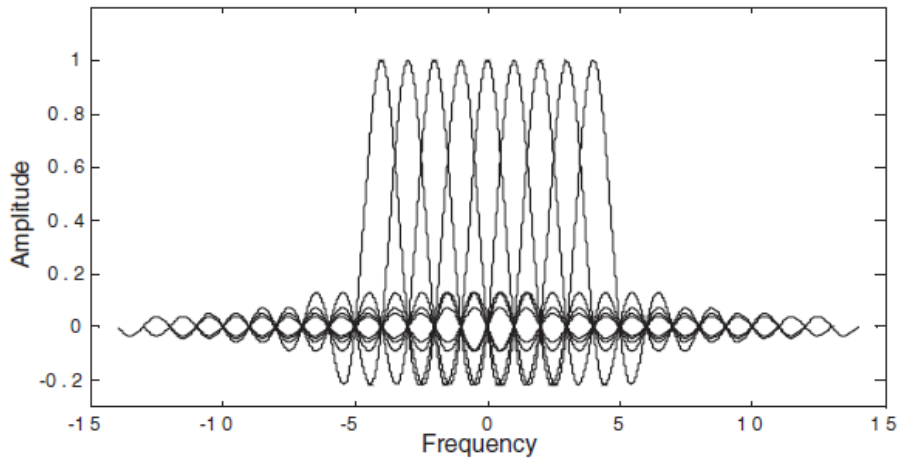


**Figure 2.4:** OFDM signal spectrum (linear scale)

The OFDM transmitter maps the message bits into a sequence of symbol which will be subsequently converted into  $N$  parallel streams. Each of  $N$  symbols from serial to parallel conversion (S/P) is carried out by the different subcarrier. Let  $X_l[k]$  denote the  $l^{\text{th}}$  transmit symbol at the  $k^{\text{th}}$  carrier with  $l=0, 1, 2, \dots, \infty$  and  $k=0, 1, 2, \dots, N-1$ . Due to the S/P conversion, the duration of transmission time for  $N$  symbols is extended to  $N \cdot T_s$ , which forms a single OFDM symbol with a length of  $T_{\text{sym}}$  (i.e.,  $T_{\text{sym}} = N \cdot T_s$ ). Let  $\Psi_{l,k}(t)$  denote  $l^{\text{th}}$  OFDM signal at the  $k^{\text{th}}$  subcarrier, which can be expressed as:

$$\Psi_{l,k}(t) = \begin{cases} e^{j2\pi f_k(t-lT_{\text{sym}})}, & 0 < t \leq T_{\text{sym}} \\ 0, & \text{elsewhere} \end{cases} \quad (2.2)$$

Then the passband and baseband OFDM signals in the continuous-time domain can be obtained by the expressions below:

$$x_l(t) = \text{Re} \left\{ \frac{1}{T_{\text{sym}}} \sum_{l=0}^{\infty} \left\{ \sum_{k=0}^{N-1} X_l[k] \Psi_{l,k}(t) \right\} \right\} \quad (2.3)$$

$$x_l(t) = \sum_{l=0}^{\infty} \sum_{k=0}^{N-1} X_l[k] e^{j2\pi f_k(t-lT_{sym})}$$

The continuous-time baseband OFDM signal can be sampled at  $t=lT_{sym} + nT_s$  with  $T_s = T_{sym}/N$  and  $f_k = k/T_{sym}$  to yield the corresponding discrete-time OFDM symbol as:

$$x_l[n] = \sum_{k=0}^{N-1} X_l[k] e^{j2\pi kn/N}, \quad \text{for } n = 0, 1, \dots, N-1 \quad (2.4)$$

Hence, the OFDM symbol can be generated in frequency domain and, then, applying the IFFT function the time-domain samples can be obtained.

Let be  $\{y_l[n]\}_{n=0}^{N-1}$  the sample values of the received OFDM symbol  $y_l(t)$  at  $t=lT_{sym} + nT_s$ . Then the transmitted sequence  $X_l[k]$  can be obtained exploiting the orthogonality of the subcarriers:

$$\begin{aligned} Y_l[k] &= \sum_{n=0}^{N-1} y_l[n] e^{-j2\pi kn/N} \\ &= \sum_{n=0}^{N-1} \left\{ \frac{1}{N} \sum_{i=0}^{N-1} X_l[i] e^{j2\pi(i-k)n/N} \right\} e^{-j2\pi kn/N} \\ &= \frac{1}{N} \sum_{m=0}^{N-1} \sum_{i=0}^{N-1} X_l[i] e^{\frac{j2\pi(i-k)n}{N}} = X_l[k] \end{aligned} \quad (2.5)$$

where the effects of the channel and noise are not considered. At the receiver side the signal can be computed efficiently by using the FFT algorithm. If the channel effects and the noise are considered, the received signal can be obtained as the convolution between the transmit signal with the channel impulse response plus the  $n^{\text{th}}$  noise sample  $z_l[n]$ :

$$y_l[n] = x_l[n] * h_l[n] + z_l[n] \quad (2.6)$$

## 2.3 Channel Modeling

The channel introduces some effects on the received signal that directly affect the distance measurements. A channel model is necessary to analyzing these effects, and so define the signal parameters or some strategies to reduce the errors in distance estimation and improve the performance. For indoor applications, it is not simple to define a model valid for all technologies available because different frequencies bands and different kinds of signals are used. Molisch et al. [38] provide a final report where a statistical model of an indoor channel is defined starting

from the model proposed by Saleh-Valenzuela [39]. More in details, the report contains three different models as function of the signal bandwidth and frequency spectrum occupied:

- UWB model for frequency range from 2 to 10 GHz. Models for any narrowband system within the frequency range are possible with a simple bandpass filtering operation;
- UWB model for frequency range from 100 to 1000 MHz. Again, narrowband systems located within that frequency range can obtain their specific model by filtering.
- Narrowband model for frequency range around 1 MHz.

Several parameters are defined for each model that are evaluated from tests and measurements performed in several indoor environments, e.g., homes, offices, industrial environments, body area networks, agricultural farms, and so on. The key features of the model include the law for the path gain as function of the distance and its frequency dependence, and the modified Saleh-Valenzuela model that define the main characteristics of the multipath phenomena (arrival of path in clusters, mixed Poisson distribution for ray arrival times, ...).

### 2.3.1 Path gain

To provide an adequate model for the path gain, in a first step, the definition of the transmit power spectrum is necessary. It is the product of the output spectrum of the transmit amplifier with the frequency dependent antenna efficiency  $\eta_{TX-ant}(f)$ :

$$P_{TX}(f) = P_{TX-amp} \cdot \eta_{TX-ant}(f) \quad (2.7)$$

The frequency-dependent power density at a distance  $d$  can be computed as:

$$\hat{P}(f, d) = K_0 \frac{P_{TX}(f)}{4\pi d_0^2} \left(\frac{d}{d_0}\right)^{-i} \left(\frac{f}{f_c}\right)^{-2\kappa} \quad (2.8)$$

where  $d_0$  is the reference distance (1 m),  $f_c$  the central frequency (or carrier frequency),  $K_0$  is a normalization constant and finally  $i$  and  $\kappa$  are the pathloss exponent and the decay factor respectively. These two terms depend on the environment, and on whether a LOS connection exists between the transmitter and receiver or not. Finally, the received frequency-dependent power has to be determined, by multiplying the power density at the location of the receiver with the antenna area  $A_{RX}$ :

$$A_{RX}(f) = \frac{\lambda^2}{4\pi} G_{RX}(f) \quad (2.9)$$

where  $G_{RX}$  is the receive antenna gain; and also multiply with the antenna efficiency  $\eta_{TX-ant}(f)$ . If the radiation is averaged over all incident angles, the antenna gain is unity and independent of the frequency. The frequency-dependent received power is given by:

$$P_r(d, f) = K_0 P_{TX-amp}(f) \eta_{TX-ant}(f) \eta_{RX-ant}(f) \frac{c_0^2}{(4\pi d_0 f_c)^2} \frac{1}{(d/d_0)^n (f/f_c)^{2\kappa+2}} \quad (2.10)$$

The normalization constant  $K_0$  is chosen in such way that the attenuation at distance  $d_0$  and at given frequency of  $f_c$  is equal to  $G_0$ :

$$\begin{aligned} \frac{P_r(d_0, f_c)}{P_{TX-amp}(f_c)} &= G_0 = K_0 \frac{c_0^2}{(4\pi d_0 f_c)^2} \\ K_0 &= \frac{(4\pi d_0 f_c)^2}{c_0^2} G_0 \end{aligned} \quad (2.11)$$

The pathloss model expressed by the equation (2.10) takes into account for the effects of the transmit and receive antennae, including the related parameters as the efficiency form factors and so on. The directivity or the antenna gain is not included in the model because it strictly depends by the antenna design and so by the specific application. Moreover, if the antenna is not included and the path gain is evaluated at the antenna connector, the model in (2.10) can be simplified. In this specific case, the path gain is:

$$G(f, d) = \frac{1}{\Delta} E \left\{ \int_{f-\Delta f/2}^{f+\Delta f/2} |H(\tilde{f}, d)|^2 d\tilde{f} \right\} \quad (2.12)$$

where  $H(f, d)$  is the transfer function from antenna connector to antenna connector, and  $\Delta f$  is chosen small enough that diffractions, dielectric constants, etc., can be considered constant within the bandwidth. The total path gain is obtained by integrating over the whole bandwidth of interest. The model can be further simplified considering the path gain as the product of two distinct function dependent by the frequency and distance respectively:

$$G(f, d) = G(f)G(d) \quad (2.13)$$

where the frequency dependence of the path gain is given by [40]-[41], while the function dependent by the distance can be expressed as:

$$G(d) = G_0 - 10n \log_{10} \left( \frac{d}{d_0} \right) \quad (2.14)$$

where  $n$  is the path gain exponent, which depends on the kind of the indoor environment considered (office, home, farm, etc.), and the presence or not of a direct path between the nodes of the system.

### 2.3.2 Power Delay Profile

Once defined the path loss model it is necessary define the channel impulse response of the indoor environment using a ray model. In the first simplified model the channel is represented by multiple paths or rays,  $k$ , having real positive gains,  $\alpha_k$ , propagation delays,  $\tau_k$ , and associated phase shifts,  $\theta_k$ :

$$h(t) = \sum_{k=1}^{\infty} \alpha_k e^{j\theta_k} \delta(t - \tau_k) \quad (2.15)$$

where  $\delta$  is the Dirac delta function. It should be noted that for sake of simplicity the noise introduced by the channel is not considered. If it is included and a single ray is present, the expression in (2.15) describe an Additive White Noise Gaussian (AWGN) channel model, where the transmit signal is only attenuate and shifted as function of the distance. The motion of the people and the presence of several obstacles in the environment introduce randomly time-varying functions for the channel parameters. However, the rate of their variations is very slow compared to any useful signaling rates that are likely to be considered. Thus, these parameters can be considered virtually time-invariant random variables.

This simplified model of the channel is valid in outdoor environment, where there is not the presence of massive obstacles. In indoor environment, the model is a little more complicated because when the signal propagates, the presence of walls, floor, ceiling, and so on, generate a cluster of rays and so the new channel impulse response can be obtained by:

$$h(t) = \sum_{l=0}^L \sum_{k=1}^K \alpha_{k,l} e^{i\theta_{k,l}} \delta(t - T_l - \tau_{k,l}) \quad (2.16)$$

where  $L$  in (2.16) indicates the total number of clusters,  $\alpha_{k,l}$  is the tap weight of the  $k^{\text{th}}$  component in the  $l^{\text{th}}$  cluster,  $T_l$  is the delay of the  $l^{\text{th}}$  cluster,  $\tau_{k,l}$  is the delay of the  $k^{\text{th}}$  ray relative to the  $l^{\text{th}}$  cluster with the arrival time  $T_l$ . The phase shifts  $\theta_{k,l}$  are statistically independent uniform random variables over  $[0, 2\pi)$ . The number of cluster  $L$  is assumed to be Poisson-distributed:

$$pdf_L(L) = \frac{(\bar{L})^L \exp(-\bar{L})}{L!} \quad (2.17)$$

So that the mean  $\bar{L}$  completely characterizes the distribution. The distributions of the cluster arrival times are given by a Poisson processes:

$$p(T_l | T_{l-1}) = \Lambda_l \exp[-\Lambda_l(T_l - T_{l-1})], l > 0 \quad (2.18)$$

where  $\Lambda_l$  is the cluster arrival rate. Instead the model ray arrival times is defined mixing two Poisson process:

$$\begin{aligned} p(\tau_{k,l}|\tau_{(k-1),l}) &= \beta\lambda_1 \exp[-\lambda_1(\tau_{k,l} - \tau_{(k-1),l})] \\ &+ (\beta - 1)\lambda_2 \exp[-\lambda_2(\tau_{k,l} - \tau_{(k-1),l})], k > 0 \end{aligned} \quad (2.19)$$

where  $\beta$  is the mixture probability, while  $\lambda_1$  and  $\lambda_2$  are the ray arrival rates. The mean power of different paths, named power delay profile is exponential within each cluster:

$$E\{|\alpha_{k,l}|^2\} = \Omega_l \frac{1}{\gamma_l[(1-\beta)\lambda_1 + \beta\lambda_2 + 1]} \exp(-\tau_{k,l}/\gamma_l) \quad (2.20)$$

where  $\Omega_l$  is the integrated energy of the  $l^{\text{th}}$  cluster and  $\gamma_l$  is the intra-cluster decay time constant.

### 2.3.3 Small-scale fading

Another important aspect that must be considered is the small-scale fading that can be modeled using the Nakagami distribution:

$$pdf(x) = \frac{2}{\Gamma(m)} \left(\frac{m}{\Omega}\right)^m x^{2m-1} \exp\left(-\frac{m}{\Omega}x^2\right) \quad (2.21)$$

where  $m \geq \frac{1}{2}$  is the Nakagami m-factor,  $\Gamma(m)$  is the gamma function, and  $\Omega$  is the mean-square value of the amplitude. The last parameter corresponds to the mean power, and its delay dependence is given by the power delay profile mentioned previously. The Nakagami-m factor is modeled as a lognormally distributed random variable, whose logarithm has a mean value,  $\mu_m$ , and a standard deviation,  $\sigma_m$ . Both can have a delay dependence:

$$\begin{aligned} \mu_m &= m_0 - k_m \tau \\ \sigma_m &= \widehat{m}_0 - \widehat{k}_m \tau \end{aligned} \quad (2.22)$$

instead, for the first component of each cluster, the Nakagami factor is assumed to be a deterministic and independent of delay:

$$m = \widetilde{m}_0 \quad (2.23)$$

Resuming, to generate a complete model for the channel impulse response three main effects must be take into account: the path gain, the power delay profile and the small-scale fading. Once defined the value of  $L$ ,  $L-1$  exponentially distributed variables  $x_n$  with decay constant  $\Lambda$  have to be created. For each cluster, we generate the cluster decay time and the total cluster power according to the considerations in the paragraph 1.3.2. For the first component in each cluster set the Nakagami-m factor to  $\widetilde{m}_0$ , while for the rest of the components compute the mean and the

variance according to (2.22) and (2.23). For each ray, within the cluster, calculate the amplitude  $\alpha_{k,l}$  using Nakagami-distributed variables with the parameters evaluate in previously steps. Once completely defined the cluster, the path gain should be computed using the equation in (2.10). The final channel model can be obtained multiplying the transfer function of the channel with the frequency-dependent transfer function of the channel and the frequency-dependent path gain and emission spectrum. In Figure 2.5 is reported an example of the channel impulse response valid for an indoor environment and generated by the model described above.

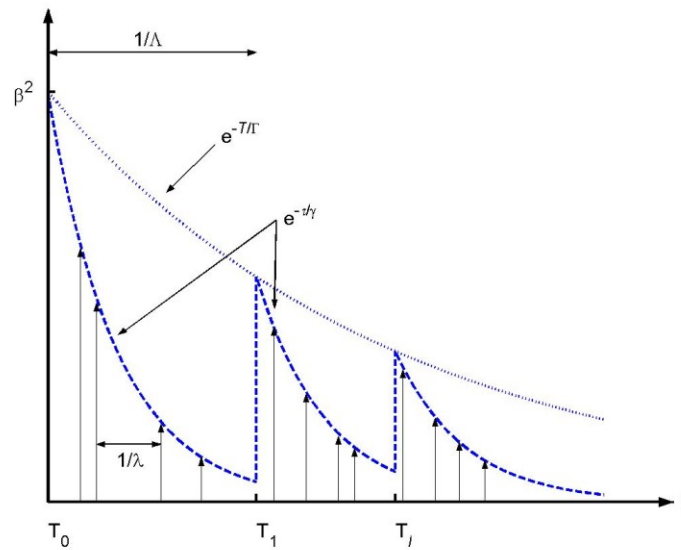


**Figure 2.5:** Example of a Channel Impulse Response for an indoor environment

From the time-domain point of view, the multipath reflections are summed with the direct signal transmitted by the antenna. Thus, if the OFDM signal is transmitted in continuous mode, the multipath replicas of the first symbol can overlap in time with the successive symbols causing inter-symbolic interference (ISI). The effective symbol duration is extended, and, in traditional communications system, data that cannot be correctly demodulate due to the presence of the signal overlaps. In this case, before the start of the OFDM Symbol a Guard Interval is introduced to protect the data from the ISI (Figure 2.6). There are different approaches to generate the guard interval: cyclical prefix, cyclical suffix, zero padding and so on. In Cho et al [42] it is possible to find more details about the OFDM modulation scheme and, also, the methods to generate the guard interval are discussed deeply.

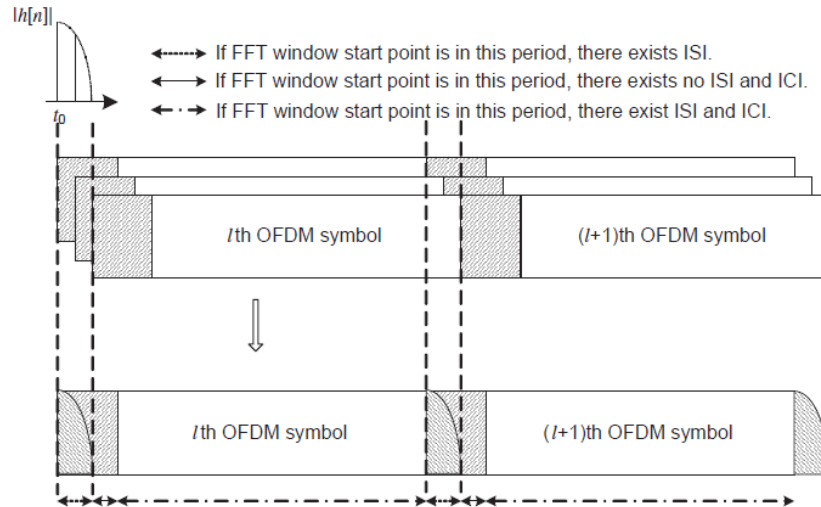
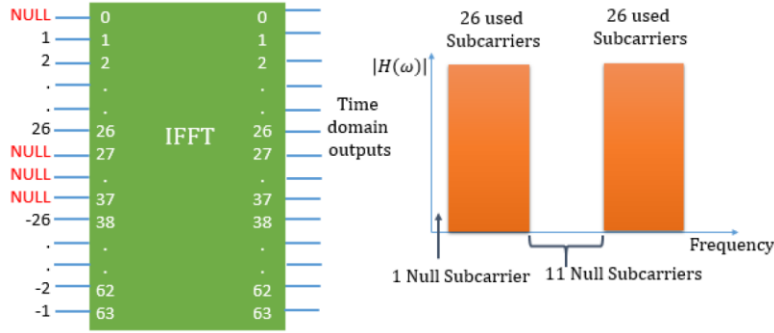


Figure 2.6: ISI effect of a multipath channel over an OFDM symbol.

## 2.4 Signal Pattern Generation

To transmit the ZC sequence over the channel, its coefficients are arranged within the spectrum of the OFDM symbol according to the pattern defined by the IEEE 802.11a standard [43]. Considering a 52-length ZC sequence with root index  $u$ , its coefficients are inserted in a 64-length row vector. The coefficients are divided into two subsets of 26 elements. The first element of the row vector is null because it will represent the value of the DC. The first 26-length subset is inserted in a row vector from position 2 to 27 that will represent the positive subcarriers. The second subset is arranged in the positions ranging from 38 to 63 that will represent the negative subcarriers of the baseband signal. Finally, the IFFT operation is performed to obtain the baseband signal in time-domain (Figure 2.7).

This procedure is performed only the first time or when the signal parameters change. Then the signal samples can be stored in a lookup table that can be read to produce the input signals for a DAC. The maximum bandwidth depends on the maximum sample rate of the DAC, i.e., by the clock used to read the samples from the lookup table. This is the main advantage of the proposed IPS because the properties of the transmit signal can be modified via software, without hardware changes.



**Figure 2.7:** Signal pattern for a 52-length ZC sequence and 64-length OFDM symbol

At the start of the system operations, different lookup tables can be created containing, for example, the same signal but with a different number of subcarriers or sequences with different root indexes. Then, the system can switch between several versions of the signal with a simple software control. Hence, the system is scalable and is able to adapt its characteristics in according to the design requirements in term of accuracy and precision.

This property is valid even for the receiver, in facts, the absence of data simplifies the hardware realization because the signal processing can be entirely performed in digital domain. The analog parts of the circuit comprise only the amplifiers and the mixer needed by the frequency conversion of the signal. Once translated to IF frequency, the signal is acquired and digitized with an ADC and the distance ranging can be obtained applying signal processing algorithms. Figure 2.8 represents the real and the imaginary part of the resulting 64-length OFDM symbol combined with a 52-length ZC sequence with  $u=1$ . The baseband signal has a bandwidth of 100 MHz sampled with a sampling frequency of 1 GSps, so its period is  $T = 1/\Delta f = 64/100 \text{ MHz} = 0.64 \mu\text{s}$ .

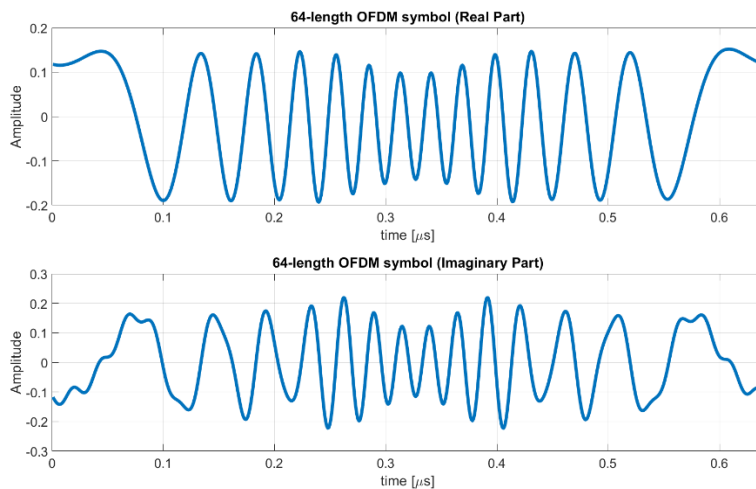


**Figure 2.8:** Real and Imaginary part of the transmit signal

## 2.5 Distance Ranging Algorithm

For sake of simplicity, an AWGN channel is firstly considered to describe the distance ranging algorithm. In this case the received signal is a copy of the transmitted signal attenuated and shifted in time by an amount that depends on the distance between the nodes. Hence, the channel introduces two main impairments, that must be evaluated for extracting the distance and further the position of the target: the carrier frequency offset  $\varphi$  (CFO) and the timing offset  $\delta$  (TO). In fact, the received baseband signal  $y$  in discrete domain can be expressed as:

$$\begin{aligned} y_l[n] &= IDFT\{Y_l[k]\} = IDFT\{H_l[k]X_l[k] + Z_l[k]\} \\ &= \frac{1}{L} \sum_{k=0}^{L-1} H_l[k]X_l[k] e^{-\frac{j2\pi(k+\varepsilon)(n+\delta)}{N}} + z_l[n] \end{aligned} \quad (2.24)$$

where  $z_l[n] = IDFT\{Z_l[k]\}$  is  $n^{\text{th}}$  sample of the Additive White Gaussian Noise (AWGN) introduced by the channel,  $N$  is the length of the OFDM signal,  $H_l[k]$  and  $X_l[k]$  are respectively the  $k^{\text{th}}$  sample of the channel impulse response and the transmitted signal in the discrete frequency domain. Tab. 2.1 shows how the TO and CFO affect the received signal, in time and frequency domain (the effects of the noise are neglected). Note that the TO in the time domain univocally determines the phase offset (PO) in the frequency domain. As predictable, the phase offset (PO =  $2\pi k\delta/N$ ) is proportional to the subcarrier index  $k$  as well as the timing offset,  $\delta$ .

TABLE 2.1: TO and CFO effects on the Received Signal

	Received Signal	TO ( $\delta$ )	CFO ( $\varepsilon$ )
Time-Domain	$y_l[n]$	$x_l[n+\delta]$	$e^{j2\pi n\varphi/N}x_l[n]$
Freq-Domain	$Y_l[k]$	$e^{j2\pi k\delta/N}X_l[k]$	$X_l[k-\varphi]$

The magnitude of  $\delta$  depends directly on the distance,  $d_m$ , between the transmitter and the  $m^{\text{th}}$  receiver. In fact, assuming the propagation velocity to be the speed of light ( $c=3\times 10^8$  m/s), the time delay can be expressed as  $\delta_m=d_m/c$ . The value of  $\delta_m$  can be estimated multiplying in the frequency domain the received signal,  $Y_l[k]$ , with the complex conjugate copy of the transmitted sequence,  $X_l[k]$ , and then performing their IFFT:

$$\begin{aligned} y_l^X[n] &= IFFT \left\{ Y_l[k] e^{\frac{j2\pi\delta k}{N}} X_l^*[k] \right\} = \\ &= \frac{1}{L} \sum_{k=0}^{N-1} Y_l[k] e^{\frac{j2\pi(n+\delta)k}{N}} X_l^*[k] = \end{aligned} \quad (2.25)$$

$$\begin{aligned}
&= \frac{1}{L} \sum_{k=0}^{N-1} H_l[k] X_l[k] X_l^*[k] e^{\frac{j2\pi(n+\delta)k}{N}} = \\
&= \frac{1}{L} \sum_{k=0}^{N-1} H_l[k] e^{\frac{j2\pi(n+\delta)k}{N}} = h_l[n + \delta]
\end{aligned}$$

In equation (2.25), the CFO is neglected for simplicity and, due to the constant amplitude of the ZC sequences, the power of the transmitted signal,  $X_l[k]$ , is set equal to one (i.e.,  $X_l[k] X_l^*[k] = |X_l[k]|^2 = 1$ ). Hence, the distance between the nodes can be estimated directly computing the cross-correlation function between the received signal and a clear copy of the transmitted sequence. Due to the properties of ZC sequences, the cross-correlation function is an impulsive function in which the pulse is placed at the time that correspond to the propagation delay. If the channel model in (2.15) is considered, the cross-correlation function exhibits a number of peaks equal to the multipath paths present in the channel impulse response. However, in discrete systems the resolution of the channel response is determined by the sampling time  $T_s$ . Thus, if a low  $T_s$  is used to sample the received signal, the estimation of the peaks in the cross-correlation function should lack accuracy [44]. However, LOS scenarios guarantee the existence of a shorter direct path between the transmitter and the receiver and the distance can be estimated extracting the peak of this path in the channel impulse response. As a result, the timing offset can be estimated evaluating the maximum of the  $y_l^X[n]$ :

$$\hat{\delta}_m = \arg \max_n (|y_l^X[n]|^2) \quad (2.26)$$

The proposed system uses a TDoA algorithm to extract the distance measurements, avoiding any synchronization errors between the receivers. A GPS-like scheme is exploited comprising four receivers, placed in known positions, and a single mobile device that transmits in continuous mode the sensing signal (Figure 2.9). One receiver is set as reference of system and all the receivers share both the clock to generate the local oscillation, needed by the frequency conversion process, and the trigger signal, needed by the ADC. Hence any offsets introduced by carrier frequency or any not-perfect time-synchronization generate constants terms in the received signals, that elide when we evaluate the time difference of arrival between them. However, as previously mentioned, the channel introduces a CFO in the signals that determines a phase rotation in time domain. This term depends on two factors: the distance,  $d_m$ , between the  $T_X$  and the  $m^{\text{th}}$   $R_X$  and the wavelength of the carrier system,  $\lambda$ :

$$\varphi_m = \frac{d_m}{\lambda} \quad (2.27)$$

where  $\lambda$  is the ratio of the propagation velocity and the carrier frequency.

Hence the distance can be estimated in frequency domain evaluating the phase-offsets between the subcarrier of the received signal. That is, if the estimate of the phase offset slope is such that the  $m^{\text{th}}$  carrier phase offset is  $m\Delta\varphi$ , then the distance is:

$$d_m = \frac{v_p \Delta\varphi}{2\pi \Delta f} \quad (2.28)$$

where  $v_p$  is the propagation velocity ( $v_p = c$  in air) and  $\Delta f$  is the subcarrier frequency spacing ( $\Delta f = B_w/N$ ).

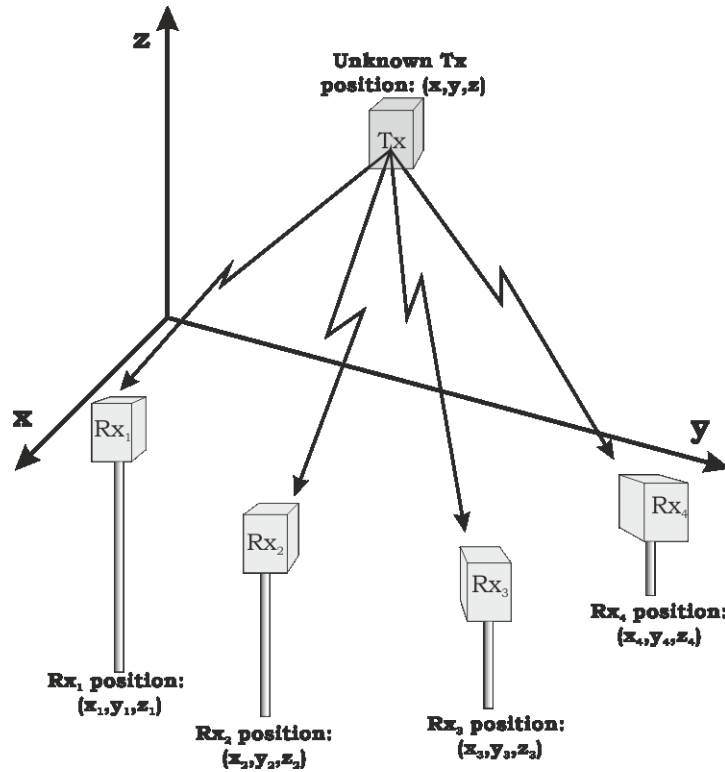


**Figure 2.9:** indoor positioning system – system architecture

The estimation of  $\Delta\varphi$  can be directly obtained by evaluating the argument of the tangent of the product between the received signal and a clear copy of the transmitted signal in the frequency domain [45]:

$$\widehat{\Delta\varphi} = \frac{1}{2\pi} \tan^{-1} \left\{ \frac{\sum_{k=0}^{L-1} \text{Im}(Y_l[k]X_l^*[k])}{\sum_{k=0}^{L-1} \text{Re}(Y_l[k]X_l^*[k])} \right\} \quad (2.29)$$

Figure 2.10 illustrates an example of the angle function estimated by equation (2.29) considering a 64-length OFDM signal combined with a 52-length ZC sequence. The example reports the angle

function in the case in which the receiver and the transmitter are placed 2.9 meters far apart. It should be noted that the value of  $\Delta\varphi$  is constant along the subcarriers and due to the linear dependence of the subcarrier frequencies, it can be estimated evaluating the slope of the best fit line. Moreover, this line exhibits an offset that depends on the phase of the central carrier system  $f_c$ . Thus, from the analysis of the angle function can be extracted two information: the subcarriers phase offset  $\Delta\varphi$  and the carrier offset  $\varphi_c$ . These two terms can be used to fine adjust the distance value computed from the time offset evaluated in time domain. However, due to its periodic nature, the carrier offset  $\varphi_c$  is the sum of an integer part,  $\varphi_{ci}$ , and a fractional part,  $\varphi_{cf}$ . The last one, estimated from the line offset, is in the  $-0.5\lambda \leq \varphi_{cf} \leq 0.5\lambda$  range, while the integer part can be computed dividing the value of the distance  $\delta_m$ , associated to the TO by the wavelength  $\lambda$ :

$$\widehat{\varphi}_{ci} = \left\lfloor \frac{\widehat{\delta}_m \cdot c \cdot T_S}{\lambda} \right\rfloor \quad (2.30)$$

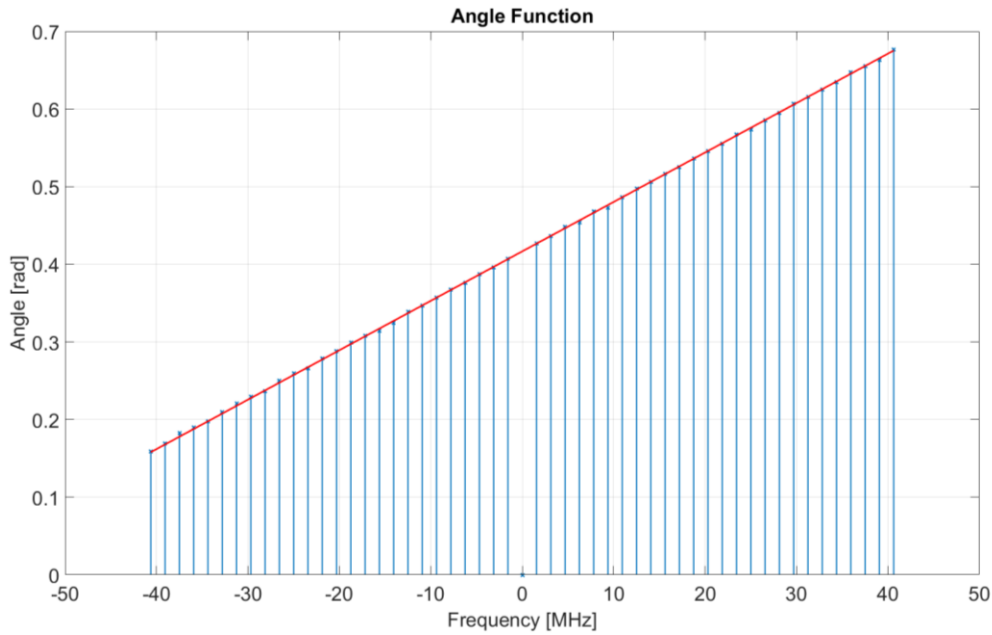


**Figure 2.10:** Example of angle function for a distance of 2.9 meters

Once estimated the TO and the CFO of the system, the target position can be calculated. However, in practice there is still an important issue affecting the measurements of the parameters necessary to carry on the estimation, that is, the symbol offset (SO). This is due to the fact that, no synchronization is performed between the signal generation process at the transmitter side and the signal acquisition process at the receivers' side. This lack of synchronization introduces a constant offset term that can be viewed as a symbol timing error. However, in our proposed system due to

the sharing of the acquisition clock among the receivers, we have the advantage that the value of this offset error is identical for all receivers. The SO affects directly the TO estimation and it must be compensated before to evaluate the TO and the CFO of the system. To facilitate the SO estimation, the system transmits the OFDM symbol  $x(t)$  followed by an its conjugate copy and two OFDM symbols composed by null subcarriers (Figure 2.11).

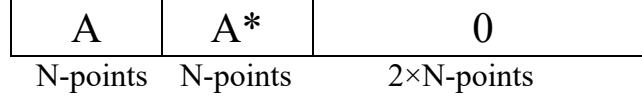


**Figure 2.11:** Symbol transmit Frame.

The correct starting point of the received frame  $y[n]$  is evaluated by arbitrarily defining a time window,  $W$ , whose length is twice the length of  $N$ . Within  $W$  the proposed system computes the circular auto-correlation of the received signal as follows:

$$P[n] = \sum_{k=0}^{W/2-1} y_k y_{n+k+W/2}^* \quad (2.31)$$

The starting point of the frame coincides with the maximum of  $P[n]$  and, thus, the arbitrary window  $W$  is moved to maximize the auto-correlation function. In this case, the maximum of  $P[n]$  occurs when the first point of  $W$  coincides with the first sample of the symbol  $A$  and, thus,  $W$  completely contains the sequence composed by the frame  $A$  and  $A^*$ . Note that to simplify the overall mathematical treatment, in (2.31) the AWGN contribution has been neglected. In practice, the effect introduced by the AWGN will be to reduce the SNR ratios, therefore affecting the measurement of the peaks' positions. This finally results in a reduction of the precision and accuracy of the system [46] and, therefore, a lower limit in terms of the maximum measurable distance.

Once the channel effects are estimated and the SO compensated, the proposed system evaluates the TDOA between the signals at the receivers' constellation end. The samples of the received signals are sent to a central processing unit that runs an algorithm that allows to extract the distances. The receivers are placed in *a priori* known spatial coordinates configuration with one of them assumed to be the origin of the system  $(0,0,0)$ . The 3-D coordinates  $(x_t, y_t, z_t)$  are extracted considering the geometrical model of the system by resolving the following system of linear equations:

$$D_1 - D_2 = \alpha_{12} = \quad (2.32)$$

$$\begin{aligned}
&= \sqrt{x_t^2 + y_t^2} - \sqrt{(x_{12} - x_t)^2 + (y_t - y_{12})^2} \\
&\quad D_1 - D_3 = \alpha_{13} = \\
&\quad \sqrt{x_t^2 + y_t^2} - \sqrt{(x_t - x_{13})^2 + (y_t - y_{13})^2} \\
&\quad D_1 - D_4 = \alpha_{14} = \\
&\quad \sqrt{x_t^2 + z_t^2} - \sqrt{(x_t - x_{14})^2 + (z_t - z_{14})^2}
\end{aligned}$$

The differential distances  $\alpha_{12}$ ,  $\alpha_{13}$ , and,  $\alpha_{14}$  are obtained estimating the amount of  $\delta_m$  and  $\varphi_m$  between the receiver  $RX_1$  and the receivers  $RX_2$ ,  $RX_3$  and  $RX_4$  respectively. Figure 2.12 illustrates a simplified 2-D version of the problem. In the 2-D position illustrated in Fig.5 the z-coordinates are fixed, and, the target is moving along the x-y axes.

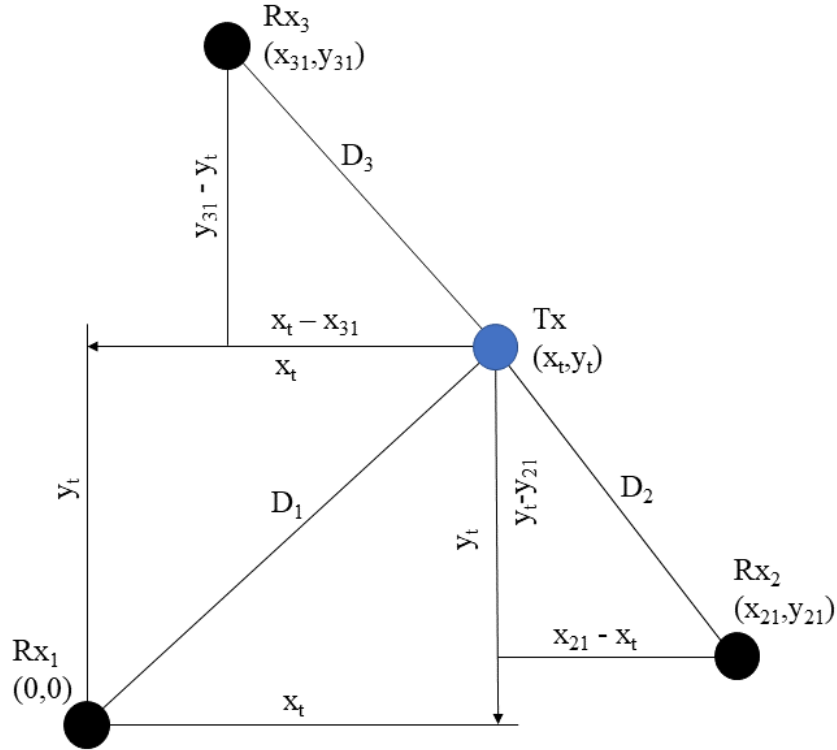


**Figure 2.12:** 2-D positioning system model.

Resuming, the algorithm consists of four main steps. Step 1 maximizes the auto-correlation function in (2.31) so that it can evaluate the correct temporal starting point of the frame. Algorithm 1 summarizes the necessary procedure for localizing the correct starting point of the frame. Step 2 takes the signals received from one of the receivers as reference, and it computes a coarse distance value evaluating every clock cycle the Time Offsets,  $\delta_m$ , of the other receivers (see Algorithm 2). Step 3 fine-adjusts the coarse values extracted in step 2. The algorithm in step 3 computes the CFO,  $\varphi_c$ , in the frequency domain and then calculate the relative distances  $\alpha_{12}$ ,  $\alpha_{13}$ , and,  $\alpha_{14}$ .

Finally, step 4 compute the position of the target by solving the equations in (2.32) (see Algorithm 4).

---

**Algorithm 2.1** Symbol Estimation

---

```

1: procedure SO_ESTIMATION( $y_l, L$ )
2:   ► Given R data points of the received sequence ( $y_l(z)$ ) with  $z=1, \dots, R$ ,
3:   ►  $N =$  OFDM signal length
4:   ►  $W =$  hypothesis window  $= 2N$ 
5:   ► extract the sequence starting point  $SO$ 
6:    $i = 1; SO=1$ 
7:   while ( $SO \neq W/2$ ) do
8:      $ya_1 \leftarrow y_1(i:i + N - 1)$ 
9:      $ya_1^* \leftarrow y_1(i + N:i + 2N - 1)$ 
10:    ► evaluate the autocorrelation function in (2.31)
11:     $P = \sum_{k=1}^L ya_1(k)ya_1^*(k)$ 
12:    ► find the maximum autocorrelation function
13:     $SO = \max(|P|^2)$ 
14:    ► if the SO is aligned with half of the hypothesis
15:      ► window return SO and exit from while cycle.
16:    ► else the window is moved
17:     $i = i+2N - SO$ 
18:  end while
19:  return  $SO$ 
20: end procedure

```

---

**Algorithm 2.2** Coarse Distance Estimation

---

```

1: procedure COARSE_DIST_EST( $y, X, SO, Ts, v$ )
2:   ► Given  $y(i,j)$  matrix of the received sequences with  $i = 1, \dots, R$  and  $j = 1, \dots, 4$ 
3:   ►  $X(z)$  transmitted signal spectrum with  $z = 1, \dots, N$ 
4:   ►  $N =$  OFDM signal length
5:   ►  $SO =$  frame starting point

```

---

---

```

6: ▶  $T_s$  = sampling time
7: ▶  $v$  = propagation velocity
8: ▶  $Fp$  = frame periods =  $\lfloor R / (2N) \rfloor - 1$ 
9: ▶ evaluate the differential time delays
10:  $k = SO$ 
11: for  $p \leftarrow 1$  to  $Fp$  do
12:   for  $j \leftarrow 1$  to 4 do
13:      $a(:, j) \leftarrow y(k:k + 2L - 1, j)$ 
14:     ▶ apply the Fast Fourier Transform and evaluate
15:     ▶ the cross-correlation function in (2.25)
16:     ▶ using the received sequences  $A, A^*$ 
17:     ▶ and the spectrum  $X(z)$ 
18:      $r_{xx}a(:, j) = IFFT\{FFT\{a(1:N, j)\} \times X^*\}$ 
19:      $r_{xx}a^*(:, j) = IFFT\{FFT\{a(N + 1:2N, j)\} \times X\}$ 
20:     ▶ extract the maximum from the single
21:     ▶ correlation function and evaluate the relative
22:     ▶ peak with a parabolic interpolation.
23:      $ma(p, j) = \text{parabolic\_interp}\left(\max_i(r_{xx}a(:, j))\right)$ 
24:      $ma^*(p, j) = \text{parabolic\_interp}\left(\max_i(r_{xx}a^*(:, j))\right)$ 
25:     ▶ compute the average between the value
26:     ▶ extracted for the sequence  $A$  and  $A^*$ .
27:      $pk(p, j) = \frac{ma(p, j) + ma^*(p, j)}{2}$ 
28:   end for
29:    $k = k + 2N$ 
30: end for
31: ▶ evaluate the peak average using the values
32: ▶ computed in each period
33: for  $j \leftarrow 1$  to 4 do

```

---

---

```

34:    $pf(j) = \text{mean}_i(pk(:, j))$ 
35:   end for
36:   ► calculate the differential peaks converted in
37:   ► distance values
38:   for  $j \leftarrow 1$  to 3 do
39:      $\widehat{dc}(j) = (pf(1) - pf(j + 1)) \cdot T_s \cdot c$ 
40:   end for
41: return  $\widehat{dc}$ 
42: end procedure

```

---

**Algorithm 2.3** CFO Estimation per period

---

```

1: procedure CFO_EST ( $R_{xx}A, R_{xx}A^*, \lambda$ )
2:   ► Given  $R_{xx}A(i, j)$  and  $R_{xx}A^*(i, j)$  the FFT of the cross-correlation function in (4) of the
   sequence A and A* respectively with  $i=1, \dots, L$  and  $j = 1, \dots, 4$ .
3:   ►  $N =$  OFDM signal length
4:   ►  $\lambda =$  carrier wavelength
5:   ► extract the angle function in (2.29) and compute the
6:   ► average between the values extracted for the
7:   ► sequence A and A*
8:   for  $j \leftarrow 1$  to 4 do
9:      $\varphi(j) = \frac{1}{4\pi} (\text{angle}(R_{xx}A(:, j)) - \text{angle}(R_{xx}A^*((:, j))))$ 
10:   end for
11:   ► compute the difference of carrier frequency
12:   ► offset and convert in fine distance values
13:   for  $j \leftarrow 1$  to 3 do
14:      $\widehat{df}(j) = (\varphi(1) - \varphi(j + 1)) \times \lambda$ 
15:   end for
16: return  $\widehat{df}$ 
17: end procedure

```

---

**Algorithm 2.4** Target Position Extraction

---

- 
- 1: **procedure** TARGET\_POS( $\widehat{dc}$ ,  $\widehat{df}$ ,  $x_{12}, y_{12}, x_{13}, y_{13}, x_{14}, z_{14}$ )
  - 2: ▶ Given  $\widehat{dc}$  array of the coarse distance values, and
  - 3: ▶  $\widehat{df}$  array of the fine distance values
  - 4: ▶  $x_{12}, y_{12}$  = x-y distance between RX<sub>1</sub> and RX<sub>2</sub>
  - 5: ▶  $x_{13}, y_{13}$  = x-y distance between RX<sub>1</sub> and RX<sub>3</sub>
  - 6: ▶  $x_{14}, z_{14}$  = x-z distance between RX<sub>1</sub> and RX<sub>4</sub>
  - 7: ▶ calculate the differential distances
  - 8:  $\alpha = \widehat{dc} + \widehat{df}$
  - 9: ▶ compute the target position using (2.32)
  - 10:  $\alpha(1) = \sqrt{x_t^2 + y_t^2} - \sqrt{(x_{12} - x_t)^2 + (y_t - y_{12})^2}$
  - 11:  $\alpha(2) = \sqrt{x_t^2 + y_t^2} - \sqrt{(x_t - x_{13})^2 + (y_t - y_{13})^2}$
  - 12:  $\alpha(3) = \sqrt{x_t^2 + z_t^2} - \sqrt{(x_t - x_{14})^2 + (z_t - z_{14})^2}$
  - 13: **return**  $x_t, y_t, z_t$
  - 14: **end procedure**
- 

## 2.6 Conclusions

To evaluate the position of an active target placed in an indoor environment, the proposed system exploits a GPS-like scheme composed by a single transmitter and four receivers. To avoid any synchronization error due to the frequency and the phase shift introduced by the frequency sources of the system, one receiver is selected as origin of the system and the positions are evaluated computing the Time Difference of Arrival between the received signals.

The target positions are extracted using a range signal that combine the properties of the well-known Zadoff-Chu sequences with the characteristics of the OFDM modulation scheme. The resulting signal is very robust against the multipath reflections that represent the main problem of every indoor positioning system.

Considering a pair of receivers, the difference distance between them can be computed in both time and frequency domain exploiting the properties of the Zadoff-Chu sequences and the OFDM modulation. Hence, the proposed system requires only signaling techniques that can be implemented in digital domain without analog hardware processing. This latter represents the most

important advantage of the proposed system because the resulting hardware architecture is very scalable and feasible in according to the design specifications.

In the next chapter a model will be implemented to evaluate the performance limits of the proposed solution and to define the characteristics of the transmit signal as the bandwidth, the minimum signal to noise ratio, the number of subcarriers and so on.

### 3 Indoor Positioning System: System Modeling

A parametric system model is implemented in MATLAB in order to define the signal parameters, such as number of subcarriers, bandwidth, ZC length and so on. The use of this model allows analyzing the performance of the distance ranging algorithm for different channel impulse responses. Initially, an AWGN channel will be considered to evaluate the performance of the system in ideal conditions and compute the mean error and the system precision as a function of the Signal to Noise Ratio (SNR). Then, a multipath channel impulse response will be investigated to extract the minimum difference between the rays that the proposed system is able to detect. Again, the system performance will be analyzed to evaluate the system precision and accuracy in severe multipath conditions.

#### 3.1 Additive Gaussian White Noise channel

In the first model, the system is composed by a single transmitter and two receivers and the difference distance between them is extracted. We considered an AWGN channel composed by a single ray related to the direct path connecting the nodes. A transmitter power of 0 dBm is set and for the path gain, only the distance dependence, expressed in (2.14), is considered. In presence of a LOS path, the exponent factor  $n$  varies from 1.63, for offices, to 1.79 in residential environments [38]. In the system model an average value of 1.71 is considered. The antenna characteristics are neglected, and the only error source is the gaussian noise introduced by the channel. The symbol offset is modeled as a uniformly distributed random variable and the received signals are considered as baseband signals obtained performing a direct I/Q demodulation. The sampling time is set to 1 GHz but to achieve a very high resolution in time-delay a 100 GHz sampling frequency is considered. In other words, the signal is generated considering a sampling frequency of 100 GHz, then a very precise time-shift is introduced and, finally, the signal is down-sampled to 1 GHz to apply the distance ranging algorithm.

In the test-bench the transmitter is placed to a fixed position  $(0,0,0)$  and reference receiver is placed at coordinate  $(1m,y_0,z_0)$  while the second receiver is moved from 1.1 meters to 10.1 meters with step of 0.01 meters along the x-axis. It should be noted that with two receivers the system is able to estimate only the difference of distance between the nodes. Thus, the coordinate along the x and z axes can be neglected.

### 3.1.1 Bandwidth vs SNR

In the first set of simulations, the impact of the signal bandwidth as a function of the SNR is investigated. An OFDM symbol composed by 64 subcarriers is generated combined with a 52-length ZC sequence with root index equal to 1. As described in [37], the value of the root index  $u$  directly affects the performance of the synchronization algorithm and determines the amount of shift present in the Channel Impulse Region (CIR). The value of  $u$  must be relative prime to sequence length and chosen such that it guarantees the presence of the minimum shift in the CIR region. For all simulations and measurements  $u$  is set to +1 which corresponds to a minimum possible shift of  $\pm 1$  [37]. The number of subcarriers is chosen in according to the IEEE 802.11a specifications [43], however, in the next set of simulation this number is varied to evaluate the system performance as function of their value.

Figure 3.1 reports the system precision in TO estimation as function of the Signal to Noise Ratio. It should be noted that when the SNR increases the precision improves as well with a linear function in logarithmic scale or, equivalent, with an exponential function in linear scale.

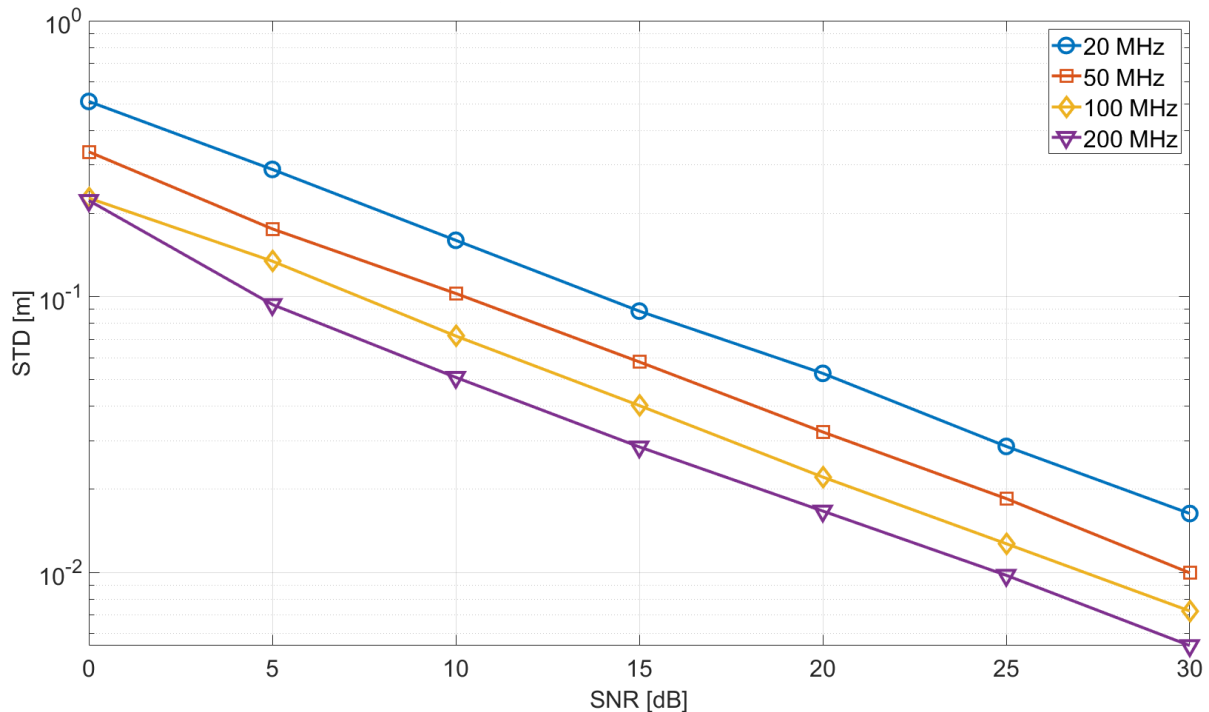
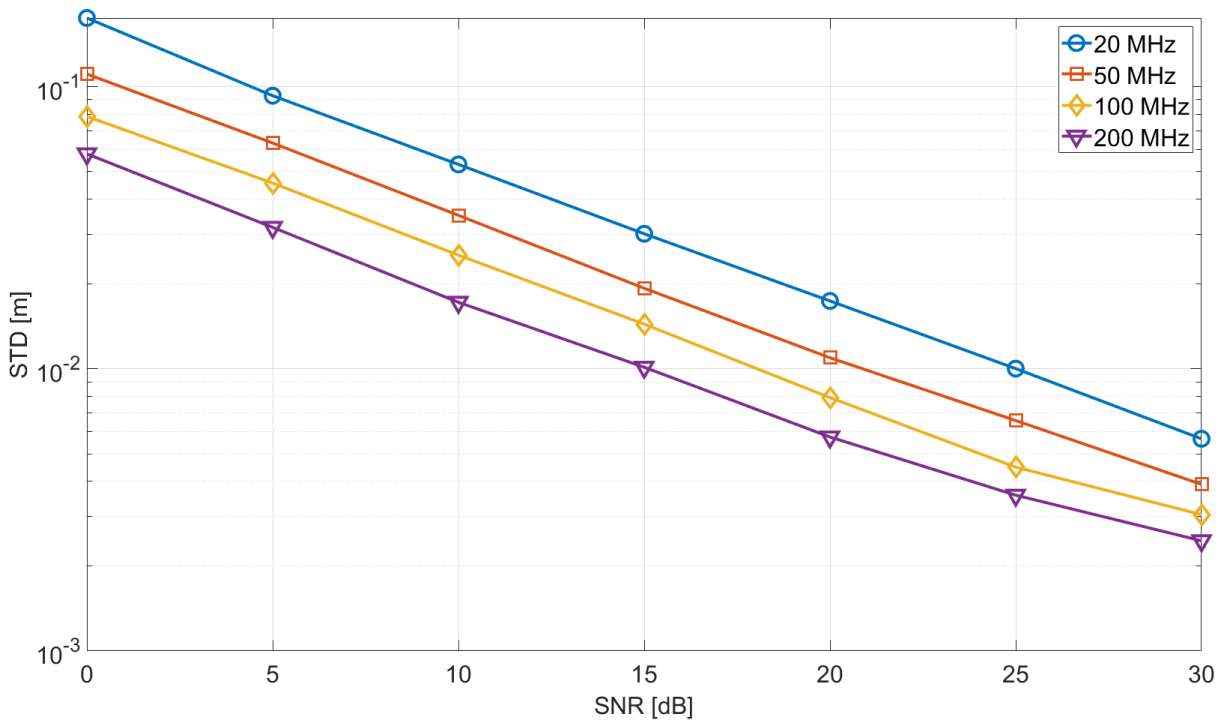


Figure 3.1: Fig. 1 System Precision in time domain as function of the SNR

Moreover, as expected from the theory, the system exhibits higher precisions when the bandwidth is increased. Hence, the system precision is affected only by the errors introduced by the sampling process for a SNR of 30 dB.

Similar considerations are valid for the distance estimates extracted in frequency domain from the subcarriers phase. It should be noted, from Figure 3.2, that the system is more precise in frequency domain than in time domain. In fact, setting a fixed value for the signal bandwidth, the CFO measurements exhibits a lower standard deviation than the TO estimations (Figure 3.3). Considering for example a bandwidth of 100 MHz, the distance measurements in frequency domain are about three times more precise than the estimates in time domain.



**Figure 3.2:** System precision in frequency domain as function of the SNR

This result is due to noise introduced by the channel that degrades the peak estimation in time domain. Moreover, as mentioned, the precision in time domain is dominated by the sampling time of the system, while the subcarriers phase is evaluated computing a best-fit linear function that is able to filter the noisy values. From the graphs it is possible to conclude that the system is able to extract the target distance with a mm-precision (in frequency domain) using a signal with a bandwidth of only 100 MHz and a SNR of 20 dB using only raw data (no further processing is applied).

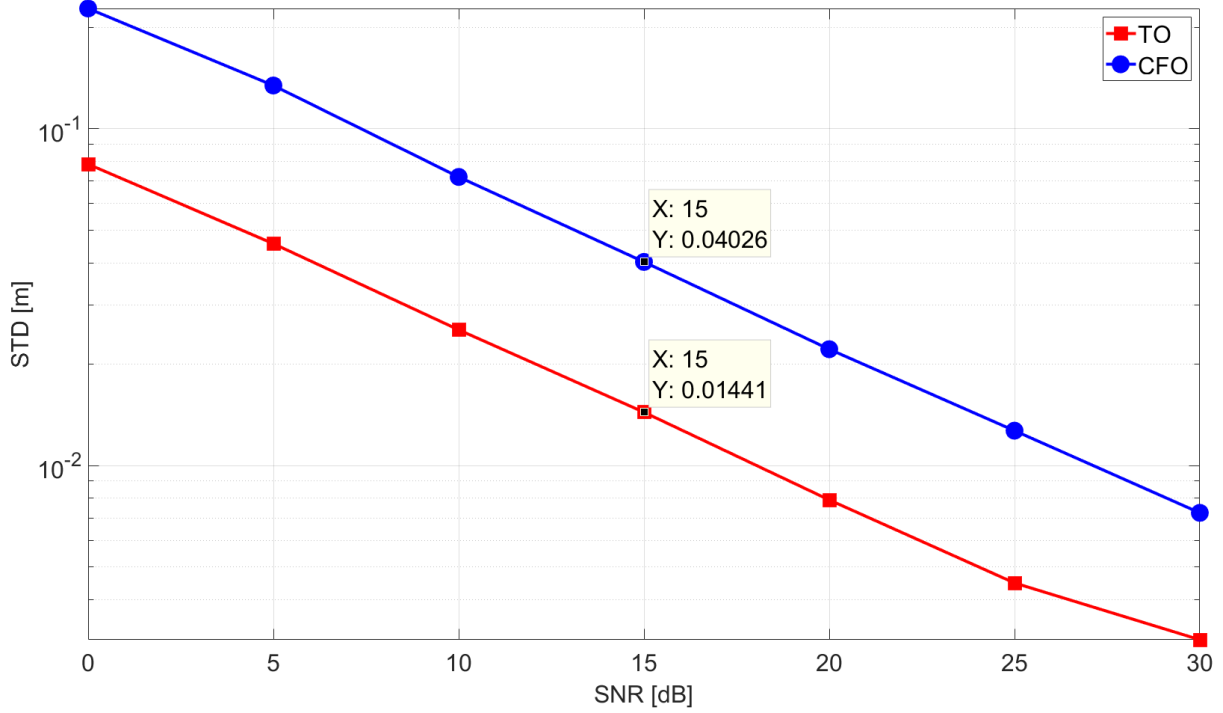


**Figure 3.3:** TO and CFO estimation as function of the SNR. The values are extracted for a bandwidth of 100 MHz.

In terms of accuracy, the proposed system exhibits the same behavior of the precision as a function of the SNR at receiver. The Figure 3.4 and Figure 3.5 show the accuracy of the system for different signal bandwidth values and SNR. The increment of the signal bandwidth leads to an improvement of the system accuracy. The latter is evaluated computing the mean of the absolute value of the error, as expressed below:

$$accuracy = E[|e|] = E[|d - \hat{d}|] \quad (3.1)$$

where  $d$  is the ideal distance value and  $\hat{d}$  is its estimation computed by the proposed system.

Note from the curves that for 100 MHz of signal bandwidth and 20 dB of SNR, the proposed system achieves a mm-accuracy evaluating the distance in frequency-domain.

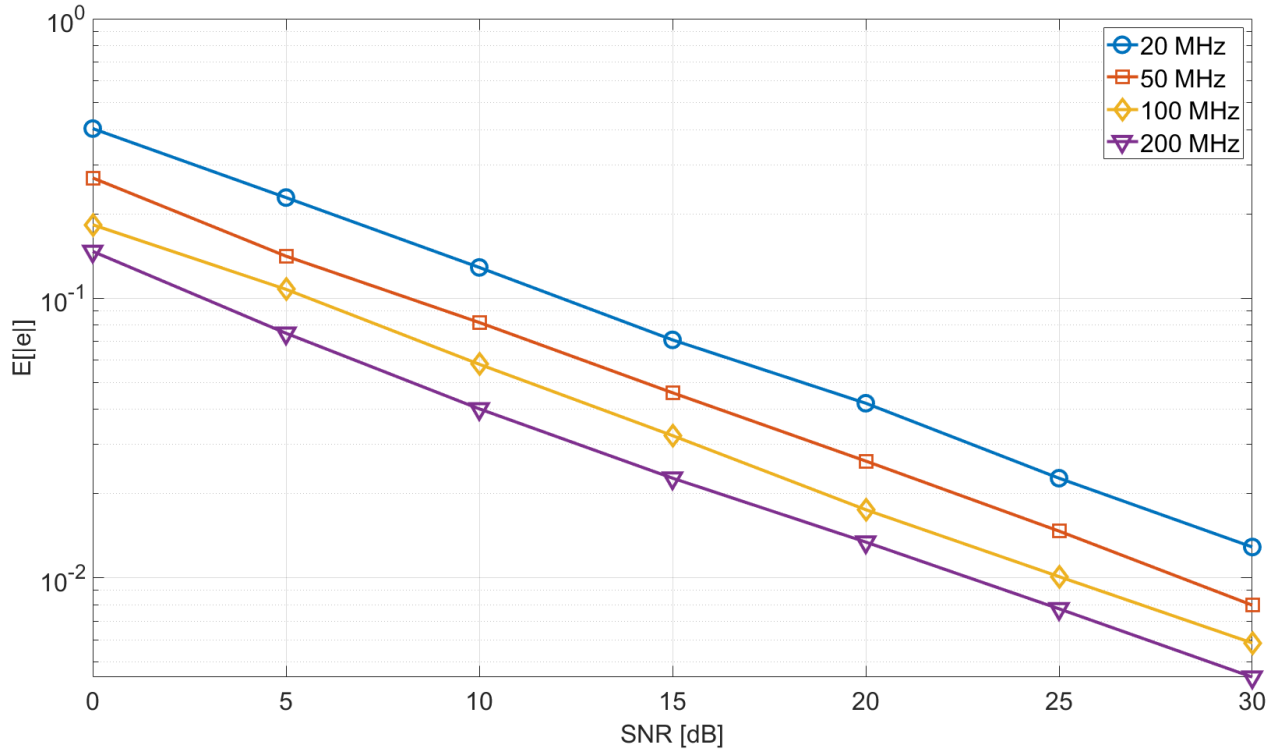


Figure 3.4: System Mean Error as function of the SNR, evaluated in time-domain

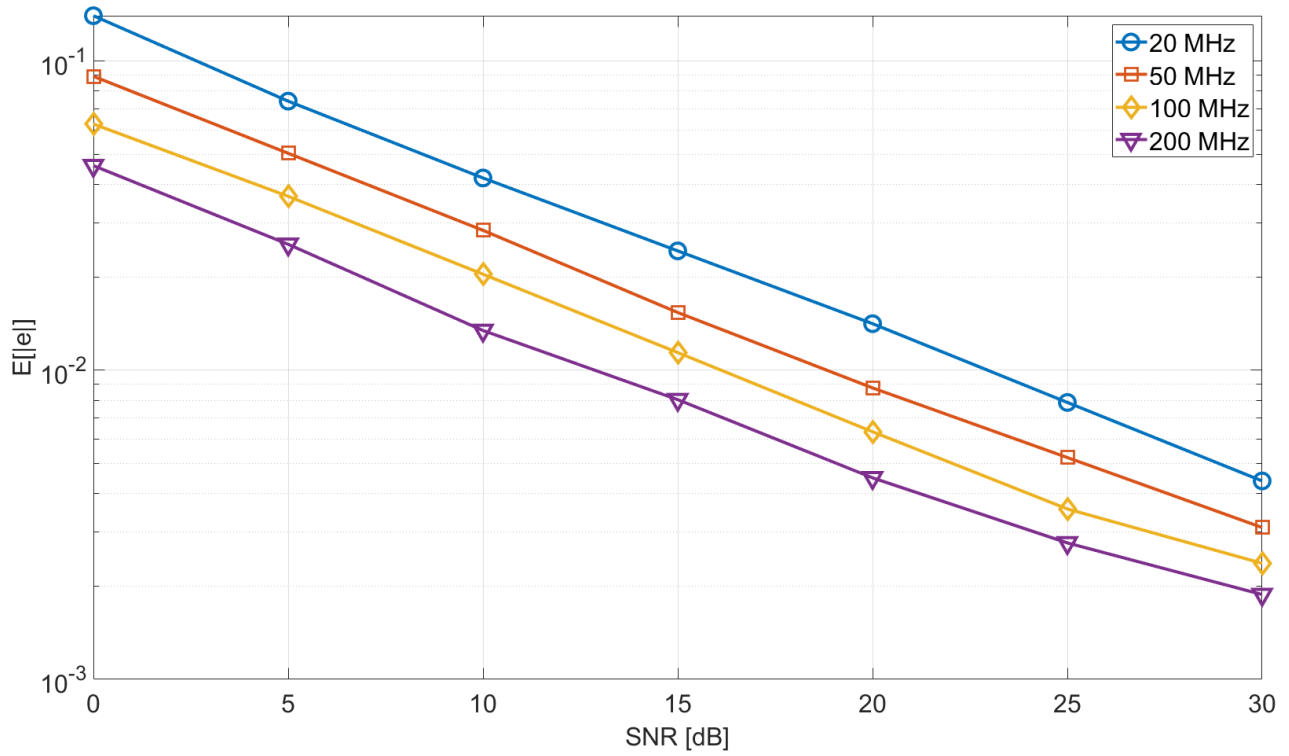
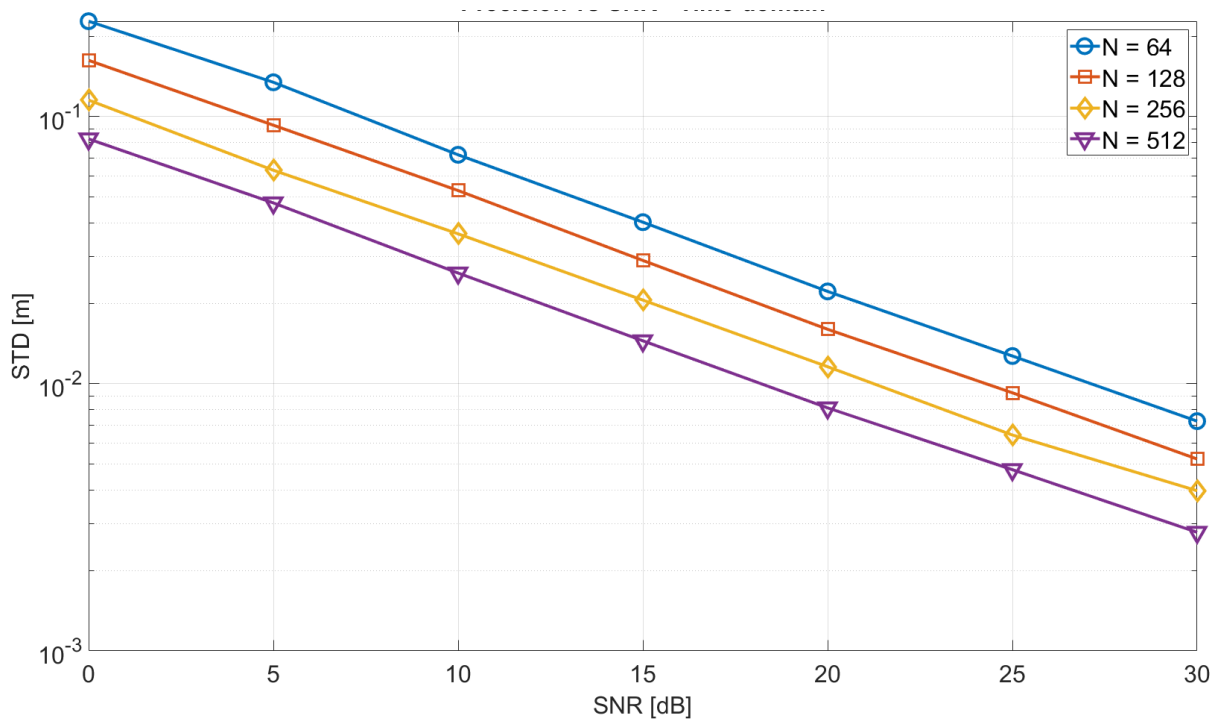


Figure 3.5: System Mean Error as function of the SNR, evaluated in frequency-domain

### 3.1.2 Subcarriers vs SNR

Both the precision and the system accuracy are computed considering a fixed number of subcarriers. Once evaluated the performance of the system as a function of the signal bandwidth, the number of subcarriers is varied to observe if there is a relationship with the accuracy and the system precision. In this test-bench the other parameters are not modified, and, a fixed value of 100 MHz is set for the signal bandwidth. Figure 3.6 sketches the estimates of the TO as function of the SNR and for different lengths of the OFDM symbol. Note that, for a fixed bandwidth, the increment of the number of subcarriers leads to an improvement in system precision. In fact, considering a SNR of 20 dB the system precision varies from 2 cm, in the case of 64 subcarriers, to 8 mm if a 512-length OFDM signal is used. Hence a precision improvement of 2.5 times is obtained increasing eight times the number of subcarriers.



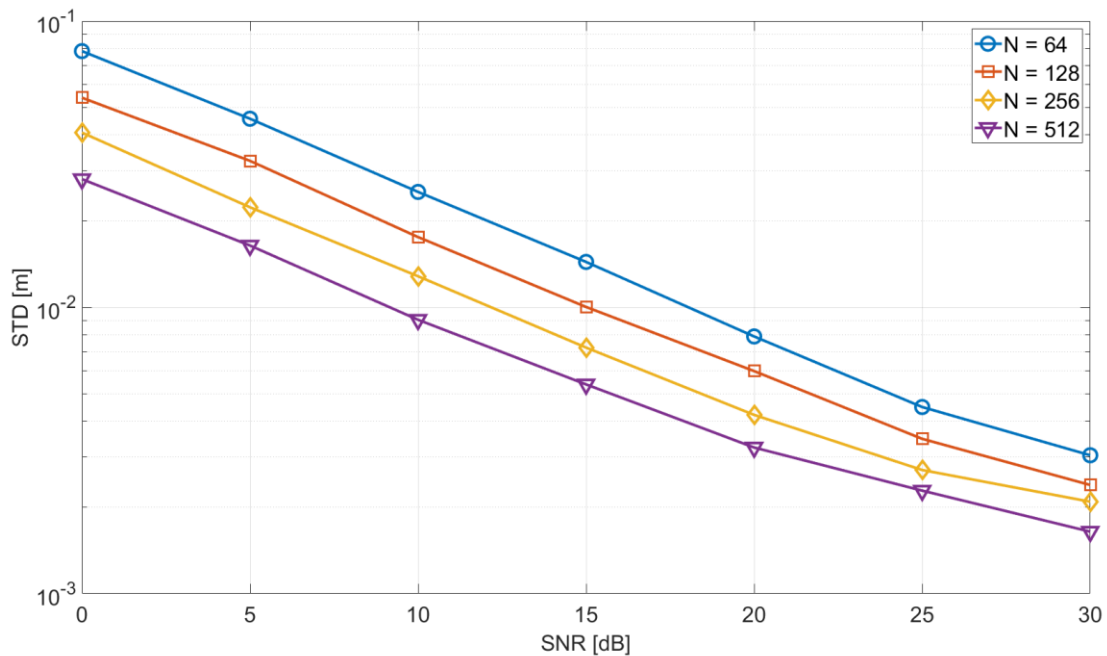
**Figure 3.6:** Time-domain system precision as function of SNR and the number of subcarriers

Figure 3.7 shows the distance estimate computed in frequency domain as function of the SNR and the number of subcarriers. Considering 100 MHz of signal bandwidth and a 512-length of OFDM symbol, the system achieves a system precision lower than 1 cm even for a SNR equal to 10 dB. It should be noted that the increment in system precision is not constant when the SNR increases. In fact, for SNR greater than 15 dB the curves are not linear functions and seem to tend to an

asymptotic value, that for a 512-length OFDM symbol is about 1 mm. This asymptotic value can be computed from the expression below:

$$\sigma^2 \geq \frac{3}{4\pi^2 T \cdot SNR \left( \left( f_c + \frac{B_W}{2} \right)^3 - \left( f_c - \frac{B_W}{2} \right)^3 \right)} \quad (3.2)$$

where T is the OFDM period ( $T=1/\Delta f$ ), and  $f_c$  is carrier central frequency. The expression in (3.2) is named Cramer-Rao Lower Bound (CRLB) [47] and defines the lower limit of any distance ranging systems. Moreover, it illustrates the relationship between the system precision and the signal parameters: to improve the system precision it is possible to increment the signal duration or, better, the signal bandwidth or carrier frequency. Figure 3.8 reports an example of CRLB for different values of subcarriers (that define the signal period T) and considering a  $f_c$  equal to 5.8 GHz with a signal bandwidth of 100 MHz.



**Figure 3.7:** Frequency-Domain System precision as function of SNR and the number of subcarriers

Finally, a comparison between the time and frequency domain as function of the SNR is reported in Figure 3.9. The curves are extracted considering a 512-length OFDM symbol with 100 MHz of signal bandwidth. For SNR lower or equal to 15 dB, the frequency domain measurements are 2.7 times better than the time-domain estimates. Instead, for SNR greater than 15 dB, due to the curve compression in frequency domain, the system precision is improved by a factor of 1.68.

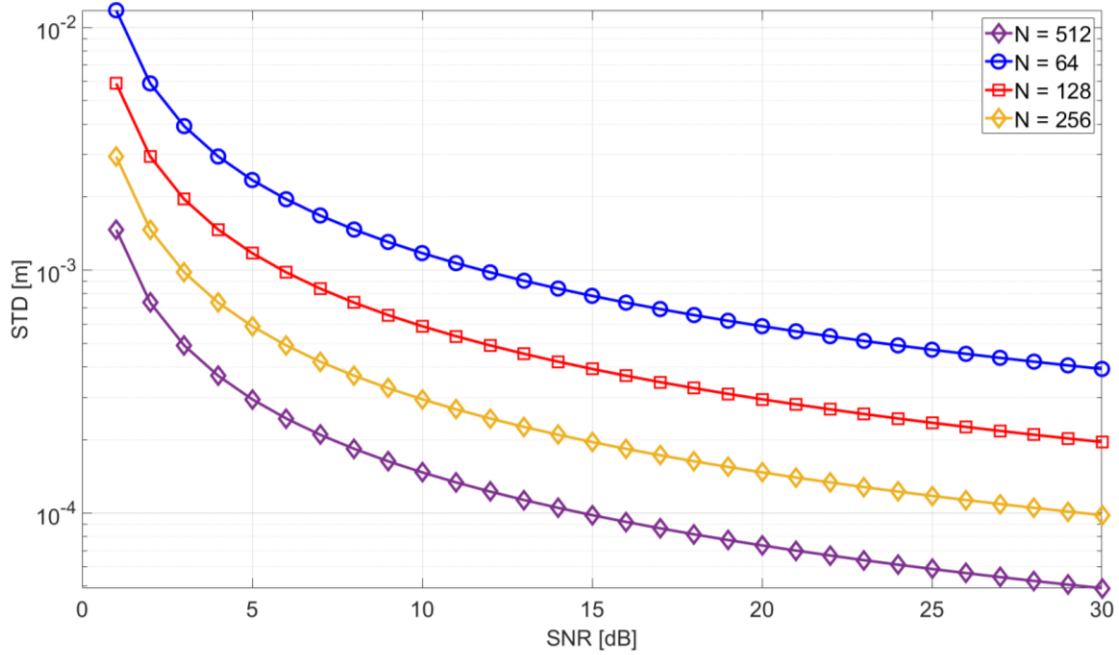


**Figure 3.8:** CRLB as function of the SNR and for different values of subcarriers

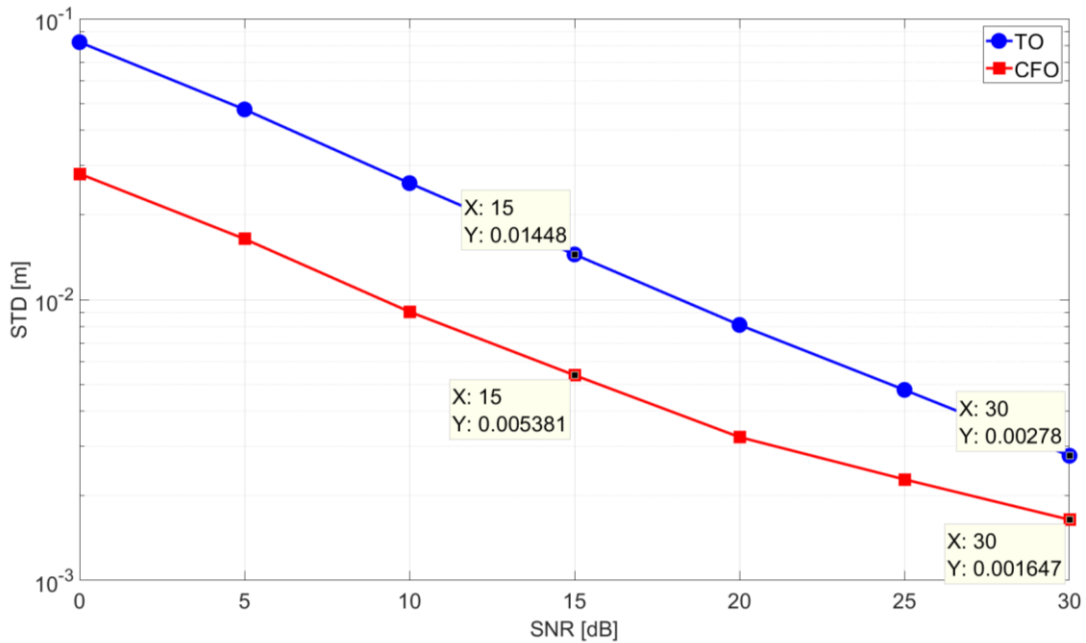


**Figure 3.9:** TO and CFO estimation as function of the SNR. The number of subcarriers is set to 512.

From the analysis of the graphs extracted by the system model, it is possible to conclude that, in presence of noisy channels, an increment of the number of subcarriers leads to an improvement of the system precision. This result is possible because the TO and the CFO estimates are computed considering a higher number of points. However, it is necessary to remind that if the number of points is increased, the system complexity increases as well. Moreover, the period of the signal is

longer when a high number of subcarriers is used. In fact, a 64-length OFDM symbol with a 100MHz of bandwidth has a period equal to  $0.64 \mu\text{s}$  while a 512-length signal has a period 8 time greater than the previous one ( $5.12 \mu\text{s}$ ). This can be a problem in real time indoor positioning systems where a very large number of samples should be processed with a reduced time.

Identical considerations are valid for the system accuracy that is improved when a high number of subcarriers is used. Figure 3.10 and Figure 3.11 report the average of the absolute values of the error computed for both time and frequency domain. Note that the system accuracy, in time domain, is improved by a factor of 2.74 when the number of subcarriers varies from 64 to 512. Instead, in frequency domain, the system accuracy is improved by a factor of about 2.5 with the same increment of the OFDM length.

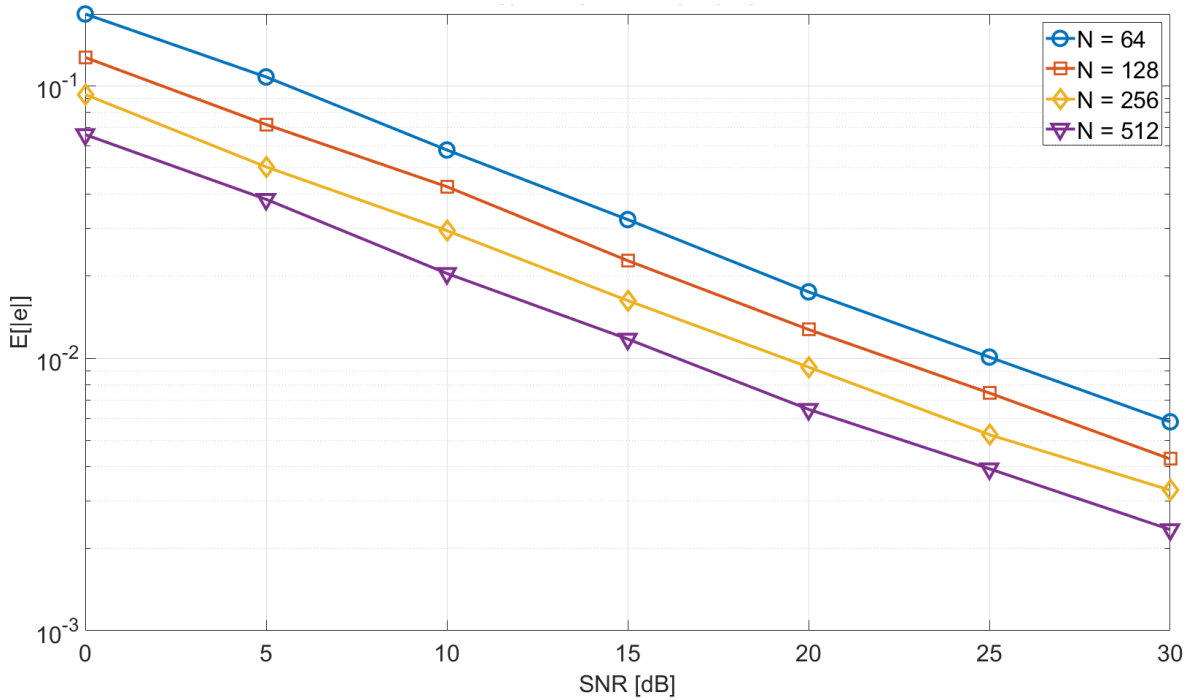


**Figure 3.10:** Time-Domain System Accuracy as function of the SNR and the OFDM length. The signal bandwidth is set to 100 MHz.

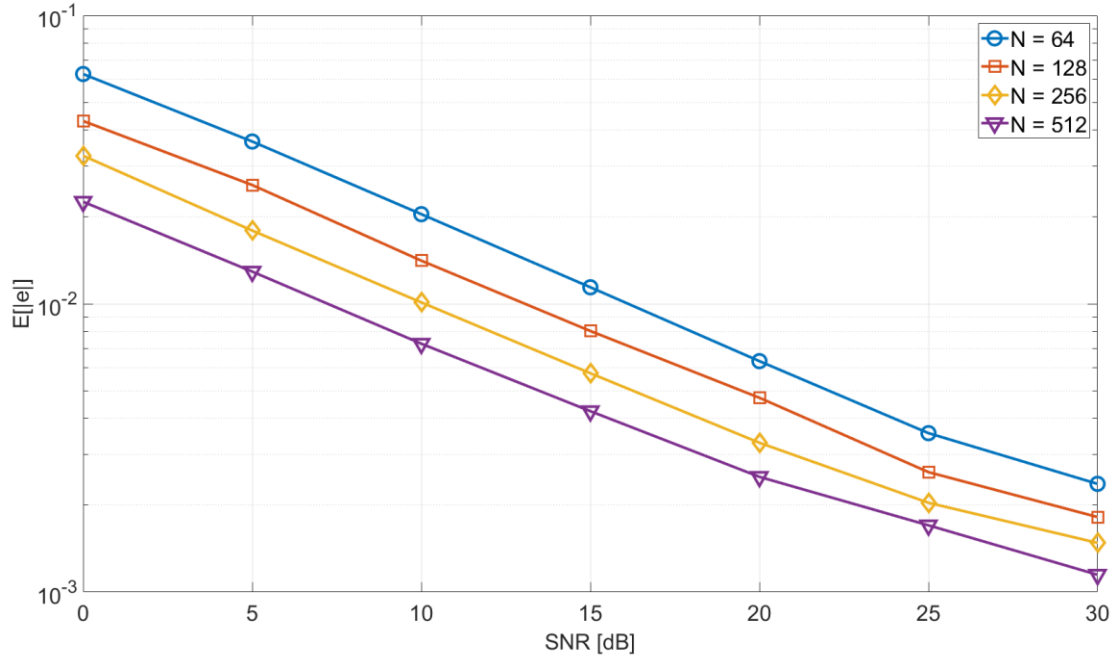


**Figure 3.11:** Frequency Domain System Accuracy as function of the SNR and the OFDM length. The signal bandwidth is set to 100 MHz.

### 3.2 Multipath Channel

In the first test-bench the transmitter is placed at fixed position  $(0,0,0)$  while the first receiver is placed at the coordinates  $(1m,y_1,z_1)$ . The second receiver is placed to 2.5 meters far apart from the first receiver. The system parameters are identical to the previous test-bench while the simple multipath model in (2.15) is considered. Thus, the channel impulse response comprises a tap related to the LOS path and a second tap related to a single multipath ray. In the first subset of simulations, it is evaluated the impact of a near indirect path on the system performance. Hence, the distance of the indirect path is varied in range 2.6 to 3.1 meters and the accuracy and system precision are estimated extracting the first of arrival path from the cross-correlation function.

Figure 3.12 shows the system precision, evaluated in time domain, as a function of the NLOS path amplitude and for different SNRs. The values are estimated considering a 64-length OFDM signal with 100 MHz of bandwidth. Also, Considering  $A$  as the amplitude of the direct path, the indirect ray has an amplitude equal to  $\alpha A$ . Note that, when the indirect path amplitude raises the system precision decreases as well. Obviously, the same considerations are valid even for the system accuracy as showed in Figure 3.13. Moreover, for low SNRs the system is not able to extract the

correct distance in time-domain with a mm-precision even in presence of indirect path with low amplitude.

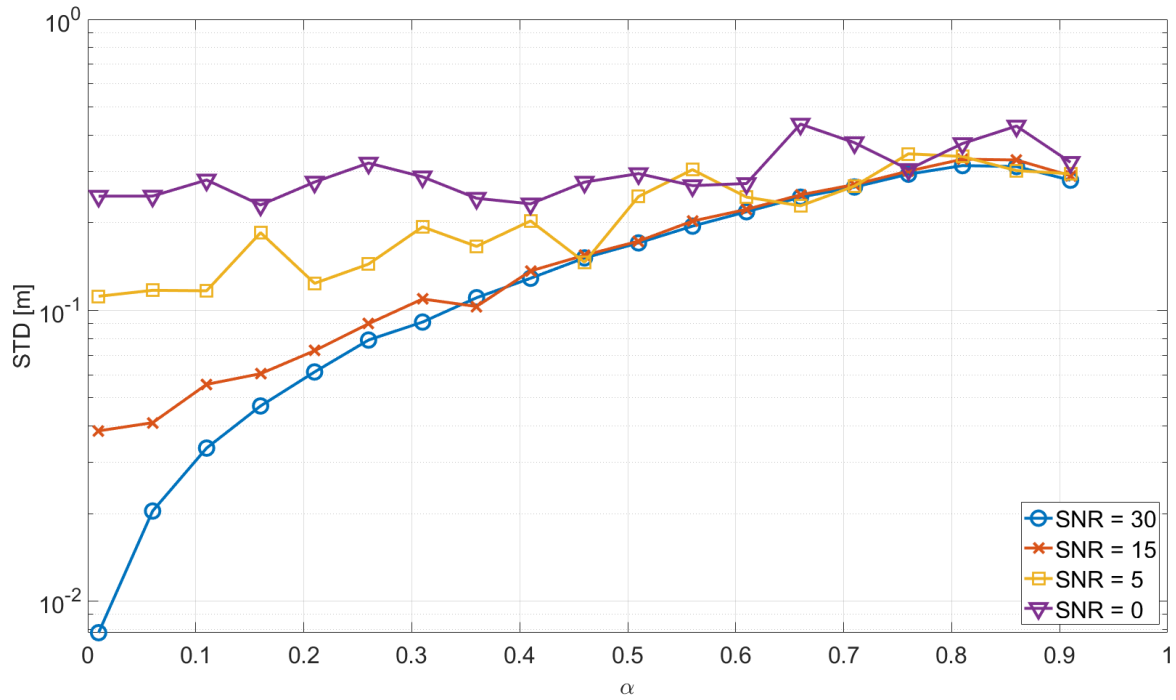


Figure 3.12: TO system precision considering a 64-length OFDM symbol with 100 MHz of bandwidth.

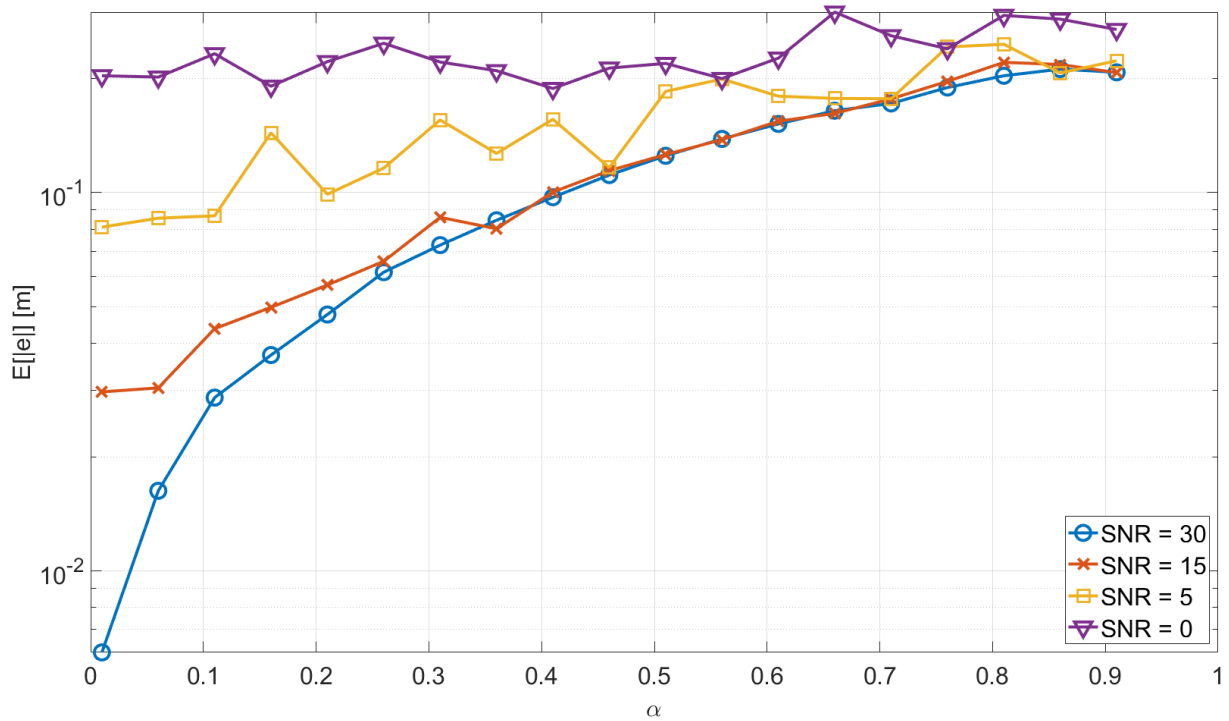
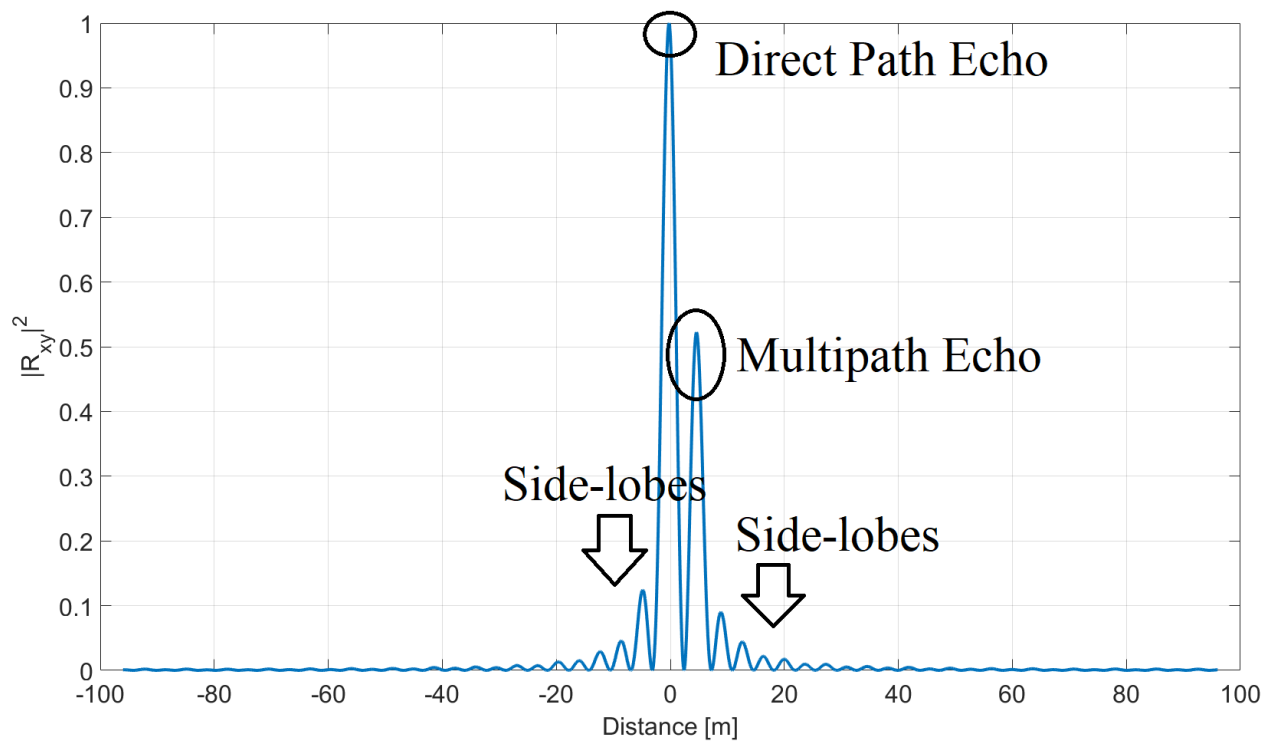


Figure 3.13: TO system accuracy considering a 64-length OFDM symbol with 100 MHz of bandwidth.

It should be noted that even in presence of a single indirect path the accuracy and the system precision decrease dramatically than the case of AWGN channels. Ideally, the cross-correlation function should present two distinct pulses placed at time shift that correspond to the time delay of paths. However, the real systems have not an infinite memory, so the data are truncated, and the pulses in cross-correlation are *sinc* functions with an aperture of the main lobe that depends on the number of considered samples. The presence of a secondary *sinc* peak close to the main lobe modifies the curve determining a shift in peak position. This effect is more evident for high amplitudes of the indirect path that determines low level of system precision and accuracy (Figure 3.14).



**Figure 3.14:** Cross-Correlation in time domain in presence of multipath echos.

Also, if the indirect path length is increased with respect to that of the direct path, its influence is still evident in the main peak estimation. In facts, the sidelobes of the indirect path interferes with the lobes of the direct echo, determining again a time shift in cross-correlation function (Figure 3.15). Note that the influence of the secondary path grows when its amplitude increases as well. Moreover, if the peaks of the sidelobes of the main path overlap with the null points of the echo sinc function, any mutual interference is not present, and the error is dominated only by the noise introduced by the channel.

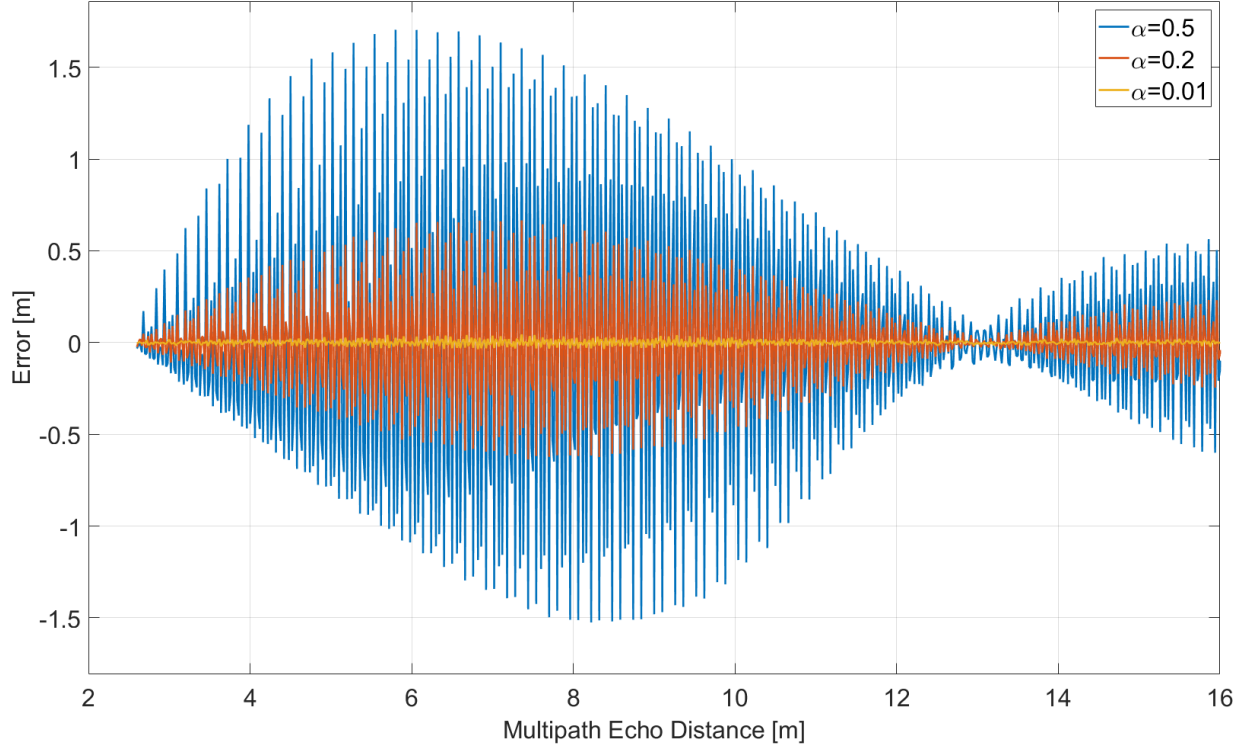


**Figure 3.15:** Error as function of the multipath echo distance and amplitude

Figure 3.16 and Figure 3.17 illustrates the system precision and accuracy computed in frequency domain extracting the subcarriers phase shift. Again, the estimates in frequency domain results more accurate e precise than the time domain but the system is not able to achieve a mm precision without using any additional strategy to reduce the impact of the close multipath ray. However, it should be noted that the precision and the system accuracy is quite similar even for low SNRs. Considering the multipath model in (2.15) the time offset in frequency domain is the sum of complex sinusoidal wave with a phase determined by the amount of the multipath distance:

$$TO_{frequency-domain} = \sum_{i=1}^M e^{j2\pi k \delta_i / N} \quad (3.3)$$

with M is the total number of echoes multipath. The presence of multipath introduces a phase distortion in angle function that can be viewed as a sinusoidal function overlapped on the linear function relative to the direct path (Figure 3.18). Hence, the relationship in (2.29) is not valid if any technique for reducing the multipath influence is not implemented.

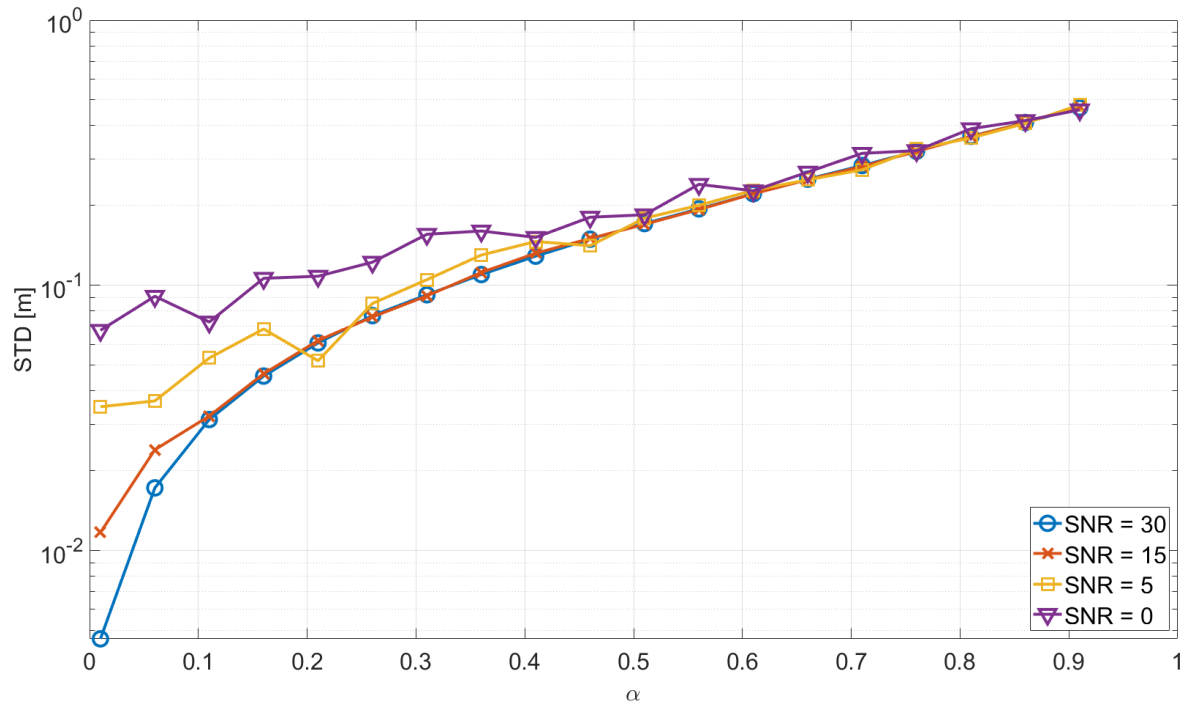


Figure 3.16: CFO System precision considering a 64-length OFDM symbol with 100 MHz of bandwidth.

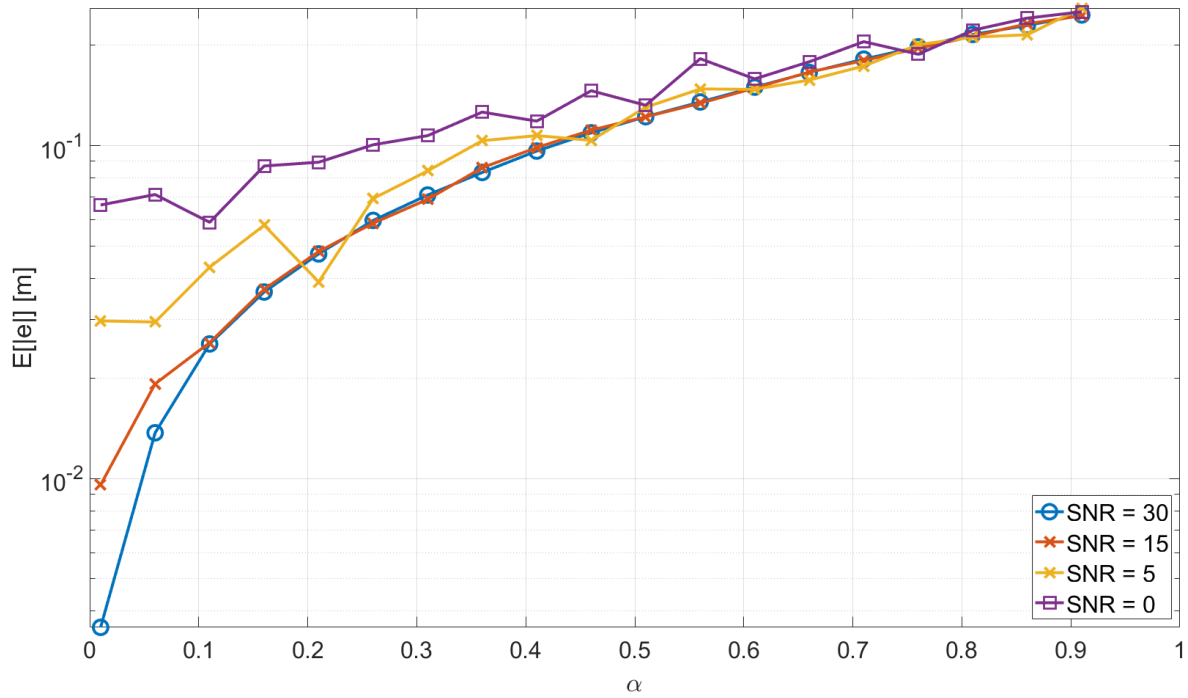
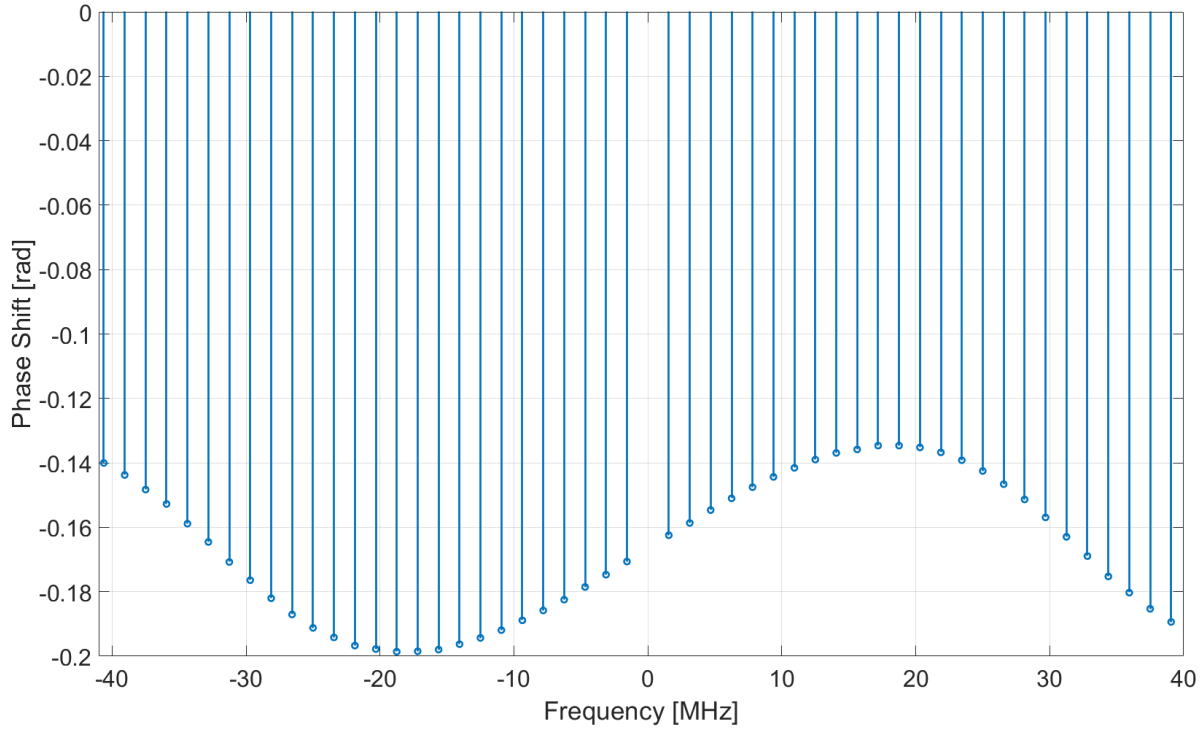


Figure 3.17: CFO System accuracy considering a 64-length OFDM symbol with 100 MHz of bandwidth.



**Figure 3.18:** Angle function considering an undirect path placed to 4.5 m away from the direct path and with  $\alpha=0.2$ .

Two main approaches are possible to reduce the multipath effects: the use of antennas with a narrow directivity diagram, and, the implementation of techniques for echo estimation and cancellation. The first one acts directly on the channel impulse response reducing the number of indirect paths that reach the receiver and their amplitudes. The second one is independent by the first approach and acts on the estimates of the cross-correlation and the angle functions used to evaluate the direct path at receiver. These two techniques are independent and can be combined to obtain a *clean* channel impulse response. The use of a high directivity antenna allows to focalize the transmit power only in the direction that correspond to the direct path between the transmitter and the receiver. In other words, the model of the channel described in (2.16) changes because the received power of the single rays in the clusters not depends only by the geometric attenuation and the frequency but is related even to the directivity diagram of the antenna. Hence, the path gain expressed in (2.10) must be modified to take in account of the effects of the directivity diagram. Although the use of antennas with a narrow directivity diagram strongly reduces the presence of the multipath at the receivers, an increased number of antennas is required to cover the entire scenario raising the costs and the system complexity. Thus, the design of the antenna depends on the considered scenario and must be traded-off the coverage area and the directivity diagram.

The second approach exploits the properties of the ZC sequences and the result expressed in (2.26) to estimate the amplitude and the time shift of each multipath echo. Then a Finite Impulse Response (FIR) filter can be generated to equalize the signal to delete the indirect paths in the channel impulse response. A necessary condition to apply this method is that the multipath echoes in the channel impulse response estimated by (2.26) be separable. In fact, if the indirect path is too close to the direct echo, the channel impulse response exhibits a single pulse with an amplitude and a time shift that is an average of the two rays [12]. In this case the method is unsuitable, and the use of a high directivity antenna is the only viable approach to reduce the multipath effects. Cygansky et al. [12] explore the performance limits of a distance estimation algorithm that use a multicarrier signal in presence of a direct path and a single multipath echo. From the measurements, it was defined a *breakdown distance* for the multipath echo as function of the signal bandwidth and the signal to noise ratio. If the multipath distance is lower than the breakdown point, the related pulse, in the channel impulse response, is not separable. On the contrary, when the multipath echo is placed at a distance greater than the breakdown point, the related pulse appears in the channel impulse response and it is separable from the direct path. As mentioned, the breakdown distance depends on the signal bandwidth and the signal to noise ratio. An increment of these two parameters decreases the breakdown point as well, and the system is more precise and accurate because it is possible to estimate and remove multipath echoes closer to the direct path.

### **3.2.1 Multipath Echo Estimation Algorithm**

In the next test-bench the breakdown distance is evaluated as function of the signal bandwidth, and also, a multipath echo algorithm is implemented to improve the accuracy and the precision of the system. To simplify the algorithm design, the noise is neglected and only the multipath effects are considered. Again, for sake of simplicity, the channel impulse response comprises a direct echo and a single multipath ray. The first one is fixed and equal to 1.5 meters, on the contrary, the position of the indirect path varies from 1 cm away from the direct echo of the second receiver up to 15 meters, with steps of 50 cm. The other operation conditions, as the transmit power, or the number of subcarriers, are the same as in the previous testbenches. To calculate the breakdown distance as function of the signal bandwidth it is considered an indirect path with an amplitude of  $0.9 \cdot A$ , with  $A$  the amplitude of the direct echo.

Observing the Figure 3.14 it should be noted that if the multipath echo has a strong amplitude and it is placed at time greater than the width of the main lobe, it is possible to estimate and remove it by means of an iterative algorithm based on the descendent gradient method [48]-[51].

Let define  $H(z)$  as the transfer function of the channel impulse response in discrete domain, and  $x(z)$  the row vector of the samples of the transmitted signal. Representing the transmission with block diagrams, the received signal can be obtained passing  $x(z)$  through the transfer function of the channel as depicted in

Figure 3.19 (a). In other words,  $y(z)$  can be obtained multiplying the  $z$ -transform of the transmit signal,  $X(z)$  with  $H(z)$ . The last is the  $z$ -transform of the expression in (2.15) and can be represented by:

$$H(z) = \sum_{k=0}^{K-1} \alpha_k z^{-\tau_k} \quad (3.4)$$

where  $K$  is the total number of rays, and  $\alpha_k$  and  $\tau_k$  are respectively the amplitude and the time shift (in discrete domain) of the  $k^{\text{th}}$  echo. To equalize the channel and so remove the multipath echoes, a discrete filter with an inverse transfer function of  $H(z)$  can be added to the system. Let define  $G(z)$  the discrete transfer function of the equalizer filter and imposing that the gain loop  $A_V$  of the system represented in

Figure 3.19 (b) is equal to the unity,  $G(z)$  can be obtained by:

$$A_V = \frac{G(z)}{1 - G(z)H(z)} = 1 \rightarrow G(z) = \frac{1}{1 - H(z)} = \frac{1}{1 + \sum_{k=1}^K \alpha_k z^{-\tau_k}} \quad (3.5)$$

Considering the case in the test-bench where is present the direct path (with  $\tau_k$  forced to zero), and, a single multipath echo (with  $\tau_k$  equal to  $k$ ), the transfer function  $H(z)$  can be written as:

$$H(z) = 1 + \alpha_1 z^{-k} \quad (3.6)$$

The above expression represents the typical transfer function of a Finite Impulse Response (FIR) filter. Hence, to equalizer the channel and so remove the multipath echoes,  $G(z)$  must be an Infinite Impulse Response (IIR) filter with a transfer function inverse than the expression in (3.6). Unfortunately, this type of filter becomes unstable if  $|\alpha_k| > 1$  and so the  $G(z)$  can be only approximate by a series expansion of finite length:

$$G(z) \approx \begin{cases} \sum_{v=0}^{K-1} (-\alpha_k)^v \cdot z^{-vk} & \text{for } |\alpha_k| < 1 \\ \frac{z^k}{\alpha_k} \sum_{v=0}^{K-1} \left(-\frac{1}{\alpha_k}\right)^v \cdot z^{vk} & \text{for } |\alpha_k| > 1 \end{cases} \quad (3.7)$$

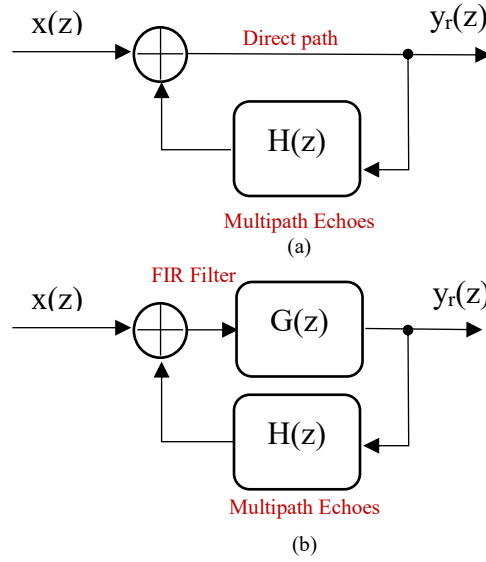


**Figure 3.19:** (a) Block diagram of the system in presence of multipath and with the FIR equalizer filter (b).

The expression above represents the transfer function of a non-recursive filter with complex coefficient if  $\alpha_k$  is a complex value. This formulation leads to a complex and expensive realization of the equalizer filter. However, to ensure causality for  $|\alpha_k| > 1$  the conditions reported below should be imposed:

$$\begin{cases} (-\alpha_k)^i & \text{for } |\alpha_k| < 1 \text{ and if } z = ik; 0 \leq i < K \\ -\left(-\frac{1}{\alpha_k}\right)^{K-1} & \text{for } |\alpha_k| > 1 \text{ and if } z = ik; 0 \leq i < K \\ 0 & \text{else} \end{cases} \quad (3.8)$$

this formulation shows that the  $G(z)$  values are non-zero for  $z=ik$  only, resulting in a large reduction of the realization cost compared to a general conventional transversal structure.

Moreover, the series given in (3.7) can be written in the special form:

$$\sum_{v=1}^{K-1} p^v, \text{ where } p = \begin{cases} -\alpha_k \cdot z^{-k} & \text{if } |\alpha_k| < 1 \\ \frac{z^k}{\alpha_k} & \text{if } |\alpha_k| > 1 \end{cases} \quad (3.9)$$

that can be factorized in the following way, if  $K = 2^N$ ,  $N \in \mathbb{N}$ :

$$\sum_{v=0}^{2^N-1} p^v = (1+p) \cdot (1+p^2) \cdot (1+p^4) \dots (1+p^{2^{N-1}}) \quad (3.10)$$

Applying the causality condition in case of  $|\alpha_k| > 1$  it is possible to derive a cascade structure of a digital FIR equalizer, equivalent to the transversal for discussed above.

$$G(z) = \begin{cases} \prod_{u=0}^{N-1} [1 + (-\alpha_k)^{2^u} \cdot z^{-2^u k}] & \text{if } |\alpha_k| < 1 \\ \prod_{u=0}^{N-1} [(-\alpha_k)^{-2^u} + z^{-2^u k}] & \text{if } |\alpha_k| > 1 \end{cases} \quad (3.11)$$

The application of this cascaded form permits a drastic reduction in hardware cost. In fact, it requires only  $n$  complex multiplications. The same system can be realized by a cascade of  $1D \times n$  blocks that include one coefficient, i.e., the total number of complex multiplications is reduced to  $1D \times n$ .

The variable coefficients of  $G(z)$  can be computed and adjusted by means of well-known gradient methods. The distance ranging algorithm described in the second chapter was slightly modified to include the estimation of the multipath echoes. Since the presence of multipath, in time domain, modifies the amplitude and the position of the main peak, it is considered, as quality criterion for the algorithm, the error in time-shift and amplitude estimation:

$$\begin{aligned} \mathbf{F}_1 &= \hat{\boldsymbol{\tau}}_i - \boldsymbol{\tau}_{i-1} \\ \mathbf{F}_2 &= \hat{\boldsymbol{\alpha}}_i - \boldsymbol{\alpha}_{i-1} \end{aligned} \quad (3.12)$$

where  $\hat{\boldsymbol{\tau}}_i$  and  $\hat{\boldsymbol{\alpha}}_i$  are the time-shift and the amplitude of the FIR coefficients estimated at  $i^{\text{th}}$  iteration cycle step. Often, in descendent gradient-based algorithms the standard deviation of the error is considered as quality criterion. Since the time-shifts or the difference in amplitudes can be positive or negative, it is considered directly the error of these quantities for including the sign within the iterative algorithm. Using the method of steepest descent to minimize the cost function (3.12) the coefficients are updated according to:

$$\begin{aligned} \boldsymbol{\tau}_i &= \hat{\boldsymbol{\tau}}_i - \gamma_1 \cdot \mathbf{F}_1 \\ \boldsymbol{\alpha}_i &= \hat{\boldsymbol{\alpha}}_i - \gamma_2 \cdot \mathbf{F}_2 \end{aligned} \quad (3.13)$$

The coefficients  $\gamma_1$  and  $\gamma_2$  determine the convergence speed of the algorithm and are dynamically adjusted in each iteration cycle. More in details the value of  $\gamma_1$  varies in range from 0.1 to 1.5 while  $\gamma_2$  is chosen in the range 0.1 to 1.1. The increment of these coefficients is inversely proportional

to the standard deviation of the functions  $\mathbf{F}_1$  and  $\mathbf{F}_2$  respectively that determine even the stop condition of the algorithm. Hence, after that the symbol offset is recovered and before to estimate the direct path, the cross-correlation is computed between the received signal, affected by multipath, and a clean copy of the transmitted signal. If the multipath echoes reach the receiver from a distance greater than the breakdown distance, the cross-correlation function exhibits a pulse of the direct path and a series of pulses for the echoes multipath. The peaks are estimated applying a threshold on the cross-correlation function and for each of these the time shift  $\hat{\tau}_i$  and the amplitude  $\hat{\alpha}_i$  are estimated. Then, the quality criterion in (3.12) are evaluated and the related standard deviations are computed:

$$\begin{aligned} \mathbf{e}_{1,i} &= E \left\{ \left| \mathbf{F}_{1,i} \right|^2 \right\} \\ \mathbf{e}_{2,i} &= E \left\{ \left| \mathbf{F}_{2,i} \right|^2 \right\} \end{aligned} \tag{3.14}$$

where  $E\{\cdot\}$  is the expectancy operator. The algorithm achieves the *lock condition* if  $\mathbf{e}_{1,i} = \mathbf{e}_{2,i} = 0$ , i.e., the algorithm has minimized the expression (3.12) and has estimated the multipath peaks if no-variations are observed in amplitude and in time-shift of the multipath peaks. Once achieved the lock condition the FIR filter in (3.11) is generated and the equalizer signal  $x_{eq}(z)$  is obtained computing the convolution of this filter and a clean copy of the transmitted signal. Finally, the received signal  $y_r(z)$  can be equalized summing the signal  $x_{eq}(z)$ , and so, the related distance can be computed applying the algorithm 2.3 and 2.4 described in chapter 2. The algorithm 3.1 summarizes the steps of the multipath cancellation algorithm.

---

**Algorithm 3.1** Echo Estimation

---

- 21: **procedure** ECHO\_ESTIMATION( $y_r, x, th, Ts, c, P$ )
  - 22: **►** Given N data points of the received sequence ( $y_r(z)$ ) with  $z=1, \dots, N$ ,
  - 23: **►**  $x(z)$  = clean copy of the transmitted signal with  $z=1, \dots, N$ ,
  - 24: **►**  $N$  = OFDM signal length,
  - 25: **►**  $th$  = peak threshold,
  - 26: **►**  $T_s$  = sampling time
  - 27: **►**  $c$  = propagation velocity
  - 28: **►**  $P$  = maximum number of iteration cycles
  - 29: **►** initialize the coefficients  $\gamma_{1,1}$  and  $\gamma_{2,1}$
-

---

```

30:    $\gamma_{1,1} = \gamma_{2,1} = 0.1$ 
31:   ► compute the cross-correlation function  $R_{xy}(z)$ 
32:    $R_{xy}(z) = \sum_{k=0}^{N-1} y(k)x^*(z+k)$ 
33:   ► extract the peaks from the cross-correlation function
34:   for  $i \leftarrow 1$  to  $N$  do
35:     if  $R_{xy}(i) \geq th$ 
36:        $\hat{\alpha}_1(i) \leftarrow R_{xy}(i)$ 
37:        $\hat{t}_1(i) \leftarrow i \cdot T_s$ 
38:     end if
39:   end for
40:   for  $p \leftarrow 2$  to  $P$  do
41:     ► initialize to zero the FIR filter vector  $g(z)$  with  $z=1, \dots, N$ 
42:      $g_{p-1}(z) = 0$ 
43:     ► generate the FIR filter vector  $g(z)$ 
44:      $g_{p-1}(\tau_{p-1}) = -\alpha_{p-1}$ 
45:     ► compute the equalizer sequence  $x_{eq,p}(z)$ 
46:      $x_{eq,p}(z) = x(z) * g_{p-1}(z)$ 
47:     ► equalize the received signal
48:      $y_{eq,p}(z) = \frac{(x_{eq,p}(z) + y_r(z))}{2}$ 
49:     ► compute the cross-correlation  $R_{xy_{eq,p}}(z)$ 
50:      $R_{xy_{eq,p}}(z) = \sum_{k=0}^{N-1} y_{eq,p}(k)x^*(z+k)$ 
51:     ► evaluate the new peaks from  $R_{xy_{eq,p}}(z)$ 
52:     for  $i \leftarrow 1$  to  $N$  do
53:       if  $R_{xy_{eq,p}}(i) \geq th$ 
54:          $\hat{\alpha}_p(i) \leftarrow R_{xy_{eq,p}}(i)$ 
55:          $\hat{t}_p(i) \leftarrow i \cdot T_s$ 
56:       end for
57:     ► compute the quality factor in (3.12) and the standard deviation in (3.14)

```

---

---

```

58:       $F_{1,p} = \hat{\tau}_p - \hat{\tau}_{p-1}$ 
59:       $F_{2,p} = \hat{\alpha}_p - \hat{\alpha}_{p-1}$ 
60:       $e_{1,p} = E\{F_{1,p}\}$ 
61:       $e_{2,p} = E\{F_{2,p}\}$ 
62:      ► check the variation of the standard deviation
63:      if ( $e_{1,p} == 0 \ \&\& \ e_{2,p} == 0$ )
64:          return  $y_{eq}$ 
65:      end procedure
66:      else
67:          ► update the row vectors  $\alpha$  and  $\tau$  according to (3.13)
68:           $\tau_p = \hat{\tau}_p - \gamma_{1,p-1} \cdot F_{1,p}$ 
69:           $\alpha_p = \hat{\alpha}_p - \gamma_{2,p-1} \cdot F_{2,p}$ 
70:          ► update the coefficients  $\gamma_{1,p}$  and  $\gamma_{2,p}$ 
71:           $\gamma_{1,p} = \gamma_{1,p-1} + (1/e_{1,p})$ 
72:           $\gamma_{2,p} = \gamma_{2,p-1} + (1/e_{2,p})$ 
73:      end if
74:  end for
75:  return  $y_{eq}$ 
76: end procedure

```

---

The critical aspect of this technique lays in the value of the threshold. In fact, if a high value of the threshold is considered, the algorithm is not able to estimate all peaks in the cross-correlation function and, thus, the distance would be affected by the error. On the contrary, low values for the threshold lead to false positive estimations in the peak extraction due to the presence, for example, of the sidelobes of the *sinc* function. The figures 3.12, 3.13 and 3.17 evidence that peaks with an amplitude greater than  $0.2 \cdot A$  ( $A$  is the amplitude of the direct echo) leads to an error greater than 10 cm. Hence, if the threshold value is set to 0.2, and the peaks lower than this value are not considered (in the hypothesis that are deleted) combining this technique with the use of a high directivity antenna the system precision and accuracy are strongly improved. Moreover, if the combination of the *sinc* function of the peaks generates sidelobes greater than the threshold, these

are filtered observing the model of the channel impulse response illustrated in Figure 2.5. The first echo of each single cluster contains the largest part of energy, thus, the vector of the amplitudes associated to the estimated multipath echoes is a strictly descendent function. Any peak that violates this behavior is discarded in the computation because is related to a false multipath echo. Another critical factor in the echo cancellation algorithm regards the updating of the terms  $\gamma_1$  and  $\gamma_2$ . As mentioned before, these terms determine the convergence speed of the method: big values call for less iteration cycles to achieve the lock condition. On the other hands, values too big can generate instability in the FIR filter coefficients calculation, bringing the algorithm to fail the lock condition. This problem is under investigation to find an optimal solution for the updating. However, a sub-optimal solution is found performing several simulations and observing the results. In fact, the best tradeoff between speed and convergence of the method is achieved varying the coefficients with a step equal to the inverse of the standard deviation evaluated in (3.14).

Figure 3.20 shows the *breakdown distance* as function of the signal bandwidth. It should be noted that its value exponentially decreases with a linear increment of the signal bandwidth, until to achieve to an asymptotic value of 1 meter about. From the measurements it is possible to find an interpolating function,  $y(x)$ , with the following expression:

$$y(x) = a \cdot x^b + c \quad (3.15)$$

The function  $y(x)$  is represented by the solid line in the graph and, from measurements it is possible to evaluate the values of the coefficients  $a$ ,  $b$  and  $c$ , equal to 485.3, -0.9863 and 2.309 respectively. This function can be used to predict the value of breakdown distance and choosing the signal bandwidth according to the environment where the system must operate.

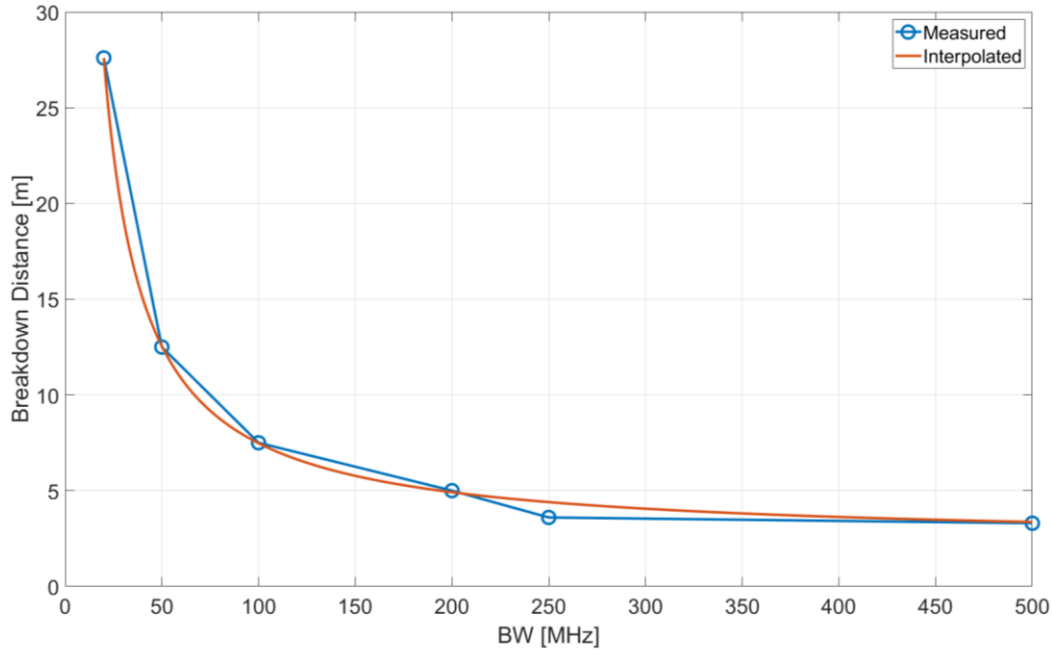


**Figure 3.20:** Breakdown distance as function of the signal bandwidth.

Starting by the computed breakdown distance, several simulations have been performed to evaluate the performance of the system with and without the echo cancellation algorithm previously described. Again, we simulated the case where the receivers are placed with 1.5 meters offset and, for sake of simplicity, are present the direct path and a single multipath echo with a variable distance. Fig. 3.21 reports the absolute error considering a 64-length OFDM symbol with 100 MHz of bandwidth. The error is computed introducing an echo multipath with  $0.9 \cdot A$  of amplitude and a SNR of 30 dB. Note that for multipath echo distance lower than the breakdown distance, there is no difference in terms of system performance with or without the echo cancellation algorithm. For echo distances greater than the breakdown distance, the presence of the echo cancellation algorithm strongly improves the distance estimation in time domain. In fact, the absolute value of the error in time-domain is improved by a 10 factor. Observing the fig. 3.22 is should possible to note that the echo cancellation algorithm leads to a strong improvement even in the frequency domain. However, due to high sensibility in frequency domain (the distance resolution is constrained by the subcarriers phase shift), the absolute value of the error is worse than the error in time domain. In fact, if the multipath echo is not completely removed, the spectrum of the equalized signal still presents a phase distortion that affects the distance estimates.

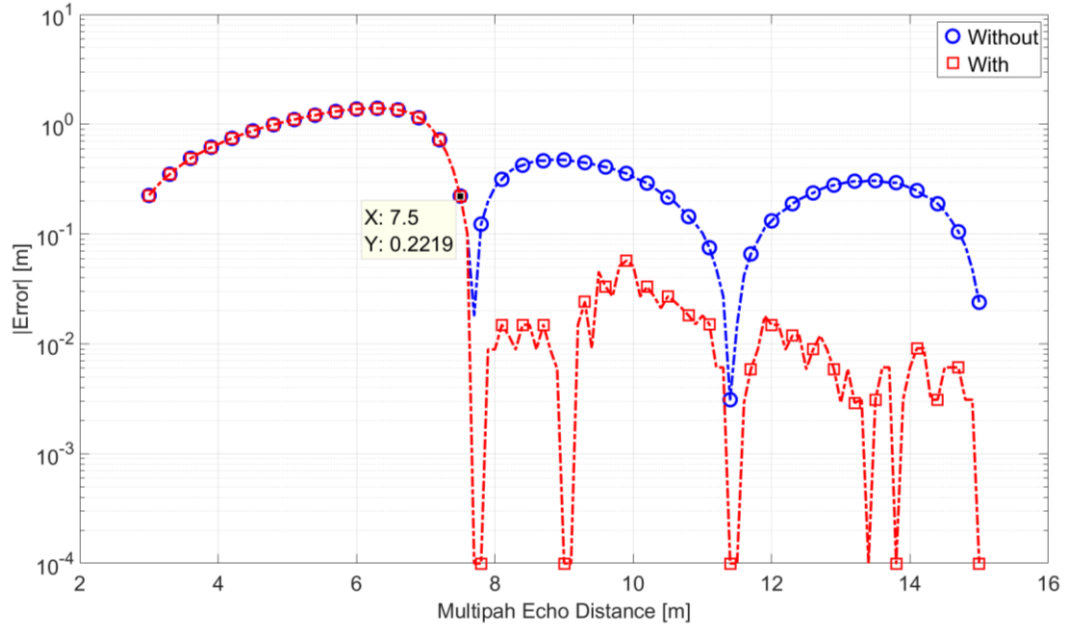


**Figure 3.21:** Absolute value of the error in time-domain as function of the multipath echo distance, using a 64-length OFDM symbol with 100 MHz of bandwidth and 20 dB of SNR.

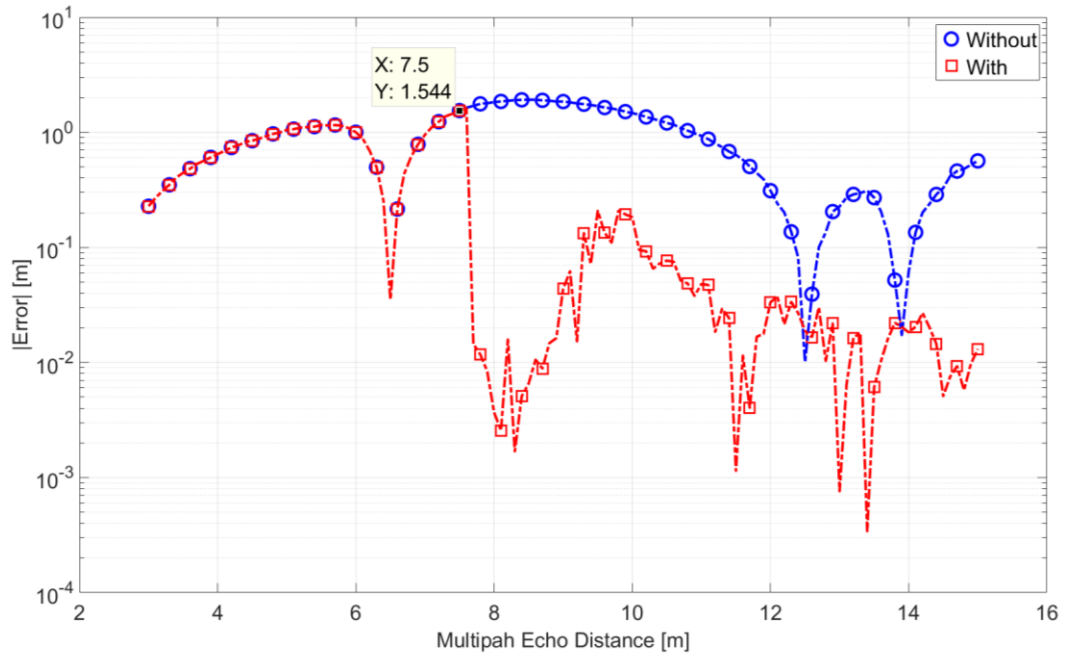


**Figure 3.22:** Absolute value of the error in frequency-domain as function of the multipath echo distance, using a 64-length OFDM symbol with 100 MHz of bandwidth and 20 dB of SNR.

From this first analysis, we conclude that the echo cancellation algorithm can improve the system precision and accuracy in presence of multipath. Moreover, when the *sinc* of the multipath echo is

placed in a position where its zeros coincide with the maximum of the *sinc* of the direct echo, the echo cancellation algorithm is able to estimate exactly the position of the undirect path, that will be completely removed.

In the next test-bench, we evaluated the system precision and accuracy for both time and frequency-domain and as function of the SNR to compare the system performance with or without the echo cancellation algorithm. The performance are evaluated considering again a 64-length OFDM symbol with 100 MHz of bandwidth. Moreover, it is considered multipath echo distances greater than the *breakdown distance* to evaluate only the improvement in the distance estimation. Figure 3.23 (a) sketches a comparison of the system precision, in time-domain, as function of the SNR and of the multipath echo amplitude in presence and in absence of the echo cancellation algorithm.

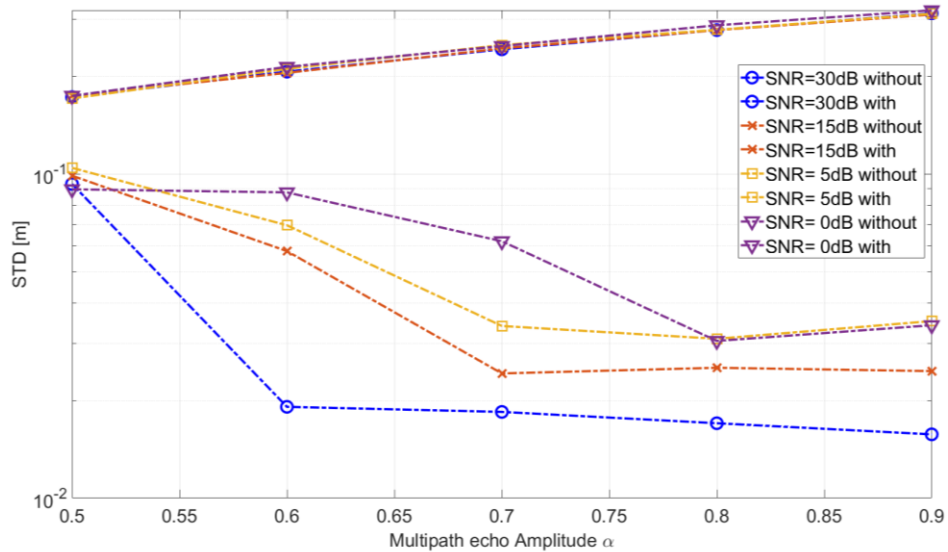


**Figure 3.23:** TO system precision as function of the SNR and the echo amplitude. The precision is evaluated considering a 64-length OFDM symbol with 100 MHz of bandwidth and 20 dB of SNR.

Note that the use of the echo cancellation algorithm improves the system precision even for low SNRs. In fact, its value is lower than 10 cm even for 0 dB of SNR and strong multipath echo amplitudes. In Figure 3.24 it is compared the accuracy achieved by the proposed system, in time-domain, again as function of the SNR and of the multipath echo amplitudes. The use of the echo cancellation algorithm strongly improves the overall performance. In fact, even for a SNR equal to 0 dB the system accuracy is better than 4 cm.

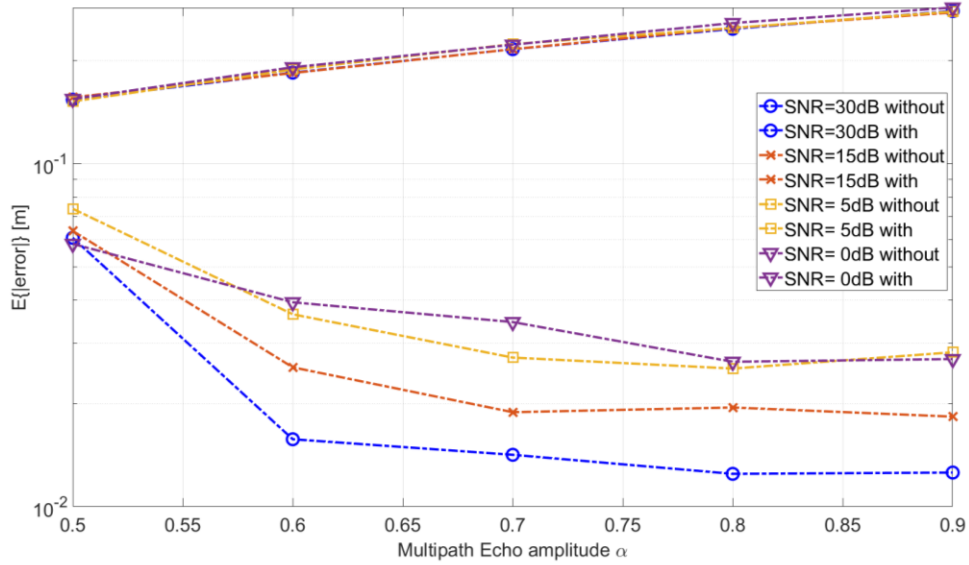
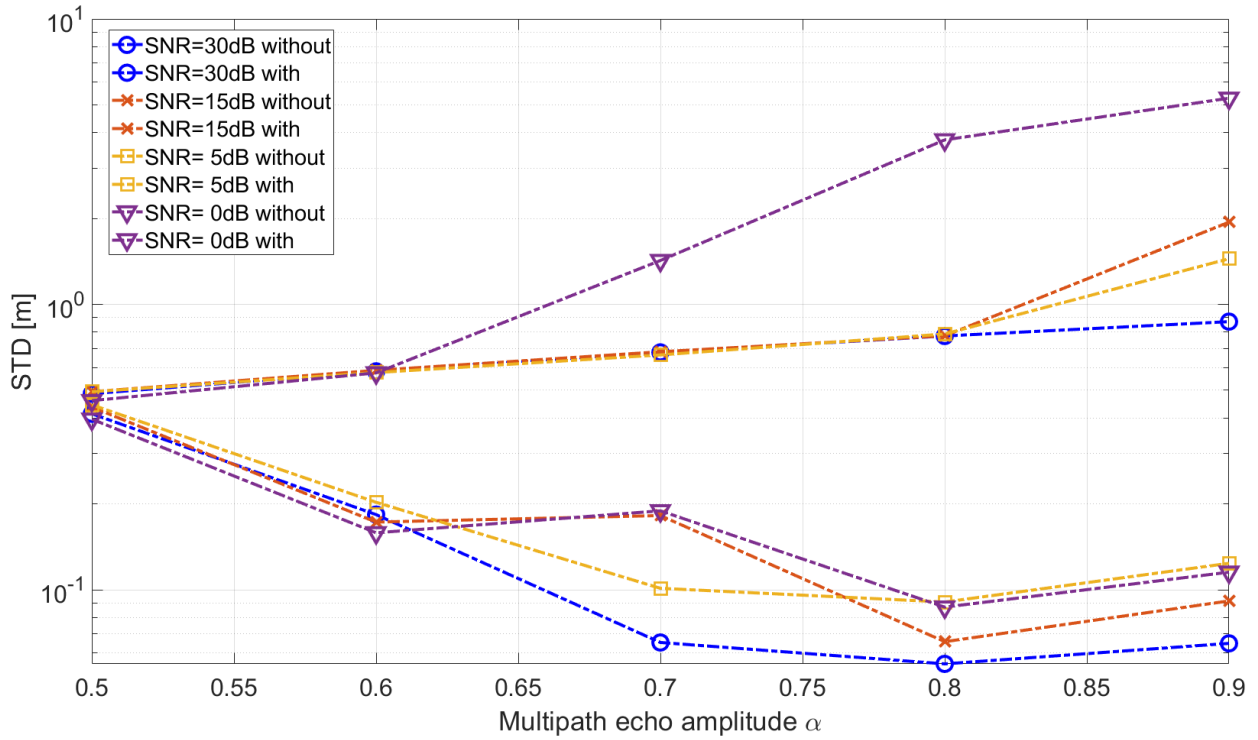


**Figure 3.24:** TO system accuracy as function of the SNR and the echo amplitude. The precision is evaluated considering a 64-length OFDM symbol with 100 MHz of bandwidth and 20 dB of SNR.

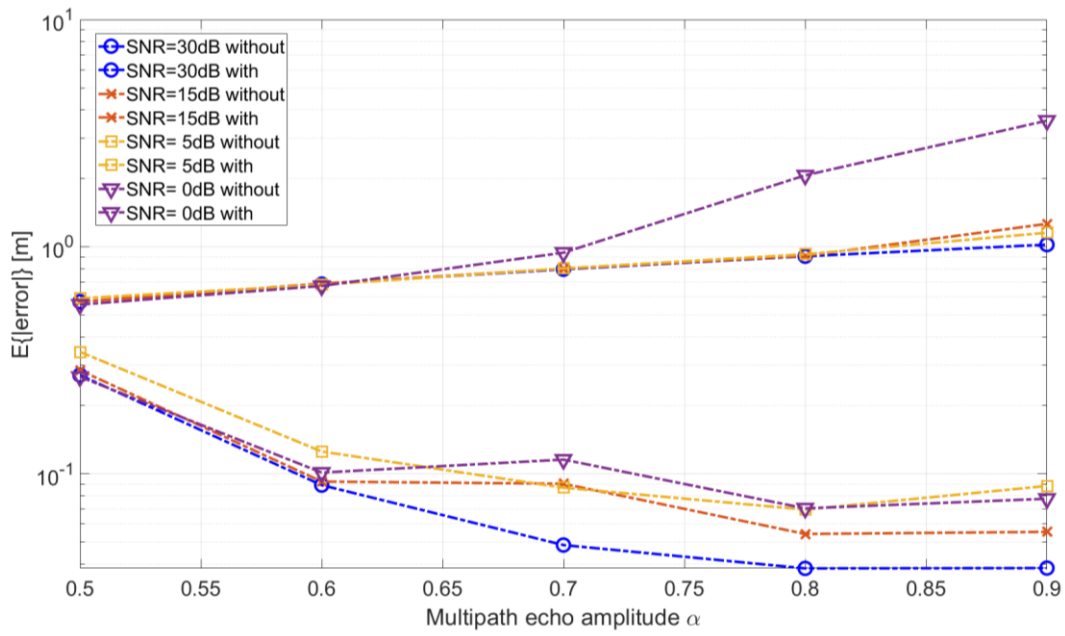
However, it should be noted for both accuracy and precision that for an amplitude of 0.5 there is not a strong improvement compared to others  $\alpha$  values. Although the algorithm is able to estimate the amplitude of the multipath echo with a good precision, the combination of the sinc functions in time domain is too severe when the echo multipath is low, and so the amplitude measurements are not sufficient to remove completely the indirect path.

Figure 3.25 and Figure 3.26 respectively report the comparison of the system precision and accuracy in frequency-domain, in presence and in absence of the echo cancellation algorithm. Again, the use of the proposed algorithm strongly improves the overall performance. However, as previously cited, if the multipath echo is not completely removed by the FIR filter, the spectrum of the signal is still distorted and so the subcarriers phase-shift is not estimated correctly by the equation (2.29).

In conclusion, due to the properties of the ZC sequences, the cross-correlation function of the received signal with a clean copy of the transmitted signal represents the channel impulse response of the system. If the multipath echoes are placed at distances greater than the breakdown distance, they can be estimated and removed with a steepest descent algorithm.



**Figure 3.25:** CFO system precision as function of the SNR and the echo amplitude. The precision is evaluated considering a 64-length OFDM symbol with 100 MHz of bandwidth and 20 dB of SNR.



**Figure 3.26:** CFO system accuracy as function of the SNR and the echo amplitude. The precision is evaluated considering a 64-length OFDM symbol with 100 MHz of bandwidth and 20 dB of SNR.

The use of the echo cancellation algorithm improves the overall performance of the system for both time and frequency-domain. The advantage of the use of this algorithm are more evident for low SNR, where the system can achieve a precision and accuracy of few cm even for a SNR equal to 0 dB. Moreover, the considerations of the previous paragraph are still valid and so for further increasing the overall performance, it is possible to raise the signal bandwidth or the number of subcarriers.

### 3.3 Kalman Filtering

Further improvements are possible considering the output of the distance ranging algorithm as the sum of the real distance value and the noise with a Gaussian probability distribution. Moreover, let consider the case of a single transmitter moved in the space region delimited by two receivers. The TDOA and so the difference distance computed by the two receivers is a straight-line function described by the equation:

$$f(t) = at + b \quad (3.16)$$

The knowledge of the model and the presence of noisy measurements allows to introduce the Kalman filter-based algorithm [52] to reduce the uncertainty in the distance estimation and improve the final accuracy and system precision. This filter uses a prediction followed by a correction to determine its state. The basic idea is that using information about the dynamics of the state, the filter will project forward and predict what the next state will be. Starting from some initial state estimate,  $\hat{\mathbf{x}}_0$ , and initial state error covariance matrix,  $\mathbf{P}_0$ , the predictor-corrector format is applied recursively at each time step, e.g. using a loop. First, the state vector is predicted from the state dynamic equation using the expression below:

$$\hat{\mathbf{x}}_{k|k-1} = \mathbf{F}_{k-1}\hat{\mathbf{x}}_{k-1} + \mathbf{G}_{k-1}\mathbf{u}_{k-1} \quad (3.17)$$

where  $\hat{\mathbf{x}}_{k|k-1}$  is the predicted state vector at the discrete time  $k$  given its previous state at discrete time  $k-1$ ,  $\hat{\mathbf{x}}_{k-1}$  is the previous estimated state vector,  $\mathbf{u}$  is the input vector, and  $\mathbf{F}$  and  $\mathbf{G}$  are matrices defining the system dynamics. Next, the state error covariance matrix must also be predicted using:

$$\mathbf{P}_{k|k-1} = \mathbf{F}_{k-1}\mathbf{P}_{k-1}\mathbf{F}_{k-1}^T + \mathbf{Q}_{k-1} \quad (3.18)$$

where  $\mathbf{P}_{k|k-1}$  represents the predicted state error covariance matrix at the discrete time  $k$  given its previous state at discrete time  $k-1$ ,  $\mathbf{P}_{k-1}$  is the previous state error covariance matrix, and  $\mathbf{Q}$  is the process noise covariance matrix. Once the predicted values are computed, the Kalman gain matrix,  $\mathbf{K}_k$ , is calculated by:

$$\mathbf{K}_k = \mathbf{P}_{k|k-1} \mathbf{H}_k^T (\mathbf{H}_k \mathbf{P}_{k|k-1} \mathbf{H}_k^T + \mathbf{R}_k)^{-1} \quad (3.19)$$

where  $\mathbf{H}$  is a matrix necessary to define the output equation and  $\mathbf{R}$  is the measurement noise covariance. The state vector is then update by scaling the difference between the measurement of the output,  $\mathbf{z}_k$ , and the predicted output,  $\mathbf{H}_k \hat{\mathbf{x}}_{k|k-1}$  by the calculated Kalman gain matrix to correct the prediction by the appropriate amount, as in:

$$\mathbf{x}_k = \hat{\mathbf{x}}_{k|k-1} + \mathbf{K}_k (\mathbf{z}_k - \mathbf{H}_k \hat{\mathbf{x}}_{k|k-1}) \quad (3.20)$$

Similarly, the state error covariance is updated by:

$$\mathbf{P}_k = (\mathbf{I} - \mathbf{K}_k \mathbf{H}_k) \mathbf{P}_{k|k-1} \quad (3.21)$$

where  $\mathbf{I}$  is an identity matrix.

For sake of simplicity, it is considered a testbench where the target is moved with a constant velocity, thus, the input control  $\mathbf{u}$  is zero. In this case the model is expressed by the equation below:

$$\begin{aligned} \hat{\mathbf{x}}_k &= \hat{\mathbf{x}}_{k-1} + \Delta t \cdot \dot{\mathbf{x}}_{k-1} \\ \dot{\mathbf{x}}_k &= \dot{\mathbf{x}}_{k-1} \end{aligned} \quad (3.22)$$

where  $\hat{\mathbf{x}}_k$  is the target position at the discrete time  $k$  (or the difference distance if is applied to a single couple of receivers),  $\Delta t$  is the time unity, and,  $\dot{\mathbf{x}}_k$  is the velocity of the target even at the discrete time  $k$ . Let define:

$$\mathbf{x}_k = (\mathbf{x}_k, \dot{\mathbf{x}}_k)^T \quad (3.23)$$

Comparing (3.23) with (3.17) it is possible to compute the transition matrix  $\mathbf{F}_k$ :

$$\mathbf{F}_k = \begin{pmatrix} 1 & \Delta t \\ 0 & 1 \end{pmatrix} \quad (3.24)$$

The proposed indoor positioning system is able to measure only the target position or the difference distance between the receivers. Any information about the velocity is extracted and can be still assumed as a noisy value. Hence, the system measurements can be arranged in a matrix:

$$\mathbf{z} = (z, 0)^T \quad (3.25)$$

and the measurement matrix is equal to:

$$\mathbf{H} = (1, 0) \quad (3.26)$$

The purpose of the  $\mathbf{H}$  matrix is to essentially convert the states into outputs. In this case  $\mathbf{H}$  is used to select only the distance measures, neglecting the velocity estimates.

The process variance matrix  $\mathbf{Q}$  and the state variance matrix  $\mathbf{P}$  can be obtained from the initial value  $\mathbf{Q}_0$  and  $\mathbf{P}_0$  that represent the noise associated to the model. In this case the effect  $\mathbf{P}_0$  is not significant and can be arbitrarily initialized to an identity matrix for simplicity. Instead, a larger

$\mathbf{Q}$  is equivalent to considering larger uncertainty in the state equations, which is equivalent to trusting the result of these equations less, which effectively means that the filter should correct more with the measurement update. Similarly, considering a larger  $\mathbf{R}$  is equivalent to considering larger uncertainty in the measurement, which is equivalent to trusting the measurement less, which effectively means that the filter should correct less with the measurement update.

Once defined all parameters of the Kalman Filter, it is applied to the proposed system to improve its accuracy and precision. In the first testbench the filter is applied to the case of additive white noise Gaussian channel. After, we take into account for all the conditions and the signal parameters mentioned in paragraph 3.1.1.

Figure 3.27 shows an example of the distance estimates using the Kalman filter. The distance are extracted using a 64-length OFDM symbol with 100 MHz of signal bandwidth and a SNR of 0 dB. The presence of the Kalman filter considerably refines the distance estimates. however, for low distances the error generated by the filter is greater than high distance. This result is due to the transition time needed by the algorithm to achieve the lock condition. Once reached this condition, the algorithm is able to track the distance values even in presence of higher errors. This problem can be overcome applying in different way the algorithm. For example more signal periods related to a fixed distance can be acquired and the resulting distance can be computed applying the Kalman filter. However, this strategy as well other approaches are under investigation.

In Figure 3.28 a comparison of the system precision in time domain is reported. The precision is evaluated as function of the SNR and using a 64-length OFDM signal with 100 MHz of signal bandwidth. Note that with the use of the filter the system is able to extract the distance with a precision lower 1 cm even for a SNR of only 5 dB. Same considerations are valid for the system accuracy in time-domain. Figure 3.29 illustrates the system accuracy as function of the SNR. Even for low SNR the accuracy is less than 1 cm achieving a sub-mm precision for SNR greater than 20 dB.

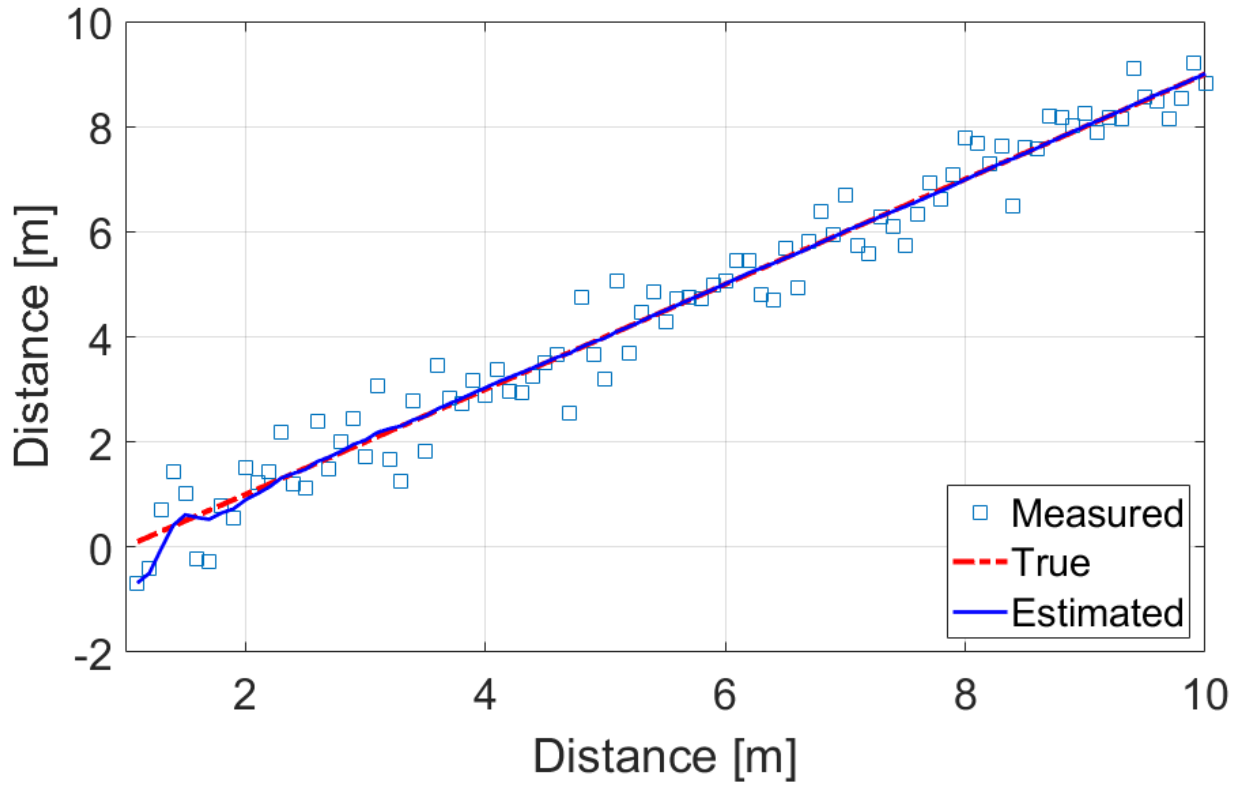


**Figure 3.27:** Difference distance estimation with the presence of the Kalman Filter

Figure 3.30 and Figure 3.31 illustrate the system precision and the system accuracy respectively evaluated in frequency domain. With only 100 MHz of signal bandwidth and 64 subcarriers the system achieves a mm precision with the use of the Kalman filter even for a SNR of 0 dB. If a cm precision and accuracy is required by the specific application, even negative SNR can be used.

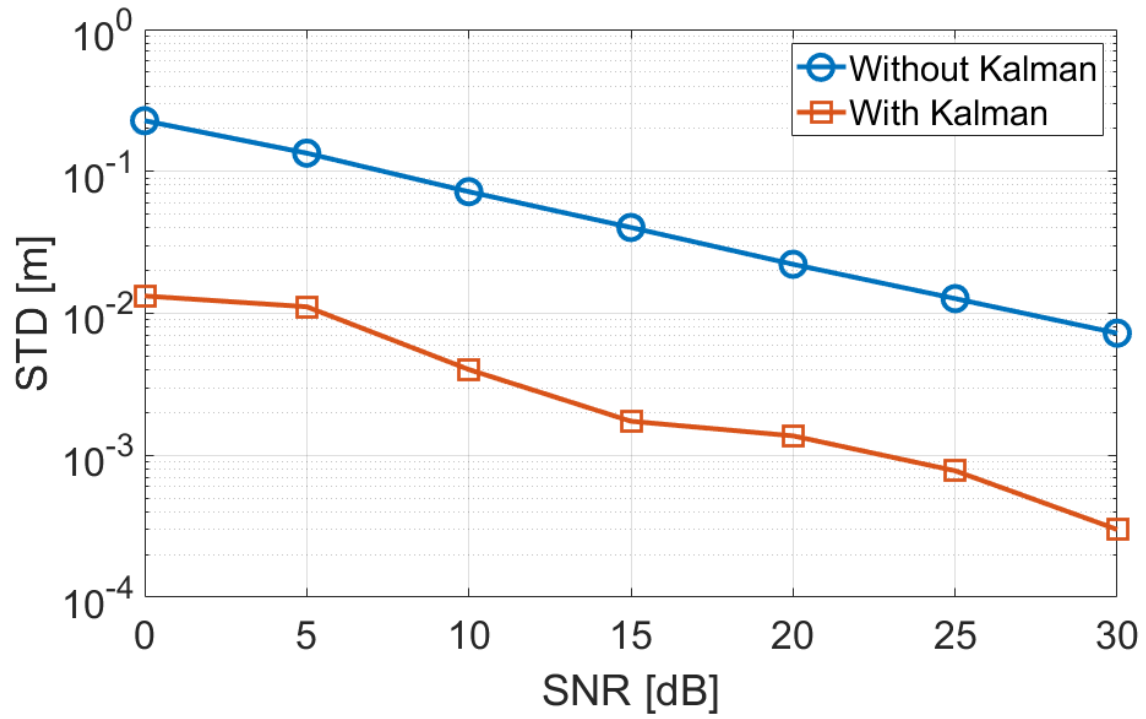


Figure 3.28: TO System precision without and with the Kalman filter.

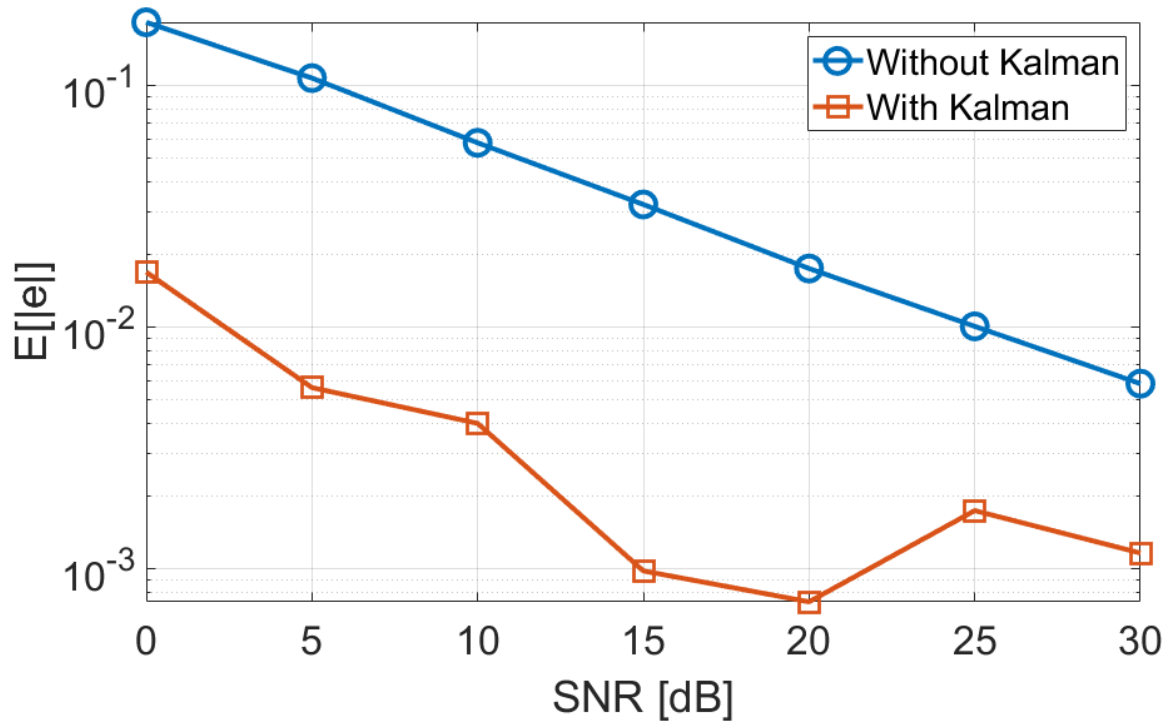


Figure 3.29: TO System accuracy without and with the Kalman filter.

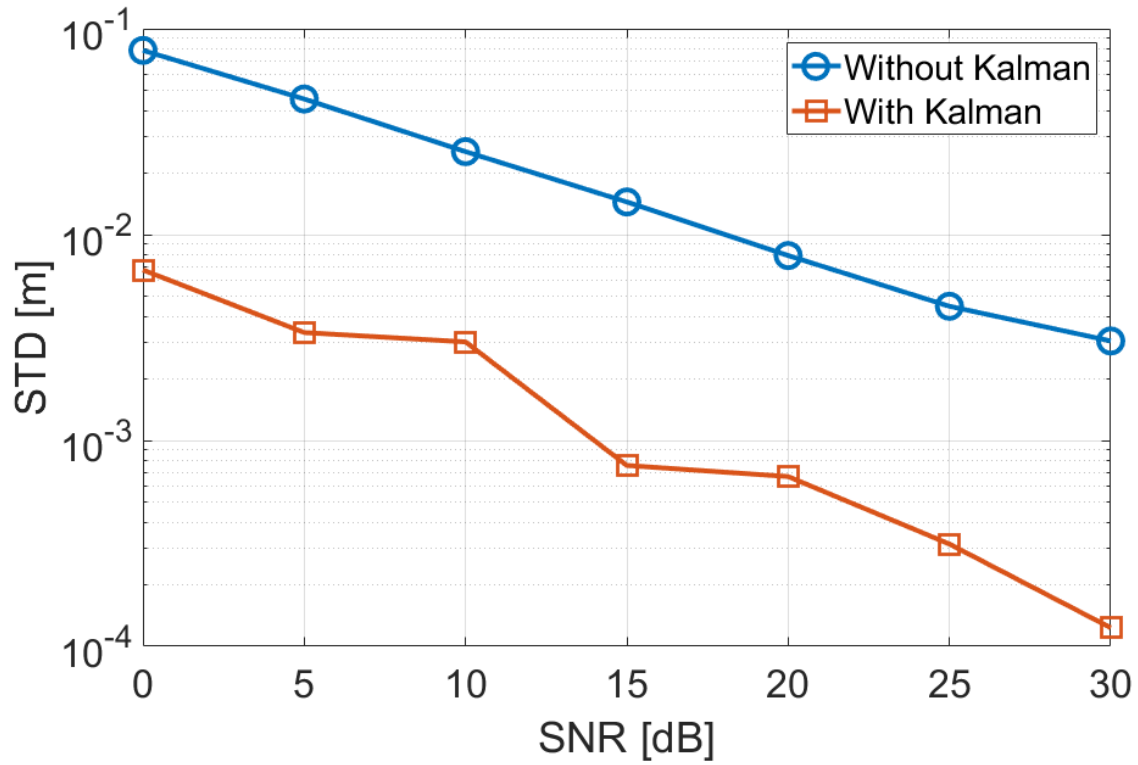


Figure 3.30: CFO System precision without and with the Kalman Filter

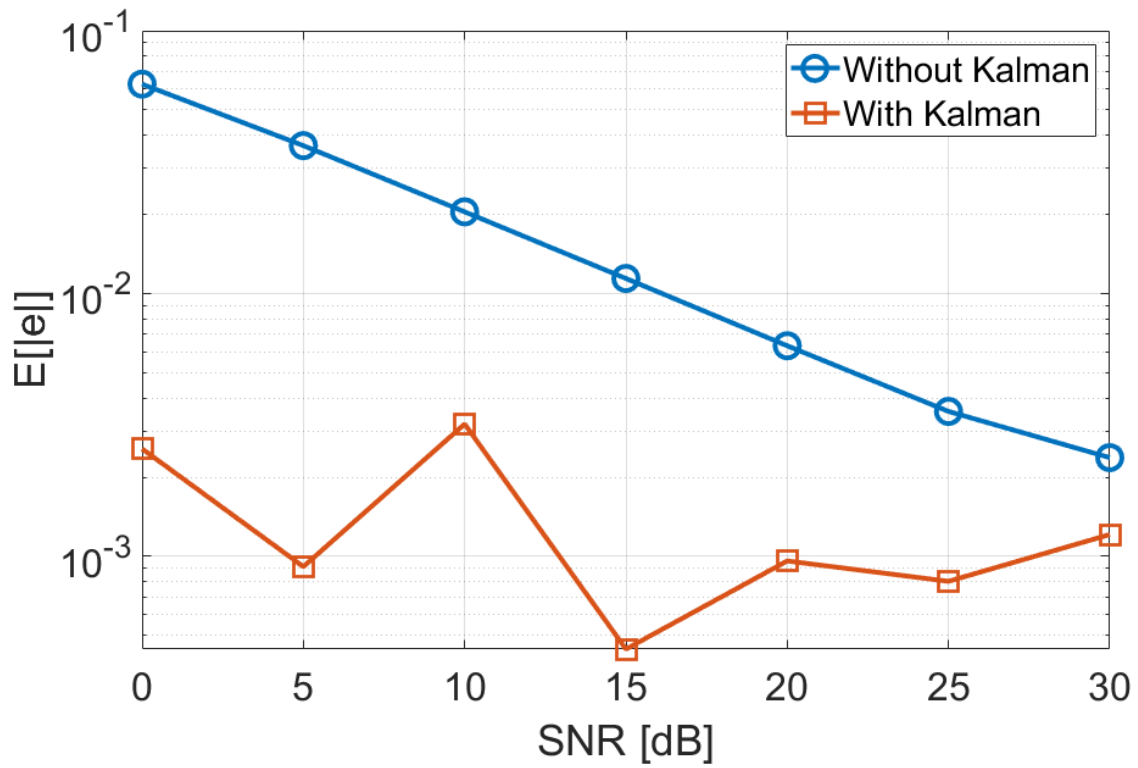


Figure 3.31: CFO System precision without and with the Kalman filter

Observing the performance of the system illustrated in the graphs, it is possible to conclude that the use of the Kalman filter, in presence of AWGN channel, improves the overall performance of the system. In others words, the Kalman filter allows to approach the limits defined by the Cramer-Rao Lower Band defined in (3.2).

The Kalman filter can be applied even in presence of multipath to improve the distance ranging accuracy and precision. In this case the measures in input to the Kalman filter are the output values of the algorithm 3.1. In other words, in presence of multipath, the system applies the echo cancelation algorithm to remove the undesired echoes and then the results go in input to the Kalman filter to track the target movement and improve the distance accuracy and precision.

To validate the system, it is considered a test-bench where a single multipath echo is present within the channel impulse response. This echo is placed beyond the breakdown distance to apply the cancellation algorithm and its amplitude is set to  $0.8 \cdot A$ , with  $A$  the amplitude of the direct echo. For sake of simplicity the system comprises two receivers and a single transmitter that is moved along the x-axis from 1.1 to 10.1 meters. The performance are evaluated considering a 64-length OFDM symbol with 100 MHz of signal bandwidth.

Figure 3.32 is reported a comparison of the system precision, evaluated in time domain, with only the echo cancellation algorithm and with the combination of the algorithm and the Kalman Filter.

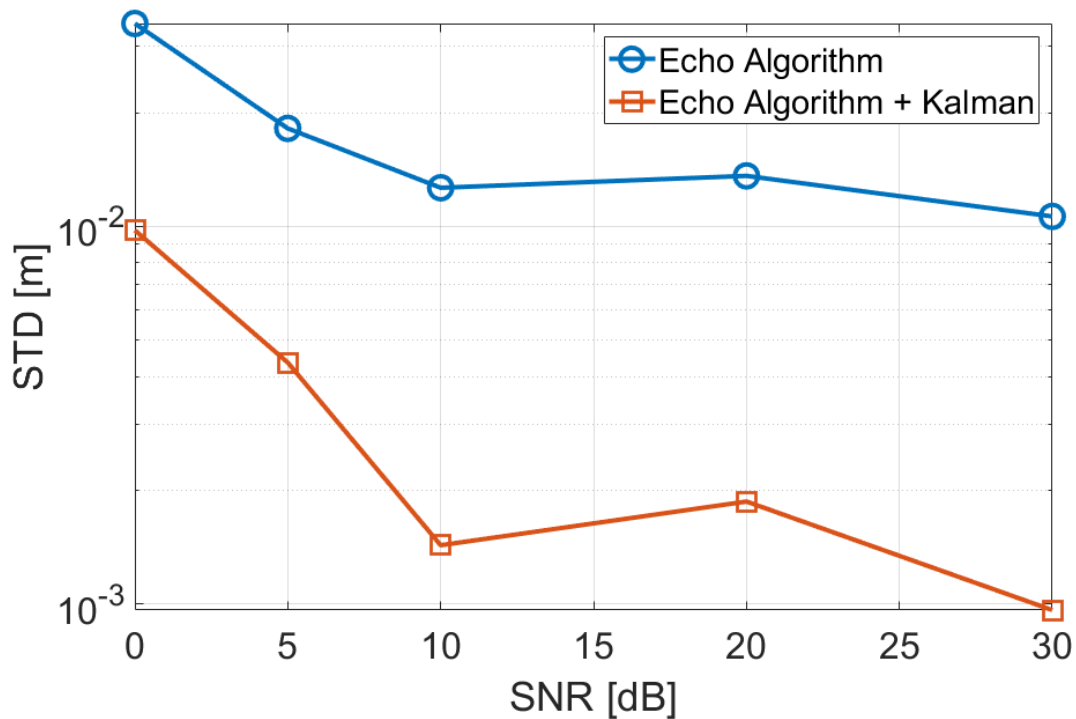


Figure 3.32: TD System precision in presence of multipath and Kalman Filter

Note that the Kalman filter allows to achieve a precision in mm range, further improving the precision achieved by the echo cancellation algorithm.

Figure 3.33 shows the accuracy of the final system. Again the Kalman filter improves the overall performance of the system. However the improvement in terms of accuracy is less evident than the precision. In fact the aim of the Kalman filter is to reduce the uncertainties of the measures that determine the lock condition together with the state predicted by the model.

The same considerations are valid in frequency domain where the system is able to achieve a mm precision with the application of the Kalman filter (Figure 3.34). In Figure 3.35, the accuracy evaluated in frequency domain is represented. The Kalman filter is able to improve the final accuracy only for low SNR. As mentioned, the output of the Kalman filter depends on the measures produced by the system. Hence, in absence of noise or for high SNRs, the measurements are affected only by the residual error of a non-perfect echo cancellation.

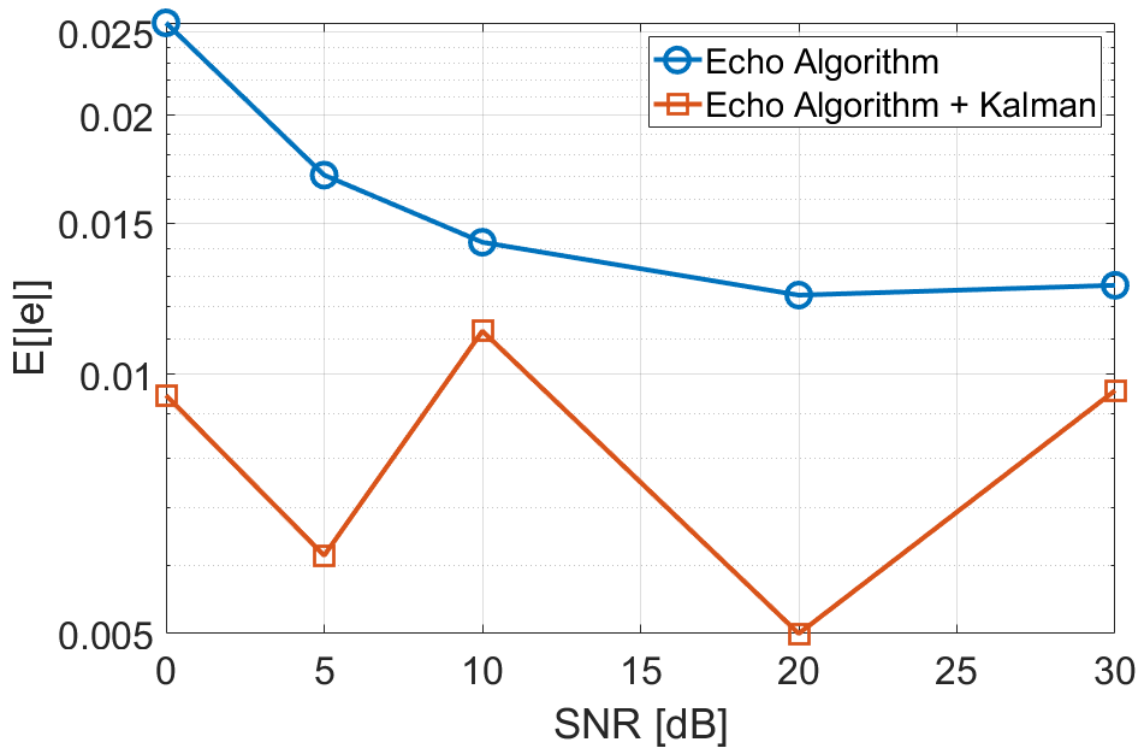


Figure 3.33: TD System accuracy in presence of multipath and Kalman Filter

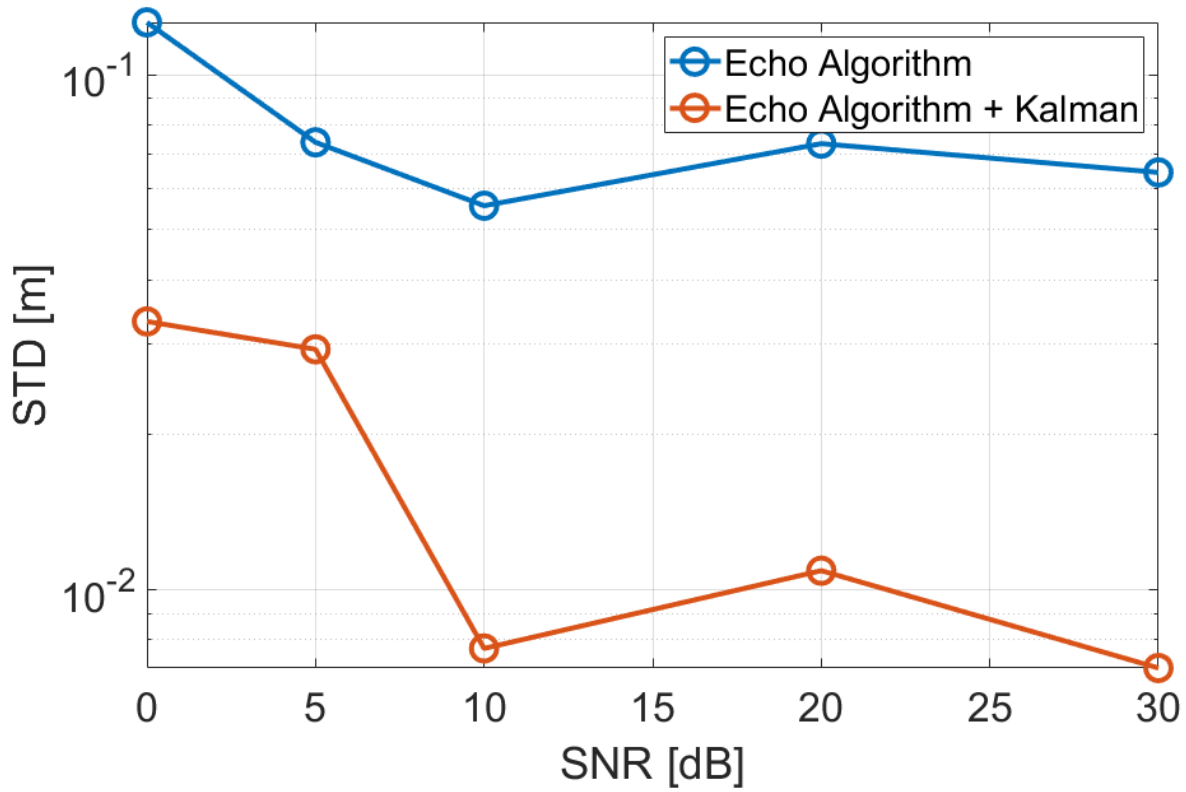


Figure 3.34: CFO System precision in presence of multipath and Kalman Filter

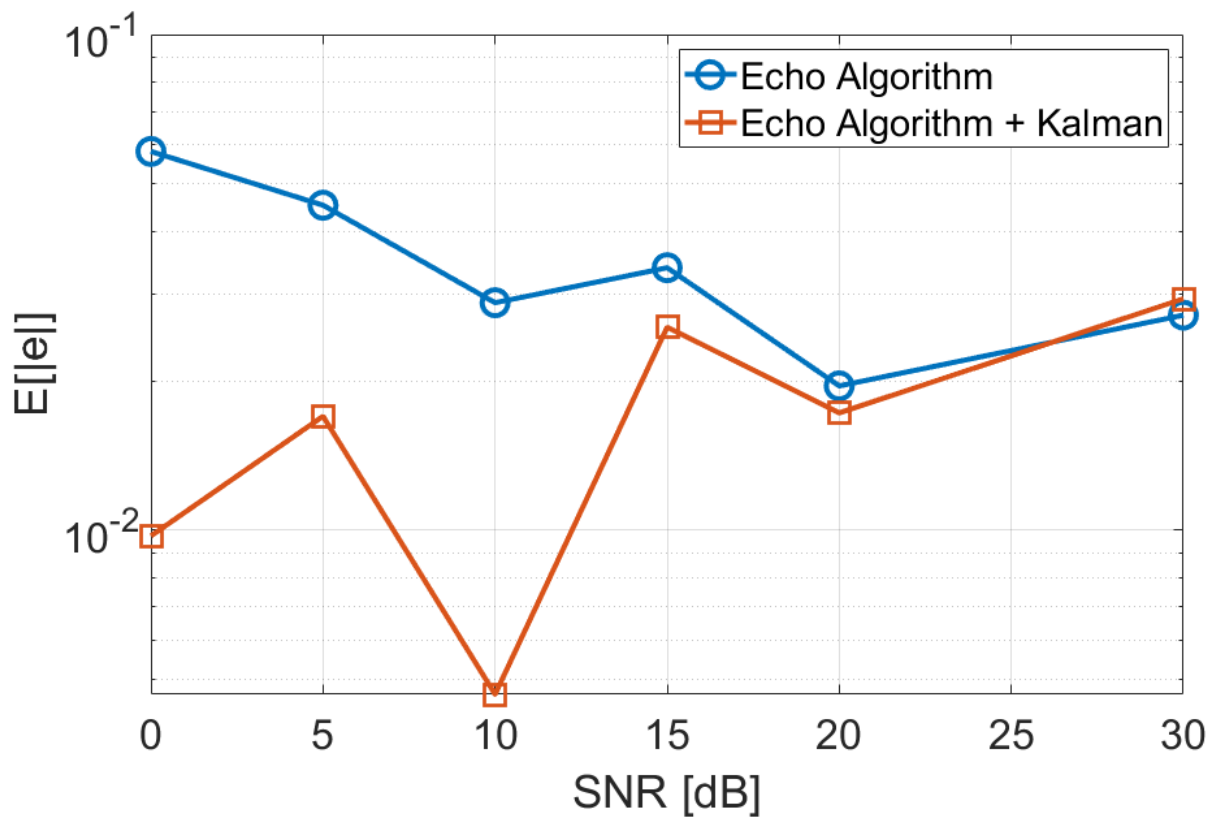


Figure 3.35: CFO System accuracy in presence of multipath and Kalman Filter

On the contrary, for low SNRs the Kalman filter removes the errors due to the noise introduced by the channel and improves the overall performance of the system. Moreover, as cited in paragraph 3.2.1, the frequency domain is more sensitive to the residual errors generated by a non-perfect echo estimation and cancellation.

### 3.4 Analog to Digital Converter: Sub-Nyquist receiver

The previous results are extracted considering models with a sampling frequency of 1 GHz and a maximum signal bandwidth of 500 MHz in order to respect the Nyquist criterion. As defined by the expression (3.2) an increase of the signal bandwidth improves the system accuracy. However, the Nyquist criterion establishes that if the signal has a bandwidth of  $Bw$ , the sampling frequency necessary to recover the information after the digital conversion must be equal to the double of  $Bw$  ( $f_N = 2 \times Bw$ ). Analog to Digital converters with sampling frequency greater or equal to 1 GHz are available on the market but they are very expensive and exhibit high power consumption. Moreover, the use of these type of ADCs requires an unaffordable hardware complexity to process the data in real-time especially in mobile applications.

To overcome these problems, it is possible to generate the signal respecting specific conditions that depend on its parameters as bandwidth, number of subcarriers, and, sampling time, in way that is possible to sub-sampled without loss information. In other words, under specific conditions that depends on the system parameters is possible to reduce the rate of the ADC, even below the Nyquist criterion, maintaining a high precision and accuracy in the distance and so in the position estimation.

In a multi-carrier signal, the available bandwidth is divided into  $N$  sub-bands partially overlapped without generating inter-channel interference. To use a de-rated ADC its sampling frequency as well as the signal parameters must be chosen in a way that, the positioning information spread over the wide bandwidth, falls into a narrower band, without destructive overlaps. Tuning the A/D rate based on the targeted estimation precision and environmental conditions further reduces the power consumption at the run time.

Let define the subsampling factor,  $k_{ss}$ , as:

$$k_{ss} = \frac{f_N}{f_s} \quad (3.27)$$

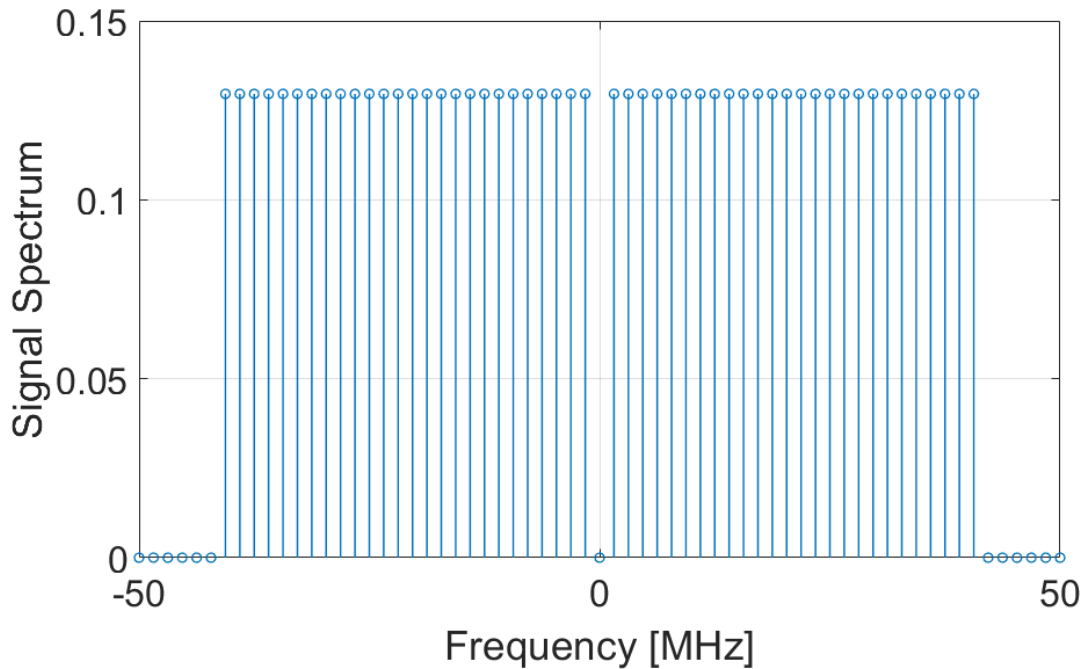
where  $f_s$  is the sampling frequency of the system that can be lower than the Nyquist sampling frequency  $f_N$ . For ease of implementation the value of  $k_{ss}$  should be positive, and, to reconstruct

the original signal, the system parameters must be chosen according to this factor. This factor plays an important role in selecting the parameters like the subcarrier frequencies and signal duration. In facts, the subcarrier frequencies are determined such they do not alias with each other after sampling. Moreover, after subsampling, the subcarriers are aliased to a narrower band. Given the frequencies of the tones and the ADC sampling rate  $f_s$ , the locations of the subcarriers, after sampling, can be found. The tones with a frequency lower than  $f_s / 2$  keep their location in the spectrum of the sampled signal. For other tones, new frequency component,  $f_i^n$  in the spectrum is calculated by:

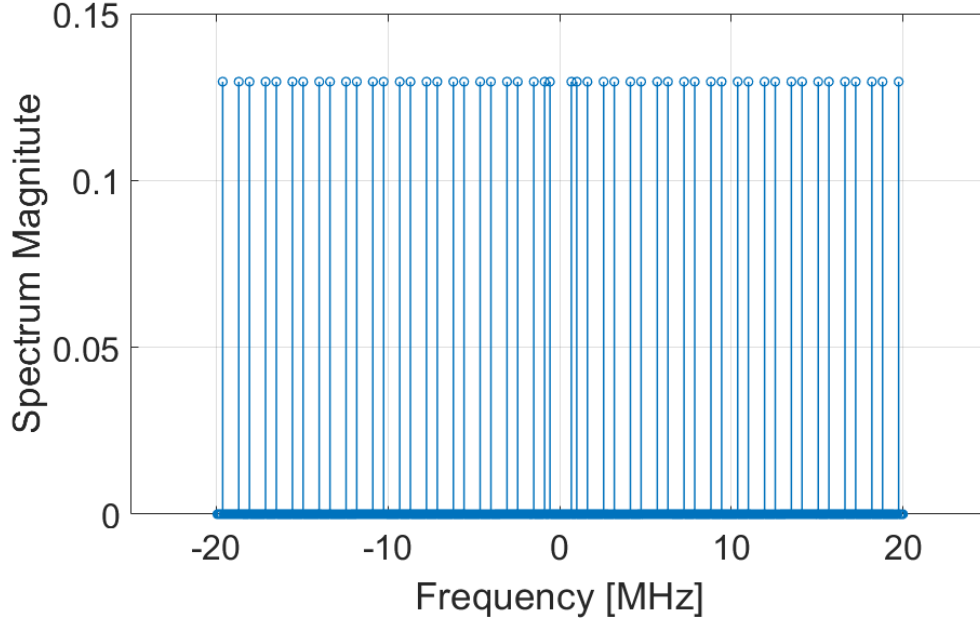
$$f_i^n = \text{mod}\left(f_i^o, \frac{f_s}{2}\right) \quad (3.28)$$

where  $f_i^o$  is the original frequency of the tone  $i$ . This expression can be used to prevent the alias between the subcarriers. Alternatively, when the subcarriers are fixed, the  $k_{ss}$  factor can be chosen, verifying the new locations of all the subcarriers. More than one possible  $k_{ss}$  can be found for a given signal construction.

Figure 3.36 illustrates an example of the spectrum of a 64-length OFDM signal of 100 MHz of bandwidth after the process of sub-sampling. It should be noted that the subsampling reduces the signal bandwidth and the subcarriers are arranged in the spectrum according to (3.27).



(a)



(b)

**Figure 3.36:** (a) Signal Spectrum before the subsampling (b) Signal spectrum after subsampling.

To ensure a perfect signal reconstruction, the signal duration must be properly organized. If  $P$  is the period of the subsampled signal, the received signal must contain  $k_{ss} \times P$  periods to ensure that the sufficient number of samples is used for Fourier transform.

Hence after the subsampling process, the subcarrier locations are shuffled and to evaluate the distance, the frequency components must be recovered in a transposed order:

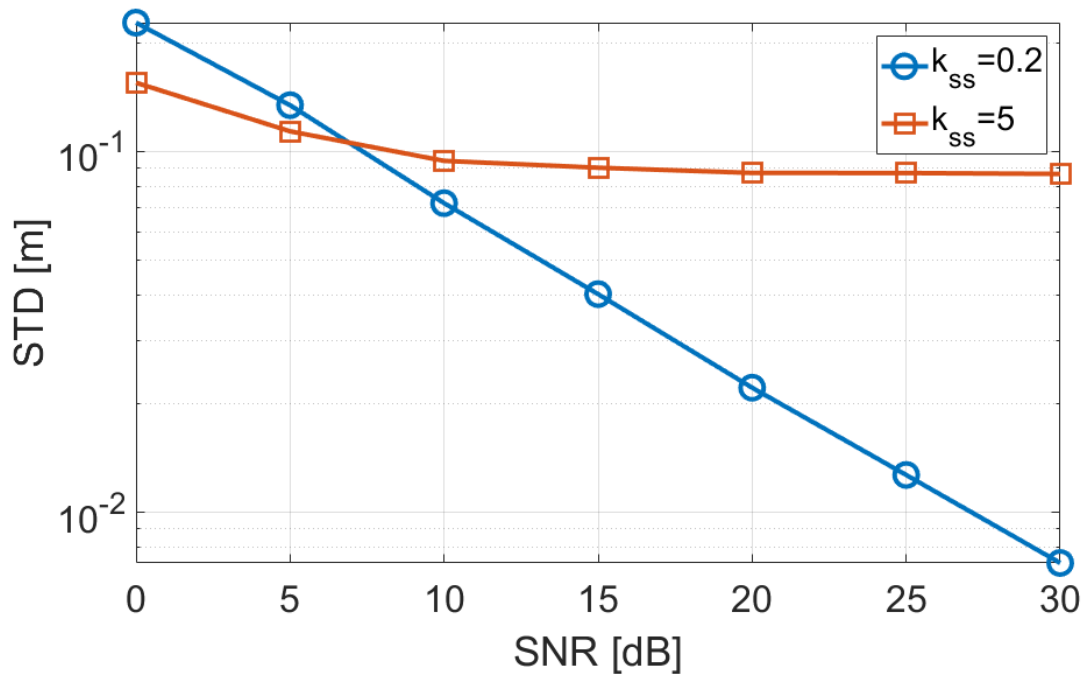
$$b_n = \text{mod}(b_0 \times k_{ss}, \text{size}_{fft}) \quad (3.29)$$

where  $b_n$  and  $b_0$  are the new and old bin locations respectively.

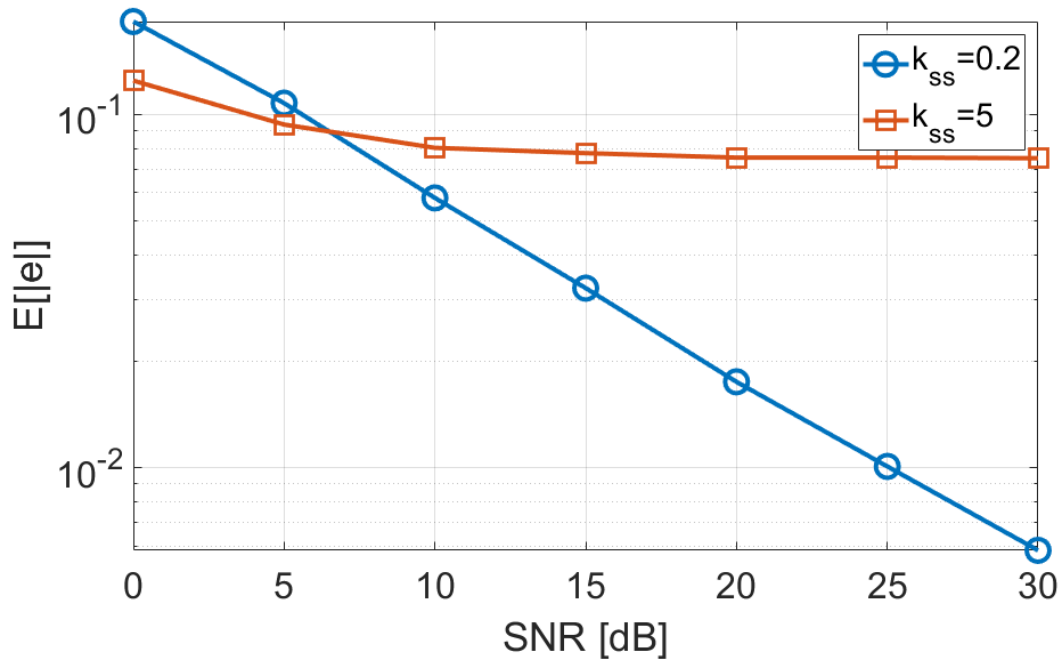
However, it is not possible to choose an arbitrary value for  $k_{ss}$ , because the subsampling introduces a SNR degradation caused by the noise folding. In facts, for a fixed transmitted power, the noise folding decreases the SNR of the sampled signal proportional to the subsampling factor, as given by the expression below:

$$SNR_{new} = SNR_{old} - 10 \times \log(k_{ss}) \quad (3.30)$$

Figure 3.37 reports a comparison of the system precision and accuracy, in time-domain, with two different subsampling factors. It is considered a 64-length OFDM symbol with 100 MHz of bandwidth and so in the first case the sampling time is equal to 1 GSPS, whereas, for  $k_{ss} = 5$  the sampling time is only 40 MSPS. For sake of simplicity, an AWGN channel is considered but the results can be easily extended to the case of multipath channel.



(a)



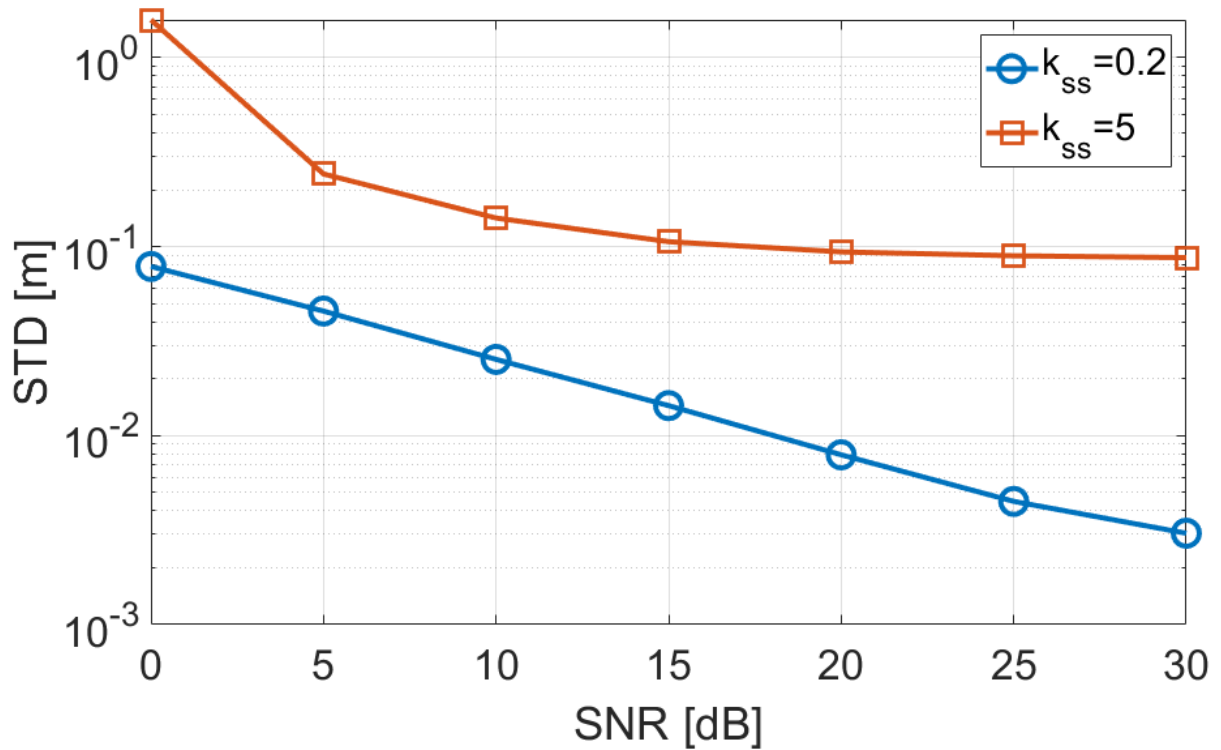
(b)

**Figure 3.37:** (a) Comparison of system precision in time-domain for different  $k_{ss}$  (b) Comparison of system precision in time-domain for different  $k_{ss}$ .

Note that the noise folding introduced by the subsampling process strongly degrades the system performance even for high SNR. After the subsampling process, the system is not able to achieve a mm precision, so, for these conditions it is not suitable for healthcare applications. Same

considerations are valid in frequency domain as sketches in Figure 3.38, where the precision and the accuracy are worse than the measures in time domain. However, from the results obtained in paragraph 3.3, to improve the estimates even in presence of strong noise, it is possible to apply the Kalman filter. Moreover, the results of the previous chapters are still valid. Hence, if a mm precision and accuracy are required using a low-rate ADC, the signal bandwidth and the number of subcarriers can be increased, changing the value of the subsampling factor. The proposed system is based on the SDR architecture. Thus, the main advantage is that a change in signal bandwidth or in the number of subcarriers implies a simple software modification. Any hardware changes are not necessary.

In conclusion, the subsampling process allows to reduce the demand of the ADC block that is the critical crucial component in the SDR receiver. The subsampling process degrades the SNR due to the noise folding. However, the system performance can be improved with the use of different strategy as the Kalman filter or increasing the signal bandwidth and the number of the subcarriers.



(a)

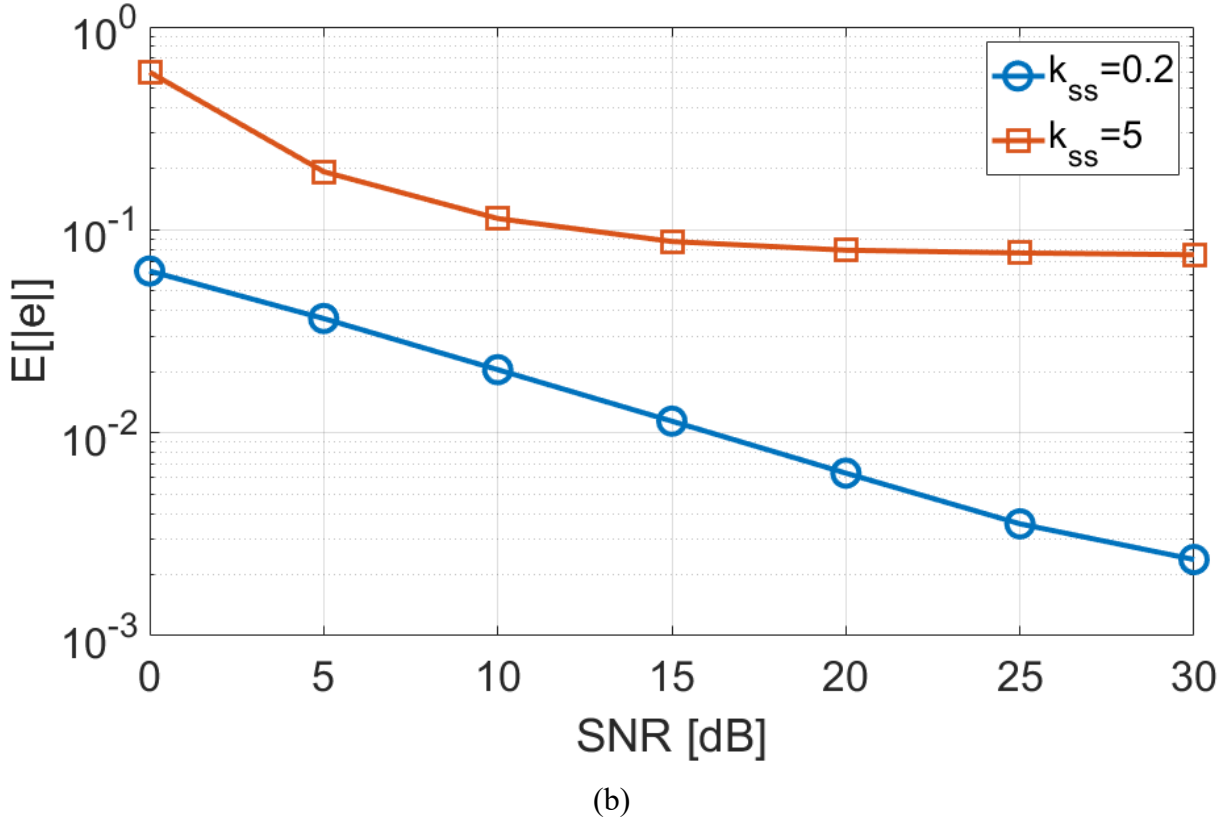


Figure 3.38: (a) Comparison of system precision in frequency-domain for different  $k_{ss}$  (b) Comparison of system precision in frequency-domain for different  $k_{ss}$ .

### 3.5 Conclusions

To evaluate the precision and the accuracy achievable by the proposed solution, a system model was implemented by means of MATLAB. The system was simulated in ideal conditions considering an additive white noise gaussian channel and the performance were evaluated as function of the signal to noise ratio at receiver, signal bandwidth and the number of subcarriers. If a mm precision and accuracy are required, these three parameters must be increased in according to the Cramer-Rao lower bound.

Once defined the system performance in ideal conditions, the multipath was introduced in the channel response. This latter significantly affects the distance estimates and introduces an error that must be compensated to achieve a high accuracy and precision. It was defined the breakdown distance as the minimum distance of the multipath echo that the system is able to notice. If the multipath echo has a distance lower than the breakdown value, the system is not able to distinguish the direct path from the indirect paths. An echo cancellation algorithm was implemented to improve the overall performance of the system when the multipath echo distance is greater than

the breakdown value. It tends to evaluate the channel impulse response analyzing the cross-correlation function in time domain and constructs a FIR filter to equalize the channel.

A Kalman filter was studied and implemented to further improve the system performance. This latter is the best estimator filter that can be used to track targets that are moving in according to a specific model. The model simulations have demonstrated that the use of the Kalman filter strongly improve the overall performance of the system guaranteeing a precision and an accuracy in the mm range required by the biomedical applications.

Finally, it was introduced a technique to reduce the sampling rate of the analog to digital converter and consequently decrease the costs of the system. It allows to transmit signal with a wide or ultra-wide bandwidth using the subsampling theorem. In this case is not necessary to introduce an ADCs with high sampling frequency that are very expensive and consume huge power. On others hand, from the analysis of the simulation results the precision and the accuracy degrade even for high SNR. However, to increase the overall performance of the system is possible to increase the bandwidth, the number of subcarriers and applying the Kalman filter. The advantage of the proposed solution is that all these operations can be performed without change the hardware but simply with a software instruction.

In the next chapter will be showed the measurements of the distance performed by the proposed system. Due to the limits of the laboratory instrumentations and to simplify the hardware design, it is chosen to transmit a 64-length OFDM symbol with 100 MHz of bandwidth. From the analysis of the model these signal parameters represent a good tradeoff between system complexity and system performance.

# 4 Indoor Positioning System: Hardware Design & Measurements

The main advantage of the proposed indoor positioning system is that the distance measurements, necessary to evaluate the target position, are computed entirely in digital domain. No analog processing is performed. Moreover, the use of the Zadoff-Chu sequences considerably simplifies the hardware architecture because the transmit signal can be generated in digital domain using look-up tables to store the signal samples and a Digital to Analog Converter is used to obtain the analog baseband signal. The absence of data in the transmit signal yields the presence of demodulators useless at the receiver side.

## 4.1 Transmitter and Receiver Architectures

The aim of the system design is to obtain a hardware for both the transmitter and the receiver able to adapt its properties and characteristics as function of the design requirements in terms of precision and accuracy. To satisfy this design requirement the transmitter and the receiver are based on the Software Defined Radio architecture illustrated in Figure 4.1.

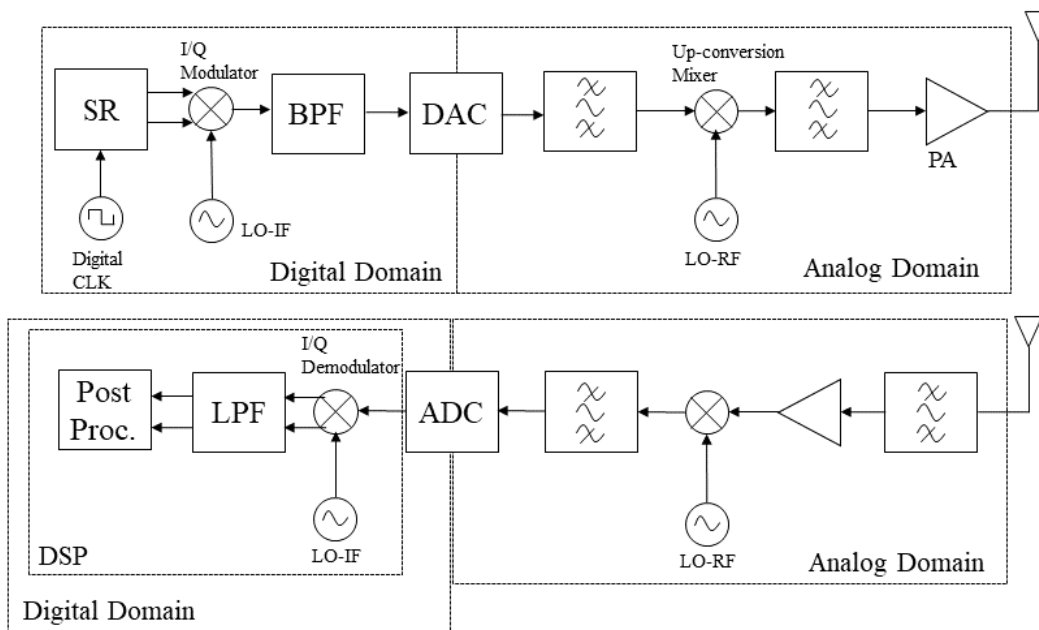


Figure 4.1: System Architecture of the transmitter and the receiver.

At the transmitter side the signal is generated in digital domain only the first time and the resulting samples can be stored in lookup tables or shift registers (SR) of a Digital Signal Processor (DSP)

or a Field Programmable Gate Arrays (FPGA). Here, different versions of the signal as function of the number of subcarriers or of the root index of the Zadoff-Chu sequence can be stored. One of them can be selected with a simple software instruction. An external digital clock allows to read the stored samples and feed them to a digital I/Q demodulator. Since the IF up-conversion is performed in digital domain, the resulting signal doesn't exhibit any mismatch error in amplitude or in time-delay due to the different paths between the two channels. Moreover, the IF frequency can be easily adjusted changing the frequency of the Local oscillator in digital domain and, the bandpass filter necessary to remove the unwanted frequency components can be adjusted as function of the signal specifics. Once generated the IF signal, the samples are transmitted to the Digital to Analog Converter to obtain the analog signal that is up-converted to RF by a simple mixer. Finally, a power amplifier amplifies the signal before to transmit on the channel.

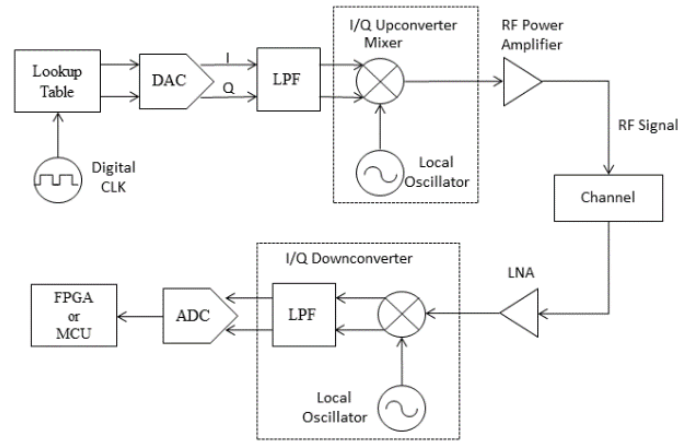
At the receiver side, a first passband filter removes the unwanted frequencies components and the result is amplified by Low-Noise amplifier. Then, the signal is down-converted to IF-frequency by a mixer and before being fed to the Analog to Digital converter it can be amplified by a Variable Gain Amplifier (VGA). Then, the IF signal is acquired by the ADC and the baseband signal is obtained performing the I/Q demodulation in digital domain to avoid any mismatch. The distance ranging algorithm can be applied to the resulting signal and the estimates are transmitted to a central unit to evaluate the target position applying the geometrical model of the system.

The use of the SDR architecture allows to obtain a system able to manipulate multiple radio standards. In facts, with this architecture it is possible to introduce different signals or standard to evaluate the target position without change the system hardware. Moreover, the data can be fused with the pilot subcarriers needed by the estimate process using different schemes of modulation (QAM, PSK, ASK, ...).

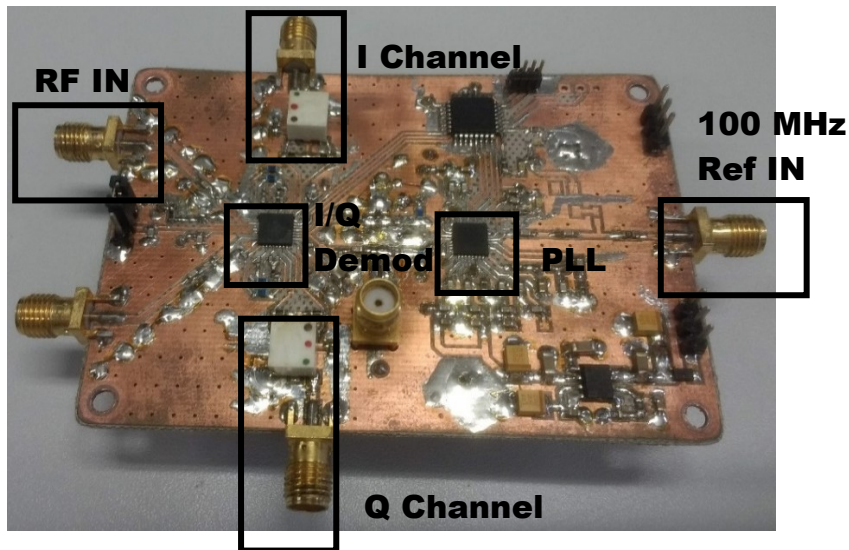
## **4.2 AWGN Channel Measurements**

In a first analysis, the proposed system is validated in ideal conditions, estimating the length of different cables that represent an AWGN channel. In these test-benches a modified version of the architecture represented in Figure 4.1 is implemented (Figure 4.2 (a)). The signal samples are generated in MATLAB and then are stored into the memory of the Keysight vector signal generator. The latter generates the analog baseband I/Q signal and then performs the up-conversion to RF frequency.

The receiver exploits a homodyne architecture where the RF signal is directly down-converted to baseband frequency by the LT5586 I/Q demodulator of the Linear Technology [53]. For both I and Q channel, the component integrates a variable gain amplifier with a gain comprised in range from 0 to 10 dB divided in 8 steps. The LO source is provided by the Phase Locked Loop ADF5355 of the Analog Devices [54] programmed by an external microcontroller. The I/Q channels are acquired by a scope and the resulting samples are processed offline by a MATLAB script.



(a)



(b)

**Figure 4.2:** (a) System Architecture of the transmitter and the receiver for the first test-bench. (b) Receiver printed circuit board.

To evaluate the length of the cables, the proposed system transmits a 64-length OFDM signal with 100 MHz of signal. At the receiver side, the system acquires 10 signal periods with a sampling time of 1 GSPS. Finally, the signal is up(down)-converted to 5.8 GHz and it propagates with a velocity equal to the 70% of the light speed, due to dielectric constant of the cables. Table 4.1

reports a subset of the cable lengths computed by the proposed system. The resulting values are compared with the lengths evaluated with the Keysight Network Analyzer. It should be noted that the proposed system is able to compute the cable lengths with a very high accuracy and precision.

Table 4.1: AWGN channel Measurements

Network Analyzer [m]	Test-Bench #1 [m]	Test-Bench #2 [m]	Test-Bench #3 [m]	Test-Bench #4 [m]
0.9864	0.98743	0.98833	0.98828	0.98839
1.9746	1.978	1.9787	1.9769	1.979
2.9688	2.9757	2.9766	2.9731	2.9755
3.9608	3.9697	3.9586	3.967	3.9635
4.9559	4.9646	4.9667	4.964	4.9688

Figure 4.3 illustrates the absolute error of the estimation as function of the cable length. Note that the measurements fit the results obtained with the model described in chapter 3. For an ideal channel, the error in the distance estimation depends only by the SNR of the received signal and from its parameters. As reported in the graphs, the system is able to evaluate the cable lengths with an absolute error lower than 1 cm.

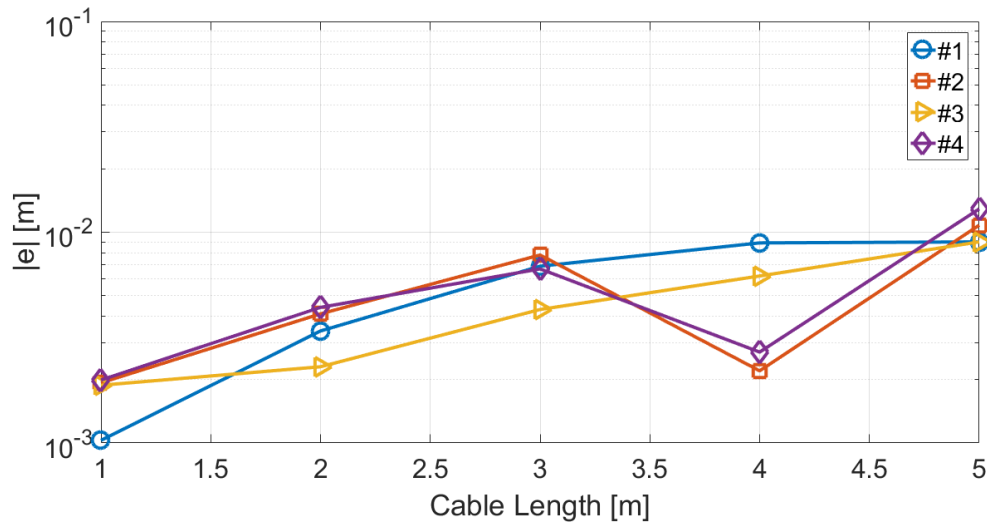
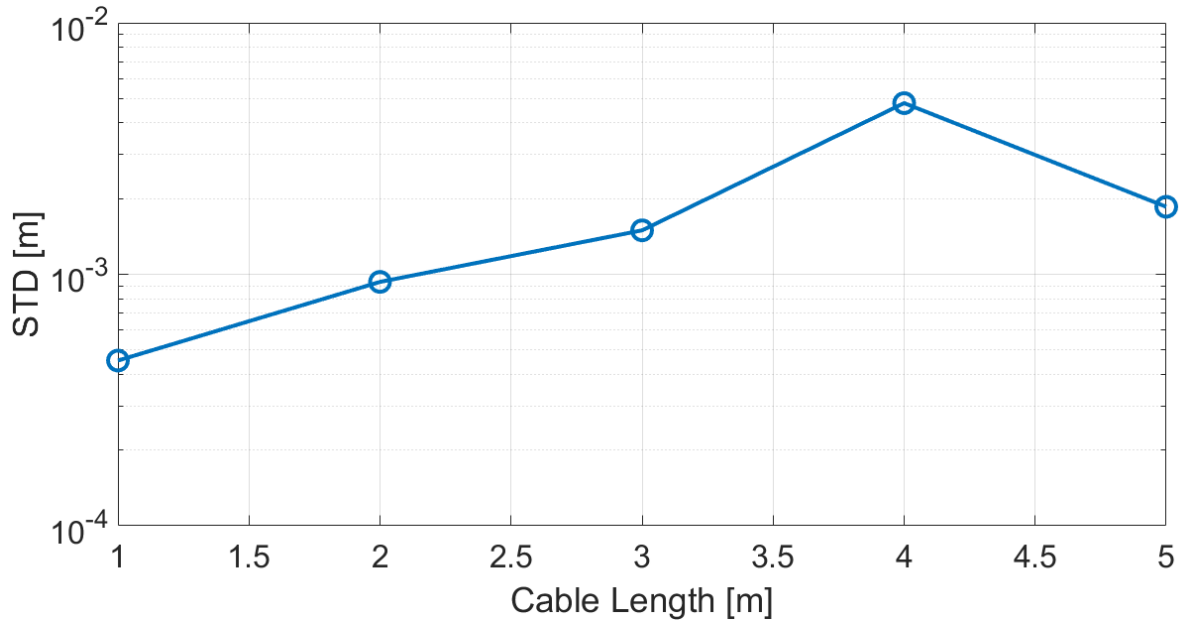
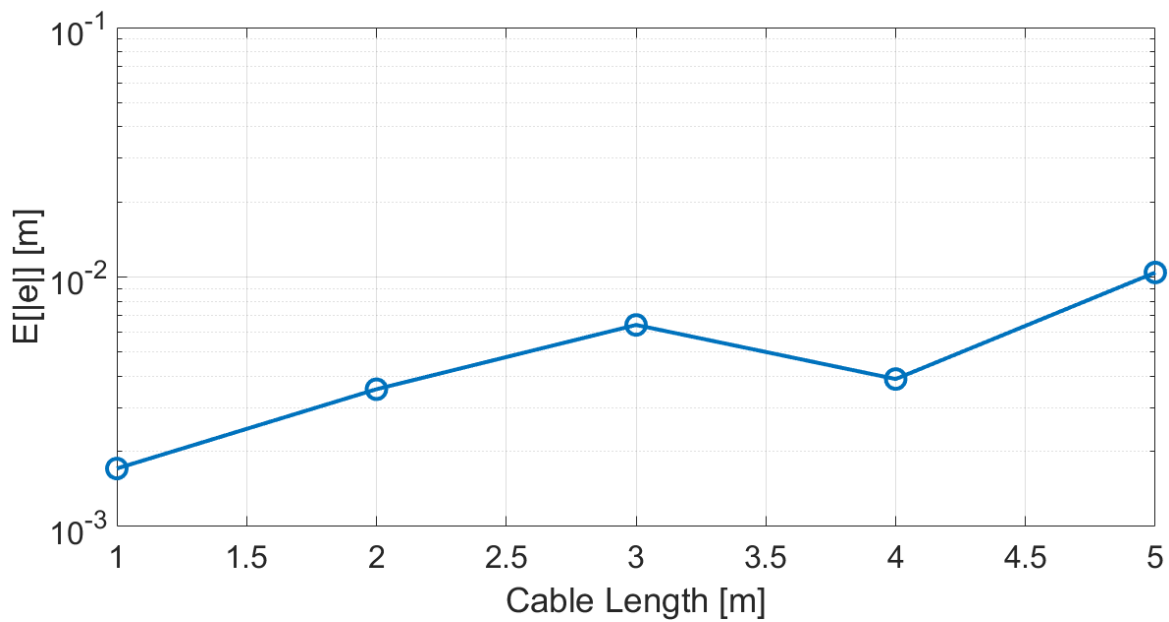


Figure 4.3: Absolute error in AWGN channel measurements.

The system precision and the accuracy are reported in Figure 4.4 (a) and (b) respectively. Note that the system, for an AWGN channel, is able to estimate the distance (or in this case the cable length) with a mm precision and accuracy.



(a)



(b)

**Figure 4.4:** (a) System precision (b) System accuracy

The performance reported in the previous charts are evaluated from the raw data provided by the algorithm, thus any further processing as for example the Kalman filter, is not applied. Moreover, the final length values are computed adjusting the values extracted in time-domain with the estimates calculated in frequency domain.

## 4.3 Radio Channel

### 4.3.1 Test-bench #1

Once evaluated the precision and the system accuracy for an AWGN channel, the system was tested transmitting the sense signal on the radio channel using a microstrip patch antenna. The latter was designed with a coaxial probe fed connector, using Keysight Advanced Design System (ADS). The core of the antenna measures  $19.3 \times 12.3$  cm while the entire geometry including the ground layer is  $28.6 \times 22.6$  cm (Figure 4.5).

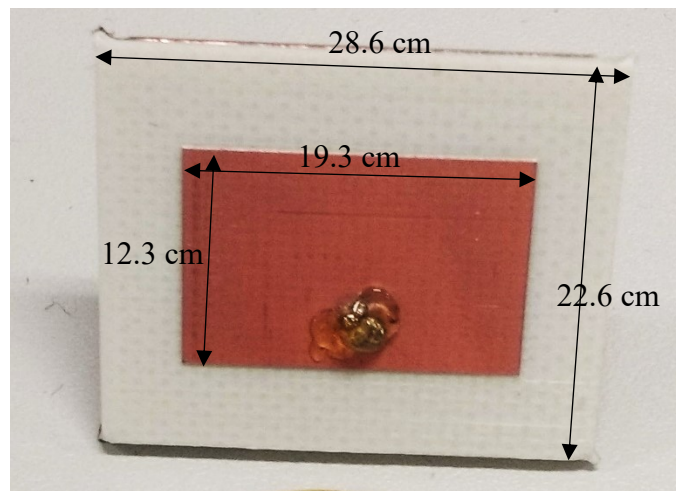
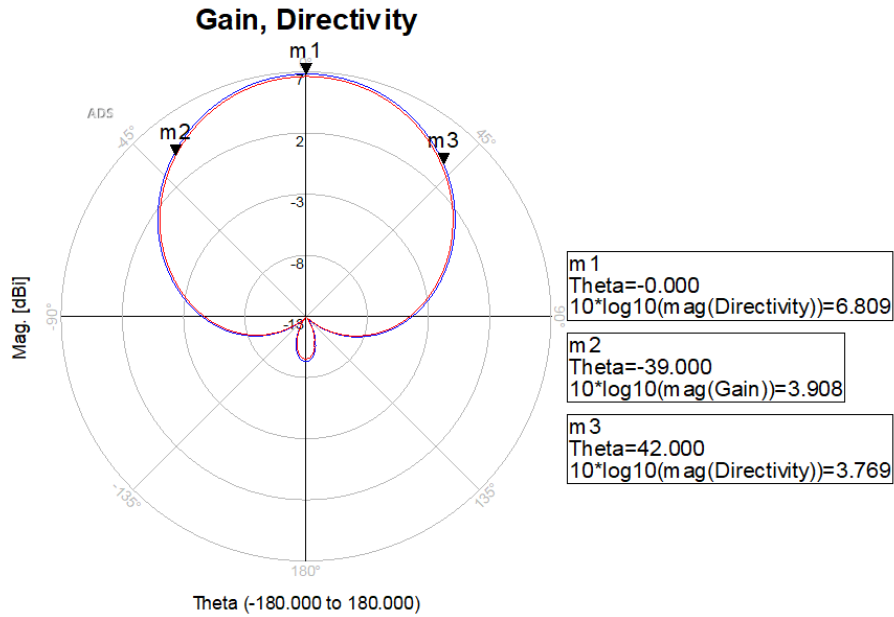
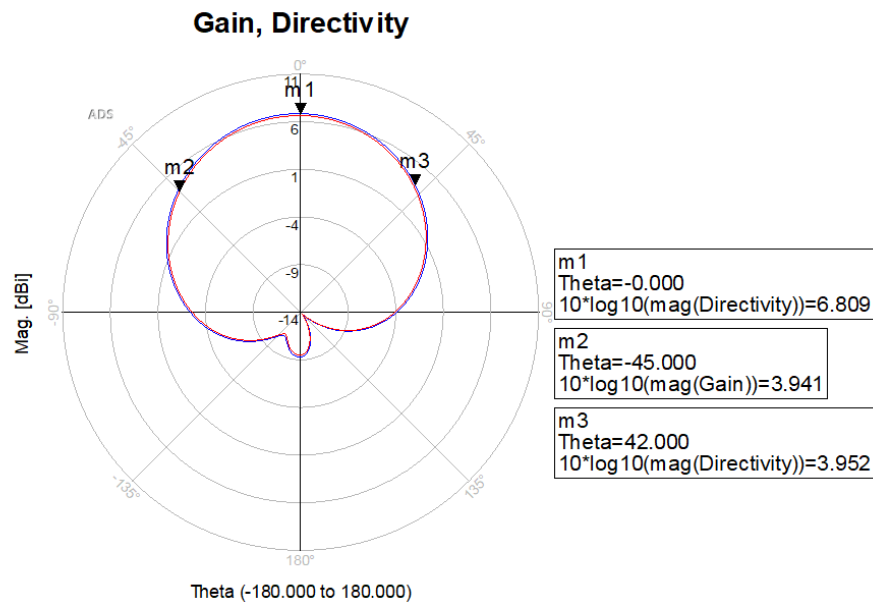


**Figure 4.5:** Microstrip Patch antenna with coaxial probe fed connector

It exhibits a gain of 6.8 dB at 5.85 GHz, with a gain directivity of  $81^\circ$ , in horizontal plane, and  $87^\circ$  in azimuth plane (measured as 3-dB gain) as showed in Figure 4.6. In Figure 4.7 there is a comparison between the input matching simulations computed by ADS and the matching measurements performed with the Keysight Network Analyzer. It should be noted that the measurements are slightly shifted towards higher frequencies due to a non-perfect fabrication process. Thus, the patch antenna has a center frequency of 5.95 GHz with a bandwidth of 200 MHz (measured as 10 dB input matching). Finally, the antenna was built using the two layers RO4003C laminate substrate with a 1.52 mm thickness and a dielectric constant of 3.38 [55].



(a)



(b)

**Figure 4.6:** Directivity Diagram for the horizontal (a) and azimuthal planes (b).

The system comprises a single transmitter that transmits a 64-length OFDM symbol with 100 MHz of signal bandwidth. The transmitter was placed in front of a single receiver to reduce the multipath interferences for extracting the LOS path from the strongest peak of the channel impulse response. The receiver is the same used in the previous test-bench and again 10 periods of the signal are acquired from the scope with a sampling time of 1 GSPS. The antenna transmits the signal with a

power of 0 dBm to guarantee a high SNR at the receiver. Moreover, it was placed at different distance that are previously measured with a track laser system with an accuracy of 2 mm and a spatial resolution of 1 mm.

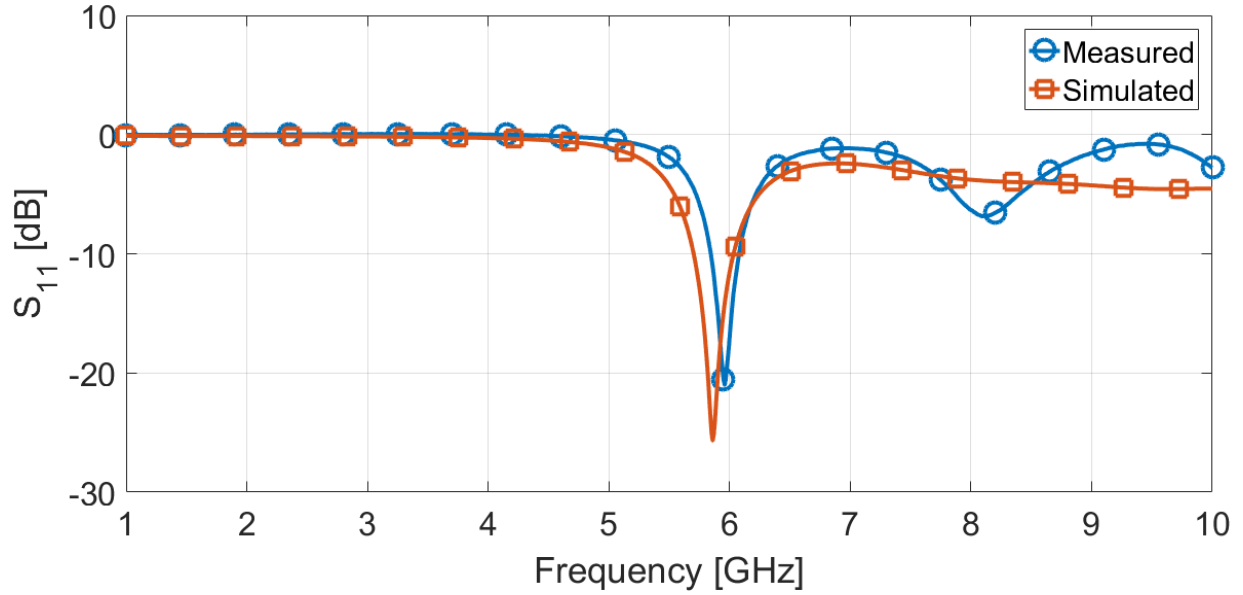


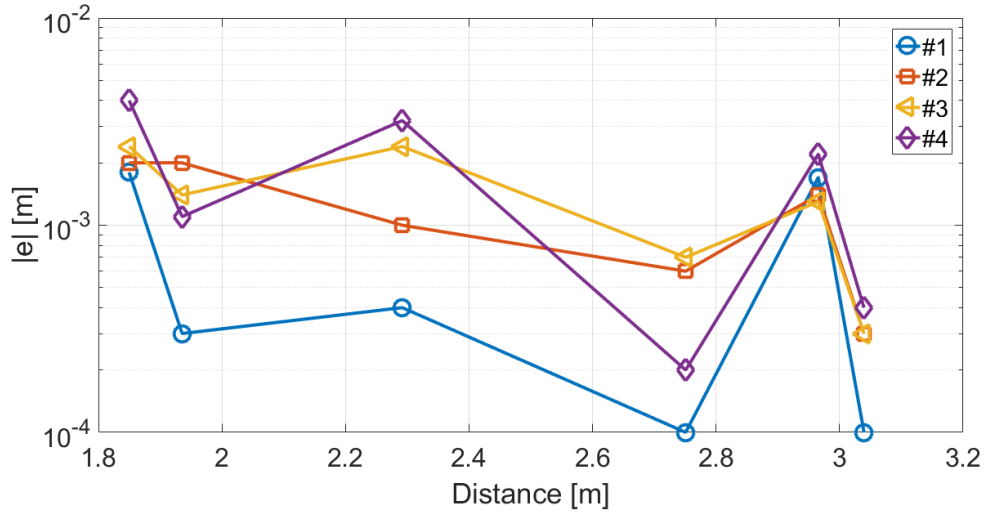
Figure 4.7: Microstrip Patch Antenna input matching

Table 4.2 reports a subset of the distances extracted by the proposed system compared with the measures of the track laser system. Again, the proposed system is able to evaluate the distance with a high precision and accuracy.

Table 4.2: Radio channel: Distance Measurements

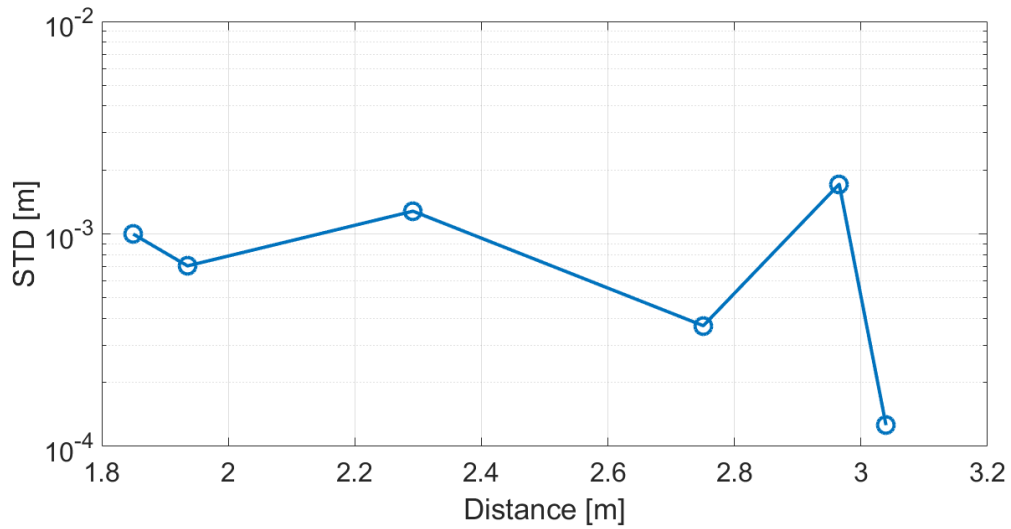
Laser [m]	Test-Bench #1 [m]	Test-Bench #2 [m]	Test-Bench #3 [m]	Test-Bench #4 [m]
1.8497	1.8479	1.8477	1.8473	1.8457
1.9355	1.9352	1.9335	1.9341	1.9344
2.2919	2.2923	2.2929	2.2943	2.2951
2.4817	2.4813	2.4829	2.4835	2.4835
2.7508	2.7509	2.7502	2.7501	2.7506
2.9655	2.9672	2.9641	2.9642	2.9633
3.0395	3.0395	3.0398	3.0398	3.0399

In fact, it should be noted from the Figure 4.8 that the absolute error as function of the distance is lower than 1 cm for all test-benches.

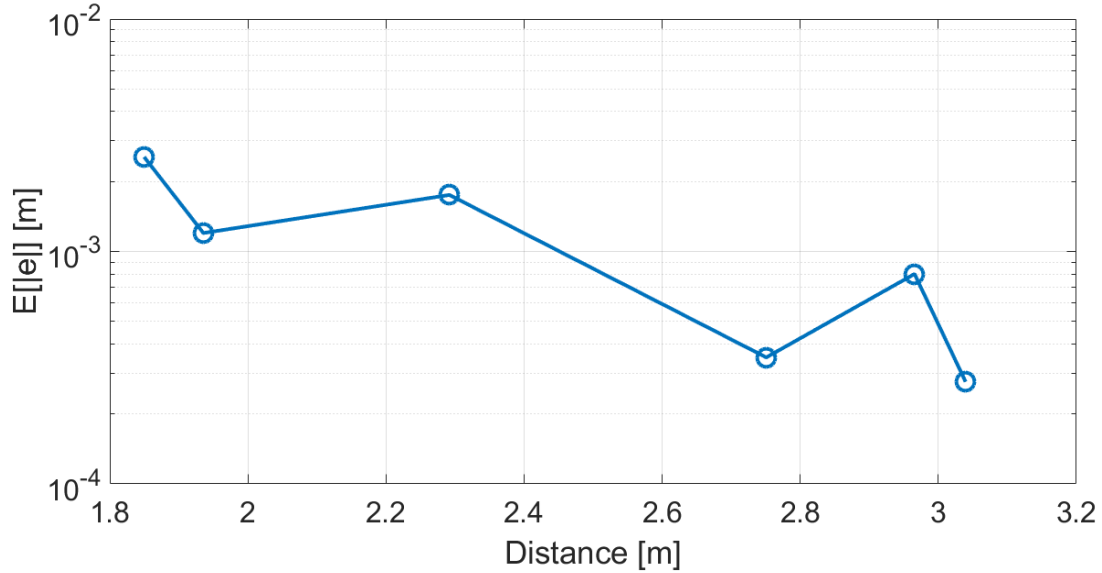


**Figure 4.8:** Radio Channel: absolute error as function of the distance

The system precision and accuracy are reported in Figure 4.9 (a) and (b) respectively. Note that the system is able to evaluate the distance between the transmitter and the receiver with a mm precision and accuracy. This result is due to the high SNR at the receiver. As mentioned, the signal is transmitted with a power of 0 dBm and the transmitter was placed in front of the receiver minimizing the multipath. However, these results are very promising and demonstrates the validity of the proposed system but it has to be stressed in severe multipath conditions before to implement the entire system.



(a)



(b)

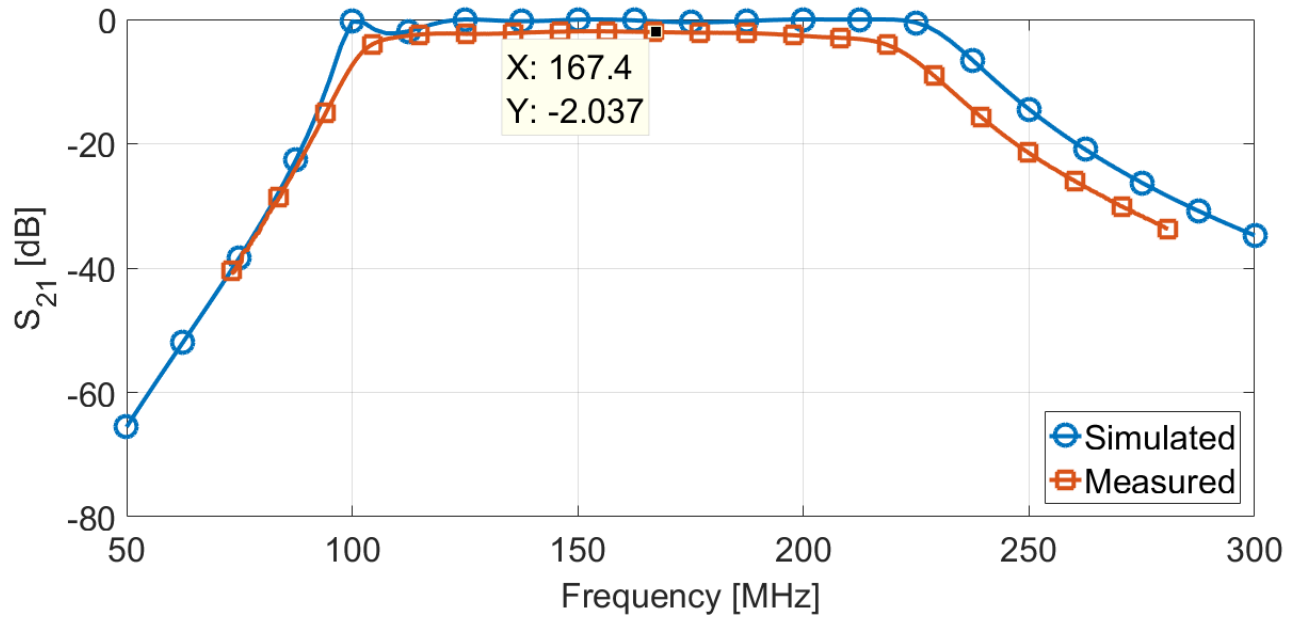
Figure 4.9: Radio Channel: (a) system precision, (b) system accuracy

### 4.3.2 Transmitter and Receiver Design

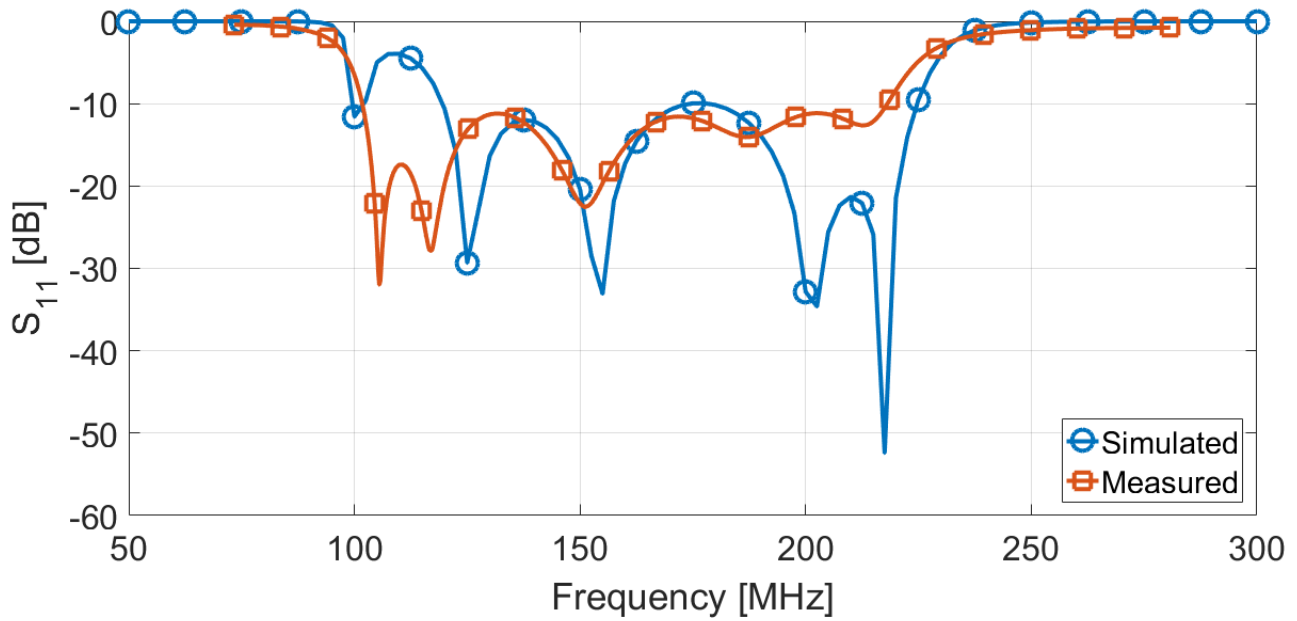
To exploit the properties provided by the SDR architecture, the receiver is re-designed according to the system represented in Figure 4.1. The IF signal is generated in digital domain by a MATLAB script and the samples are stored into shift-registers generated by a FPGA. These samples fed the DAC3482 of the Texas Instruments [56] that provides the analog signal to an intermediate frequency of 170 MHz. The output of the DAC must be filtered by an analog filter to eliminate the unwanted component frequencies introduced by the DAC conversion process. Hence, by means of Keysight ADS, a Chebyshev bandpass filter is designed. Due to the low IF frequencies, the passband filter is made with lumped components. The use of lumped inductors and capacitors allows to realize a filter that strongly matches the CAD simulations. However, this approach is not valid for high frequencies because the parasitic introduced by these components can significantly modify the behavior of the filter. Moreover, for high frequencies the Self-Resonant Frequency of the lumped components must be far away from the operating frequency of the circuit, to avoid any auto-oscillation conditions that induce instability for the system. When this condition is not satisfied, the filter must be designed with microstrip lines or with coplanar waveguides [57].

Figure 4.10 reports the bandpass and the input/output matching of the 5<sup>th</sup> order Chebyshev filter designed with ADS. The realized filter has a flat bandpass of 100 MHz about centered to 170 MHz

with an insertion loss of only 2 dB. Moreover, the filter has an input and output return loss lower than 10 dB over all the bandwidth.



(a)



(b)

**Figure 4.10:** IF analog Chebyshev: (a) bandpass, (b) input/output matching.

After the filtering process, the IF signal is upconverted to RF frequency by the Mini-Circuits double balanced mixer ADE-35+ [58]. For the design of transmitter board is chosen a RF frequency of 3.3 GHz to reduce the manufacture costs. The LO is provided by the on-board PLL

ADF4355 [59] programmed by an 8-bit microcontroller. The output of the mixer is amplified by the ADL5611 of the Analog Devices [60] (Figure 4.11), while the unwanted frequencies generated by the mixer conversion process is removed by an external filter realized with transmission lines (Figure 4.12).

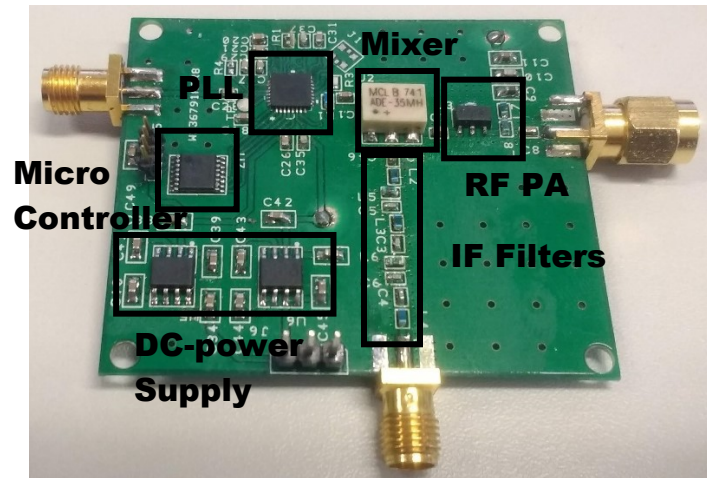


Figure 4.11: PCB Transmitter analog front-end.

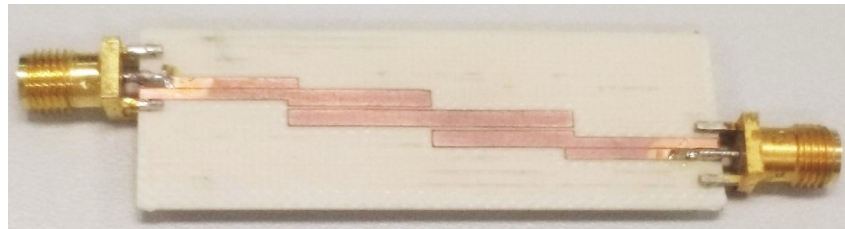
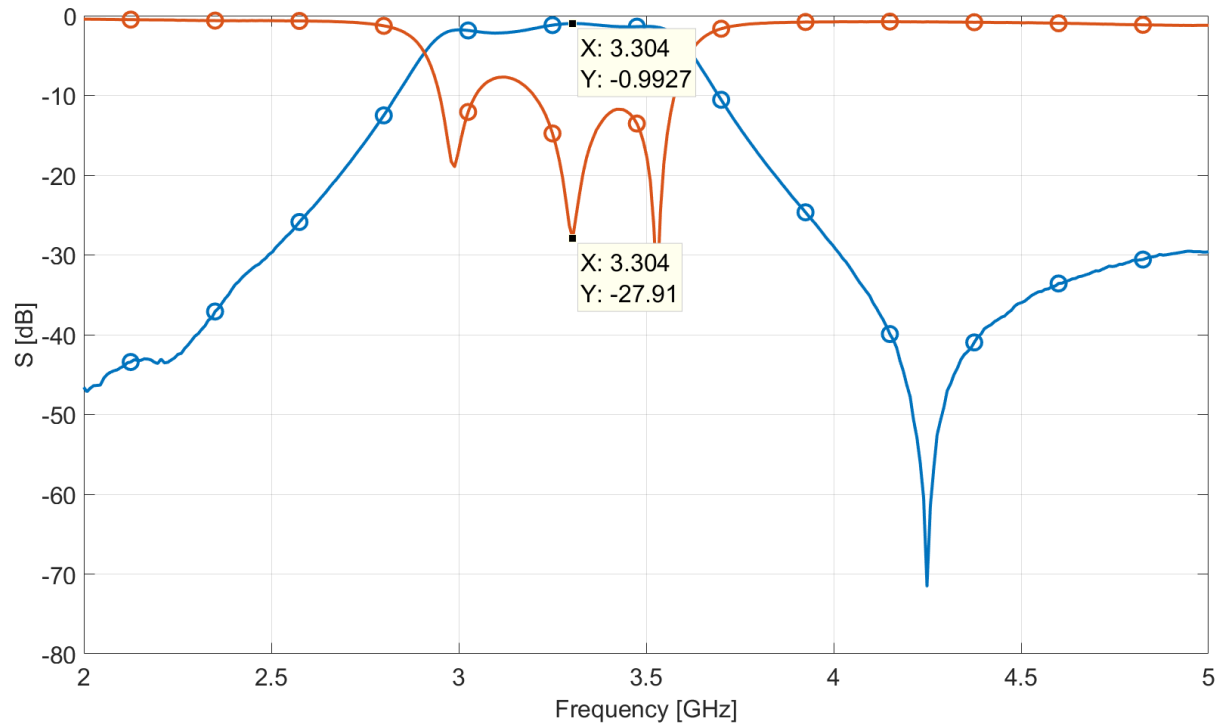


Figure 4.12: RF-Passband filter realized with coupled transmission lines.

The passband filter is realized with coupled transmission coupled lines using the dielectric RO4003C with a thickness of 0.81 mm and a dielectric constant of 3.38. It measures 18.6 mm × 56.3 mm and the scattering parameters measured by means of the network analyzer are represented in Figure 4.13. Note that the realized filter exhibits a large bandwidth of 500 MHz centered to 3.3 GHz with an insertion loss of about 1 dB in the passband frequencies.



**Figure 4.13:** RF-Passband filter measures of scattering parameters.

The receiver exploits essentially the same analog hardware used to design the transmitter front-end. In Figure 4.14 is sketched the final version of the analog front-end of the receiver. The received signal is firstly amplified by the same RF amplifier used in the transmitter path. Then the signal is down-converted to IF frequencies with ADE-35+, and, it is amplified by the ADL5535 of the Analog Devices [61]. An on-board PLL provides the LO source for the mixer conversion, and, finally, the resulting signal is filtered by the same filter previously designed for the transmitter path. The transmitter and the receiver boards require a DC-power supply of 6 V with a current consumption of 160 mA, due essentially to the PLL and the two amplifiers. The reference 100-MHz signal needed to the input of the PLL is provided by the external clock generator LMK04828 of the Texas Instruments [62]. The latter provides even the trigger signal in input to the ADC of the scope. Each receiver board shares these two signals to avoid any synchronization error due to the frequency and phase offset. The resulting board is very compact, in fact, it measures  $61.82 \times 54.8$  cm without considering the connectors. Both the receiver and the transmitter boards are made on FR4 substrate with a thick of 0.8mm and a dielectric constant of 4.6.

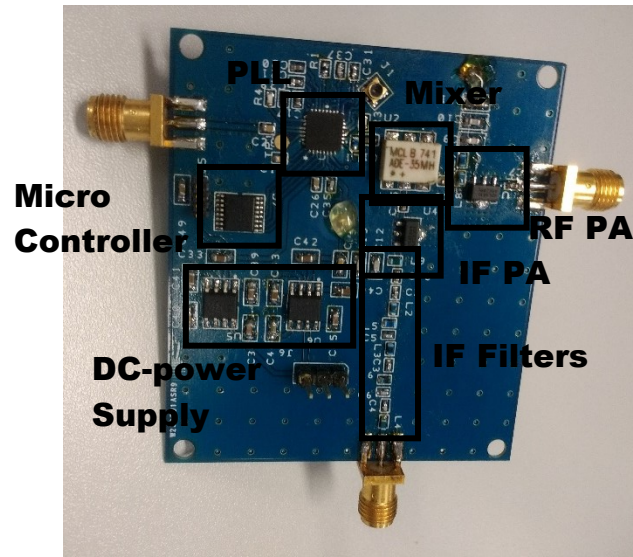


**Figure 4.14:** PCB Receiver analog front-end.

Due to the different central frequency used by the designed boards ( $f_c = 3.3$  GHz), the microstrip antenna is re-designed according to new values. In this case, the feed of the patch antenna is realized with a microstrip line. This kind of feed has the advantage that it can be etched on the same substrate of the antenna, so the total structure remains planar. The drawback is the unwanted radiation from the feed line, which leads to an increase in the cross-polar level. Also, in the millimeter-wave range, the size of the feed line is comparable to the patch size, leading to an increased undesired radiation. Moreover, the patch antenna with microstrip line feed has less bandwidth than the antenna with coaxial probe feed or proximity fed [63].

Figure 4.15 sketches the patch antenna realized on the RO4003C substrate with a thick of 1.52 mm and a constant dielectric of 3.38. It measures  $5 \times 5$  cm and exhibits a gain of 6 dBi @ 3.3 GHz with  $80^\circ$  of directivity in horizontal plane and  $139^\circ$  in azimuth plane (measured as 3-dB gain). Figure 4.16 reports the measure of the input matching for the patch antenna compared with the results of the simulations performed with Keysight ADS. Due to non-perfect of the manufacture process, the resonant frequency of the fabricated antenna is shifted downwards by about 50 MHz. Hence, the patch antenna has a center frequency of 3.3 GHz with a bandwidth of 100 MHz measured as 9 dB input matching.

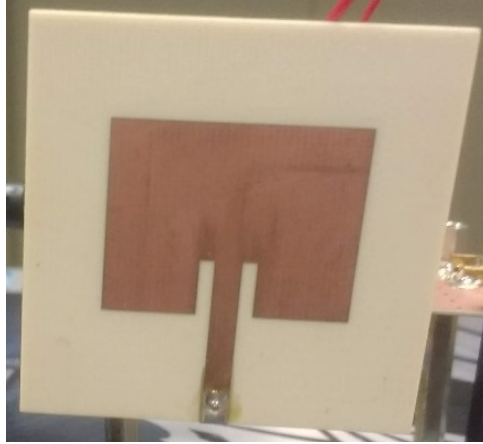


Figure 4.15: Patch antenna with microstrip line feed for 3.35 GHz.

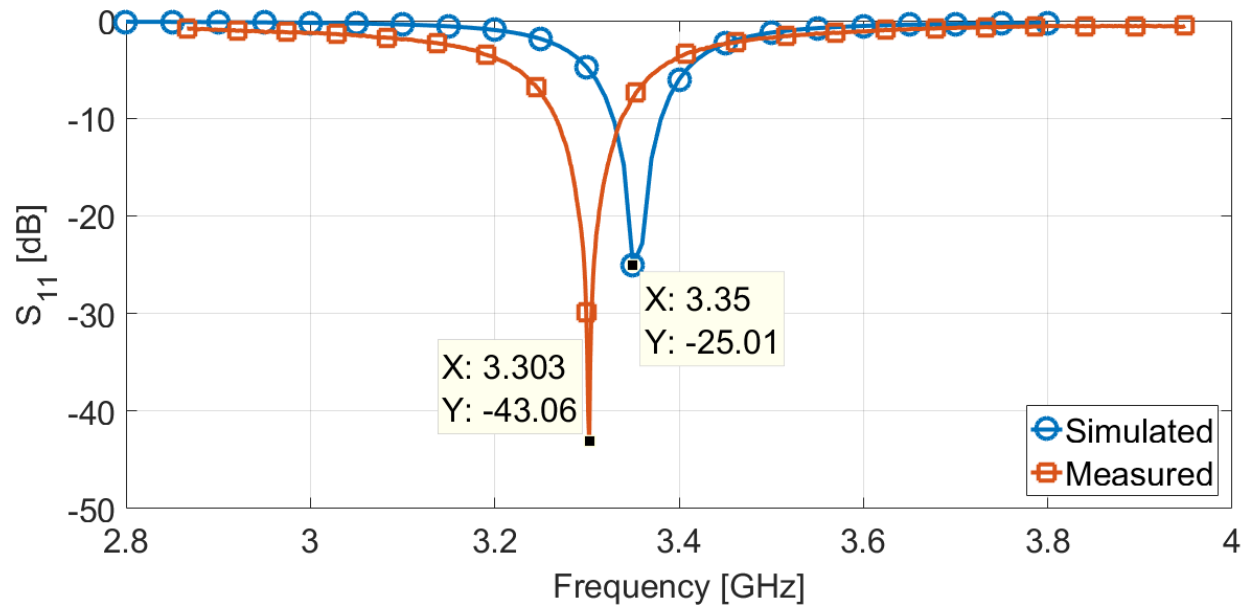


Figure 4.16: Input matching of the Patch antenna with microstrip line feed.

### 4.3.3 Test-bench #2

In the next test-benches the transmit antenna is mounted on a metallic bar and it is moved along the x-axis with steps of 2 cm by means of a dc motor. The system comprises four receivers placed in well-known positions while the transmitter is placed about 2.5 meters away from the receivers. The receiver number 1 is used as system origin to apply the TDoA algorithm described in the previous chapters. In the set {A, C, E} the antenna is moved from Left to Right, while in the set {B, D, F} it is shifted in opposite way. The distances are evaluated using a 64-length OFDM signal with a bandwidth of 100 MHz. At the receiver-side it is acquired 10 signal periods with a sampling time of 1GSPS.

The aim of these test-benches is to evaluate the system precision in severe multipath condition.  
Table 4.3 and

Table 4.4 report the distance values extracted for the two subsets.

Table 4.3: Distance Measurement for the subset {A, C, E}.

| <b>Rx<sub>1</sub> vs Rx<sub>2</sub></b> |
|---|---|---|---|---|
| <b>A [m]</b>                            | <b>C [m]</b>                            | <b>E [m]</b>                            | <b>AVG [m]</b>                          | <b>STD [m]</b>                          |
| 0.507206                                | 0.491681                                | 0.476161                                | 0.491683                                | 0.015522                                |
| 0.460597                                | 0.459575                                | 0.453306                                | 0.457826                                | 0.003948                                |
| 0.497492                                | 0.491858                                | 0.484988                                | 0.491446                                | 0.006262                                |
| 0.520191                                | 0.52103                                 | 0.53124                                 | 0.524154                                | 0.006151                                |
| 0.526535                                | 0.527368                                | 0.533893                                | 0.529265                                | 0.004029                                |
| 0.445144                                | 0.45155                                 | 0.45754                                 | 0.451411                                | 0.006199                                |
| 0.318019                                | 0.317117                                | 0.319355                                | 0.318164                                | 0.001126                                |
| 0.259753                                | 0.267415                                | 0.272211                                | 0.26646                                 | 0.006284                                |
| 0.247244                                | 0.242295                                | 0.240116                                | 0.243219                                | 0.003653                                |
| 0.286936                                | 0.273961                                | 0.278281                                | 0.279726                                | 0.006607                                |
| <b>Rx<sub>1</sub> vs Rx<sub>3</sub></b> |
<b>A [m]</b>	<b>C [m]</b>	<b>E [m]</b>	<b>AVG [m]</b>	<b>STD [m]</b>
1.567484	1.576108	1.562142	1.568578	0.007047
1.564262	1.57372	1.578614	1.572199	0.007296
1.611808	1.618137	1.616943	1.615629	0.003363
1.75518	1.764572	1.769158	1.76297	0.007125
1.969535	1.972177	1.969552	1.970421	0.001521
2.038999	2.037623	2.036214	2.037612	0.001393
1.724751	1.720485	1.718803	1.721347	0.003066
1.403304	1.396963	1.386106	1.395458	0.008697
1.252643	1.254106	1.259284	1.255345	0.00349
1.321477	1.320761	1.319619	1.320619	0.000937
<b>Rx<sub>1</sub> vs Rx<sub>4</sub></b>				
<b>A [m]</b>	<b>C [m]</b>	<b>E [m]</b>	<b>AVG [m]</b>	<b>STD [m]</b>
0.732103	0.758825	0.747159	0.746029	0.013397
0.724587	0.738713	0.740233	0.734511	0.008628
0.779325	0.78148	0.782485	0.781097	0.001615
0.819595	0.816823	0.827755	0.821391	0.005683
0.748775	0.739918	0.751844	0.746846	0.006193
0.675819	0.667632	0.676385	0.673279	0.004898
0.691865	0.683522	0.687993	0.687793	0.004175

0.672092	0.677596	0.660737	0.670141	0.008597
0.568121	0.570287	0.575533	0.571314	0.003811
0.564778	0.553951	0.552315	0.557015	0.006773

Table 4.4: Distance Measurement for the subset {B, D, F}.

| <b>Rx1 vs Rx2</b> |
|-------------------|-------------------|-------------------|-------------------|-------------------|
| <b>B [m]</b>      | <b>D [m]</b>      | <b>F [m]</b>      | <b>AVG [m]</b>    | <b>STD [m]</b>    |
| 0.173157          | 0.184977          | 0.177222          | 0.178452          | 0.006005          |
| 0.266681          | 0.27943           | 0.26929           | 0.2718            | 0.006735          |
| 0.256816          | 0.263911          | 0.273344          | 0.26469           | 0.008292          |
| 0.269274          | 0.284367          | 0.274518          | 0.276053          | 0.007663          |
| 0.316204          | 0.304487          | 0.311468          | 0.31072           | 0.005894          |
| 0.455984          | 0.448553          | 0.465043          | 0.456526          | 0.008258          |
| 0.540701          | 0.549139          | 0.548158          | 0.545999          | 0.004615          |
| 0.51997           | 0.529668          | 0.534132          | 0.527923          | 0.00724           |
| 0.486986          | 0.496166          | 0.498732          | 0.493961          | 0.006176          |
| 0.451342          | 0.444007          | 0.454674          | 0.450008          | 0.005458          |
| <b>Rx1 vs Rx3</b> |
<b>B [m]</b>	<b>D [m]</b>	<b>F [m]</b>	<b>AVG [m]</b>	<b>STD [m]</b>
1.254198	1.251338	1.248346	1.251294	0.002926
1.311153	1.326269	1.307817	1.31508	0.009832
1.253226	1.259385	1.266348	1.259653	0.006565
1.387167	1.392171	1.38688	1.38874	0.002975
1.714453	1.704278	1.706305	1.708345	0.005386
2.023134	2.016039	2.022463	2.020545	0.003917
1.965344	1.967218	1.961463	1.964675	0.002935
1.757993	1.754909	1.757263	1.756722	0.001611
1.618297	1.618373	1.626367	1.621012	0.004637
1.576029	1.571015	1.583084	1.576709	0.006063
<b>Rx1 vs Rx4</b>				
<b>B [m]</b>	<b>D [m]</b>	<b>F [m]</b>	<b>AVG [m]</b>	<b>STD [m]</b>
0.533283	0.527315	0.527325	0.529307	0.003443
0.554785	0.561658	0.552599	0.556347	0.004728
0.578947	0.582985	0.585475	0.582469	0.003294
0.673014	0.675854	0.667818	0.672229	0.004075
0.687328	0.678691	0.689245	0.685088	0.005622
0.67368	0.672481	0.681622	0.675928	0.004968
0.742838	0.756236	0.755605	0.751559	0.00756
0.814699	0.816569	0.819284	0.816851	0.002306
0.781746	0.785732	0.791742	0.786407	0.005032
0.735777	0.7369	0.740257	0.737645	0.002331

It should be noted that the system is able to evaluate the distance with a very high precision as showed by the charts sketches in Figure 4.17 and in Figure 4.18. In fact, the standard deviation in the distance measures is lower than 1 cm with a worst case of 1.5 cm red highlighted in the tables. These results have demonstrated the high repeatability degree of the proposed ranging system even in severe multipath condition. However, from the geometrical model defined by the equations (2.32) the distance measures should be approximated by a straight line. The plot of one of the subsets represented in the tables evidences that the estimates are not strictly linear but exhibit inflection points (Figure 4.19).

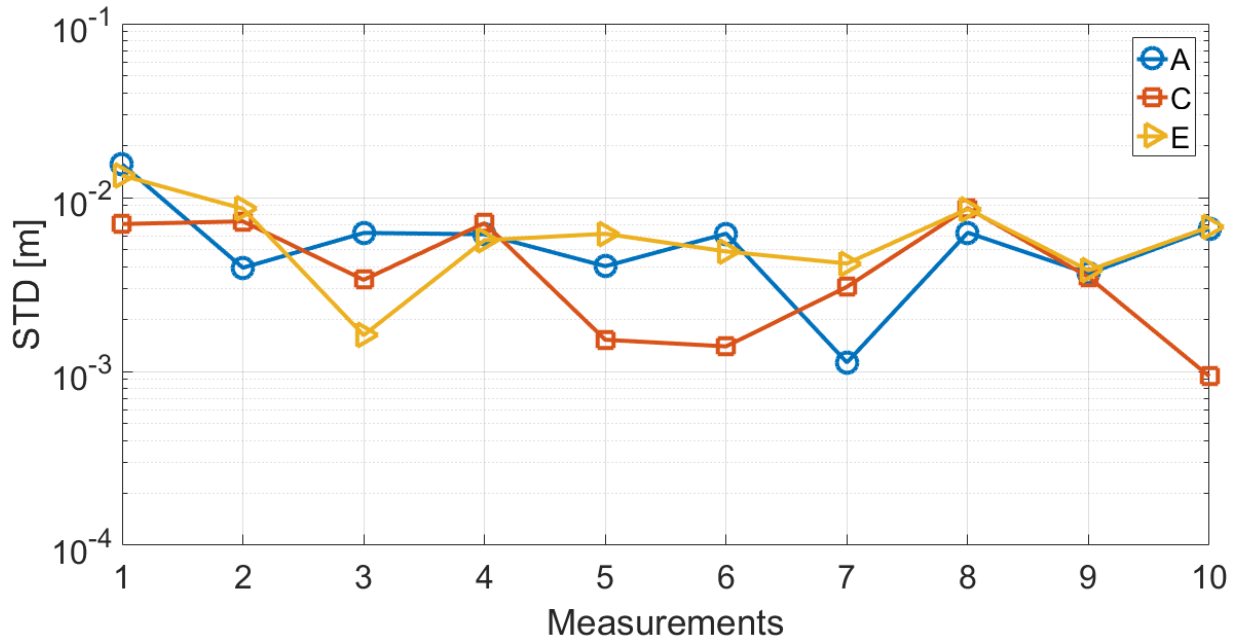


Figure 4.17: System precision for the subset {A, C, E}.

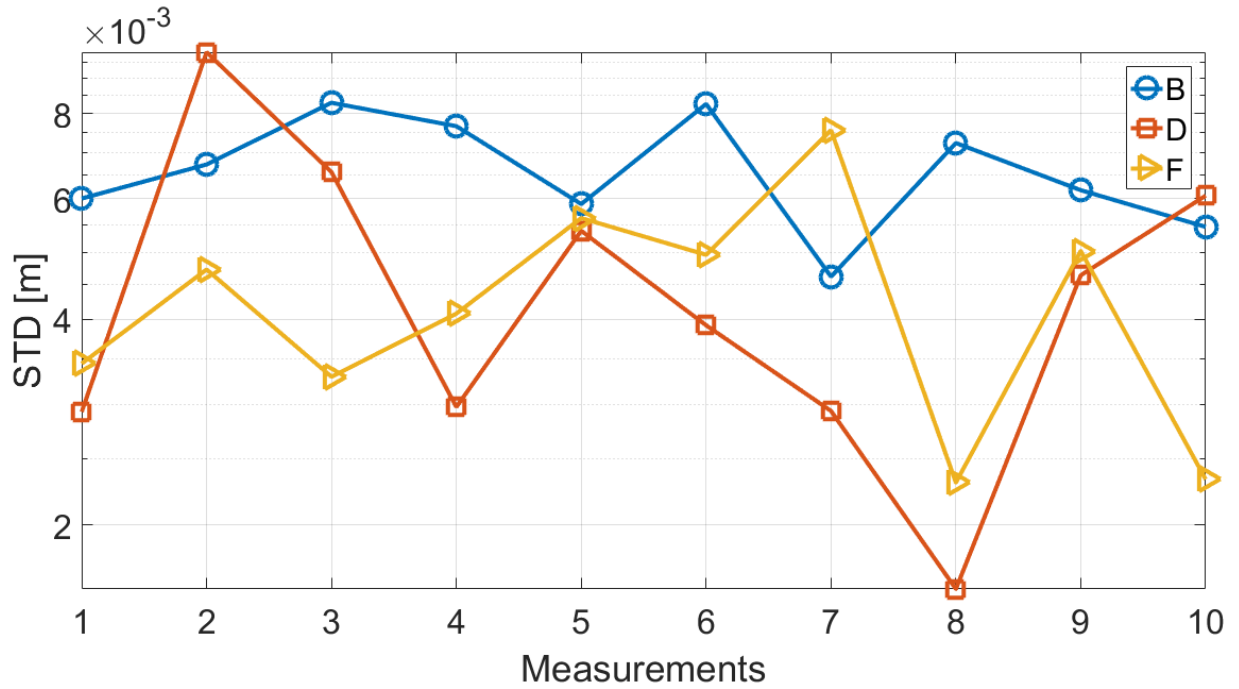


Figure 4.18: System precision for the subset {B, D, F}.

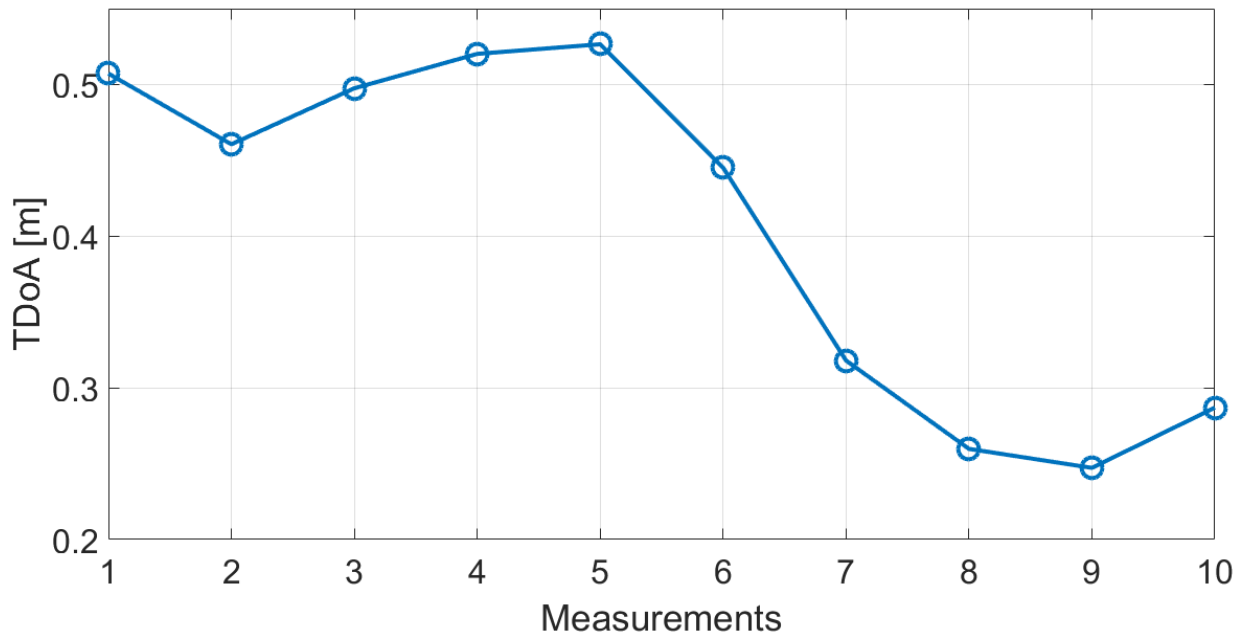
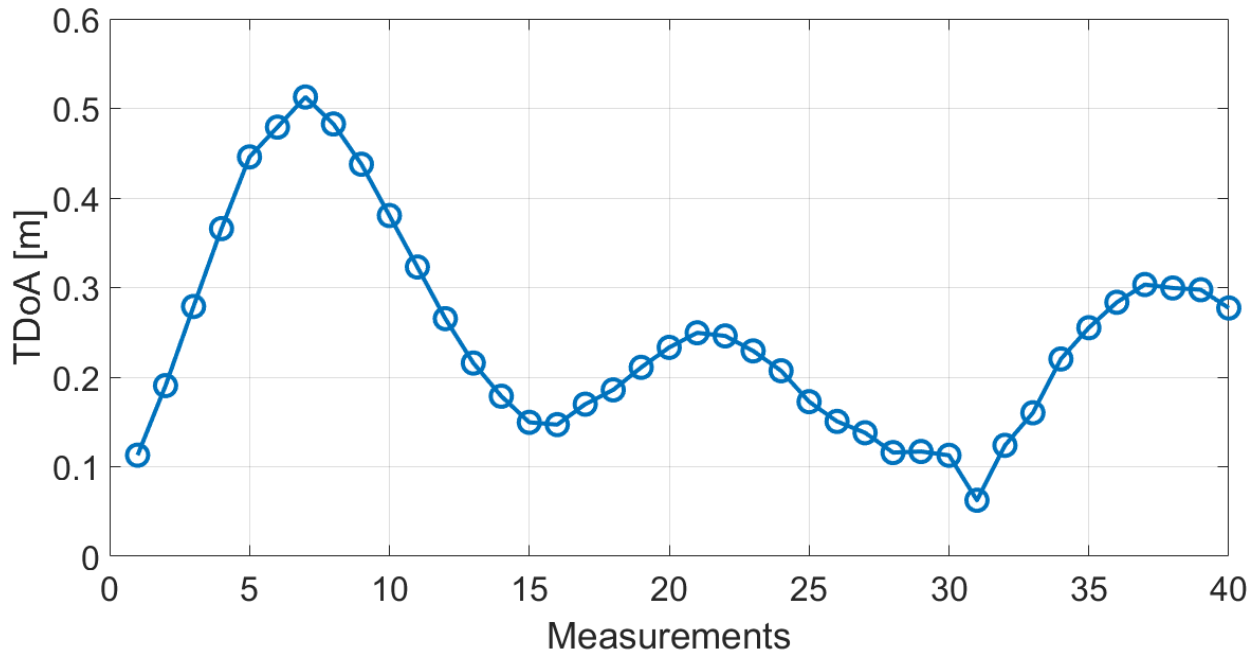


Figure 4.19: TDoA between the receiver 1 and the receiver 2 evaluated for the subset A.

This problem is more visible if the transmit antenna is moved in the same previous range with a step of 0.5 cm, as depicted in the graph below.



**Figure 4.20:** TDoA between the receiver 1 and the receiver 2 evaluated for the subset A. The antenna is moved with steps of 0.5 cm.

The system was tested in a very harsh indoor environment as the laboratory. The presence of walls, desks, metallic door, and so on, very close to the receivers, generate multiple reflections of the signal that affect the system measurements. Moreover, the microstrip patch antenna has a very low directivity and, thus, it receives signals generated from any angle or direction without significant attenuation.

To deeply study this problem and find an appropriate solution, the receivers are placed close to the metallic door of the laboratory. The transmit antenna is placed to a distance of 3m from the receivers and it is moved from left to right with steps of 0.5 cm. Two sets of measurements are performed: in the first one the doors are opened, while in the second one, the doors are closed.

Note from the Figure 4.21 that multipath, in a severe indoor environment, significantly affects the measurements extracted by the proposed system. When the doors are closed, signal reflections are generated and received by the patch antenna. As mentioned in the model description, the presence of the multipath echoes introduces a shift in the peak of the cross-correlation function in time domain, and, a phase distortion of the subcarriers in frequency domain.

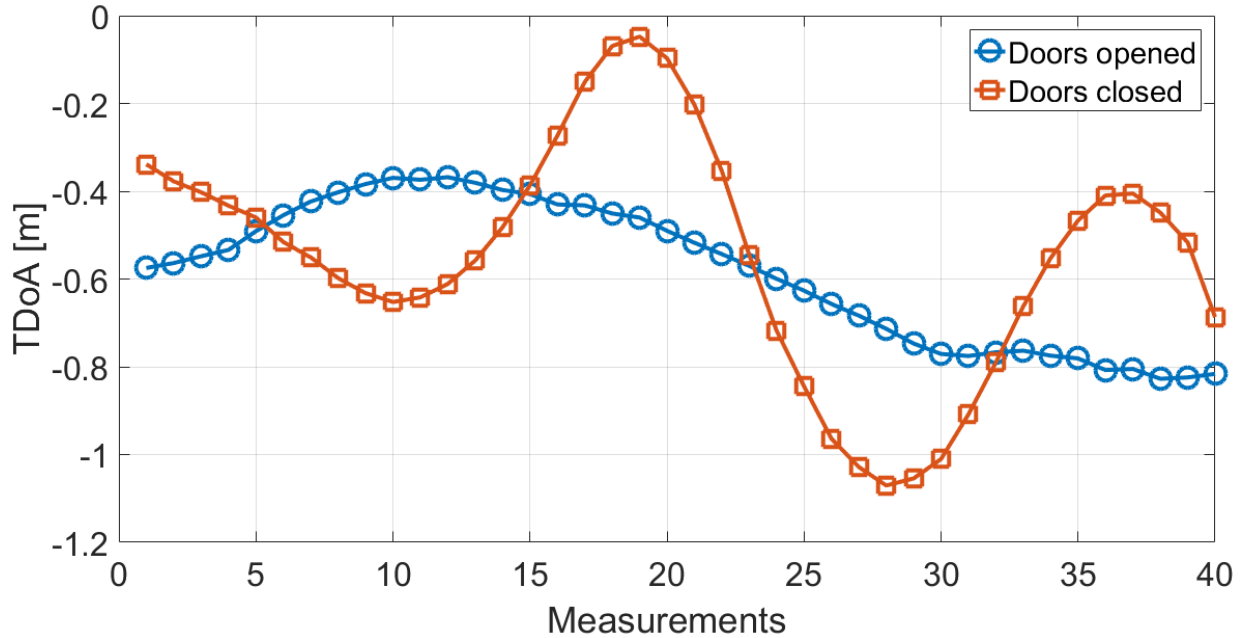


**Figure 4.21:** TDoA between the receiver 1 and 2 in presence of a metallic doors.

Hence, the multipath reflections must be reduced placing the system far away from metallic objects and floor or ceiling and, also, the directivity for both the transmit and receive antenna must be reduced as well. As mentioned, the microstrip patch antenna exhibits a very low directivity for both the horizontal and the azimuthal planes. Hence, any interference or multipath reflection is received by the antenna without a significant attenuation especially in indoor environment. One possible solution to reduce the effects of the low antenna directivity is to increase the antenna dimension. For the patch antenna, the size can be increased realizing an array of patch where the electric and magnetic field of each element is constructively combined to obtain a single directivity diagram. Figure 4.22 shows the 2x2 array patch designed to improve the performance of the system. It was chosen a corporate feed network to obtain a compact design on the same board of the antennas. The size of the array is 8.5cm x 8.5 cm, and, it exhibits a gain of 10 dB with 48° of directivity in azimuthal plane and 56° in horizontal plane. In Figure 4.23 are represented the directivity diagrams for the array designed while in Figure 4.24 is represented the input matching measured compared with the simulations performed with Keysight ADS. The final array has a bandwidth of 100 MHz, measured as 9 dB input matching, with a center frequency of 3.35 GHz. It should be noted that the antenna measurements and the CAD simulations perfectly matches. The antenna array is made on the RO4003C substrate with a thickness of 1.52 mm and a dielectric constant of 3.38.

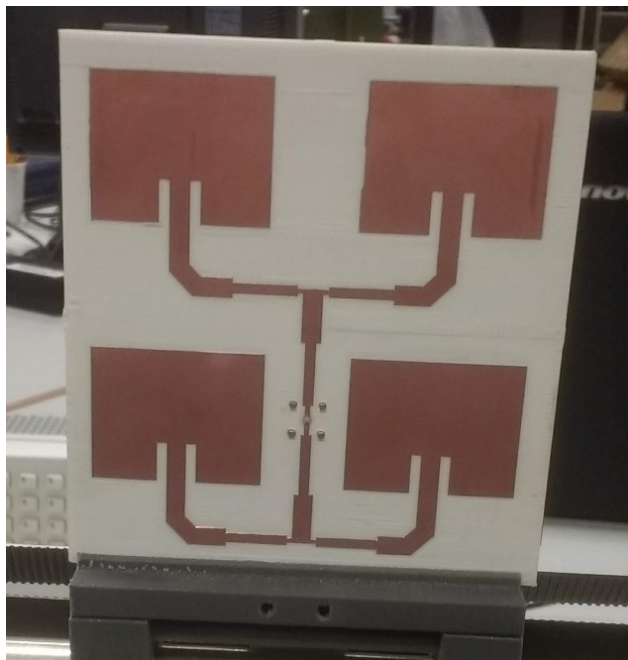
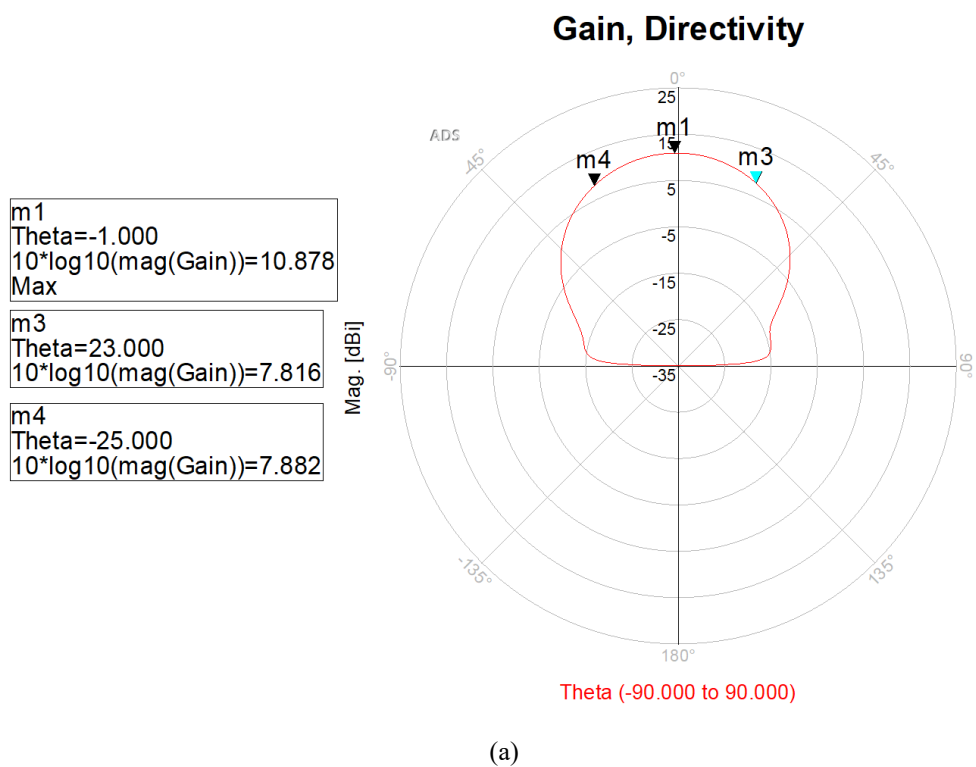
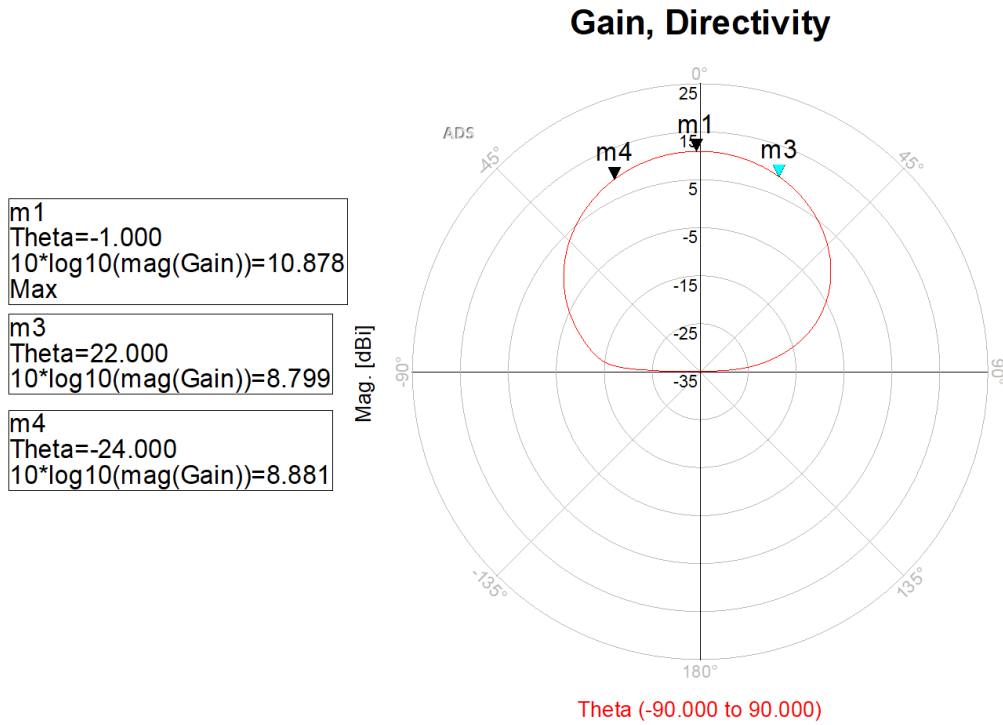


Figure 4.22: Array 2x2 of microstrip patch antennas with corporate fed network.





(b)

Figure 4.23: Array of 2x2 of microstrip patch antennas directivity diagram (a) azimuthal plane (b) horizontal plane.

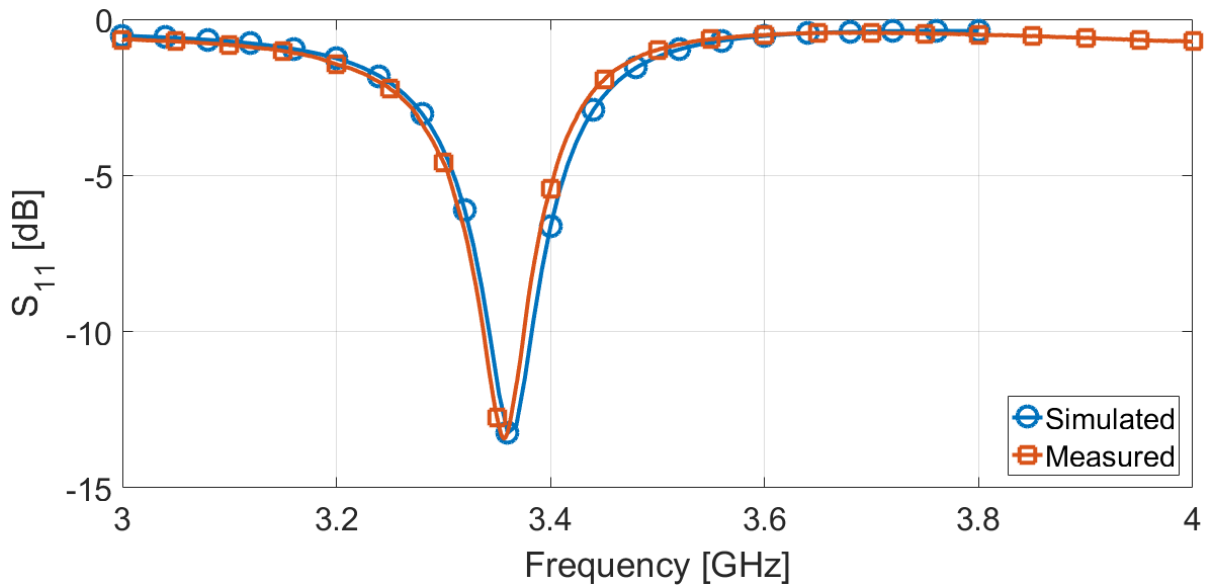
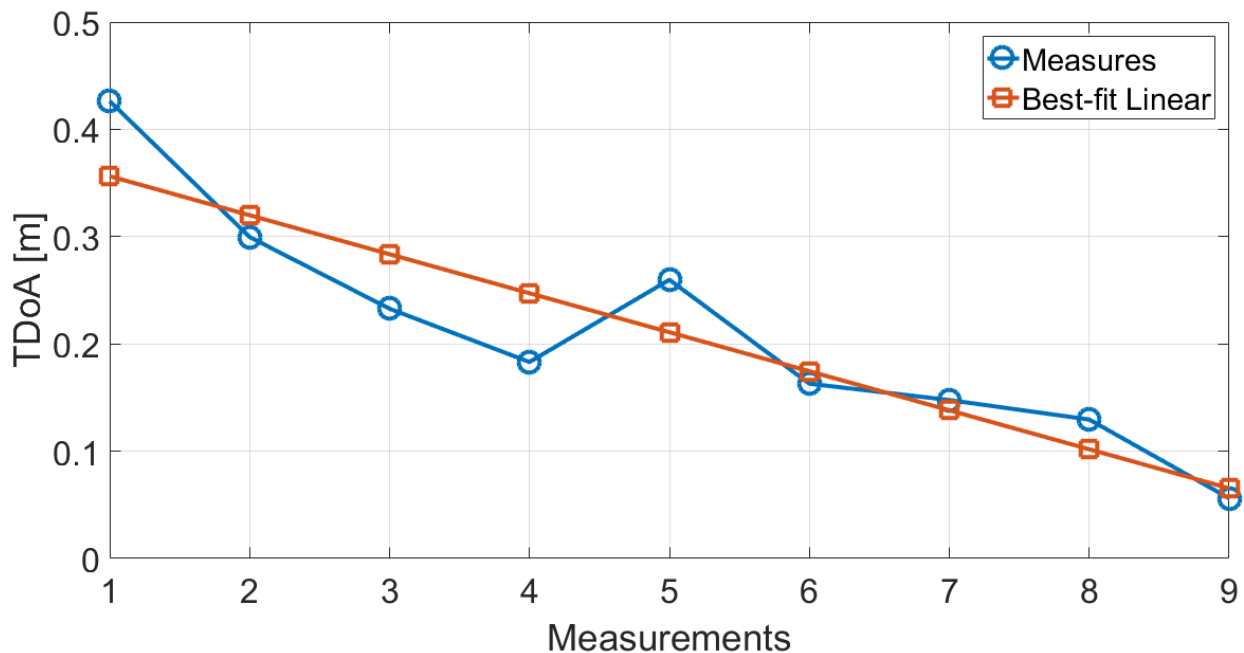


Figure 4.24: Array of 2x2 of microstrip patch antennas input matching.

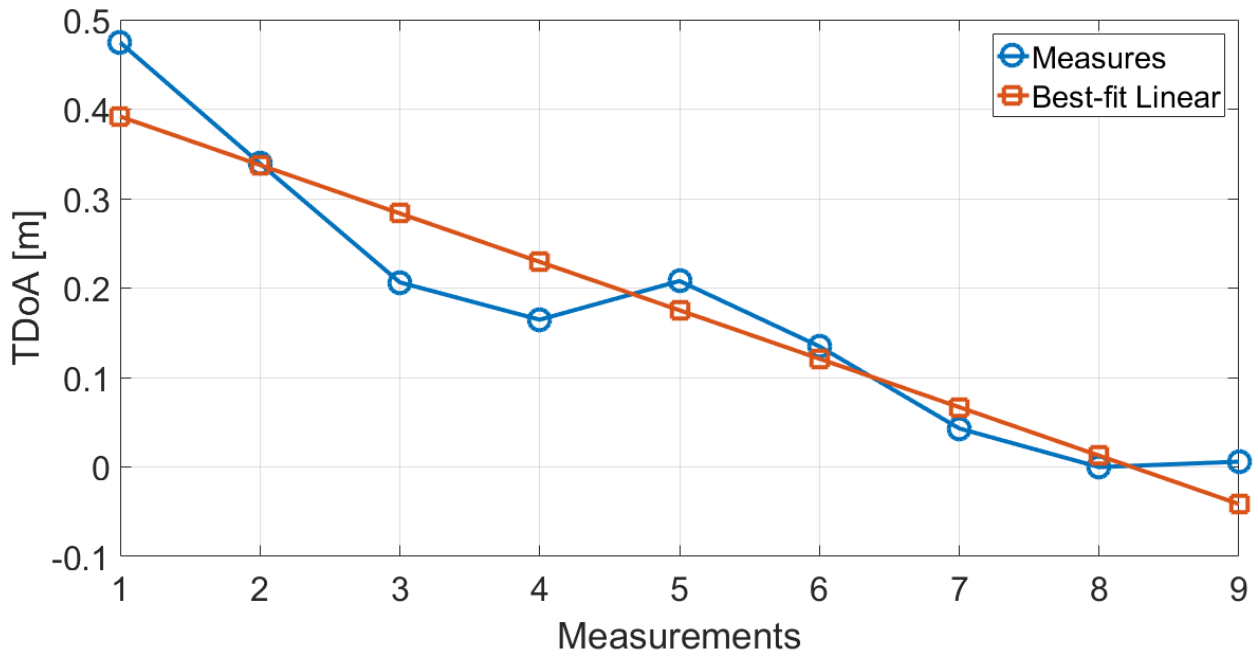
### 4.3.4 Test-bench #3

A new set of tests were performed using the antenna array for both transmitter and receivers. The transmit antenna was mounted on a metallic bar 1.50 meters long and it is moved from left to right

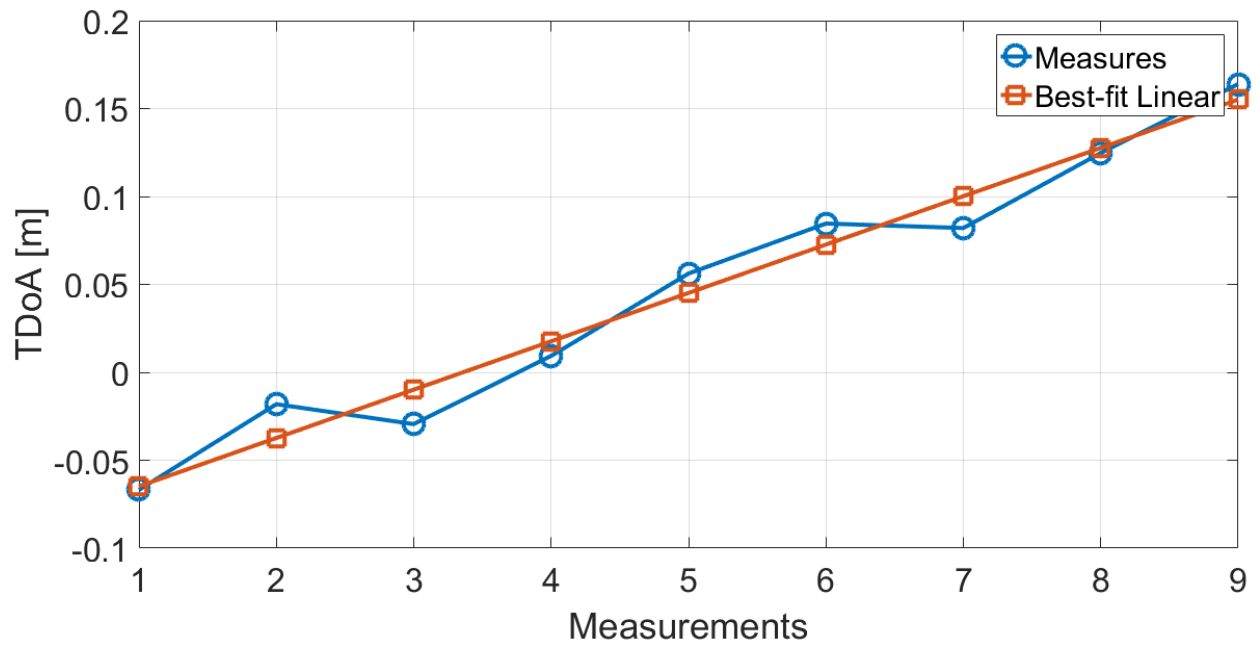
with 10 cm steps. Finally, the transmit antenna is placed 3m far away from the receivers, and to evaluate the distances the system uses a 64-length OFDM symbol with 100 MHz of signal bandwidth. At the receiver-side 10 signal periods are acquired with a sampling time of 1GSPS. In Figure 4.25 are reported the distance estimates for the three receivers using the receiver number 1 as system origin. It should be noted that the use of the patch antenna array for both the transmitter and the receivers significantly increase the performance of the proposed system. In fact, the TDoA measurements fit the model of the system and now they can be best approximated by a linear function. However, increasing the directivity of the antenna, the localization region is reduced as well. In other words, when the target is placed in a position that is not covered by the directivity diagram of the constellation receivers, its localization may be not possible or not accurate. This problem is more evident in indoor environment where the distances are limited by the size of the room (5m ÷ 10m). In outdoor applications this problem is less appreciable because the target can be moved for long distances. Moreover, in outdoor applications, the multipath has less influence on the system because the absence of walls, obstacles, floor, and so on generates a lower amount of signal reflections. Hence, in these applications is not necessary to use an antenna with a narrow directivity.



(a)



(b)



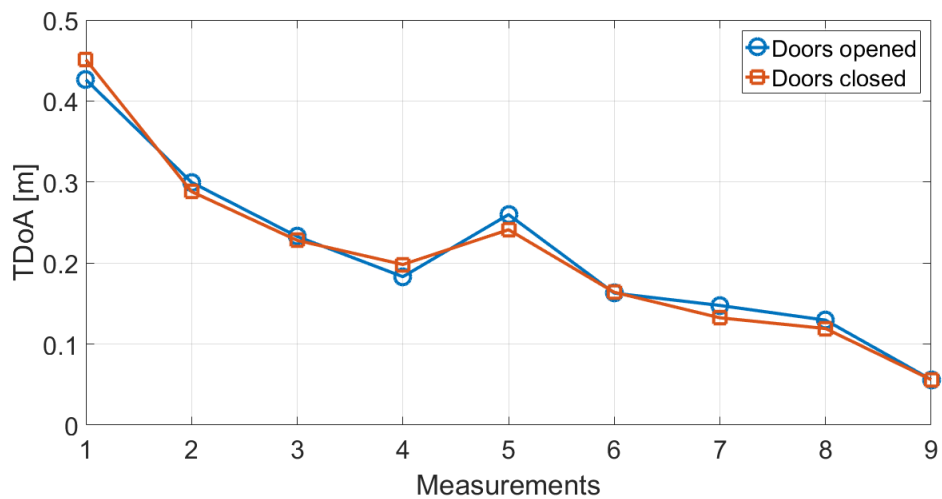
(c)

**Figure 4.25:** TDoA estimates using the patch antenna array for bot transmitter and receivers (a) Rx<sub>1</sub> vs Rx<sub>2</sub> (b) Rx<sub>1</sub> vs Rx<sub>3</sub> (c) Rx<sub>1</sub> vs Rx<sub>4</sub>.

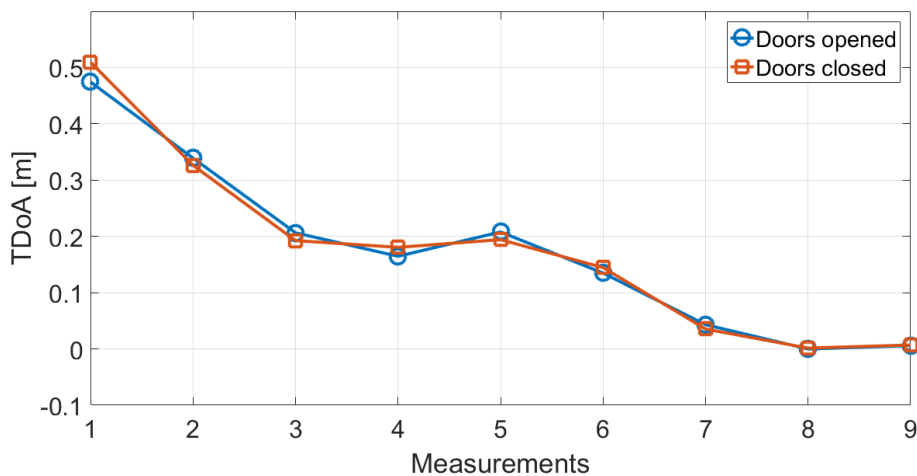
From the analysis of the results, the multipath reflections have less impact on the distance measurements. To validate the results, it is repeated the test of the receivers placed close to the metallic doors. The system transmits a 64-length OFDM symbol with 100 MHz of bandwidth and

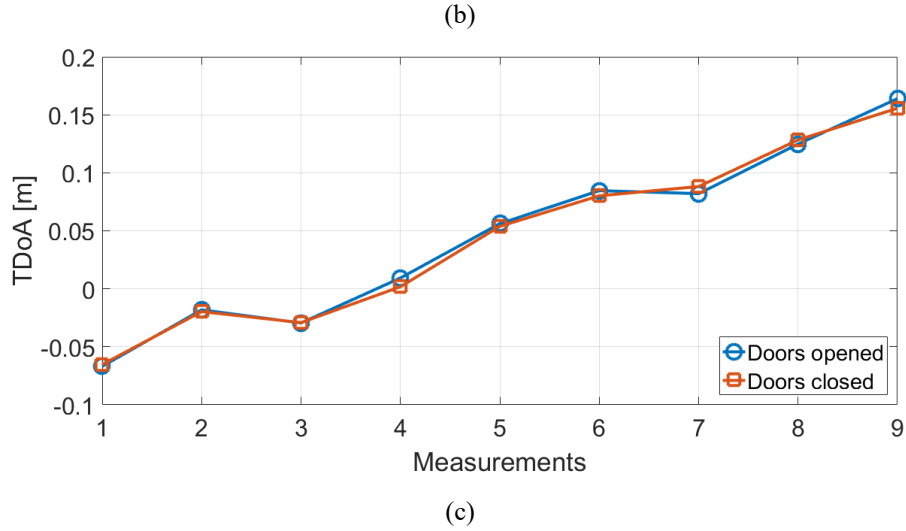
use the patch antenna array for both the transmitter and the receivers. At the receiver-side it is acquired 10 signal periods with a sampling time of 1GSPS.

Figure 4.26 illustrates the distance estimates computed by the proposed system for the three receivers taking the receiver number 1 as system origin. It should be noted that with the use of the patch antenna array for both the transmitter and the receivers has removed the multipath reflections introduced by the metallic port close to the receivers. In fact, it is out of the range of the antenna directivity diagram and so the reflections don't reach the receivers. However, note from Figure 4.26(a) the fifth TDoA measure between the receiver 1 and 2 is affected by an error due the presence of other obstacles in laboratory near these two receivers. Hence, the multipath still affects the distance measurements and it must be mitigated before to evaluate the target position. The only solution possible is to further increase the number of the array element to reduce the directivity diagram.



(a)





**Figure 4.26:** TDoA estimates using the patch antenna array for bot transmitter and receivers. The receivers are placed close to the metallic doors (a) Rx<sub>1</sub> vs Rx<sub>2</sub> (b) Rx<sub>1</sub> vs Rx<sub>3</sub> (c) Rx<sub>1</sub> vs Rx<sub>4</sub>.

## 4.4 Conclusions

The proposed indoor positioning system exploits the Software Defined Radio Architecture to evaluate the position of an active target. The system comprises four receivers and a single transmitter that sends an OFDM symbol composed by only pilot subcarriers. The absence of data and the SDR architecture leads to a system scalable and feasible to the design requirements in terms of precision and accuracy. In fact, different versions of the transmit signal as function of the number of subcarriers or the root index of the ZC sequence can be generated in digital domain only the first time. One of them can be selected with a simple software instruction without modify the analog hardware of the system. Moreover, the distance and so the target position is computed in digital domain without analog hardware processing. Hence different signal processing techniques can be implemented to improve the overall performance of the system.

To validate the proposed solution, it was tested in severe multipath conditions and using a microstrip patch antenna. The results have demonstrated the high precision achieved by the proposed system in the distance estimation. In fact, it results lower than 1 cm for different distance values. However, the measurements are not accurate due to the presence of the multipath reflections generated by the presence of the obstacles of the indoor environment. These reflections introduce echoes in the channel impulse response that can be not eliminate by the echo cancellation algorithm described in the chapter three because they have a distance lower than the breakdown distance.

To improve the system accuracy, a 2-D microstrip patch antenna array composed by four elements was designed. The use of this antenna with a narrow directivity diagram for both the transmitter and the receivers improves the overall performance of the system because it reduces the multipath reflections. However, for harsh indoor environments, the directivity diagram of the antenna must be reduced to remove the multipath influence on the distance estimates.

To improve the performance of the proposed system and maintains compact size, the LO frequency will be increased. A 2-D antenna array with 16 elements with a narrow directivity will be designed to evaluate the distance between receivers placed in a harsh environment as the laboratory.

Once removed the multipath influence on the distance estimates the target position will be evaluated.

In chapter 5 will be discussed the design of the integrated circuits for the first two blocks of the analog front-end: the low-noise amplifier and the down/up conversion mixer. A novel design strategy will be presented and implemented based on the well-known  $g_m$  over  $I_D$  methodology. The blocks will be designed to cover a wide-band of frequencies as required by the Software Defined Radio architecture.

## 5 Indoor Positioning System: Integrated Circuit Design

The proposed indoor positioning system exploits the Software Defined Radio (SDR) architecture to obtain a system scalable and feasible with the simplest hardware architecture. With simple software changes, the system is able to adapt its characteristics as function of the design requirements in terms of precision and distance accuracy. The analog front-end for both the transmitter and the receiver should be designed for large signal bandwidth operations to allow the changes in the signal properties.

This chapter is focalized on the design of the integrated circuits for the two main blocks of the transmitter and the receiver chain: the Low-Noise Amplifier (LNA) and the up/down conversion mixer. Moreover, for both, it introduces a novel synthesis procedure, based on a systematic design methodology, that facilitates the design procedure and is able to extract the best performance of the circuit consuming less time than the traditional approaches. The blocks are designed using the IHP SiGe process technology with a MOS channel length of 130 nm.

### 5.1 Systematic Design Approach

The traditional design approaches are based on the square law model for the drain current in saturation region ( $I_{D,sat}$ ):

$$I_{D,sat} = \frac{1}{2} \mu_n C_{ox} \frac{W}{L} (V_{GS} - V_{TH})^2 \quad (5.1)$$

where  $\mu_n$  is the electrons mobility,  $C_{ox}$  is the gate oxide capacitance, the  $W/L$  is the ratio between the width and the MOS channel length,  $V_{GS}$  is the gate-source voltage and, finally,  $V_{TH}$  is the MOSFET threshold. Given the continuous shrinking of the channel length of the MOSFETs employed in today's integrated circuits, the equations (5.1) become grossly inaccurate. With the current nanometer channel lengths, several second order effects are no longer negligible and must be considered [64]. One of the most common second-order effects is the Channel Length Modulation (CLM). The change of the drain-source voltage  $V_{DS}$  causes the depletion region to vary and, also, changes the effective channel length. This variation can be indicated with  $\delta L(V_{DS})$  and the current  $I$  is inversely proportional to the channel variations:

$$I \propto \frac{1}{L - \delta(V_{DS})} \approx \frac{1}{L} \left( 1 + \frac{\delta(V_{DS})}{L} \right) \rightarrow \frac{I_{DS}}{I_{DS_0}} = (1 + \lambda V_{DS}) \quad (5.2)$$

where  $\lambda$  is the channel modulation that allows to take in account the channel length variations as function of the drain-source voltage. Another important aspect that should be included in the MOSFET model regards the threshold voltage. In fact, it goes down with the increasing of the drain voltage. This effect is called Drain Induced Barrier Lowering (DIBL) and it can be modeled [65]:

$$V_{TH} = V_{TH0} - \eta V_{DS} \quad (5.3)$$

The expression above allows to consider the variations of the threshold from its nominal value  $V_{TH0}$  as function of the drain-source voltage through the factor  $\eta$ . Moreover, the source and the substrate of the MOSFET formed a P-N diode. At high electric field, some moving electrons may have enough energy (hot electrons) and will knock off electrons of Si lattice to create currents and eventually cause junction to break down (avalanche breakdown). This is called Substrate Current Body (SCBE). In other words, if we push drain voltage to a high enough level, the drain current  $I_D$  (not  $I_{DS}$ ) and substrate current will suddenly increase. If device operated in SCBE dominated region for a long time, the electrons may be trapped in the gate oxide and create defects and cause long term problem. From the analog circuit designers stand point, the SCBE may lower the output resistance so operating MOSFET in SCBE region is probably not a good choice.

These are only the main second-order effects that are more evident with the decrease of the MOSFET dimension. The model used for describing the MOSFET behavior includes several hundred parameters, thus, it results too complicated to come up with a simple abstraction for different analog circuits. Moreover, there is not a unified treatment model for all operating regions of the MOSFET. When  $V_{GS} \leq V_{TH}$  the current does not go to zero and the device is in the sub-threshold region. The current in or near the sub-threshold region have an exponential expression, this is because the transistor itself forms a lateral BJT. The sub-threshold or weak inversion current is dominated by the diffusion current and it has an expression similar to the BJT current equation:

$$I_{DS} = \frac{W}{L} I_{DS,0} e^{\frac{q(V_{GS}-V_{TH})}{nkT}} \left( 1 - e^{-\frac{qV_{DS}}{kT}} \right), n > 1 \quad (5.4)$$

where  $k$  is the Boltzmann and  $q$  is the charge of the electrons measured in Coulomb.

The non-ideal factor of channel control,  $n$ , varies with bias, the typical value for  $n$  is around 1.5. The MOS device in weak inversion region is usually slow, because very small current drives a large gate-source capacitor,  $C_{GS}$ . In the weak inversion region, the  $V_{TH}$  matching is poor, and the model is not well defined. On contrary, if the transistor operates in strong inversion it consumes

more power than the weak inversion but exhibits the best performance in terms of speed. The region in the middle between strong and weak inversion is named moderate inversion and due to the shrinking of the supply voltage in modern applications, it became more attractive for the designer. In fact, in this region the transistor can achieve the best tradeoff between speed and DC-power consumption. However, no closed form equation exists for this operating region and some models such as EKV uses weak and strong inversion equations to interpolate the moderate inversion region. The EKV models or BSIM models are too complicated to generate any close form equations for traditional hand analysis.

Using a table-based approach, as the  $g_m/I_D$  method, is more convenient, both in terms of design time and accuracy of the results. To use this method, a series of lookup tables are generated, starting from the DC-analysis of the transistor. On a second step, different width-independent figures of merit, intimately linked to the design specifications, can be extracted and the designer can choose the correct inversion region for the various MOSFETs and determine the W/L ratios necessary to match the required design specifications. The  $g_m/I_D$  ratio, a.k.a. transconductance efficiency, allows to define the inversion region for the transistor. Using the square law model of the MOSFET when it operates in saturation region, the transconductance  $g_m$  is defined by:

$$\begin{aligned}
 g_m &= \mu_n C_{ox} \frac{W}{L} \sqrt{\frac{2I_{DS}}{\mu_n C_{ox} \frac{W}{L}}} \\
 g_m &= \sqrt{2\mu_n C_{ox} \frac{W}{L} I_{DS}} \propto \sqrt{I_{DS}} \\
 g_m &= \frac{1}{2} \mu_n C_{ox} \frac{W}{L} (V_{GS} - V_{TH})^2 \frac{1}{\frac{1}{2} (V_{GS} - V_{TH})} \\
 g_m &= \frac{2I_{DS}}{(V_{GS} - V_{TH})}
 \end{aligned} \tag{5.5}$$

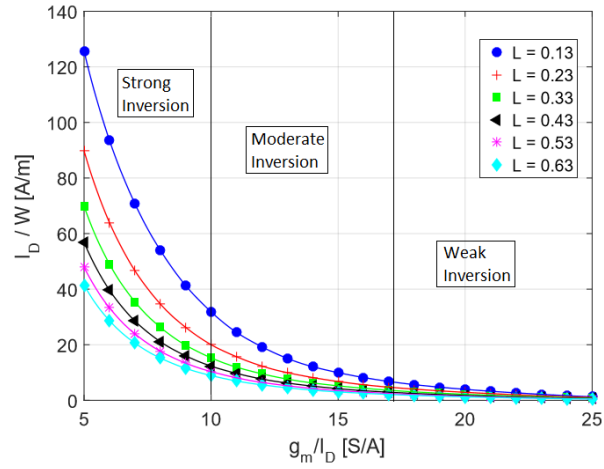
Hence the ratio  $g_m$  over  $I_D$  depends only by the overdrive voltage  $V_{OV} = V_{GS} - V_{TH}$  that define the operating region of the MOSFET. The strong inversion occurs for values of  $g_m/I_D$  in the 5-8 S/A range, while for larger values (in the 20-25 S/A range) the transistor operates in weak inversion. The choice of the inversion region is essentially determined by the trade-off between speed (transit frequency,  $f_T = g_m/C_{GG}$ ), intrinsic gain ( $g_m/g_{DS}$ ) and efficiency ( $g_m/I_D$ ) and depends on the target application. In strong inversion, the transistor exhibits higher speed than in weak inversion, but

the intrinsic gain is lower. Furthermore, in strong inversion, the drain current is higher and so the transistor dissipates more power than in the other regions. In weak inversion, that is, for an increased  $g_m/I_D$  ratio, the intrinsic gain increases, while the  $f_T$  decreases. This is due to the fact that the width of the transistor, and so its total intrinsic capacitances, are increased. Finally, the drain current decreases for increasing values of  $g_m/I_D$ , which means that the DC power consumption drops. The region in the middle between strong and weak inversion is defined as moderate inversion and usually shows a good compromise in terms of speed, gain and power consumption. Figure 5.1 shows the graphs for transit frequency, intrinsic gain and  $I_D/W$  ratio versus  $g_m/I_D$  for the NMOS transistor valid for the IHP process used. The curves are sketched for different channel lengths,  $L$ , and for a drain-source voltage,  $V_{DS}$ , equal to half the DC-power supply,  $V_{DD}$ . The  $g_m/I_D$  design method is both scalable and easily adaptable to the design of different target systems. These charts represent the starting point for implementing a design approach related to a specific analog block. The resulting design flow provides the designer with the flexibility to start by choosing any of the tabulated figures of merit as his primary objective and then proceed by systematically extracting all other features depending on the specific performances to be optimized.

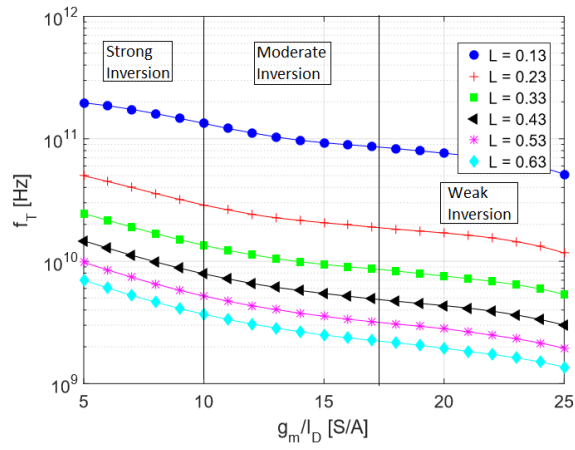
## 5.2 Low Noise Amplifier Design

According to the specifications imposed by the Federal Communications Committee (FCC), the UWB transmitted signal must be characterized by a very wide bandwidth ( $> 500$  MHz), allocated in the 3.1-10.6 GHz frequency range and with a power density of  $-41$  dBm/Hz [22]. The need for a Low Noise Amplifiers (LNA) with flat gain over a wide frequency band is imperative to increase the very limited power of the UWB signal received by the antenna.

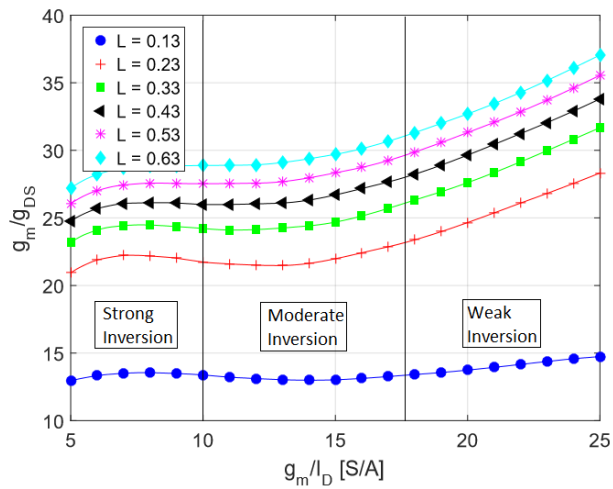
Distributed Amplifiers (DA) were first introduced by Percival in 1936 [66] and are very attractive for UWB applications due to their flat gain over a large bandwidth and to their good matching performances.



(a)



(b)



(c)

**Figure 5.1:** (a)  $I_D/W$  vs.  $g_m/I_D$  (b) transit frequency  $f_T$  vs.  $g_m/I_D$  (c) intrinsic gain  $g_m/g_{DS}$  vs.  $g_m/I_D$  for the IHP 0.13  $\mu\text{m}$  process.

A conventional DA is composed by several MOSFETs with the gates and the drains connected through two transmission lines. Unfortunately, in a CMOS process the routing interconnections have typical lengths in the order of a few hundreds of microns so they cannot be used as transmission lines for frequencies below 30 GHz. In a monolithic integrated DA, the transmission lines are artificially implemented with ladders of reactive lumped-element (see Figure 5.2).

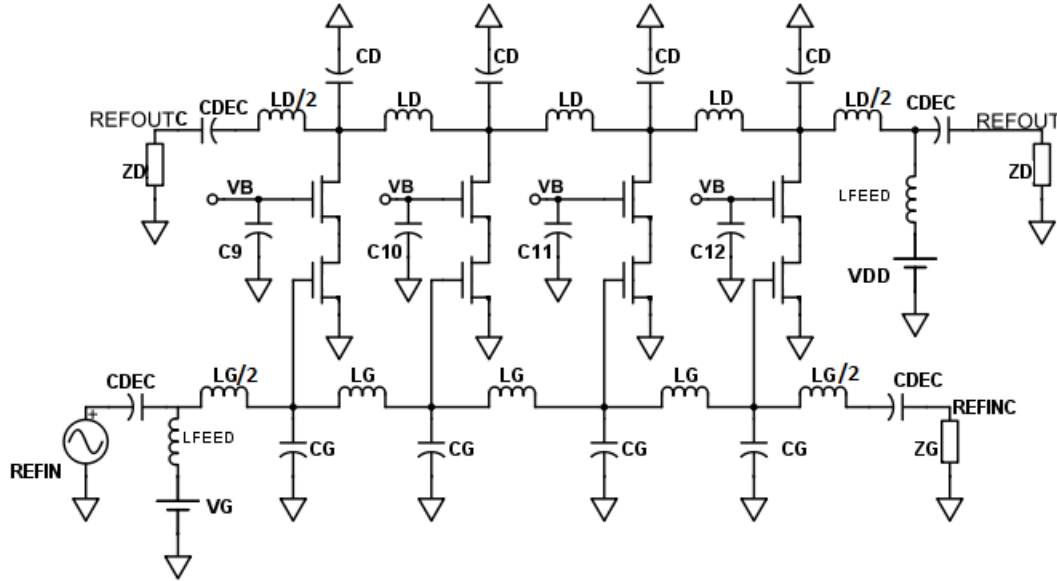


**Figure 5.2:** Architecture of a conventional four stages Distributed Amplifier.

The major drawback of DAs is the upper bound on the achievable voltage gain caused by the losses of the transmission lines. The achievable voltage gain is given by:

$$G = \frac{N g_m Z_0}{2} \quad (5.6)$$

where  $g_m$  is the transconductance of the transistors,  $N$  is the number of stages and  $Z_0$  is the common value of the characteristic impedance for the drain and the gate lines. Theoretically, according to (5.6) the gain is proportional to the number of DA stages, but due to the losses of the lines, namely  $A_D$  and  $A_G$ , the number of DA stages is upper bounded by an optimal value,  $N_{opt}$ , that can be expressed by the following relationship:

$$N_{opt} = \frac{\ln(A_D/A_G)}{A_D - A_G} \quad (5.7)$$

In literature, different techniques and ad hoc circuit architectures have been introduced to improve the various performance metrics of the amplifier, including gain [67]-[68], noise figure [69], power consumption [70] and input/output matching [71]. Each of these methods relies on a very specific

transistor size. Typically, the size of the MOSFETs is determined by the value of  $g_m$  required to achieve the target gain.

Alternatively, instead of improving only a single performance metric one can design the DA to optimize the tradeoff between all DA parameters (gain, noise figure, input/output matching and DC power consumption) by applying the  $g_m/I_D$  methodology [64]. This dissertation describes a new systematic approach to design a conventional DA that achieves an optimal tradeoff between the design specifications. The approach requires generating a series of lookup tables that exploits the  $g_m/I_D$  methodology.

The  $g_m$  over  $I_D$  methodology was exploited for developing a framework that can be used to assist designers in optimizing the design of a conventional DA. The framework was entirely implemented in MATLAB and it takes the design requirements as inputs and returns the transistors and DA parameters that optimally match the specifications, as outputs. The design flow implemented by the proposed framework is illustrated in Figure 5.3. Starting from the gain and bandwidth specifications, the minimum and maximum number of DA sections are computed. The maximum number of stages must be lower or equal to the optimum value defined in (5.7). At this point, the tool extracts a feasible range of  $g_m$  values as function of the number of stages, gain and bandwidth. The lower bound of the range can be calculated from (5.6). This is the minimum  $g_m$  that allows achieving the desired gain. The upper bound can be computed based on the maximum desired bandwidth. Since both transmission lines must exhibit equal propagation properties the following synchronism condition must hold true:

$$L_G C_{GG} \approx L_D C_{DD} \quad (5.8)$$

where  $C_{GG}$ ,  $C_{DD}$ ,  $L_G$ ,  $L_D$  are respectively the total gate and drain capacitances and inductances for the MOSFET. Moreover, the two lines must have the same characteristic impedance:

$$Z_G = \sqrt{\frac{L_G}{C_G}} = Z_D = \sqrt{\frac{L_D}{C_D}} \quad (5.9)$$

Under these conditions, the bandwidth can be computed according to the equation below:

$$BW \cong \min \left( \frac{1}{\pi} \sqrt{\frac{1}{C_{GG} L_G}}, \frac{1}{\pi} \sqrt{\frac{1}{C_{DD} L_D}} \right) \quad (5.10)$$

For the n-channel MOSFET included in the IHP process,  $C_{GG}$  is greater than  $C_{DD}$ , so the bandwidth is limited by the value of total gate capacitance. For example, a bandwidth of 15 GHz corresponds

to a total gate capacitance of 409.38  $fF$  imposing an inductance value of 1.1 nH. From the value of  $C_{GG}$ , performing a DC-analysis, the method computes the maximum  $g_m$  that allows achieving the desired bandwidth. For each  $g_m$  in the range, the method computes the transistor parameters under different inversion regions, by applying the  $g_m/I_D$  methodology. In this step, to obtain the highest possible value of transit frequency (see Figure 5.1), minimum channel length is assumed in all inversion regions.

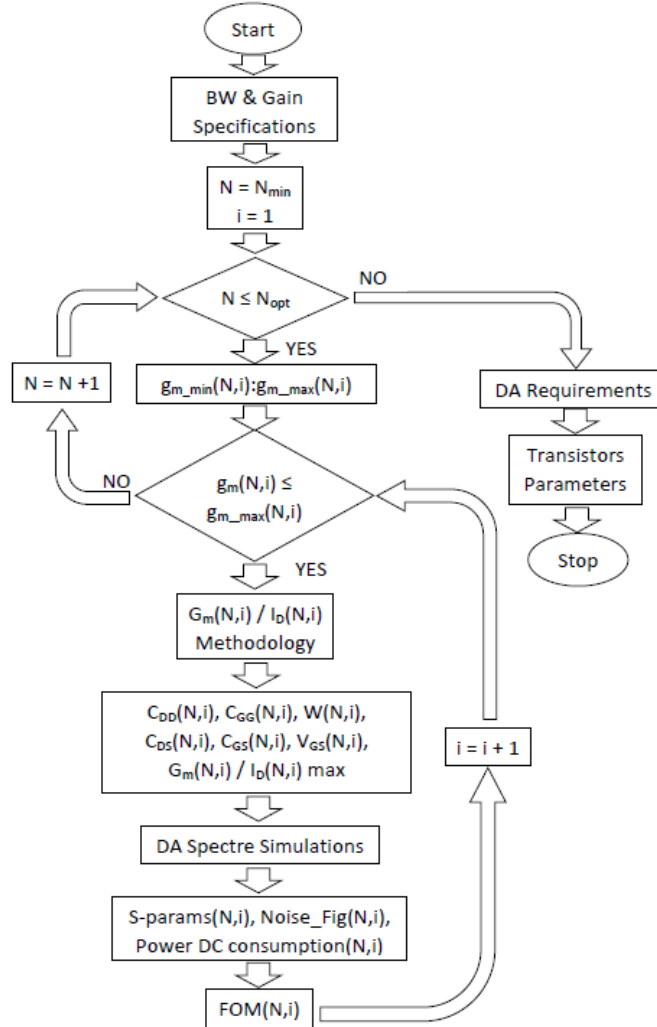


**Figure 5.3:** Design Framework's Flow Chart.

As mentioned, in weak inversion the transistors exhibit a DC- power consumption lower than in strong inversion. However, for a fixed channel length ( $L$ ), the width ( $W$ ) of the MOSFET increases and so do the intrinsic capacitance  $C_{GG}$  and  $C_{DD}$  (see Figure 5.4). The framework computes, for each  $g_m$ , the maximum value of the  $g_m/I_D$  ratio that satisfies the bandwidth specification.

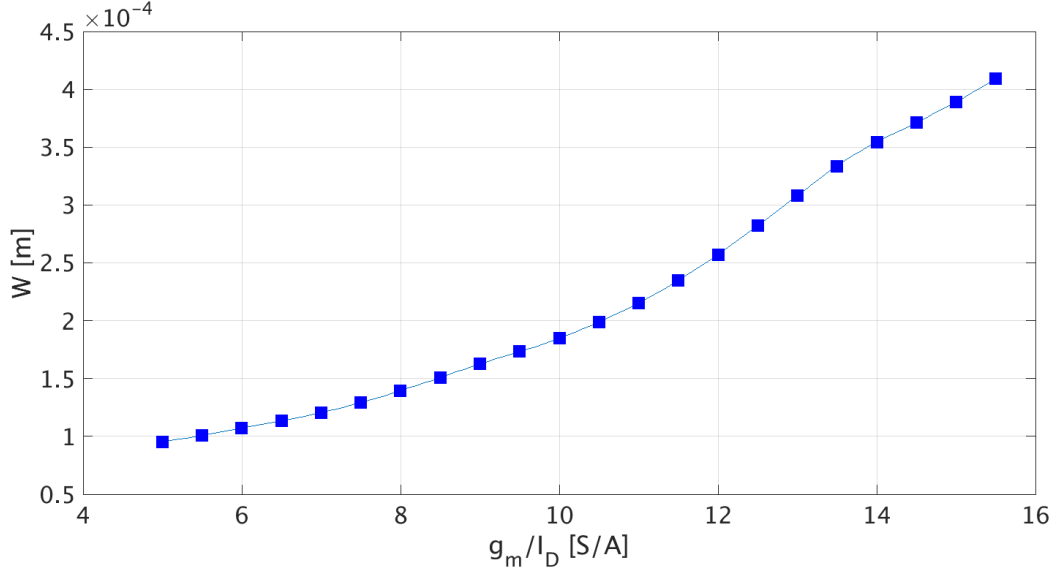


**Figure 5.4:** Transistor widths as function of  $g_m/I_D$  for a  $g_m$  of 60 mS.

At the end of this step, the method generates a vector with the transistor parameters ( $W/L$  ratio, DC-bias voltage, extra gate-source and drain-source capacitances) determined as a function of the  $g_m/I_D$  ratio. The resulting values are used by the algorithm to perform a series of SPECTRE simulations and extracting the DA S-parameters, the noise figure and the DC power consumption, as a function of  $N$  and  $g_m/I_D$  (see Figure 5.5). These characteristics can be used for calculating the Figure of Merit (FOM) of the DA. The designer can define any suitable FOM according to its own specifications. However, in the proposed DA design the FOM is expressed as in [71]:

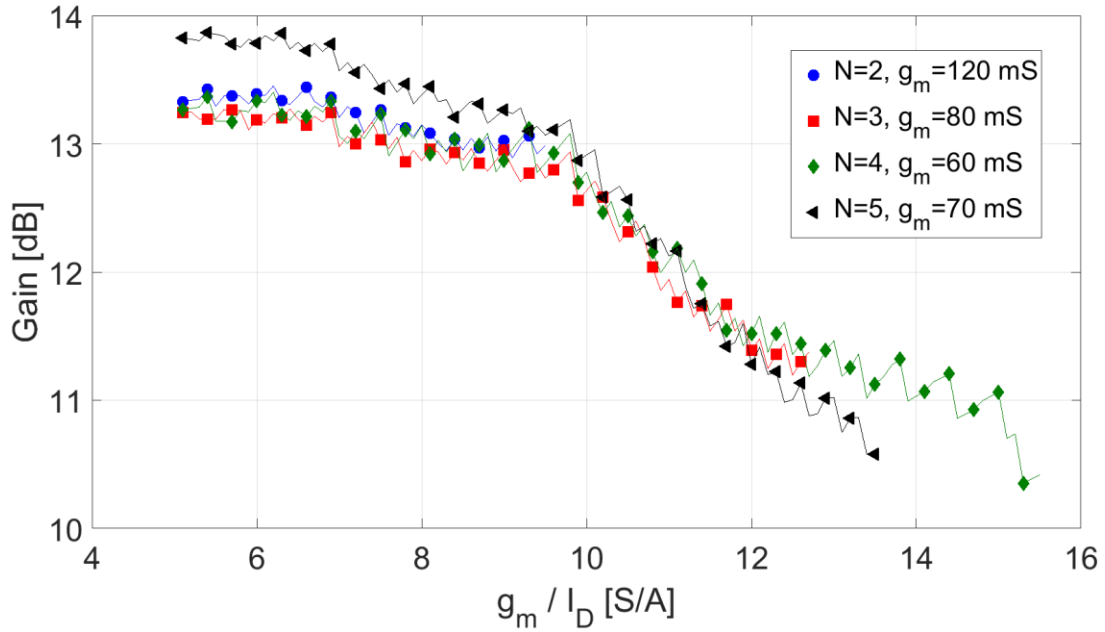
$$FOM_{1[GHz/mW]} = \frac{S_{21[dB]} \cdot BW_{[GHz]}}{NF_{[dB]} P_{DC[mW]}} \quad (5.11)$$

where  $BW$  is the bandwidth,  $NF$  is the average noise figure,  $P_{DC}$  is the total DC power consumption and  $S_{21}$  is the transducer gain of the DA expressed in decibel. The FOM is a quality index that describes the trade-off between gain,  $BW$ , noise figure and DC power consumption achievable by the DA. Hence, higher FOM values indicate a better trade-off between these parameters.

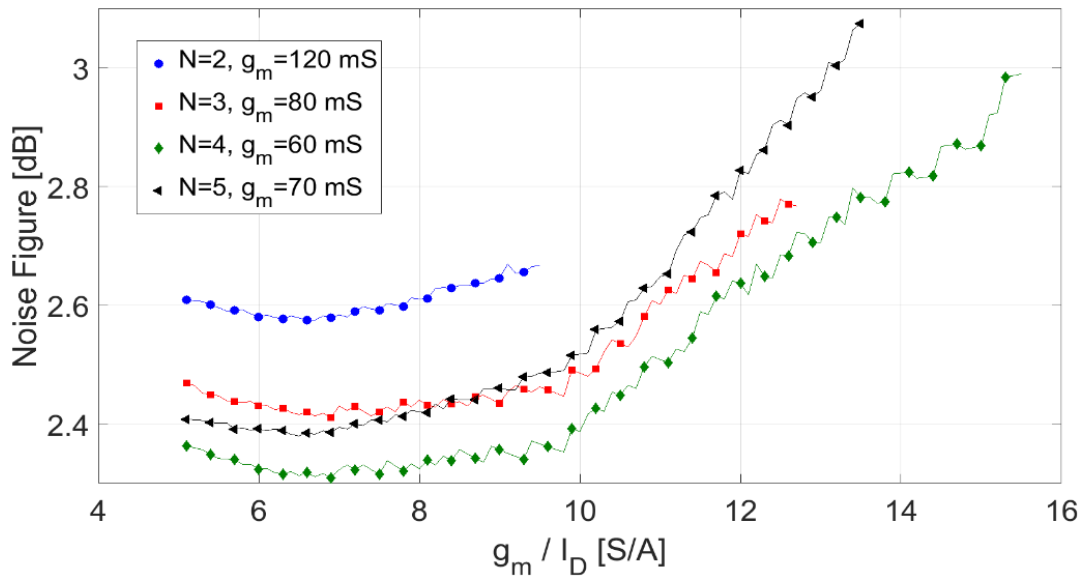
Finally, the simulation results and the FOMs are inserted into the lookup tables to extract the optimal transistor parameters ( $C_{GS}$ ,  $C_{DS}$ ,  $W/L$ ,  $g_m$ ,  $g_m/I_D$ ) and the DA configuration ( $N$ ) that allows achieving the design specifications.

Figure 5.5 summarizes graphically the lookup tables generated in the final step of the framework. The lookup tables provide very useful insights in the design of the DA. For example, we notice that the FOM increases linearly when it passes from strong to moderate inversion. This is primarily

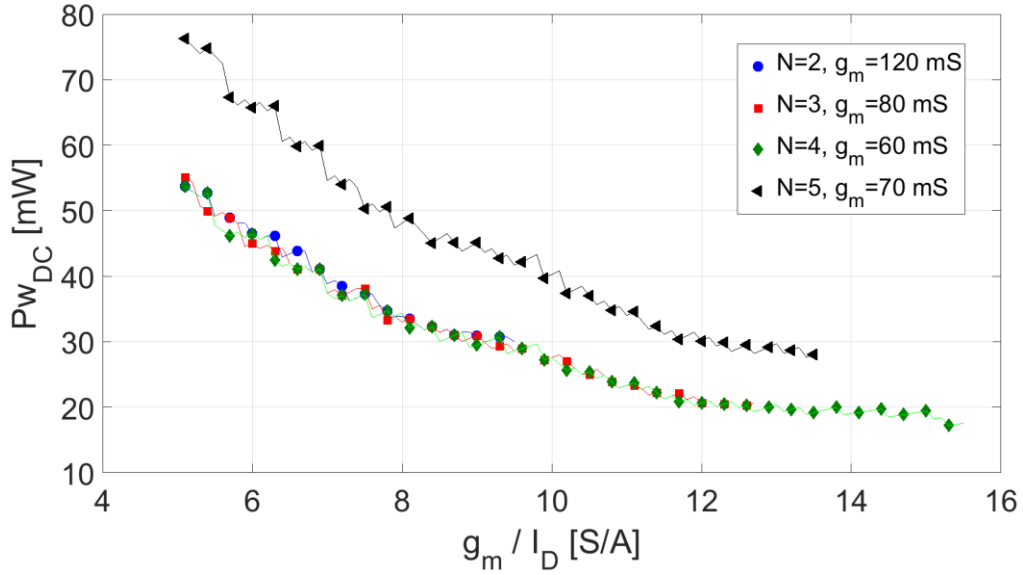
due to the decrement of DC power consumption. In moderate inversion, the FOM exhibits a local maximum due to the optimal tradeoff between gain, noise figure and power DC consumption. When moving from moderate to weak inversion, the FOM decreases, due to the decrement in gain and noise figure.



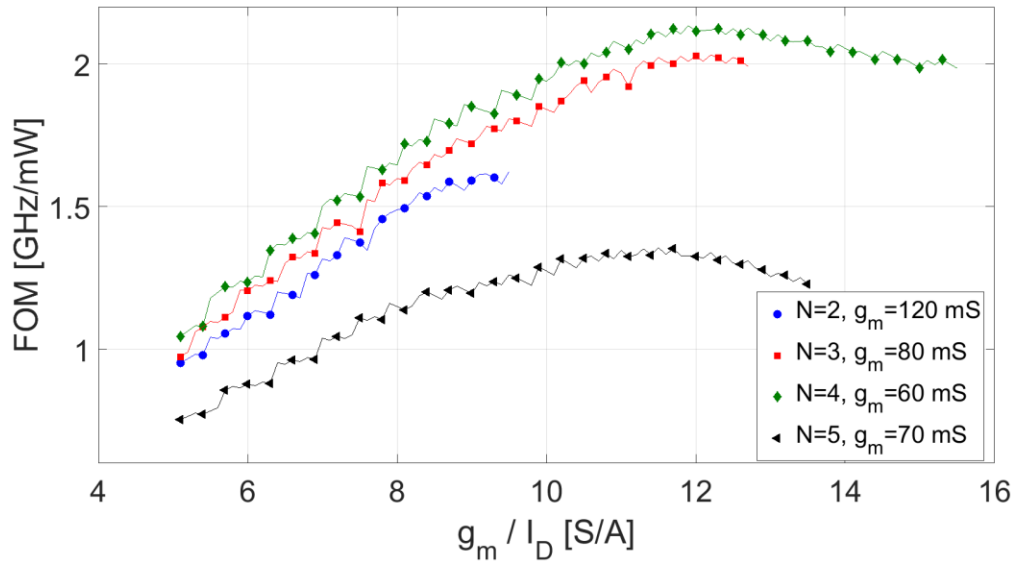
(a)



(b)



(c)



(d)

**Figure 5.5:** Examples of DA Lookup Tables - (a) Gain vs.  $g_m/I_D$  (b) Noise Figure vs.  $g_m/I_D$  (c) Power DC consumption vs.  $g_m/I_D$  (d) FOM vs.  $g_m/I_D$ .

The framework allows the designer to customize the criteria (i.e. the FOM) used for exploring the lookup tables and automatically extract the DA parameters that optimally match the desired design requirements. For example, when a low power DC design is required the moderate or weak inversion is likely to be the best choice while, when a high DA gain is required, the best region to bias the transistors is likely to be strong inversion.

To validate the proposed framework and compare the relative performances achievable, two distributed amplifiers with different number of stages were designed. The two primary specs were

a gain of 13 dB and a bandwidth of 15 GHz. This latter specification aimed to achieve the maximum flat gain in the UWB frequency range. For convenience, the same value of 1.1 nH was chosen for the drain and gate inductors. Consequently, the total drain and gate capacitances were set to a value of 440 fF. The intrinsic capacitances of the MOSFETs partly contribute to the desired line capacitances but additional capacitances need to be inserted to obtain the required value. As further design specifications, an average noise figure lower than 4 dB over the entire band and a DC power consumption lower than 30 mW were imposed. Finally, a maximum 10 dB target value for the input/output return losses was also imposed.

The inductors were designed using the toolkit developed by IHP for Keysight ADS. Two different values were implemented, namely  $L_D$  and  $L_D/2$ . Starting from the inductive values and from the inductor geometries (number of turns, diameters, line widths, etc.) the CAD tool extracts the equivalent circuit schematic for each inductor, including all parasitic effects. In a subsequent step, the CAD tool performs an electromagnetic simulation using ADS Momentum to refine the inductors' parameters models. Cadence Virtuoso directly imports the results and uses the refined inductors models in the circuit schematic. In Figure 5.6 are reported the quality factor of the two inductors as a function of the frequency. The first inductor has two turns, a diameter of 177  $\mu\text{m}$ , a line width of 11  $\mu\text{m}$  and shows a quality factor of 22.56 at 10 GHz; the second has two turns, a 105  $\mu\text{m}$  diameter, a 7  $\mu\text{m}$  line width and shows a quality factor of 14.71 at the same frequency.

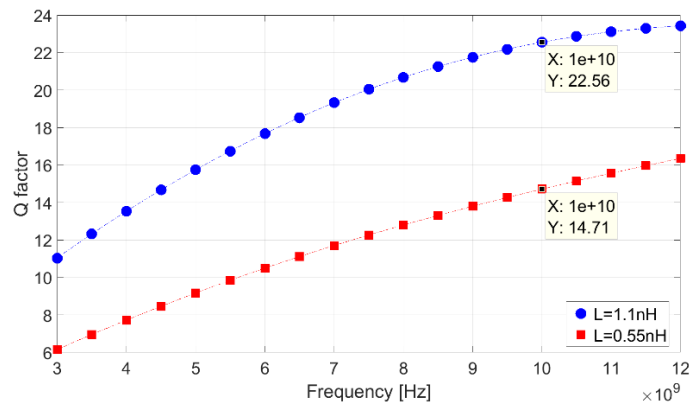


**Figure 5.6:** Inductors Q factor vs. frequency.

To apply the proposed framework and generate the lookup tables for the DA designs, a minimum number of stages equal to two was chosen, whereas the maximum value was set to five to satisfy the equation (5.7). To apply the  $g_m/I_D$  methodology and maximize the output signal swing, a value of  $V_{DD}/2$  was imposed for the drain-source voltage ( $V_{DS}$ ), with  $V_{DD}=1.2\text{V}$  being the DC supply voltage.

The results obtained using the framework are sketched in Figure 5.5. The framework was able to extract for each N the value of  $g_m$  and the other parameters that optimally match the specifications. Table 5.1 summarizes the main parameters computed for the various configurations. According to (5.6), the gain depends on N and  $g_m$ , so for N=2 a greater value of  $g_m$  has to be imposed for achieving the same gain obtained for N=4. More in details, with N=2 a  $g_m$  of 120 mS must be chosen, while for N=4 the required  $g_m$  is 60 mS. As expected, with different values of  $g_m$ , the DA exhibits different  $g_m/I_D$  maximum values. In fact, the maximum inversion region for N=2 corresponds to a value of transconductance efficiency equal to 9.5 S/A, while for N=4 the transistor can be biased in an inversion region with  $g_m/I_D$  equal to 15.5 S/A. This consideration leads to different levels of DC power consumption achievable by the various DA configurations. With N=4 and  $g_m=60$  mS the optimal  $g_m/I_D$  is 15.5 S/A and the DA dissipates only about 18 mW, while with N=2 and  $g_m=120$  mS the optimal  $g_m/I_D$  ratio is 9.5 S/A and the DA dissipates a power consumption of about 30 mW.

TABLE 5.1: DA performance vs. number of stages

DA Stages	N=2	N=3	N=4	N=5
$(g_m/I_D)_{\max}$ [S/A]	9.5	12.7	15.5	13.5
$g_m$ [mS]	120	80	60	70
$P_{WDCmin}$ [mW]	30@9.5 S/A	21@12.7 S/A	18@15.5 S/A	28@13.5 S/A
$NF_{\min}$ [dB]	2.57@6.7 S/A	2.4@6.9 S/A	2.37@6.5 S/A	2.3@6.9 S/A
$FOM_{1\max}$ [GHz/mW]	1.61@9.2 S/A	2.02@12 S/A	2.13@11.9 S/A	1.35@11.5 S/A
$FOM_{2\max}$ [GHz/mW·mm <sup>2</sup> ]	2.7@9.2 S/A	3.38@12 S/A	2.67@11.9 S/A	1.35@11.5 S/A

Note from Figure 5.5 that the best performances in term of FOM are achieved with four stages. In fact, in this configuration, the DA can be optimally biased in moderate inversion where it exhibits a low power level and reasonable performances in term of gain and noise figure. However, as power is lowered, the gain and the noise figure increase. To guarantee the design specifications, with  $g_m=60$ mS, for a four stages DA, a  $g_m/I_D$  ratio of 9.8 S/A is required.

As previously discussed, the designer can modify and customize the FOM expression as desired. For example, if chip area is included, the FOM can be expressed as follows:

$$FOM_{2[GHz/mW \cdot mm^2]} = \frac{S_{21[dB]} \cdot BW_{[GHz]}}{NF_{[dB]} P_{DC[mW]} Area[mm^2]} \quad (5.12)$$

In an analog design, inductors occupy significantly more area than MOSFETs, resistors and capacitors. Considering an inductor area of roughly  $200 \times 200 \mu\text{m}^2$ , with  $N=3$  the chip area for the optimal design results in  $0.6 \text{ mm}^2$  while with  $N=4$  the chip area required for the optimal design is about  $0.8 \text{ mm}^2$ .

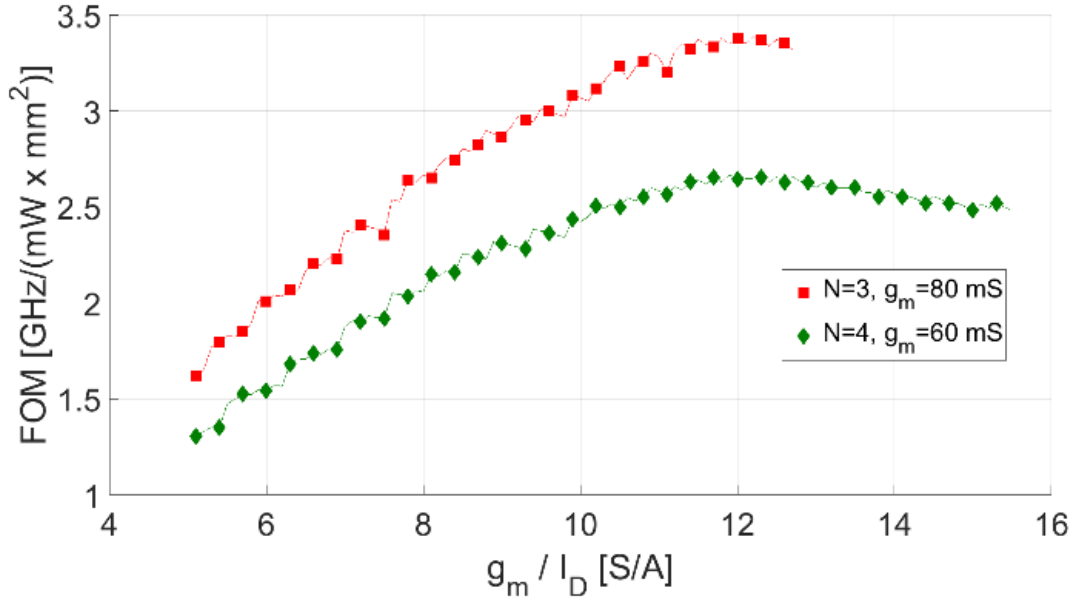


**Figure 5.7:** FOM<sub>2</sub> vs  $g_m/I_D$ .

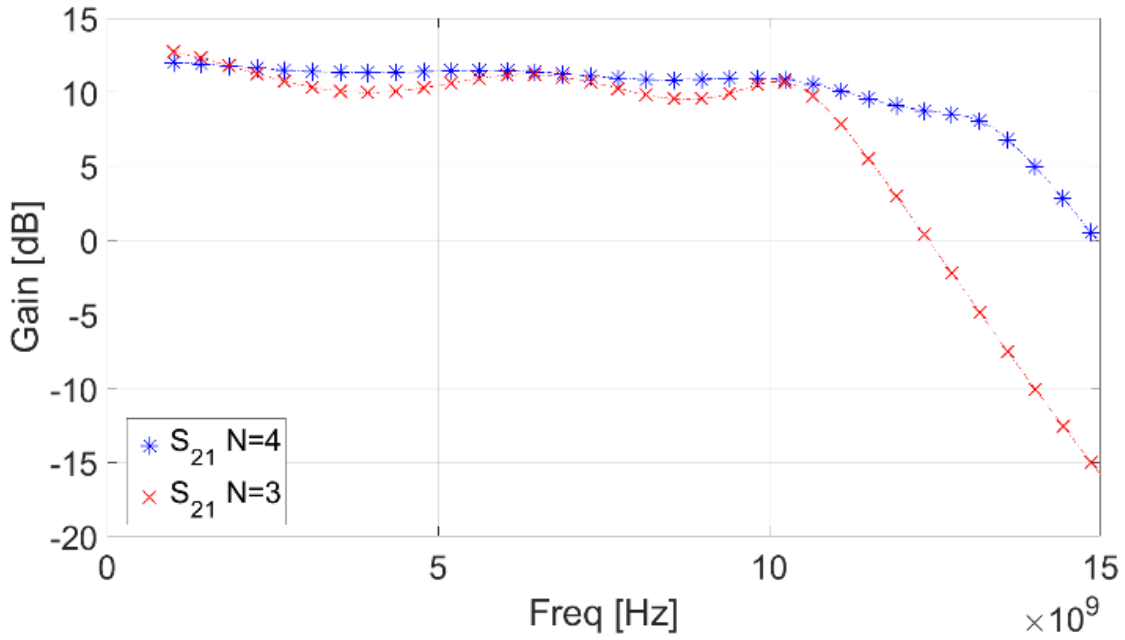
Including the new FOM in the proposed framework, the optimal solution for the configuration  $N=3$ , requires  $g_m=80$  mS and  $g_m/I_D$  of 9 S/A. Figure 5.7 shows that when considering chip area as one of the criteria defining the FOM the design achievable with  $N=3$  is considerably better than the one with  $N=4$ .

To evaluate the accuracy of the framework two DA configurations ( $N=3$  and  $N=4$ ) were implemented and their theoretical and post-layout simulation performances compared. The performances were assessed using the S-Parameters extracted by Cadence Virtuoso.

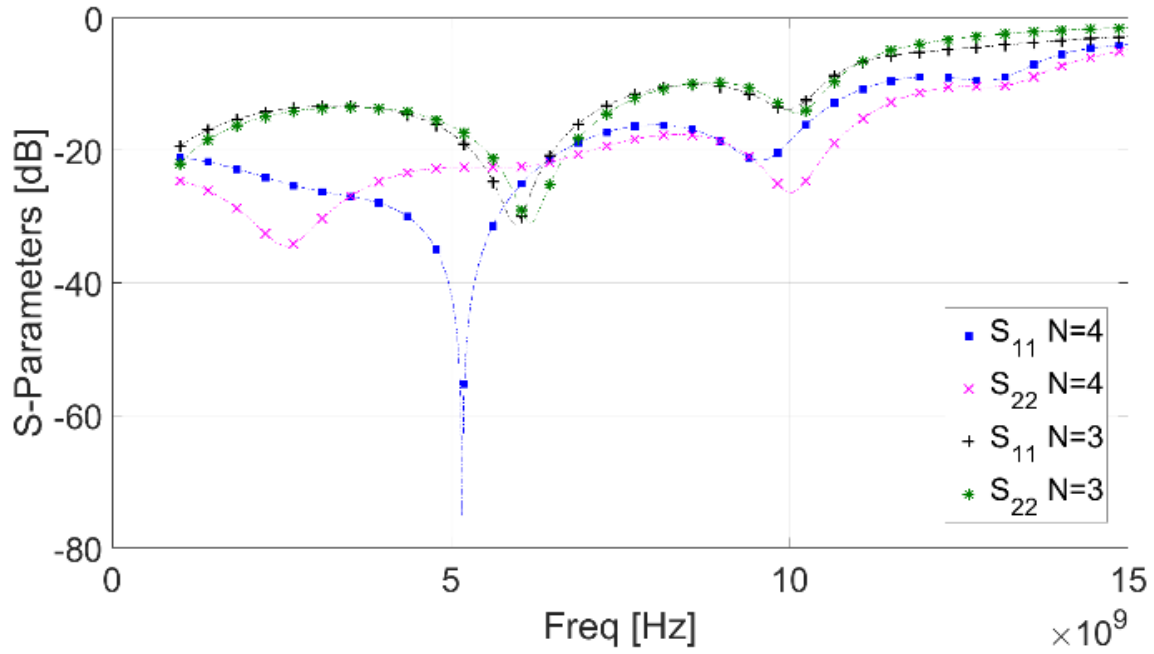
Figure 5.8(a) compares the gain of the two DAs. Due to the losses introduced by the parasitic in the circuit, the two DAs exhibits a gain slightly lower than the target value. Furthermore, since any parasitic capacitance in the layout increases the value of  $C_G$  and  $C_D$ , the amplifier bandwidth is correspondingly reduced (3 to 10 GHz range) when compared to the ideal expected value.

However, the DAs were both able to guarantee a gain in excess of 11 dB over all the frequencies allocated for the UWB standard. The performances achieved are comparable with other state of the art work reported in literature (see Table 5.2).

Figure 5.8 (b) shows that with  $N=4$  the DAs exhibit very good impedance matching: the input and the output return losses are lower than  $-16$  dB in the 3.1-10.6 GHz frequency range with an average value of  $-23.86$  and  $-21.95$ , respectively. With  $N=3$  the input/output return losses are lower of  $-10$  dB in the 3.1-10.6 GHz frequency range with an average value of  $-15$  dB.



(a)



(b)

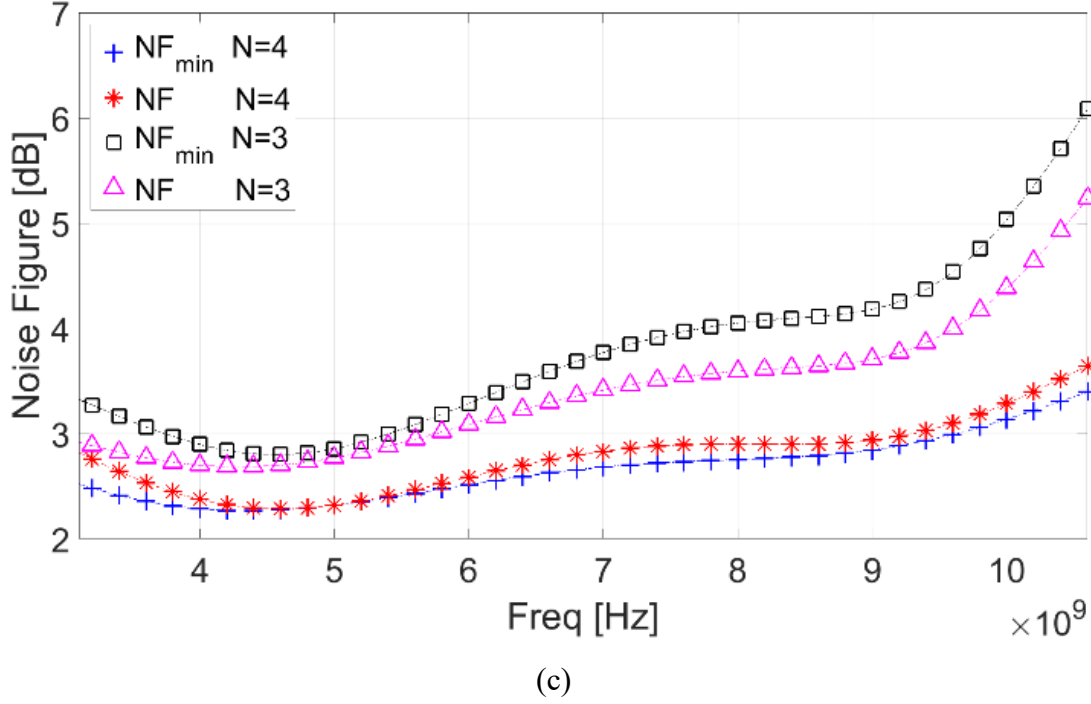


**Figure 5.8:** DAs performances (a) Transducer gain (b) Input/Output Return Loss (c) Noise Figure of the proposed DAs.

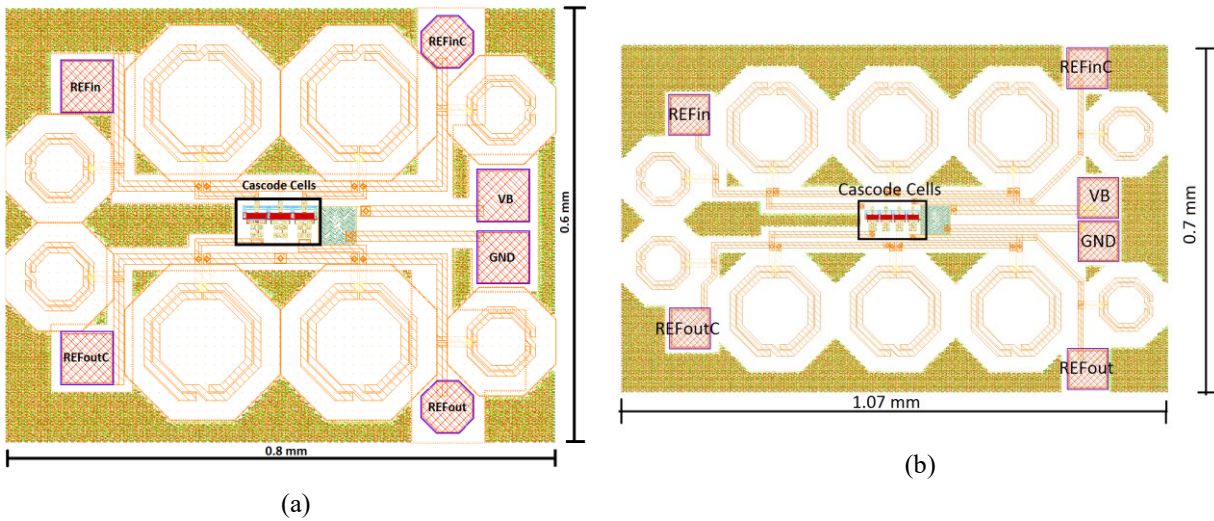
Figure 5.8 (c) reports the noise figure of the DAs. As expected, the parasitic effects present in the circuit improve decrease the output noise figure. In fact, with N=4 the theoretical 2.4 dB average noise figure is improved raised to a mean value of 2.65 dB in post-layout simulation. With N=3 the parasitic effects improve decrease the final noise figure of the system, obtaining a final mean value of 3.7 dB. Finally, the DAs dissipate only 26 mW with a DC-power supply of 1.2 V, so the effective FOM value is 1.60 GHz/mW with N=4 and 1.14 GHz/mW with N=3.

Figure 5.9 shows the final layout of the two DAs. The first chip measures 1.07 mm by 0.7 mm (that is an area of 0.75 mm<sup>2</sup>) while the second DA measures 0.8 mm by 0.6 mm (that is an area of 0.48 mm<sup>2</sup>). Including the area in the FOM a value of 2.24 GHz/(mW × mm<sup>2</sup>) is obtained with N=4 and a value of 2.38 GHz/(mW × mm<sup>2</sup>) is obtained with N=3.

The proposed approach allows to design DAs that achieve performances comparable with the other systems present in literature, but without the need to rely on complex circuit solutions. In addition, for N=4 the DA exhibits a better match in terms of input/output return losses and noise figure than any other structure. Moreover, the design with three stages presents an occupied area of 0.48 mm<sup>2</sup>, this is only a few micrometers larger than the DA in [74].

**TABLE 5.2:** Reported Performances of CMOS DAs for UWB systems

Ref.	Tech.	BW [GHz]	G [dB]	S11/S22 [dB]	NF avg [dB]	P <sub>DC</sub> [mW]	Area (mm <sup>2</sup> )	FOM <sub>1</sub> [GHz/mW]	FOM <sub>2</sub> [GHz/mW·mm <sup>2</sup> ]
[71]	0.13 um	3-9.4	12	<-7 / <-8	3.3	30	0.82	1.21	1.48
[73]									
(HG mode)	0.13 um	3-10	20.4	<-10 / <-10	3.29	37.8	0.88	1.64	1.86
[73] (LG mode)	0.13 um	3-10	11	<-10 / <-10	4.25	6.86	0.88	3.77	4.28
[74]	0.13 um	3-10	15	<-12 / <-15	3.34	26	0.43	1.73	4.02
[75]	0.13 um	2.2-9	9.8	<-10 / <-9.2	4.25	30	0.68	0.69	1.01
[76]	0.18 um	3-10	18	<-10 / <-9	6	54	2.2	0.55	0.5
This Work N=4	0.13 um	3-10	11	<-16 / <-18	2.65	26	0.75	1.60	2.24
This Work N=3	0.13 um	3-10	11	<-10 / <-10	3.7	26	0.48	1.14	2.38



**Figure 5.9:** (a) Final three stages DA layout (b) Final four stages DA layout.

### 5.3 Active Mixer Design

The most commonly used mixer in direct-conversion receivers is the conventional double balanced Gilbert cell. The main benefits are good port-to-port isolation and low even-order harmonic distortion [77]. The architecture of the conventional Gilbert cell mixer is shown in Figure 5.10. The cell is composed of a stack of three MOS transistor pairs, so it requires large voltage headroom to keep the transistors biased in saturation, and it results in a large DC-power consumption.

A differential transconductance stage (TS) composed by the transistors pair M1 and M2 converts the RF voltages at the input ports in current signals for the switching stage (SS) composed by the transistors M3-M6. Finally, the switching stage is driven by the Local Oscillator (LO) to reverse the polarity of the RF inputs at the LO frequency rate. Ideally the balanced structure should cancel any RF and LO frequency component appearing at the output. Since the Intermediate Frequency (IF) stage output is a differential signal the LO appear at the output as a common mode.

In literature, different techniques and ad hoc architectures have been proposed to improve the various performance metrics of the Gilbert cell. For example, MacEachern et al. [78] successfully improve conversion gain and system linearity by using the charge injection method. Unfortunately, this method requires a significant increment of the DC-current and therefore has the drawback of further increasing DC-power consumption. Wei et al. [79] utilize a folded structure in order to reduce the number of stacked transistors. As a result, the mixer can work with a lower DC-power supply, however the current mirror topology in the folded structures reduces the conversion gain and introduces large parasitic capacitances that deteriorate bandwidth.

Seo et al. [80] exploit a switched biasing technique for the tail current source  $I_{BIAS}$ . This technique allows reducing the noise figure of the entire system but requires a number of stacked transistors greater than the conventional cell and, therefore it requires significantly larger power consumption than the conventional cell. Each of these methods focuses on improving only a specific aspect of the Gilbert mixer and relies on a fixed size (i.e. a fixed W/L ratio) for all the transistors. Typically, the size of the MOSFETs is fixed by the value of  $g_m$  required to achieve the target conversion gain. The use of a design methodology based on  $g_m$  over  $I_D$  approach allows to achieve an optimal tradeoff between the various performance metrics of a Gilbert cell mixer without using any ad-hoc architecture but, rather, relying on a systematic approach for calculating the W/L transistor's ratios required for achieving the design specifications. To apply the design methodology the expression of the conversion gain is necessary.

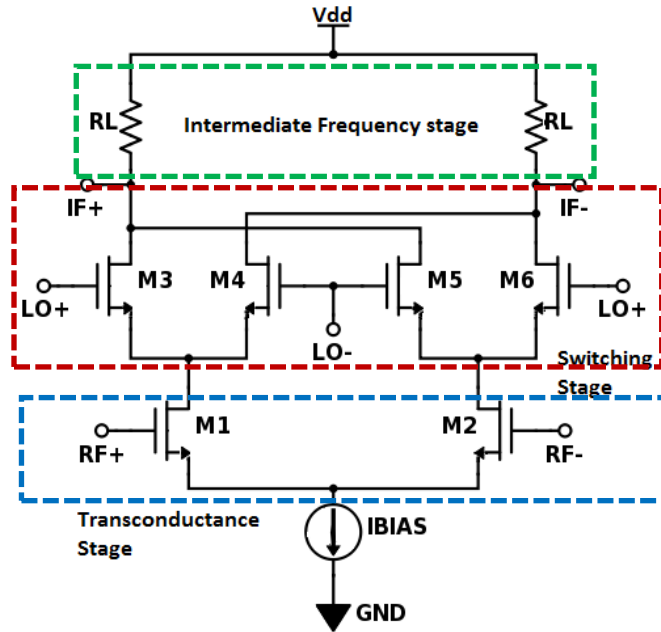


**Figure 5.10:** (a) Architecture of a conventional double balanced Gilbert cell mixer

Given the desired value of the load resistance  $R_L$ , the mixer conversion gain ( $A_V$ ) is determined by the transconductance value ( $g_m$ ) of the transistors M1 and M2:

$$A_v \cong \left(\frac{2}{\pi}\right) g_m R_L \quad (5.13)$$

The traditional design approach starts from (5.13), and consists of first selecting the value of  $g_m$  required to achieve the target gain.

Then choosing a value for the width  $W$  and the channel length  $L$  of the MOS transistor relying on the square law equation of the drain current  $I_D$ :

$$g_m = \sqrt{\frac{2K_n W I_D}{L}} \quad (5.14)$$

where  $K_n$  is the product of the oxide capacitance of the MOSFET ( $C_{ox}$ ) and the electron mobility ( $\mu_n$ ). The drain current of the transistors is set based on the tail current of the transconductance stage (TS):

$$\begin{aligned} I_{BIAS} &= 2 \times I_{D(TS)} \\ I_{D(SS)} &= 2 \times I_{D(TS)} \end{aligned} \quad (5.15)$$

As previously mentioned, for the nano-metric channel lengths of the MOSFETs employed in today's integrated circuits, the square-law equation (5.13) has become grossly inaccurate. Hence,

in the proposed framework, the W/L ratio of the transistors in the mixer's schematic are selected exploiting a systematic approach based on the  $g_m/I_D$  methodology. The algorithm implemented in the proposed framework considers the transistors in the switching stage and the transconductance stage separately. By varying independently, the  $g_m/I_D$  of the two stages the algorithm allows to search the solution space for the optimal bias point that meets design specifications. The optimal solution is reached through the following steps:

- Given the target gain and the load resistance specifications, use (5.13) to derive the value of  $g_m$ ;
- Once the value of  $g_m$  has been set, sweep  $g_m/I_D$  (that is the inversion level of the transistors) in the range 5÷25, and let the framework computes the corresponding current levels  $I_{D(SS)}$  and  $I_{D(TS)}$ ;
- Exploiting the lookup table of the current density ( $I_D/W$ ), computes the values of  $W_{(SS)}$  and  $W_{(TS)}$  for all inversion levels explored. Set the channel length L to the minimum value of 130nm to maximize speed;
- Perform systematic DC analysis of the mixer by independently varying the  $g_m/I_D$  ratio for the TS and SS. For each bias point computes the DC-power consumption of the mixer.
- For each solution, check that the circuit is correctly biased (that is all transistors operates in saturation) and compare the DC-power consumption with the design specification. Discard any unfeasible solution.
- For each solution left from the previous step, compute the conversion gain of the mixer. Discard any further solution that exhibit a conversion gain lower than the design specifications.
- Repeat the previous step for the noise figure and the third-order intercept of the system.
- Explores the pruned solutions space and extract the optimal bias point, that is the bias point that allows to achieve the best tradeoff among the performance metrics of the mixer.

To achieve the best balance between the different performance metrics, the following figure of merit (FOM) is defined:

$$FOM = \frac{CG_{[dB]} \cdot IIP3_{[mW]}}{NF_{[dB]} P_{DC[mW]}} \quad (5.16)$$

where CG is the conversion gain expressed in dB, IIP3 is the third-order intercept in mW, NF is the average noise of the mixer in dB and  $P_{DC}$  is the DC-power consumption in mW.

The proposed framework has been validated on the design of a Gilbert cell mixer biased with a DC-power supply of 1.5V. The design requirements were:

- a conversion gain greater than 10 dB;
- a DC-power consumption lower than 3 mW;
- a resistive load of 500 Ohms;
- a target third-order intercept (IIP3) better than -5 dB.

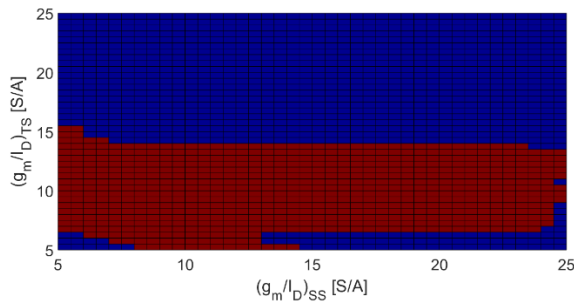
These design specifications were chosen to compare our mixer with similar papers present in literature and reported in Table 5.3. The circuit metrics used to validate our design have been computed considering a LO sine wave with a frequency of 5.7 GHz and a maximum power of 0 dBm.

Figure 5.11(a) sketches the solution space extracted by the proposed design framework. Observing Figure 5.11(a) it is possible to infer that the transistors of the transconductance stage (TS) should be biased in a  $g_m/I_D$  range between 5÷13 S/A while the transistors of the switching stage (SS) can be basically biased anywhere in the inversion region. Figure 5.11(b) shows the behavior of the IIP3. When the MOSFETs, in SS, are biased in the  $g_m/I_D$  range between 5÷10 S/A, the IIP3 linearly decays as the biasing point of the TS passes from strong to weak inversion. When biasing the transistors of the SS in weak inversion, the IIP3 curve changes its behavior and it becomes a parabolic curve with a local maximum for  $g_m/I_{D(SS)}$  of 20 S/A. The values of IIP3 were computed considering an RF sine source composed of two tones, one at 5.8 GHz and the other one at 5.85 GHz. The behavior of the average noise figure (Figure 5.11(c)) over the Ultra-Wide Bandwidth (UWB) frequencies range (3.1÷10.6 GHz) is very similar to that of the IIP3. When the SS is biased in strong inversion, the noise figure exponentially decays as the MOSFETs in the TS pass from strong to moderate inversion. However, once the MOSFETs in the SS reach the moderate inversion, the noise figure slowly decreases and finally reaches a value lower than 12 dB. Figure 5.11(d) sketches the conversion gain of the mixer with respect to the  $g_m/I_D$  of the two stages. Observing the figure, we see that the conversion gain has a parabolic trend in both  $g_m/I_D$  directions, reaching an absolute maximum value of 13.5 dB when the transistors in both stages are biased in moderate inversion. The DC-power consumption of the mixer is sketched in Figure 5.11(e). It is essentially determined by the  $g_m/I_D$  ratio of the MOSFETs in the TS. In fact, it exponentially decays when the bias point of this stage passes from strong to weak inversion. On the contrary, when the bias point of the SS moves from strong to weak inversion, the DC-power consumption is

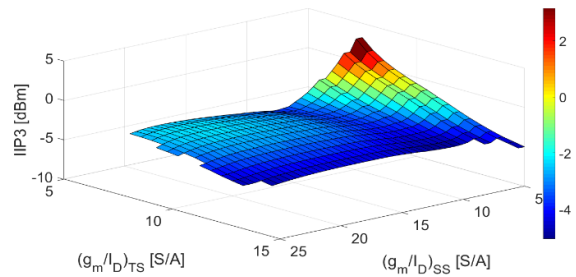
approximately constant. This type of behavior is strictly related to the working principles of the Gilbert cell. As previously mentioned, the transconductance stage must convert the input voltage signal into a current signal, while ideally, the switching stage transistors must only reverse the polarity of the RF inputs at the LO frequency rate.

Finally, Figure 5.12 sketches the FOM as a function of  $g_m/I_{D(TS)}$  and  $g_m/I_{D(SS)}$  ratios. Due to the behavior of the IIP3 and the average noise figure of the system, the graph of the FOM exhibits an irregular trend. However, it reaches a local maximum when the TS is biased in moderate inversion and the SS is biased between moderate and weak inversion.

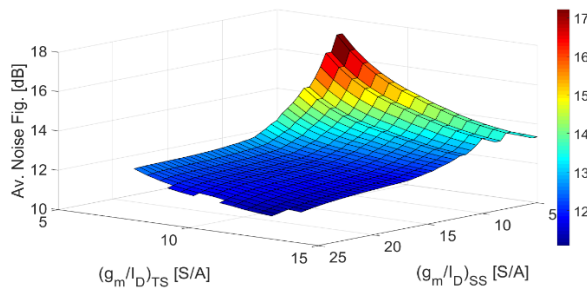
The optimization algorithm returns as optimal solution  $g_m/I_{D(SS)} = 18 \text{ S/A}$  and  $g_m/I_{D(TS)} = 10.5 \text{ S/A}$ . To find out how to optimally bias the transistors, the algorithm searches for the maximum value of FOM. The maximum value of FOM provides the best tradeoff among conversion gain, noise figure, IIP3 and DC-power consumption. Although, the design optimization procedure illustrated is applied to the design of a Gilbert cell, the proposed framework is completely general and represents an extremely scalable and flexible tool. It does not constrain the user to a fixed design flow; the designer can choose to maximize performances with respect to any suitable figure of merit.



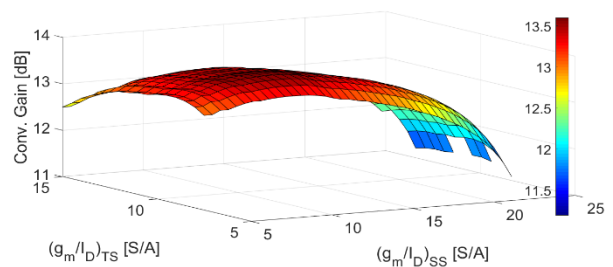
(a)



(b)



(c)



(d)

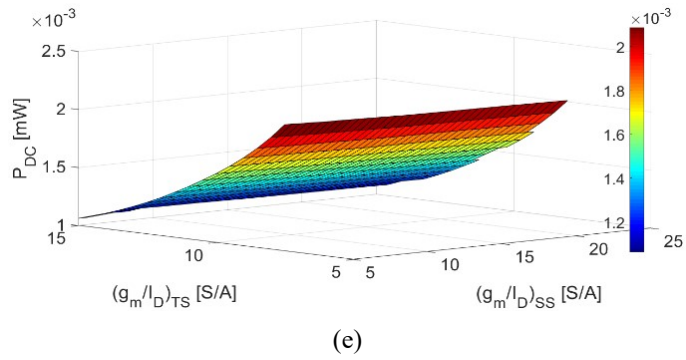


**Figure 5.11:** (a) Solution space versus  $g_m/I_{D(TS)}$  and  $g_m/I_{D(SS)}$  ratios. (b) IIP3 of the mixer versus  $g_m/I_{D(TS)}$  and  $g_m/I_{D(SS)}$  ratios. (c) Average Noise Figure versus  $g_m/I_{D(TS)}$  and  $g_m/I_{D(SS)}$  ratios. (d) Conversion gain of the mixer versus  $g_m/I_{D(TS)}$  and  $g_m/I_{D(SS)}$  ratios. (e) DC-power consumption of the system versus  $g_m/I_{D(TS)}$  and  $g_m/I_{D(SS)}$  ratios.

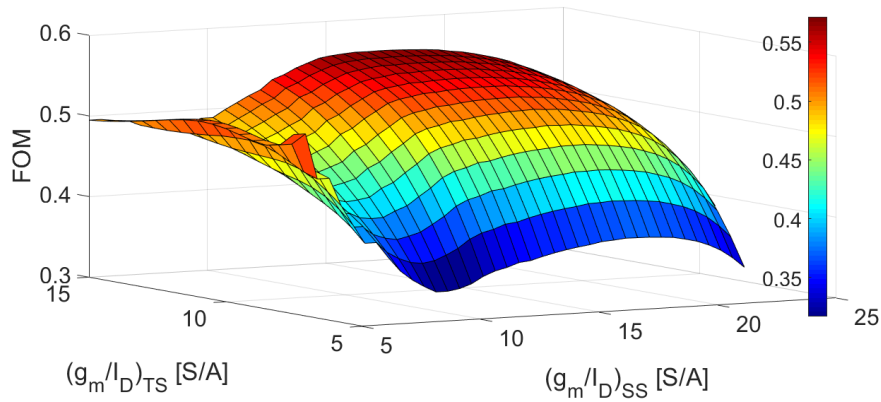
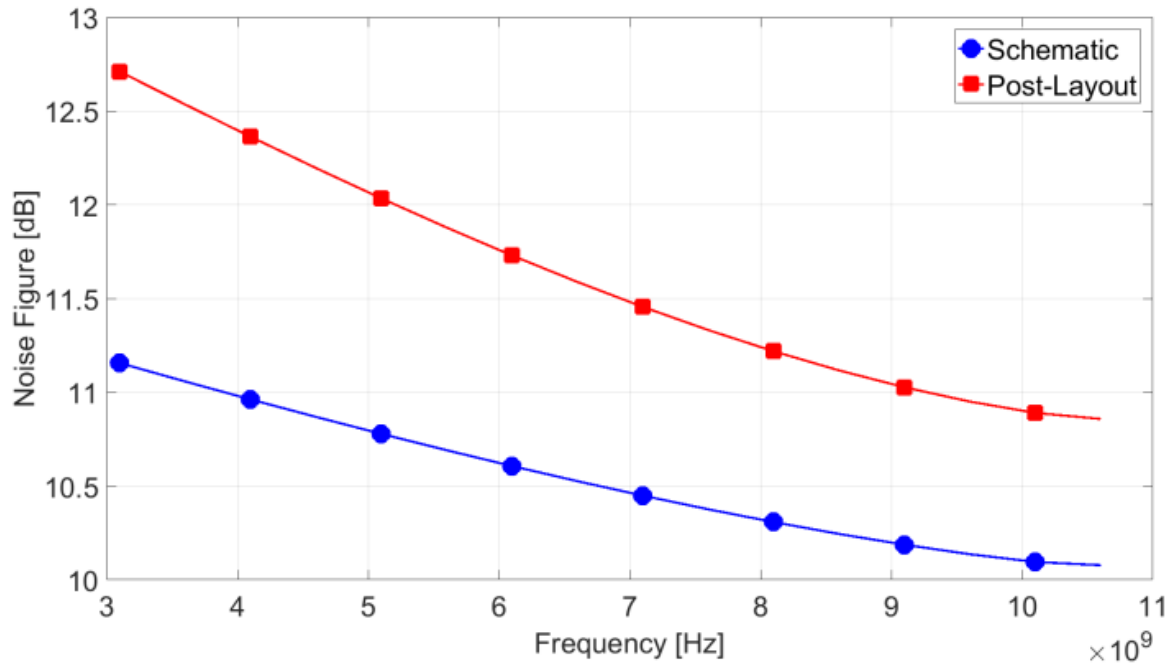
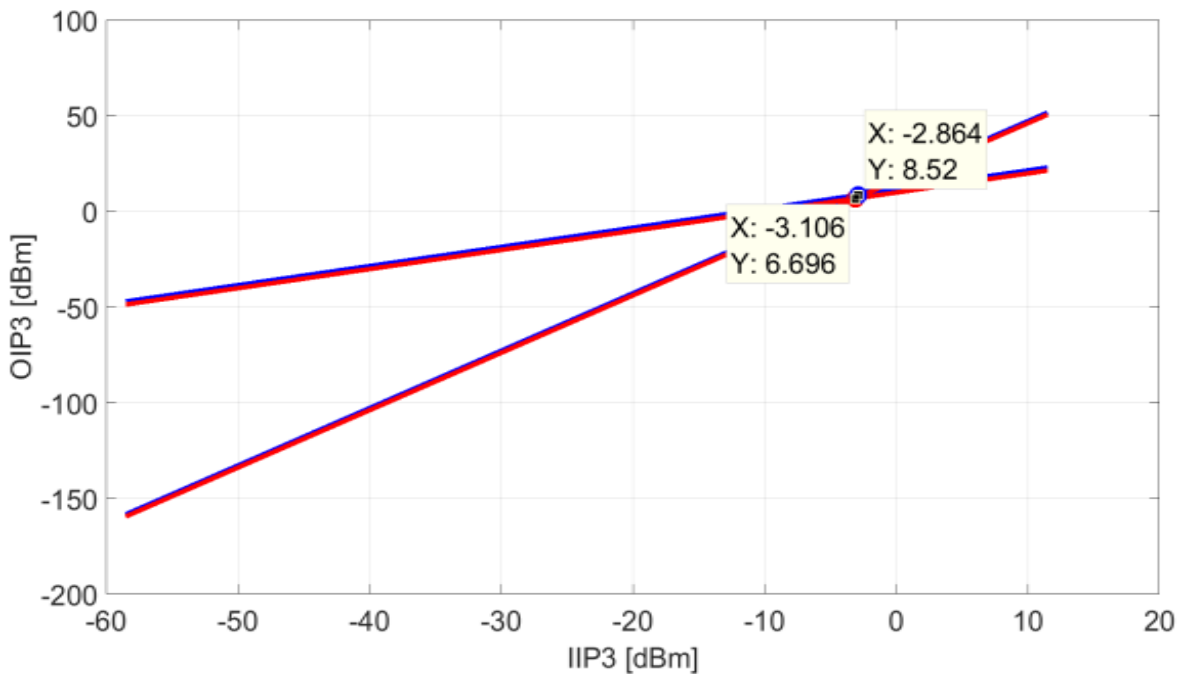


**Figure 5.12:** FOM versus  $g_m/I_{D(TS)}$  and  $g_m/I_{D(SS)}$  ratios.

The final performances for the CMOS Gilbert mixer designed with the proposed methodology are reported in



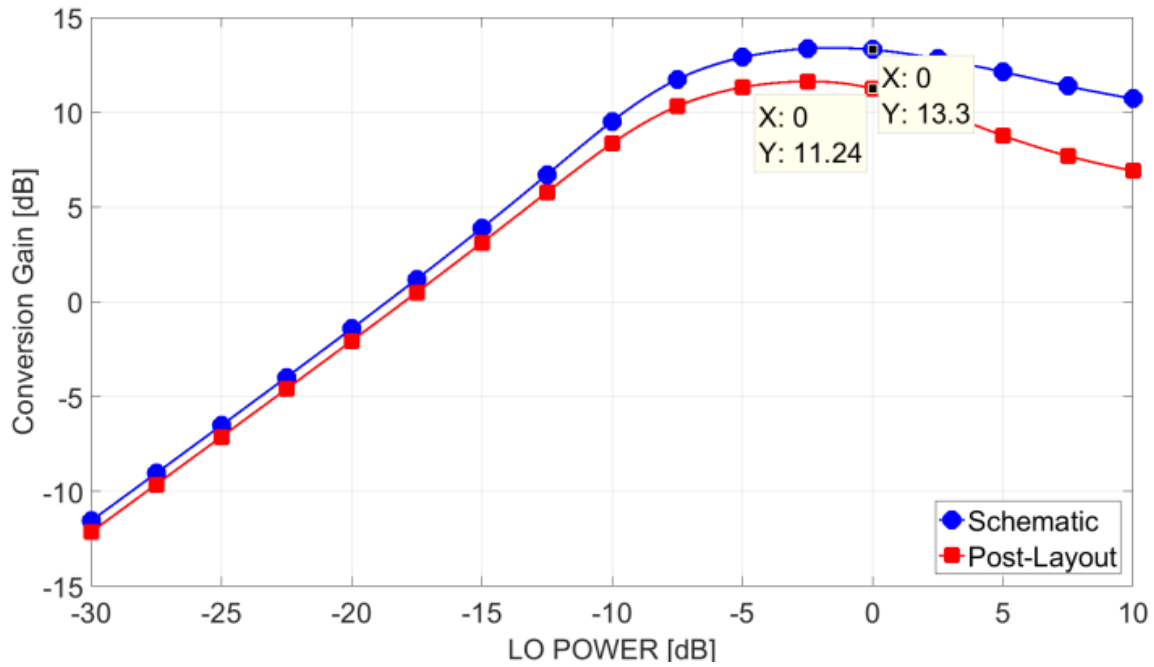
(b)



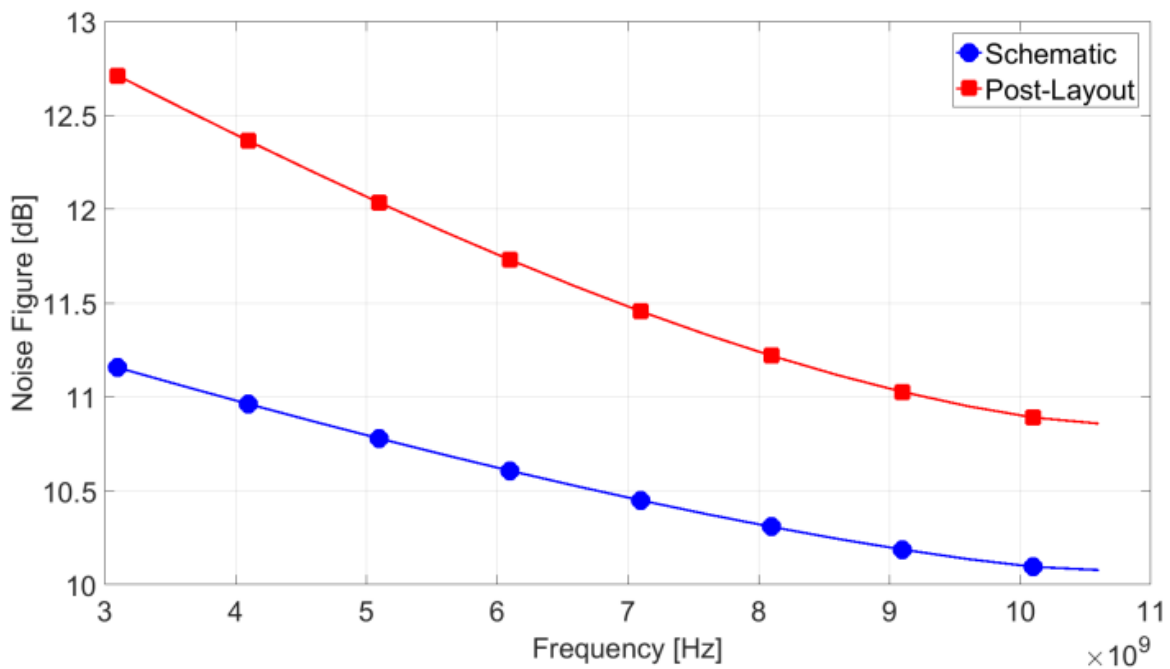
(c)

Figure 5.13 and were evaluated using Cadence Virtuoso. The final conversion gain is about 11 dB with a LO power of 0 dBm. This value is lower than the ideally expected value of 13 dB due to the losses introduced by the parasitic in the circuit and the introduction of the CMOS current mirror. The circuit parasitic also affect the other performance metrics. In fact, the final average

noise figure is about 1.1 dB greater than the schematic value of 10.5 dB; the final IIP3 is -3.1 dBm lower than the ideal value of 2.8 dBm. Finally, the circuit dissipates only 2.1 mW with a power supply of 1.5 V. Nevertheless, the proposed methodology allowed us to select a biasing point at which the performance metrics exceed design specifications.



(a)



(b)

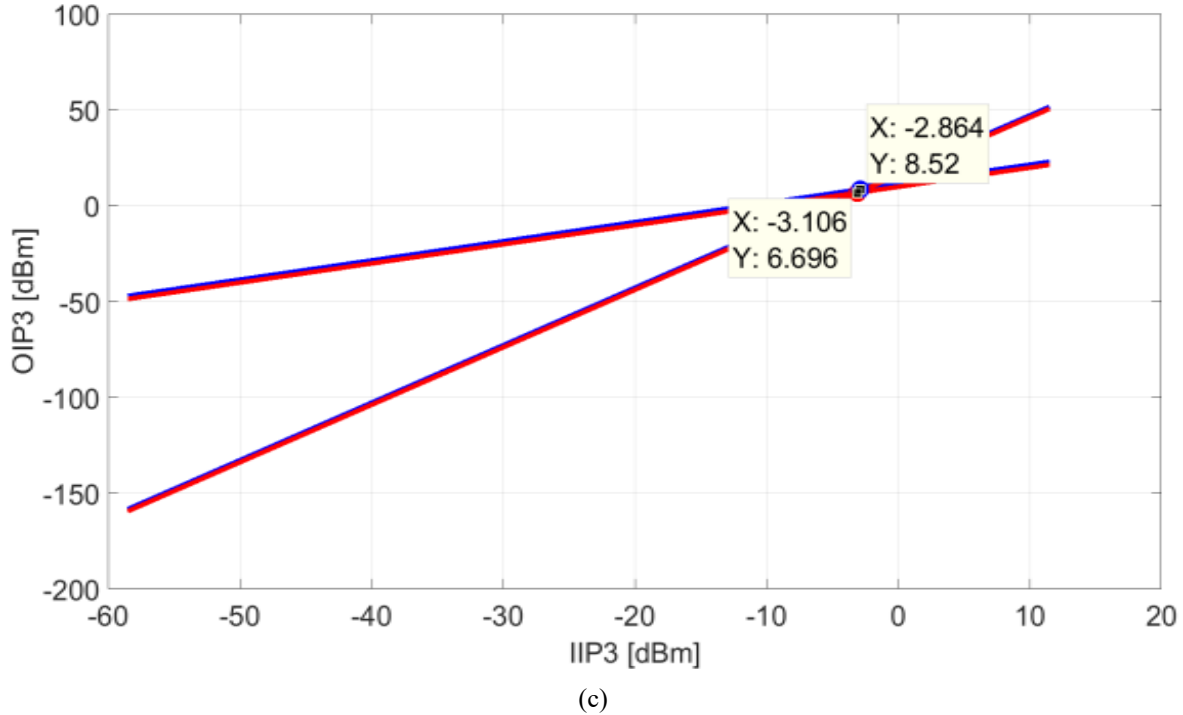


**Figure 5.13:** Post-Layout mixer conversion gain vs LO power (b) Post-Layout mixer noise figure vs frequency (c) Post-Layout mixer IP3.

Table 5.3 compares the quality of the design solution obtained against several comparable CMOS Gilbert mixer designs present in literature. As indicated by the FOM values summarized in the table, the main advantage of our design is a better tradeoff between the main performance metrics. In addition, the mixer designed with our proposed framework, exhibits the lowest DC-power consumption. The  $g_m/I_D$ -based approach we followed allows to optimize the mixer transistor sizes and to achieve the desired specifications without making use of complex architectures or ad hoc circuit solutions. In general, the  $g_m/I_D$  approach exploited can also be extended to the design of more complex architectures presented in literature.

Finally, Figure 5.14 shows the layout of the core of the designed mixer. In final layout, the ideal bias current generator was realized with a CMOS current mirror. The chip-core without bonding pads and baluns measures 0.021 mm by 0.031 mm (that is an area of 651  $\mu\text{m}^2$ ).

TABLE 5.3: Reported Performance of CMOS Gilbert Mixers

Ref.	CMOS Tech.	G [dB]	IIP3 [dBm]	NF Av. [dB]	P <sub>DC</sub> [mW]	FOM
[80]	0.13 um	8	-3	11.2	5.57	0.12
[81]	0.18 um	10	4	10	10	0.16
[82]	0.13 um	8.95	-2.2	11.4	3.7	0.16
[83]	0.13 um	21	-1.8	15.7	18.3	0.06
[84]	0.18 um	13.5	-3.25	21.22	7.2	0.06
This Work	0.13 um	11.24	-3.1	11.6	2.1	0.32

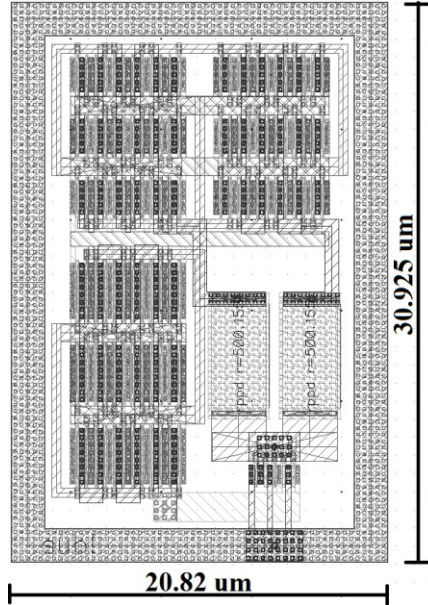


Figure 5.14: Final Layout of the Double-Balanced Gilbert Cell Mixer.

## 5.4 Conclusions

The  $g_m$  over  $I_D$  approach can be extended to generate a series lookup tables that facilitate the design of a specific analog block, without performing a hand analysis or a trial and error calculation. However, this methodology is strongly related to the process technology used in the circuit design. If the process changes, the lookup tables must be again computed and generated. Moreover,  $g_m$  over  $I_D$  depends even on the circuit topology considered. In fact, in [85]  $g_m$  over  $I_D$  was applied to design a regulated cascode circuit used as transimpedance amplifier. Due to its feedback structure,

the amplifier exhibits a behavior that not correspond to the theory described by the lookup tables generated by  $g_m$  over  $I_D$  approach.

In this work, the  $g_m$  over  $I_D$  methodology was used to successfully design the main block of the transmitter and the receiver chain of the indoor positioning system described in the previous chapters. Next works will focalize on the design of the last analog blocks of the chain: the analog to digital converter and the digital to analog converter.

## References

- [1]. Mautz Rainer, “Indoor Positioning Technologies”, PhD dissertation in Application in Positioning and Engineering Geodesy, Feb. 2012, Zurich
- [2].F. V. Diggelen, “Indoor GPS theory & implementation”, IEEE Proc. Position Location and Navigation Symposium, pp. 240 – 247, April 15-18, 2002
- [3].A. Harder, L. Song, and Y. Wang, “Towards an Indoor Location System Using RF Signal Strength in IEEE 802.11 Networks”, IEEE Proc. of International Conference on Information Technology: Coding and Computing, 2005.
- [4].P. Bahl and V. N. Padmanabhan, “RADAR: An Inbuilding RF-based User Location and Tracking System”, IEEE Proc. INFOCOM, Tel-Aviv, Israel, March 2000
- [5].A. Ali, L. A. Latiff, and N. Fisal, “GPS-free Indoor Location Tracking in Mobile Ad Hoc Network (MANET) Using RSSI”, IEEE Proc. Microwave Conference, October 2004
- [6].F. Forno, G. Malnati, and G. Portelli, “Design and Implementation of a Bluetooth Ad Hoc Network for Indoor Positioning”, IEEE Proc., Col. 152, No. 5, October 2005
- [7].L. M. Ni, Y. Liu, Y. C. Lau, and A. P. Patil, “LANDMARC: Indoor Location Sensing Using Active RFID”, IEEE Proc. International Conference on Pervasive Computing and Communications, 2003
- [8].J. Hightower, R. Want, and G. Borriello, “SpotON: An Indoor 3D Location Sensing Technology Based on RF Signal Strength”, UW CSE 00-02-02, University of Washington, Department of Computer Science and Engineering, Seattle, WA, February 2000
- [9].B. Alavi and K. Pahlavan, “Bandwidth Effect on Distance Error Modeling for Indoor Geolocation”, IEEE Proc. 14th International Symposium on Personal Indoor and Mobile Radio Communications (PIMRC’03), Beijing, China, September 7-10, 2003
- [10]. B. Alavi and K. Pahlavan, “Studying the Effect of Bandwidth on Performance of UWB Positioning Systems”, IEEE Proc. Wireless Communications and Networking Conference (WCNC), Las Vegas, USA, April 3-6, 2006
- [11]. I. C. Siwiak, P. Withington, S. Phelan, “Ultra-Wide Band Radio: The Emergence of an Important New Technology”, IEEE Proc. VTC, Vol. 2.pp. 1169 -1172, spring 2001
- [12]. D. Cyganski, J. A. Orr and W. R. Michalson, “A Multi-Carrier Technique for Precision Geolocation for Indoor/Multipath Environments”, Institute of Navigation Proc. GPS/GNSS, Portland, OR, September 9-12, 2003

- [13]. N. Priyantha, A. Miu, H. Balakrishnan, and S. Teller, "The Cricket Compass for Context-aware Mobile Applications", *IEEE Proc. MOBICOM*, July 2001
- [14]. Y. Fukuju, M. Minami, H. Morikawa, and T. Aoyama, "DOLPHIN: An Autonomous Indoor Positioning System in Ubiquitous Computing Environment", *IEEE Proc. Workshop on Software Technologies for Future Embedded Systems*, 2003.
- [15]. G. Wang, C. Gu, T. Inoue, and C. Li, "Hybrid FMCW-interferometry radar system in the 5.8 GHz ISM band for indoor precise position and motion detection," in Proc. IEEE MTT-S Int. Microwave Symp. Dig., Seattle, WA, USA, Jun. 2013, pp. 1–4.
- [16]. Siversima, "FMCW Radar Sensor – Application Note", Sweden, June 2011
- [17]. B. Waldmann, R. Weigel, and P. Gulden, "Method for high precision local positioning radar using an ultra-wideband technique," in Proc. IEEE MTT-S International Microwave Symposium Digest, 15–20 June 2008, pp. 117–120.
- [18]. Maxim Integrated, "An Introduction to Spread-Spectrum Communications" Retrieved from <https://www.maximintegrated.com/en/app-notes/index.mvp/id/1890>.
- [19]. C. Meier, A. Terzis, S. Lindenmeier, "A high precision wideband local positioning system at 24GHz", *Microwave Symposium Digest*, 2006. IEEE MTT-S International, June 2006, Page(s): 1580 – 1583.
- [20]. C. Meier, A. Terzis, S. Lindenmeier, "A robust 3D high precision radio location system" in Proc. IEEE MTT-S Int. Microw. Symp., 2007, pp. 397–400.
- [21]. "Revision of part 15 of the Commission's rules regarding ultra-wideband transmission systems," FCC, Washington, DC [Online]. Available: <http://www.fcc.gov/oet/dockets/et98-153>, notice of inquiry adopted August 20, 1998; released September 1, 1998.
- [22]. "Revision of part 15 of the Commission's rules regarding ultra-wideband transmission systems," FCC, Washington, DC, Report and order, adopted February 14, 2002; released July 15, 2002.
- [23]. M. Mahfouz, C. Zhang, B. Merkl, M. Kuhn, and A. Fathy, "Investigation of high accuracy indoor 3-D positioning using UWB technology," *IEEE Trans. Microw. Theory Tech.*, vol. 56, no. 6, pp. 1316–1330, Jun. 2008.
- [24]. T. Ayhan, T. Redant, M. Verhelst, and W. Dehaene, "Towards a fast and hardware efficient sub-mm precision ranging system", Proc. In IEEE workshop on Signal Processing Systems (SiPS), October 2012, pp. 203-208.

- [25]. T. Redant and W. Dehaene, "High resolution time-of arrival for a cm-precise super 10 meter 802.15.3c-based 60 GHz OFDM positioning application," in 2nd International Conference on Pervasive and Embedded Computing and Communication Systems (PECCS 2012), feb. 2012, vol. 2, pp. 217 – 277.
- [26]. H. Xu, C.-C. Chong, I. Guvenc, F. Watanabe, and L. Yang, "High-resolution TOA estimation with multi-band OFDM UWB signals," in Proc. IEEE Int. Conf. on Communications., Beijing, China, May 2008.
- [27]. H. K. Parikh, PhD thesis dissertation on "An RF System Design for an Ultra-Wideband Indoor Positioning System", Worchester Polytechnic Institute, Feb. 2008.
- [28]. G. Han, D. Choi, W. Lim, "A Novel Reference Node Selection Algorithm Based on Trilateration for Indoor Sensor Networks", IEEE Intl Conf. on Computer and Information Technology, 2007, Pages:1003-1008.
- [29]. Z. Yang, Y. Liu, "Quality of Trilateration: Confidence based Iterative Localization", IEEE ICDCS, June 2008, Pages: 446-453.
- [30]. Y. Qi, C. B. Soh, E. Gunawan, K.-S. Low, and A. Maskooki, "An accurate 3D UWB hyperbolic localization in indoor multipath environment using iterative Taylor-series estimation," in Proc. IEEE Veh. Technol. Conf., 2013, pp. 1–5.
- [31]. Y. Zhou, C.L. Law, Y.L. Guan, and F Chin, "Indoor elliptical localization based on asynchronous UWB range measurement", Trans. On Instrumentation and Measurements, 2011, 60, n. 1, pp. 248–257.
- [32]. W. Kim, J.-G. Lee, and G.-I. Jee. The interior-point method for an optimal treatment of bias in trilateration location. Vehicular Technology, IEEE Transactions on, 55(4):1291-1301, 2006.
- [33]. J. J. C. Jr. Wireless Location in CDMA Cellular Radio Systems. 2000.
- [34]. D. Zhang, F. Xia, Z. Yang, L. Yao, and W. Zhao, "Localization technologies for indoor human tracking," in Proc. 5th Int. Conf. Future Inf. Technol. (FutureTech), 2010, pp. 1–6.
- [35]. D. Chu "Polyphase codes with good periodic correlation properties", IEEE Trans. Inf. Theory, vol. 18, no. 4, pp.531 -532 1972.
- [36]. T. Yan-bo, G. Wan-cheng, "Symbol synchronization algorithm based on Pseudo-superimposed Zadoff-Chu in Advanced-LTE", Asia-Pacific Conference on Information Processing, pp. 140-143, 2009.

- [37]. M. M. U. Gul, X. Ma, S. Lee, “Timing and Frequency Synchronization for OFDM Downlink Transmission Using Zadoff-Chu Sequences”, *IEEE Transaction on Wireless Communications*, vol. 14, no. 14, March 2015.
- [38]. Molisch A.F., Cassioli D., Chong C., et al, “A comprehensive standardized model for ultrawideband propagation channels”, *IEEE Trans. Antennas Propag.*, 2006, 54, (11), pp. 3151-3166, doi:10.1109/TAP.2006.883983.
- [39]. A. Saleh and R. A. Valenzuela, “A statistical model for indoor multipath propagation,” *IEEE J. Selected Areas Comm.*, vol. 5, pp. 138–137, Feb. 1987.
- [40]. C.-C. Chong, Y.-E. Kim, S. K. Yong, and S.-S. Lee, “Statistical characterization of the UWB propagation channel in indoor residential environment,” *Wireless Commun. Mobile Comput.*, vol. 5, pp. 503–512.
- [41]. R. C. Qiu and I.-T. Lu, “Wideband wireless multipath channel modeling with path frequency dependence,” in *Proc. IEEE Int. Conf. Commun.*, Dallas, TX, Jun. 1996, pp. 277–281.
- [42]. Y. S. Cho, J. Kim, W. Y. Yang, and C. G. Kang, “MIMO-OFDM Wireless Communications with MATLAB”, Singapore: John Wiley & Sons (Asia) Pte Ltd, 2010.
- [43]. 802.11 Wireless Networks, The definitive guide, Matthew S. Gast, O'Reilly 2002.
- [44]. T. Ayhan, W. Dehaene, M. Verhelst, “A method for using sub-Nyquist sampling for ultra-low-power positioning systems”, *IEEE Workshop on Signal Processing Systems (SiPS)*, Oct. 2013, Taipei City, Taiwan.
- [45]. Moose, P.H. (1994) A technique for orthogonal frequency division multiplexing frequency offset correction. *IEEE Trans. Commun.*, 42, 2908–2914.
- [46]. Yan-bo, G. Wan-cheng, “Symbol synchronization algorithm based on Pseudo-superimposed Zadoff-Chu in Advanced-LTE”, *Asia-Pacific Conference on Information Processing*, pp. 140-143, 2009.
- [47]. A. Quazi, “An overview on the time delay estimate in active and passive systems for target localization,” *Acoustics, Speech and Signal Processing*, *IEEE Transactions on*, vol. 29, no. 3, pp. 527 – 533, June 1981.
- [48]. K.-D. Kammeyer, Mann R. and W. Tobergte, “A Modified Adaptive FIR Equalizer for Multipath Echo Cancellation in FM Transmission”, *IEEE J. Select. Areas Commun.*, vol. 5, no. 2, pp. 226–237, 1987.

- [49]. K.-D. Kammeyer, "Multipath Echo Cancellation in FM transmission using adaptive FIR filters", IEEE Proc. of Inter. Conf. on Acoustics, Speech, and Signal Processing (ICASSP), Tokyo, Japan, April 1986.
- [50]. H. Date, K. Fukudome and S. Kondo, "Automatic Cancellation Method of Multipath echo distortion", IEEE Trans. On Broadcasting, vol. BC-28, no. 2, June 1982.
- [51]. B. E. Fischer and I. J. LaHaie, "Echo Characterization based on Maximum-Likelihood Estimation for Antenna-Measurement Correction", IEEE Antennas and Propagation Magazine, vol. 54, no. 2, April 2012.
- [52]. R. E. Kalman, "A new approach to linear filtering and prediction problems," J. Basic Eng., vol. 82, no. 1, pp. 35–45, Mar. 1960.
- [53]. LTC5586, 6GHz High Linearity I/Q Demodulator with Wideband IF Amplifier, datasheet available on-line on [www.analog.com](http://www.analog.com).
- [54]. ADF5355, Microwave Wideband Synthesizer with Integrated VCO, datasheet available on-line on [www.analog.com](http://www.analog.com).
- [55]. RO4003C, Laminates datasheet available on-line on [www.rogerscorp.com](http://www.rogerscorp.com).
- [56]. DAC3482, Dual-Channel, 16-Bit, 1.25-GSPS, 1x-16x Interpolating Digital-to-Analog Converter (DAC), datasheet available on-line on [www.ti.com](http://www.ti.com).
- [57]. D. M. Pozar, Microwave Engineering. New York: Wiley, 2006.
- [58]. ADE-35+, Ultra broadband double balanced mixer, datasheet available on-line on [www.minicircuits.com](http://www.minicircuits.com).
- [59]. ADF4355, Microwave Wideband Synthesizer with Integrated VCO, datasheet available on-line on [www.analog.com](http://www.analog.com).
- [60]. ADL5611, 30 MHz to 6 GHz RF/IF Gain Block, datasheet available on-line on [www.analog.com](http://www.analog.com).
- [61]. ADL5535, 20 MHz to 1.0 GHz IF Gain Block, datasheet available on-line on [www.analog.com](http://www.analog.com).
- [62]. LMK04828, LMK0482x Ultra Low-Noise JESD204B Compliant Clock Jitter Cleaner with Dual Loop PLLs, datasheet available on-line on [www.ti.com](http://www.ti.com).
- [63]. C. A. Balanis, "Antenna Theory Analysis and Design", Wiley, 2005.

- [64]. F. Silveira, D. Flandre, P.G.A. Jespers, "A gm/ID based methodology for the design of CMOS analog circuits and its application to the synthesis of a Silicon-on-Insulator micropower OTA", *IEEE Journal of Solid-State Circuits*, 31 (1996) 1314-1319.
- [65]. A. Elad "EE240: Advanced Analog Integrated Circuits". Lecture Notes, UC Berkeley, 2010.
- [66]. W. S. Percival, "Thermionic Valve Circuits," British Patent Specification no. 460,562, filed 24 July 1936, granted January 1937.
- [67]. J.-C. Kao, P. Chen, P.-C. Huang, and H. Wang, "A novel distributed amplifier with high gain, low noise, and high output power in 0.18- $\mu\text{m}$  CMOS technology," *IEEE Trans. Microwave Theory Technologies*, vol. 61, no. 4, pp. 1533–1542, Apr. 2013.
- [68]. Y. Yu, Y. Chen, and D. Heo, "An ultra-low voltage UWB CMOS low noise amplifier," in *Proc. of Asia-Pacific Microwave Conf.*, Yokohama, Japan, Dec. 2006, pp. 313–316.
- [69]. K. Moez and M. Elmasry, "A low-noise CMOS distributed amplifier for ultra-wideband applications," *IEEE Trans. Circuits Syst. II, Exp. Briefs*, vol. 55, no. 2, pp. 126–130, Feb. 2008.
- [70]. S. Jose, H.-J. Lee, and D. Ha, "A Low-Power CMOS Power Amplifier for Ultra-Wideband (UWB) Applications," in *IEEE International Symposium on Circuits and Systems*, vol. 5, May 2005, pp. 5111–5114.
- [71]. Moez, K., and Elmasry, M.I.: 'A 10 dB 44 GHz loss-compensated CMOS distributed amplifier'. *IEEE Int. Solid-State Circuits Conf.*, San Francisco, CA, USA, February 2007, pp. 548–549.
- [72]. Pollissard-Quatremère G., Gosset G, Flandre D., "A modified gm/ID design methodology for deeply scaled CMOS technologies", *Analog Integrated Circuit and Signal Processing*, Springer, 78 (2014), 771-784.
- [73]. J.-F. Chang and Y.-S. Lin, "Low-power, high-gain and low-noise CMOS distributed amplifier for UWB systems," *Electron. Lett.*, vol. 45, no. 12, pp. 634–636, 2009.
- [74]. Y. J. Wang and A. Hajimiri, "A compact low-noise weighted distributed amplifier in CMOS," in *IEEE Int. Solid-State Circuits Conf.*, 2009, pp. 220–221.
- [75]. G. D. Nguyen, K. Cimino, and M. Feng, "A RF CMOS amplifier with optimized gain, noise, linearity and return loss for UWB applications," in *IEEE Radio Freq. Integrated Circuits Symposium*, 2008, pp. 505–50.

- [76]. K. H. Chen and C. K. Wang, "A 3.1-10.6 GHz CMOS cascaded two stage distributed amplifier for ultra-wideband application," in Proc. IEEE Asia-Pacific Conf. Adv. Syst. Integrated Circuits (AP-ASIC), Aug. 2004, pp. 296–29.
- [77]. B. Gilbert, "A Precise Four-Quadrant Multiplier with Sub-nanosecond Response," IEEE J. Solid-State Circuits, vol. SC-3, pp. 365–373, Dec. 1968.
- [78]. L. MacEachern, and T. Manku, "A Charge-Injection Method for Gilbert Cell Biasing", Proceeding of the IEEE Canadian Conference on Electrical and Computer Engineering (CCECE 98), pp. 365-368, 1998.
- [79]. B. Wei, Y. Dai, Y. Lu, X. Zhang, H. Liu, "A sub IV high-gain Low-Noise CMOS downconversion folded mixer for 2.4GHz ISM band applications," International Symposium on Intelligent Information Technology Application Workshops, Dec. 2008, pp.689-692.
- [80]. J.-B. Seo, K.-M. Park, J.-H. Kim, J.-H. Park, Y. S. Lee, J.-H. Ham and T.-Y. Yun, "A Low-Noise UWB CMOS Mixer Using Switched Biasing Technique," Singapore, RFIT2007-IEEE International Workshop on Radio Frequency Integration Technology, Dec. 9-11, 2007.
- [81]. Motieifar, A.; Pour, Z.A.; Bridges, G.; Shafai, C., "An Ultra-Wideband (UWB) Mixer with 0.18UM RF CMOS Technology" 2006 Canadian Conference on Electrical and Computer Engineering (CCECE), pp. 697 - 700. May 2006.
- [82]. Y. Gao, F. Huang, L. Wu, and J. Cheng, "A Low-Power Reconfigurable Mixer for MB-OFDM UWB Receivers," in Microelectronics Electronics, 2009. Asia Pacific Conference on Postgraduate Research PrimeAsia 2009, pp. 97–100, Jan.
- [83]. Chen I-C. and Yang J.-R., "2 - 13GHz Broadband CMOS Low Voltage Mixer with Active Balun Designed for UWB Systems" IEEE International Conference of Electron Devices and Solid-State Circuits (EDSSC) 2010, pp. 1-4, Dec. 2010.
- [84]. C.-H. Wu and H.-T. Chou, "A 1.2-V High-Gain UWB Mixer Utilizing Current Mirror Topology," in IEEE International Conference on Ultra-Wideband (ICUWB), 2010, vol. 1, pp. 1–4, Sept.
- [85]. G. Piccinni, C. Talarico, G. Avitabile, G. Coviello, "A Novel Design Optimization Framework for Regulated Cascode Transimpedance Amplifiers", accepted for oral presentation in IEEE European Conference on Circuit Theory and Design (ECCTD), 4-6 Sept. 2017 Catania, Italy.

## Publications by author

- [1].G. Piccinni, G. Avitabile, C. Talarico, G. Coviello “Distributed Amplifier Design for UWB positioning systems using the gm over id methodology”, IEEE International Conference on Synthesis, Modeling, Analysis and Simulation Methods (SMACD), June 2016, Lisbon Portugal.
- [2].G. Piccinni, G. Avitabile, G. Coviello, “An Improved Technique based on Zadoff-Chu Sequences for Distance Measurements”, IEEE 4th Radio and Antenna Days of the Indian Ocean (RADIO), 10-13 October 2016, Reunion Island.
- [3].G. Piccinni, G. Avitabile, C. Talarico, G. Coviello, “Gm over ID for UWB Distributed Amplifier”, IEEE 59th Midwest Symposium on Circuit and Systems (MWSCAS), 16-19 October 2016 Abu Dhabi, United Arab Emirates.
- [4].G. Piccinni, G. Avitabile, C. Talarico, G. Coviello, “UWB Distributed Amplifier Design using Lookup Tables and Gm over ID methodology” Springer Journal “Analog Integrated Circuits and Signal Processing”.
- [5].G. Piccinni, C. Talarico, G. Avitabile, G. Coviello, “Gilbert cell mixer design based on a novel systematic approach for nanoscale technologies”, Wireless and Microwave Technology Conference (WAMICON), 2017 IEEE 18th, 24-25 April 2017 Cocoa Beach FL, USA.
- [6].G. Piccinni, G. Avitabile, G. Coviello, “A novel Distance Measurement Technique for Indoor Positioning Systems based on Zadoff-Chu Sequences”, IEEE 15th International New Circuits and Systems Conference (NEWCAS), 25-28 June 2017, Strasburge, France.
- [7].G. Piccinni, C. Talarico, G. Avitabile, G. Coviello, “A Novel Optimization Framework for the Design of Gilbert Cell Mixers”, accepted for poster presentation in IEEE 60th Midwest Symposium on Circuit and Systems (MWSCAS), 6-9 August 2017 Boston, USA.
- [8].G. Piccinni, C. Talarico, G. Avitabile, G. Coviello, “A Novel Design Optimization Framework for Regulated Cascode Transimpedance Amplifiers”, accepted for oral presentation in IEEE European Conference on Circuit Theory and Design (ECCTD), 4-6 Sept. 2017 Catania, Italy.
- [9].G. Piccinni, G. Avitabile, G. Coviello, “Narrowband Distance Evaluation Technique for Indoor Positioning Systems based on Zadoff-Chu Sequences”, IEEE 13th International Conference on Wireless and Mobile Computing, Networking and Communications (WiMOB), 09-11 October 2017, Rome, Italy.

- [10]. G. Piccinni, G. Avitabile, G. Coviello, “Analysis and Modeling of a Novel SDR-based High-Precision Positioning System”, IEEE International Conference on Synthesis, Modeling, Analysis and Simulation Methods (SMACD), July, Prague, Czech Republic.